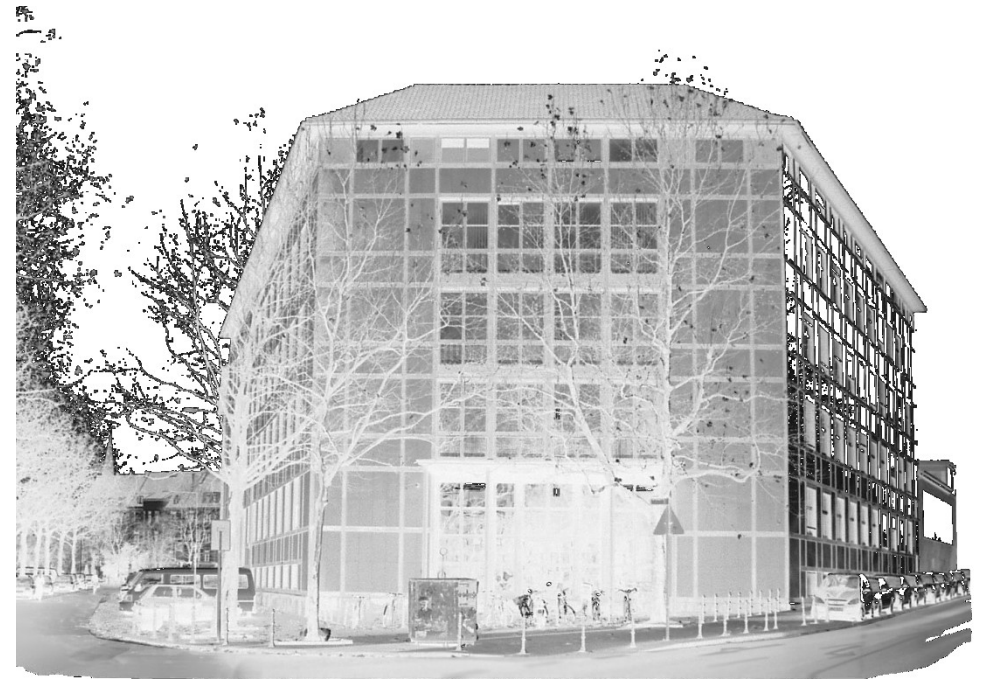


Microporosity Characteristics in Al-Si Foundry Alloys

Moritz Rudolf Martin Weidt



ISBN 978-3-944601-16-8 (E-Book)

Band 27



Ergebnisse aus Forschung und
Entwicklung
Herausgeber:
Prof. Dr.-Ing. A. Bührig-Polaczek

„Microporosity Characteristics in Al-Si Foundry Alloys“

Von der Fakultät für Georessourcen und Materialtechnik
der Rheinisch-Westfälischen Technischen Hochschule Aachen

zur Erlangung des akademischen Grades eines
Doktors der Ingenieurwissenschaften

genehmigte Dissertation
vorgelegt von **M.Sc. RWTH**

Moritz Rudolf Martin Weidt

aus Duisburg

Berichter: Univ.-Prof. Dr.-Ing. Andreas Bührig-Polaczek
Univ.-Prof. Dr.-Ing. Arne K. Dahle

Tag der mündlichen Prüfung: 07. Januar 2020

Diese Dissertation ist auf den Internetseiten der Universitätsbibliothek online verfügbar

Titel: *Microporosity Characteristics in Al-Si Foundry Alloys*

Autor: Moritz Rudolf Martin Weidt

Reihe: Ergebnisse aus Forschung und Entwicklung, Band 27 (2020)

Gießerei-Institut der RWTH Aachen

Intzestr. 5

D-52072 Aachen

Tel.: +49 (0)241 8095880

Fax.: +49 (0)241 8092276

E-Mail: sekretariat@gi.rwth-aachen.de

<http://www.gi.rwth-aachen.de>

ISBN: 978-3-944601-16-8 (E-Book)

Volltext verfügbar: [10.18154/RWTH-2020-03260](https://nbn-resolving.org/urn:nbn:de:hbz:5:1-63862-p0083-9)

D 82 (Diss. RWTH Aachen University, 2020)



Dieses Werk bzw. Inhalt steht unter einer Creative Commons Namensnennung-Keine Bearbeitung 3.0 Unported Lizenz ([Creative Commons Attribution-NoDerivs 3.0 Unported License](https://creativecommons.org/licenses/by-nc/3.0/))

Publikationsserver
Universitätsbibliothek
RWTH Aachen University
Templergraben 61
52062 Aachen
www.ub.rwth-aachen.de



Acknowledgements

The way from the first idea to the finished publication of a doctoral thesis is a long and winding path and without the guidance of many colleagues, my family and friends, I might have got lost it.

Since it was the beginning of this journey, the initial idea, first I would like to thank Dr Erwin Flender for initiating and enabling the conception of this thesis in the first place. His support was continued by Dr Marc Schneider, and for the provided aid and advice of both, I am very grateful.

I also want to thank Prof. Dr Andreas Bührig-Polaczek for providing advice. Crucial ideas that strongly shaped the way this work developed were given by Prof. Dr Christoph Beckermann, which is highly appreciated. Special thanks belong to Prof. Dr Arne Dahle, who not only inspired by hours of discussion the trajectory of this thesis, but who also helped many times in the conduction, analysis, and interpretation of experiments, who provided countless ideas, and who became a good friend on the way. Many thanks belong to Dr Dirk Schnubel, who provided essential experimental resources, as well as Toni Bogdanoff, who contributed a lot of work to the presented results.

My father Peter-Michael Weidt planted my interest in science, engineering, and technology, and thus without him, I might not have even started on the way to this thesis. My mother Brigitte Weidt and sister Lisa Greiwe supported me to keep on going even in times when I could not see the destination of this journey.

Finally, my wife Yun Zhang has to be mentioned, since she was my greatest support and provided me with the endurance and determination to complete this work. Not only did she lend me strength, but she also gave me the freedom to find my way.

非常感谢你 - 我爱你

Suzhou, People's Republic of China, 26 May 2019
Moritz Weidt

Funding

A substantial part of the results presented in this work was generated in the K2-MPPE-Project A1.20 “Integration der Gießsimulation in die betriebsfeste Bauteilauslegung von Aluminium-Gussbauteilen”.

This research was supported by the Nematik Linz GmbH, Nematik Dillingen GmbH, Materials Center Leoben GmbH, Department of Product Engineering of the Montanuniversität Leoben, AVL List GmbH, Magma Gießereitechnologie GmbH, Austrian Federal Government (Bundesministerium für Verkehr, Innovation und Technologie und Bundesministerium für Wissenschaft, Forschung und Wirtschaft) represented by Österreichische Forschungsgesellschaft mbH (FFG), Styrian and the Tyrolean Provincial Government represented by Steirische Wirtschaftsförderungsgesellschaft mbH (SFG), and Standortagentur Tirol within the COMET research program.

Contents

0. Short version.....	I
0.1. Introduction	I
0.2. Experimental procedure.....	II
0.3. Results and discussion	III
0.3.1. Industrial castings.....	III
0.3.1.1. Maximum envelope diameter versus porosity.....	III
0.3.1.2. Sphericity	V
0.3.2. Wedge casting experiments	VII
0.3.2.1. Maximum envelope diameter versus average porosity.....	VIII
0.3.2.2. Sphericity	XII
0.3.3. Synopsis of wedge castings and industrial castings.....	XIV
0.4. Conclusions	XIX
1. Introduction	1
1.1. Aluminium history and cost.....	1
1.2. Aluminium alloys	1
1.3. Casting defects.....	3
1.3.1. Macrosegregation	3
1.3.2. Inclusions	3
1.3.3. Stresses and distortion	3
1.3.4. Cavities and porosity	4
1.3.5. Discontinuities in filling	4
1.4. Porosity in aluminium and its alloys	5
1.5. Objectives and outline.....	7
2. Literature review.....	10
2.1. Fundamentals of solidification.....	10
2.1.1. Primary phase	10
2.1.1.1. Nucleation.....	10

2.1.1.2.	Grain refinement	17
2.1.1.3.	Dendritic growth	19
2.1.2.	Eutectics.....	27
2.1.2.1.	Coupled zone	33
2.1.3.	Segregation	35
2.1.4.	Freezing range.....	37
2.1.4.1.	Mushy zone.....	37
2.1.4.2.	Feeding mechanisms	40
2.2.	Porosity	41
2.2.1.	Nucleation and growth of pores.....	43
2.2.1.1.	Fundamental equations.....	43
2.2.1.2.	Pressure drop in the mushy zone.....	44
2.2.1.3.	Al-H phase diagram	45
2.2.1.4.	Hydrogen solubility	46
2.2.1.5.	Pore morphology.....	48
2.2.1.6.	Pore nucleation	50
2.2.1.7.	Gas diffusion and pore growth	53
2.2.2.	Porosity in Al-Si alloys	54
2.2.2.1.	Grain size and grain refinement.....	54
2.2.2.2.	Shrinkage	56
2.2.2.3.	Hydrogen effect.....	57
2.2.2.4.	Cooling rate and thermal gradient.....	58
2.2.2.5.	Inclusions and bifilms	59
2.2.2.6.	Effect of Si	61
2.2.2.7.	Sr and Na modification	61
2.2.2.8.	Effect of Cu and Mg.....	66
2.2.2.9.	Fe intermetallics.....	67

2.2.2.10.	Mn effect on porosity.....	70
2.2.2.11.	Surface tension.....	71
2.2.3.	Modelling of porosity.....	73
2.2.3.1.	Analytical models.....	73
2.2.3.2.	Criterion functions.....	74
2.2.3.3.	Numerical models.....	75
3.	Experimental procedure.....	77
3.1.	Preliminary castings experiments.....	77
3.2.	Industrial castings.....	83
3.2.1.	Crankcase.....	85
3.2.2.	Cylinder head.....	87
3.3.	Wedge casting experiments.....	90
3.4.	HYDRAL 40® and NITRAL 10® tablets.....	94
3.5.	HYCAL® hydrogen measurement system.....	95
3.6.	X-ray tomography.....	97
3.7.	Analysis of XCT-Data.....	98
4.	Results and discussion.....	100
4.1.	Preliminary casting experiments.....	100
4.1.1.	First experimental set.....	100
4.1.2.	Second experimental set.....	105
4.1.3.	Summary.....	108
4.2.	Industrial castings.....	109
4.2.1.	Porosity distribution.....	110
4.2.2.	Spherical and envelope diameter versus average porosity.....	114
4.2.3.	Maximum versus mean diameters.....	119
4.2.4.	Pore morphology.....	122
4.2.5.	Sphericity.....	130
4.2.6.	Prediction of the pore size distribution.....	132

4.2.7.	Summary.....	136
4.3.	Wedge casting experiments	137
4.3.1.	Hydrogen adjustment and measurement.....	138
4.3.2.	Spherical diameter and envelope diameter versus average porosity...	152
4.3.3.	Maximum versus mean diameters	164
4.3.4.	Pore morphology.....	168
4.3.5.	Sphericity	177
4.3.6.	Synopsis of wedge castings and industrial castings.....	182
4.3.6.1.	Spherical and envelope diameter versus average porosity	182
4.3.6.2.	Maximum versus mean diameters.....	190
4.3.6.3.	Sphericity	193
4.3.7.	Summary.....	196
5.	Conclusions.....	202
6.	Future work	205
7.	Bibliography.....	206
8.	Curriculum vitae.....	230
9.	Scientific publications.....	231

0. Short version

0.1. Introduction

Aluminium is a fascinating material in applications where a maximised ratio of Young's modulus to the square or cubic density is needed. These applications are first of all in the aerospace industry but more and more also in other transportation applications like lightweight vehicles. Due to the high corrosion resistance, the excellent thermal and electrical conductivity, the good formability and joining capabilities, aluminium is also favoured in many other applications like construction, packaging, and for electrical purposes.

Due to the nature of casting and solidification, there are a variety of possible casting defects. They can be related to the melting process, the handling of the melt before casting, external materials (e.g. crucible material) or gases (e.g. atmosphere above the melt's surface) that are introduced into the melt, the filling process, the mould or the fundamental solidification process.

Microporosity (in this work also just called porosity) is one of the most common defects in castings. Especially technical alloys with a wide solidification range show the strong tendency to form porosity even in areas with a large thermal gradient and small solidification rate. As long as the solidification interface is not perfectly smooth and the aluminium's gas level is above its solid solubility, micropores most likely form. If pores are trapped in the developing solid microstructure, they can develop fundamentally different shapes. This is illustrated in Figure 0-1, which shows a so-called shrinkage pore (a) and a so-called gas pore (b).

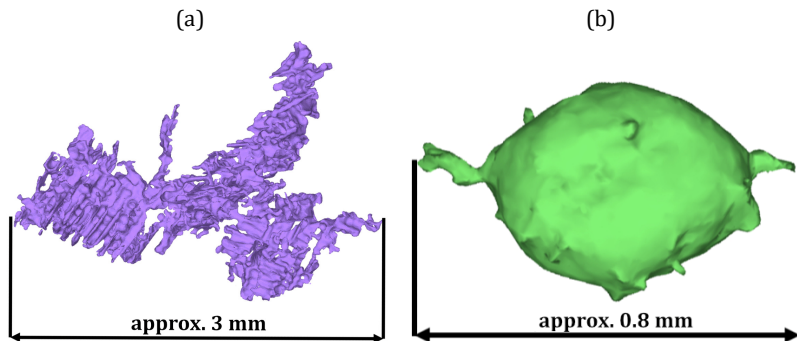


Figure 0-1: XCT-rendering of a pore which presumably formed in the late-stages of solidification (a) and of a pore which presumably formed in the initial stages of solidification (b).

If the largest discontinuity in an aluminium cast volume is a pore, it is the limiting factor for the expected local fatigue life (1–6). Thus, the prediction of the pore size distribution characteristics, based on the understanding of the causes for different pore morphologies, is of paramount importance regarding the general usefulness of a porosity prediction and the primary goal of this work.

First, an extensive industrial, experimental program is presented, which was aimed at illuminating the effect of industrial solidification conditions on the local amount and distribution characteristics of microporosity. Second, based on the findings from the industrial casting trials, laboratory wedge experiments were conducted to investigate the role of hydrogen and cooling rate on microporosity in Al-Si foundry alloys.

The experimental results from both experiments are illustrated, contextualised and discussed. Significant established relations between the total amount of porosity, pore size and pore morphology are presented. Finally, the roles of the hydrogen content and of cooling rate during the solidification of aluminium cast alloys are mapped out.

0.2. Experimental procedure

In the industrial casting trials, two engine components, a cylinder head and a crankcase were cast to investigate porosity amount and characteristics under industry conditions. These castings are representative of a broad range of aluminium cast components and cover, due to the use of a permanent mould process (cylinder head, Rotacast®) as well as a sand casting process (crankcase, CPS), a wide range of solidification rates. The castings produced in the Rotacast® process were rotary degassed once prior to the start of the production sequence. In summary, four characteristic cast alloy/cast part combinations were produced: first, AlSi8Cu3, Sr-modified, cylinder head; second, AlSi8Cu3, Sr-modified, crankcase; third, AlSi7Cu0.5Mg, Sr-modified, cylinder head; fourth, AlSi7Cu0.5Mg, Na-modified, cylinder head. In total sixty XCT samples were extracted from the four characteristic cast part/cast alloy combinations, fifteen from each set, five from each extraction position.

In the wedge casting experiments, twelve castings were produced to characterise average porosity amount and pore size characteristics under laboratory conditions. The layout of the sand mould with the wedge casting, chill, filter, and casting system was developed by Nematik Dillingen GmbH (Germany) to reproduce microstructures representative of the above described industrial castings (primarily the CPS process). The same two alloys, which were used in the production of the industrial castings, were cast. Additional to the local solidification rate, the quantitative hydrogen

content of the aluminium melt was determined by the HYCAL® hydrogen analyser system.

The scanned XCT data was divided into pore volume and dense material, which was done by a self-determined consistent threshold value on the upper border of an acceptable threshold range. The resolution of the resulting pore volumes was artificially increased by a digital superresolution image technique (7). Adjacent pores were “merged” and analysed as one bigger pore if a certain distance to pore size threshold was met or exceeded (8). The maximum diameter of the convex pore envelope was defined as the maximum envelope diameter $d_{e,max}$, sometimes also described as maximum Feret’s diameter.

The morphology of a pore was described by its sphericity ψ_i . If the calculation of the sphericity was not possible (because the surface area was not determinable) or if the calculated value was unreasonable ($\psi_i > 1$), it was excluded from the analysis. Especially at the lower resolution limit of the XCT-scan, the determination of the pore surface was not possible or very inaccurate. A volume-weighted mean sphericity ψ_{mean} , from here on only called mean sphericity, was introduced to describe the prevailing pore morphology in each specimen. It proved itself to be insensitive to the influences of resolution and small pore detection accuracy.

0.3. Results and discussion

0.3.1. Industrial castings

A total of 60 XCT specimens were analysed from two industrial aluminium castings. The whole span of typical solidification ranges of an industrial permanent mould, as well as sand mould process, were covered. Two alloys, AlSi8Cu3 and AlSi7Cu0.5Mg, were cast, two different eutectic modifiers were used and two castings, a cylinder head and a crankcase, were produced. From each casting, specimens from three positions of different solidification time were extracted, scanned, and evaluated.

0.3.1.1. Maximum envelope diameter versus porosity

In Figure 0-2 the plot of the maximum envelope diameter $d_{e,max}$ versus the average porosity g_p is shown. In general, a v-shape of the data can be observed. Based on this observation, the data is divided into two characteristic specimen populations; both populations are linearly fitted. First, the grey population (from here on called GP), consisting of the experimental sets AlSi8Cu3(Sr) cylinder head and AlSi7Cu0.5Mg(Sr) cylinder head, marked by grey points. The alloys show a significant difference in their Cu contents, but both are produced in the same process

(Rotacast® process). Second, the black population (from here on called BP), consisting of the experimental sets AlSi8Cu3(Sr) crankcase and AlSi7Cu0.5Mg(Na) cylinder head, marked by black points. The composition differences are again the same, but additionally, the eutectic modifier and the casting process differ (AlSi8Cu3(Sr) cast in the CPS and AlSi7Cu0.5Mg(Na) cast in the Rotacast® process). Both populations are fitted by a linear fit function of the respective colour. The GP shows a much steeper slope than the BP. This means the GP is far more sensitive to changes in porosity than the BP. The maximum envelope diameter $d_{e,max}$ is a direct measure of the defect size in the casting and therefore of high relevance for the prediction of defect size.

It is remarkable that in Figure 0-2 two distinguishable trends are observable. Especially above approximately 0.1 % porosity, the differences become evident. The BP consists of two production processes and Sr and Na-modified castings. There are significant differences in Cu content (approximately 2.5 wt%) and moderate differences in Si content (approximately 1 wt%) in both populations. It can be concluded that the composition differences are not directly responsible for the two observable porosity trends. The only difference is the strongly increased maximum porosity level of the AlSi8Cu3(Sr) relative to the AlSi7Cu0.5Mg(Sr) for the GP.

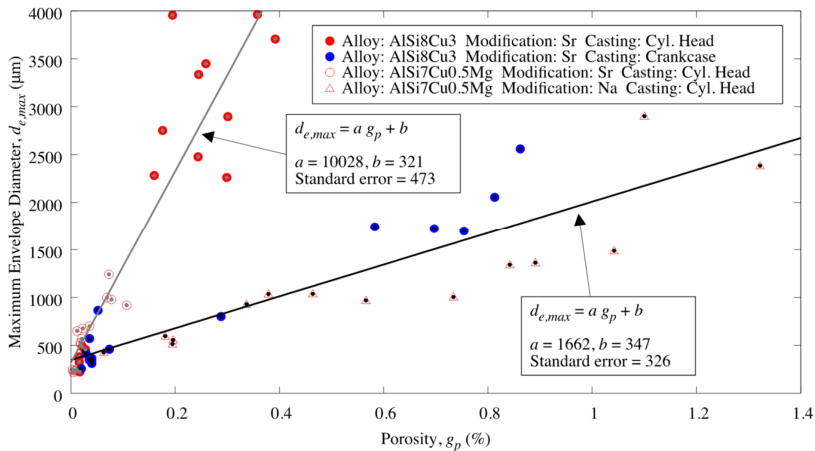


Figure 0-2: Plot of the maximum envelope diameter $d_{e,max}$ versus the average porosity g_p . Two populations are recognisable, the grey population (GP) marked by grey points and fitted by the grey line, and the black population (BP) marked by black points and fitted by the black line (224).

The higher porosity level of the alloy AlSi8Cu3(Sr), compared to the alloy AlSi7Cu0.5Mg(Sr), can be explained by several mechanisms. Cu destabilises the eutectic solidification front and leads to a eutectic mushy zone (9). The result is a reduced permeability and earlier pore formation. Moreover Cu, in conjunction with Sr-modification, increases the eutectic cell sizes and thus the size of the liquid pockets which cannot be fed at the end of solidification (10–16). Finally, Cu enlarges the solidification interval (which in turn reduces the feedability at the end of solidification), and the Al₂Cu phase shows a significant volumetric shrinkage of approx. 8.4 vol%, which is difficult to compensate.

Another difference between both alloys is the Fe content. The secondary alloy AlSi8Cu3(Sr), used for the crankcase, contains approximately 0.6 wt%, the one used for the cylinder head contains approximately 0.4 wt% Fe. Compared to the primary alloy AlSi7Cu0.5Mg(Sr), used for the cylinder head, which contains about 0.1 wt% Fe, these level are much higher. Nevertheless, all alloys contain enough Mn to ensure a favourable formation of α -Al₁₅(Fe,Mn)₃Si₂ instead of β -Al₅FeSi (all show a Mn/Fe ratio of approximately 0.65) and thus to eliminate most of the detrimental effects associated with β -Fe formation (17–26). Villeneuve et al. (24) observed the same amount of porosity in experiments with AlSi6Cu4, once cast with 1.4 wt% Fe and 0.5 wt% Mn and once with 0.37 wt% Fe and 0.05 wt% Mn. Iwahori et al. (23) found for AlSi7Cu3 with 1.15 wt% Fe a reduction in porosity for Mn additions from 0.2 to 0.3 wt% and Dinnis (27) was able to show that the reduced Al-Si nucleation frequency due to Fe additions was again increased after Mn additions. Why only the GP seems to be affected by the differences in Cu content will be discussed in the following sections.

0.3.1.2. Sphericity

The mean sphericity φ_{mean} is calculated for every specimen to quantify the pore morphology and is shown in Figure 0-3, plotted against the average porosity g_p . As in Figure 0-2, the four experimental sets are divided into the same two characteristic populations, the GP and BP. For both, a correlation with three constants is developed.

As before, the BP fits the experimental results of the experimental sets AlSi8Cu3(Sr) crankcase and AlSi7Cu0.5Mg(Na) cylinder head. At 0.01 % porosity, the fit function runs towards the limit unity. Above 0.2 % porosity, the mean sphericity becomes constant at 0.56.

The grey curve fits the specimens of the experimental sets AlSi8Cu3(Sr) cylinder head and AlSi7Cu0.5Mg(Sr) cylinder head (GP). If the porosity runs towards 0, the mean sphericity runs towards 0.8. For the maximum porosity of about 0.4 % in this

population, the sphericity drops to 0.2, and theoretically to the constant value of 0.08.

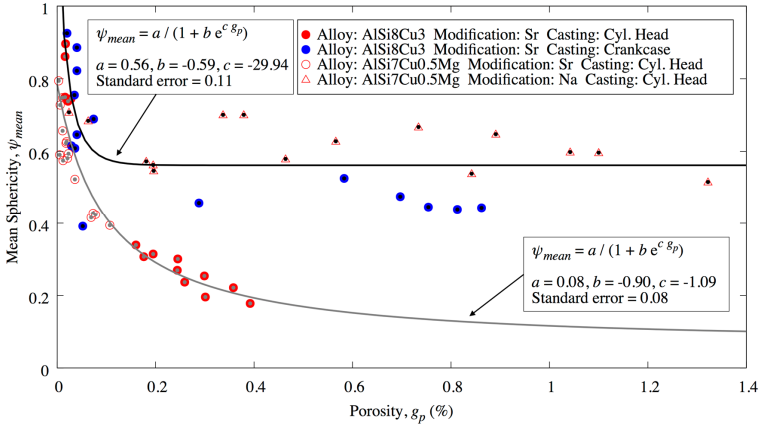


Figure 0-3: Plot of the mean sphericity versus the porosity. Grey dots mark the points considered in the grey population correlation; black points are used in the black population correlation [224].

Both functions show high sphericity values at low average porosity levels. The BP samples keep a high sphericity even at high porosity levels, which demonstrates that even large pores exhibit a highly spherical shape. The mean sphericity values of the AlSi8Cu3(Sr) crankcase are slightly lower compared to the AlSi7Cu0.5Mg(Na) cylinder head specimens, which means the limiting value of the first would be slightly lower compared to the second. The mean sphericity of the GP continuously decreases with increasing porosity. The pores are only able to grow into the solid dendritic network, and their surface area increases more strongly than that of a volume equivalent sphere.

In specimens with low porosity, the pores have enough space to grow, and impingement between pores and solid phase hardly happens. Moreover, these pores are primarily in contact with the eutectic phase, which is the only possible conclusion if impingement is not dominant. Felberbaum et al. [28] show that pores which are in contact with the eutectic show positive mean curvatures to satisfy the Laplace-Young equation, which is in agreement with the presented results. In general, for very small pores the driving force to minimise the surface energy results in highly spherical pores. This effect becomes less dominant the bigger a pore becomes. For both populations, the sphericity decreases with increasing porosity,

which can be explained by an increasing pore-solid impingement. The effect is limited in case of presumably gas-induced porosity due to its earlier nucleation, so impingement happens later and only if the hydrogen level is sufficiently high (BP). As Murphy et al. showed (29) in solidification experiments with a grain-refined AlCu20 alloy at low cooling rates, these spherical pores may even be able to push equiaxed crystals away to increase their individual space to grow unhindered while maintaining their spherical shape. The result is a relatively constant mean sphericity even at high average porosity levels. The observed behaviour also corresponds to the work of Puncreobutr et al. (30) who observed the in-situ growth of an individual pore. They measured a sphericity drop from about 0.83 to 0.6 between nucleation and a pore volume of 0.025 mm^3 ($d_s = 363 \text{ }\mu\text{m}$). Afterwards, the sphericity was observed to be constant at 0.6 up to a pore volume of and 0.054 mm^3 ($d_s = 469 \text{ }\mu\text{m}$). This pore size is equivalent to a medium-sized high sphericity pore in the present work and is very close to the constant sphericity of 0.56 for the BP for specimens of 0.2 % porosity or higher. Moreover, the initial sphericity value in Puncreobutr et al.'s work of 0.83 corresponds well with the limiting value of the GP of 0.8 if the grey fit function is extrapolated towards zero.

In case the Na modified AlSi7Cu0.5Mg cylinder head castings, the modification treatment most probably led to a strong hydrogen uptake from the atmosphere. It is reported in the literature by Thiele (31) and has been observed in experiments by Mulazimoglu et al. (32) that Na additions change the structure of the oxide layer on the aluminium surface and increase its permeability for hydrogen. The high mean sphericity values of the AlSi8Cu3(Sr) crankcase specimens are probably also associated with an increased hydrogen level, which might be introduced by the production process itself (CPS).

The level of the average porosity is one of the key factors for both specimen populations, which determines the mean sphericity. Nevertheless, g_p itself may be primarily affected by the chemical composition, eutectic modification, Fe-phases, hydrogen level or solidification rate. The second key parameter is a possible link between the hydrogen level of a sample and its mean sphericity. The mean sphericity seems to be a central porosity characteristic which could be used to determine the general behaviour of the porosity-pore distribution characteristic.

0.3.2. Wedge casting experiments

A total of 36 XCT specimens from 12 wedge castings were analysed. Two alloys, AlSi8Cu3(Sr) and AlSi7Cu0.5Mg(Sr) were cast and are very close to the alloys which were used for the industrial castings. By melt treatment, different hydrogen levels were adjusted, and quantitative hydrogen measurements were done by the state-

of-the-art measurement system "HYCAL". The goal of the wedge casting experiments was to investigate the (quantitative) effect of hydrogen and cooling rate in commonly used aluminium cast alloys on the amount, distribution, and characteristics of microporosity. This was achieved by producing a wedge casting that was designed to reproduce the solidification characteristics of the industrial CPS process.

The HYCAL measurement was not as reproducible as expected based on preceding discussions with the supplier company. The low measurement reproducibility could be attributed to the melt treatment by tablet additions, which might interfere with the measurement. The upgassing capabilities of the used HYDRAL 40® tablets seem to be limited, possibly by the low surface area of the released hydrogen-containing bubbles during submersion. Nevertheless, for applications in typical foundry practice, the achievable hydrogen levels seem to be sufficient.

The degassing capabilities of the used NITRAL 10® tablets are questionable. If the changes in porosity and DI can be attributed to the removal of hydrogen or stem from a cleaning effect or the deactivation of potential nuclei remains unclear. There are points for both theories, and also a combination of both is possible.

In the following section, the XCT results of the wedge casting experiments are presented, discussed, and compared to the XCT results generated from the industrial castings. Additionally, the results of the industrial casting experiments should be assessed in the context of the additional available information.

0.3.2.1. Maximum envelope diameter versus average porosity

The same XCT data analysis procedure as for the industrial castings is applied to obtain the maximum envelope diameter ($d_{e,max}$). Two important, influential factors were varied in the wedge castings. First, the hydrogen level determined by quantitative HYCAL hydrogen measurements. Second, the cooling rate by producing a wedge casting and extracting samples at different wedge thicknesses. The local cooling rate of each specimen is represented by the secondary dendrite arm spacing, from here on called DAS.

Figure 0-4 shows two plots of the maximum envelope diameter ($d_{e,max}$) versus the average porosity level (g_p) for each XCT specimen. The colour in Figure 0-4(a, b) indicates hydrogen content and dendrite arm spacing, respectively. There is a general increase in maximum envelope diameter with increasing porosity level. Three specimen populations seem distinguishable (see Figure 0-4(b)). In the low porosity region ($g_p < 0.5\%$) there is a very steep increase of maximum envelope diameter with porosity. Although the identification of this high gradient specimen populations might seem somewhat questionable based solely on Figure 0-4, the later presented Figure 0-6 will identify this population as a separate individual group.

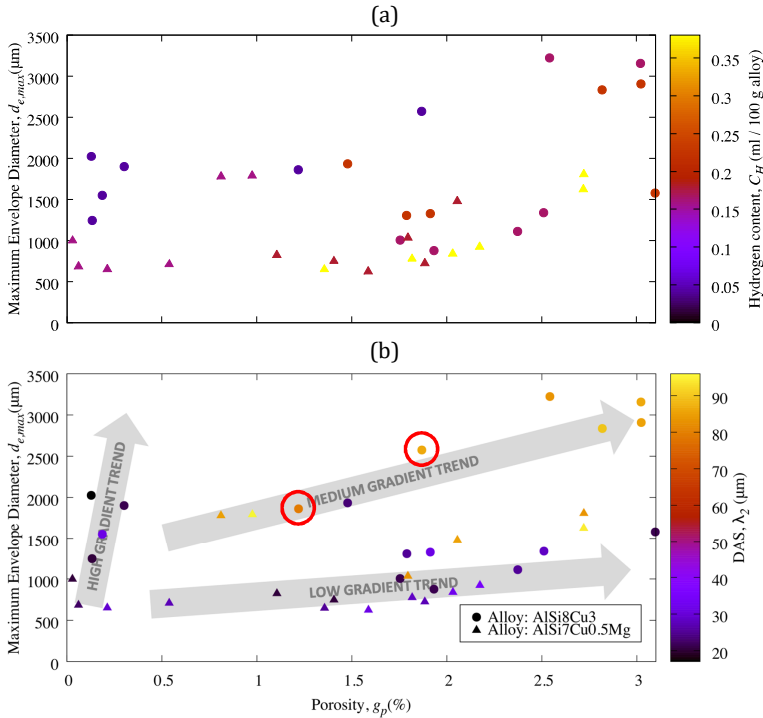


Figure 0-4: Plot of the maximum envelope diameter $d_{e,max}$ versus the average porosity g_p . The hydrogen content (a) and DAS (b) are colour-coded in the respective plots. Three presumable trends are indicated in (b). Two red circles mark specimens that are of low hydrogen level (0.04 ml / 100 g) but do not follow the GP trend line.

These samples are all low in hydrogen level, density index and dendrite arm spacing. Mind that two samples of 0.04 ml / 100 g in hydrogen show much more porosity (up to $g_p = 1.87\%$) than all the other samples of the lowest hydrogen level. These two do not follow the high gradient trend. Nevertheless, since these samples are also very different in DAS ($\lambda_2 = 79$ and $86\ \mu\text{m}$), and in this way separated from the other samples ($\lambda_2 = 17\text{--}31\ \mu\text{m}$), a different behaviour can be explained (both samples are marked by red circles in Figure 0-4(b)). The second specimen trend is characterised by a medium gradient and comprised of samples of larger DAS ($\lambda_2 \geq 83\ \mu\text{m}$). The hydrogen level of these samples is mostly in the medium range of the wedge casting

experiments ($C_H = 0.157 - 0.224$ ml / 100 g). The third presumable trend consists of the low DAS samples ($\lambda_2 \leq 34$ μm), with medium to high hydrogen content ($C_H = 0.157 - 0.380$ ml / 100 g). These samples only show a slow increase of the maximum envelope diameter with increasing porosity level.

In Figure 0-4, no indication of the influence of the alloy on the data is shown. Two alloys were cast with a significant difference in chemical composition. The alloy AlSi8Cu3 contains approximately 1 wt% more Si, 2.5 wt% more Cu, 0.1 wt% less Mg, and 0.3 wt% (about four times) more Fe than the alloy AlSi7Cu0.5Mg. The higher alloying level of the AlSi8Cu3 alloy is expected to lead only to a minor increase in solidification interval (due to the contrary effects of Si and Cu addition on the solidification interval), but to a significant extension of the terminal freezing range. Based on a calculation with the software package JMatPro®, the terminal freezing range, between a solid fraction of 85 % and 95 % (TFR₈₅₋₉₅), increases from approximately 18.5 K to 38 K from AlSi7Cu0.5Mg to AlSi8Cu3. For well-degassed melts, this difference is likely the cause of a significant increase in average porosity as was observed in the experimental sets AlSi7Cu0.5Mg(Sr) cylinder head in comparison to the AlSi8Cu3(Sr) cylinder head set, as described in Section 0.3.1 (“Industrial castings”). The extended terminal freezing range is thought to lead to an increase in average porosity by extending the width of the mushy zone and reduce the local feedability in the final stages of solidification.

No systematic influence of the chemical composition can be found in the wedge castings. This could be an indication of higher hydrogen levels, compared to the extensively rotary degassed cylinder head castings (industrial castings), and thus a higher share of the local volume deficit is compensated by early nucleation of hydrogen-induced pores, or later nucleated hydrogen inflated shrinkage pores. Interestingly, there is also no significant difference in the porosity level of two the experimental sets of industrial castings AlSi7Cu0.5Mg(Na) cylinder head and AlSi8Cu3(Sr) crankcase, which were also speculated to contain an elevated amount of hydrogen. It is possible that a certain amount of hydrogen in the melt can “mask” the porosity difference, which is normally expected due to the difference in the solidification characteristics. It cannot be proven by the presented results, but there might be three mechanisms that would explain the suppression of late-stage pores if early-stage porosity formed. First, the total volume deficit, which is created by the solidifying microstructure, is limited. If early pore nucleation compensates a substantial amount of the volume deficit, a sufficient pressure drop in the final solidification stage which leads to “shrinkage” porosity might not occur. Second, the number of potent nuclei in the melt might be limited. If early forming pores, due to hy-

drogen supersaturation, activate most of the potent nuclei, there might not be sufficient nuclei left for late-stage pores to form. Third, if early-stage pores form, they might interact with the equiaxed dendritic grains by pushing and thus rearrange the solid structure of the solidifying dendritic network, which in turn might lead to a change in the distribution of liquid pockets in the melt. As a result, the isolation or occurrence of these pools at the end of solidification might not take place to the same degree. It is also possible that two or all three mechanisms are working at the same time and in conjunction inhibit late-stage pore formation.

The correlation between the hydrogen content and maximum envelope diameter to porosity is marginal. Besides the maximum envelope diameter, the only clear indication is that samples containing below 1 % of porosity also show a relatively low hydrogen level. The two previously introduced samples, which are marked by red circles, are exceptions to the general observation. Both are low hydrogen level, but one of them shows up to 1.87 % porosity. It appears that if a certain amount of hydrogen is not exceeded, the average porosity can be low, but does not have to be. If the hydrogen level becomes higher (in the case of the presented results above 0.179 ml / 100 g), there are no samples which exhibit less than 1 % porosity, which suggests that a low hydrogen level is necessary, but not a sufficient condition to produce low porosity samples. Vice versa, if a specific hydrogen content is exceeded, it seems not to be possible to produce low porosity samples, even under high cooling rates as indicated by Figure 0-4(b). This hypothesis is not entirely in agreement with the modelling work by Carlson et al. (33). Carlson et al. predicted, based on a model which incorporates the effect of shrinkage, the induced feeding flow, local pressure variations, and the finite-rate hydrogen diffusion, that a sufficiently high cooling rate suppresses the hydrogen-induced pore formation and reduces the general average porosity level. In the present data, there are multiple samples, which show a clear indication of high hydrogen content and at the same time have a very low dendrite arm spacing (correlated to a high local cooling rate). These samples do not show the behaviour proposed by Carlson et al. It is possible that the local cooling rate was not sufficiently high to suppress pore nucleation, but DAS values of almost half the samples below 25 μm indicate the contrary. The stage in which the pores nucleate during solidification might change significantly for different hydrogen levels, and the assumptions of Carlson et al. are based on a pore-dendritic-network interaction which, if the pore formation occurs early, might not influence the final amount of porosity significantly. These explanations should be indicated by the pore morphology. If pores nucleate early during solidification, high sphericity would be expected. If the pores nucleate later in the solidification sequence, a more tortuous shape is to be expected. This aspect is discussed further in light of the presented analysis of the mean sphericity (see Section 0.3.2.2).

The dendrite arm spacing has the most noticeable effect on the shown characteristic measures. In Figure 0-4(b), the maximum defect size does seem to show a pronounced sensitivity to DAS, especially in combination with the hydrogen content. If a low hydrogen level goes along with a high solidification rate (low DAS), the maximum pore size shows a strong dependency on average porosity (high gradient population).

In case of the low hydrogen level samples, limited hydrogen agglomeration probably did not allow early pore formation. The dendritic network grew until a high fraction solid was reached. At this point, much of the total volume deficit would be still uncompensated, and because of the highly developed solid network, a significant local pressure drop is likely to occur. At this point the local feedability dropped to such a degree that the pressure was low enough to nucleate “shrinkage pores”. In this stage, every pore has only very little space, mostly in the interdendritic space. This way little pore volume can lead to the formation of large tortuous pores. A pushing of dendrites by growing pores can be excluded at this stage since the solid network is way past the dendrite coherency point and should have developed a measurable and significant shear strength and deformation resistivity (34–38).

0.3.2.2. Sphericity

Figure 0-5 shows the plot of mean sphericity versus average porosity. In Figure 0-5(a, b) colour indicates the hydrogen content and dendrite arm spacing, respectively. All 36 samples from the wedge castings exhibit a mean sphericity between about 0.25 and 0.83. A separation of the samples in different specimen populations is not as easily possible as in the previously presented figure of the maximum envelope diameter versus porosity. Nevertheless, all samples with a hydrogen level of 0.04 ml / 100 g, except the two previously identified samples of much higher DAS (also discussed by Figure 0-4(b)), seem separated from the other samples of higher hydrogen content and show a drop in mean sphericity with increasing porosity level (marked by “DROP IN SPHERICITY”). The higher hydrogen samples show a high mean sphericity value that does not decrease even at average porosity levels up to 3.1 %. In Figure 0-5(b) the plot of the mean sphericity versus porosity does not indicate any connection between sphericity and the dendrite arm spacing. There are samples with low and high DAS values showing high or low mean sphericity. As was discussed in the previous paragraph, samples of lower average porosity are also low in DAS, but low DAS samples can be found up to the highest porosity level of about 3.1 %, and they do not differentiate themselves in regard of their mean sphericity.

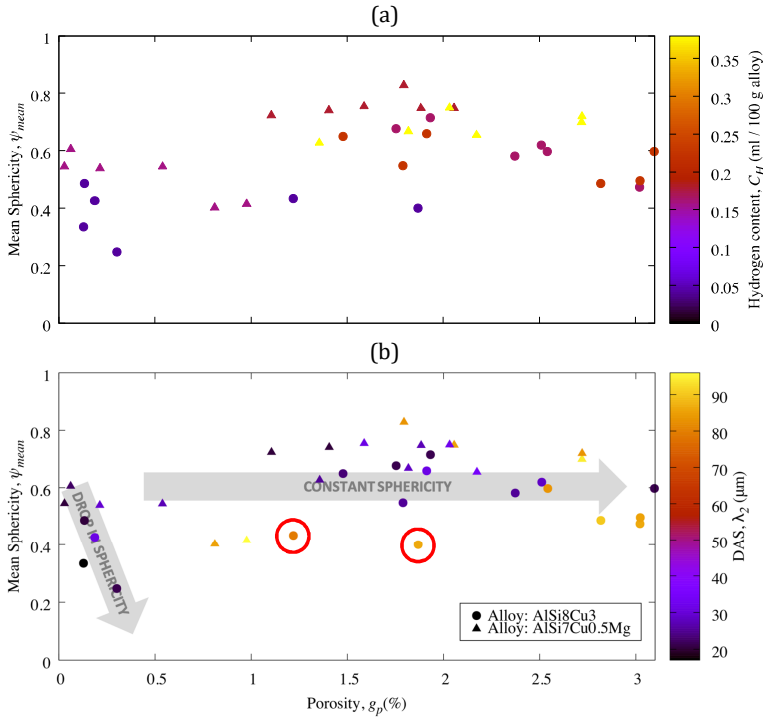


Figure 0-5: Plot of the mean sphericity ψ_{mean} versus the average porosity g_p . The hydrogen content (a) and DAS (b) are colour-coded in the respective plots. Two pre-sustainable trends are indicated in (b). Two red circles mark specimens that are of low hydrogen level (0.04 ml / 100 g) but do not show the drop in sphericity.

The samples which show a drop in mean sphericity with increasing average porosity can be directly linked to the identified high gradient population in the plot of the maximum envelope diameter versus porosity (Figure 0-4). Just as the maximum envelope diameter ($d_{e,max}$) seems directly linked to the average porosity and may follow three distinct trends, the mean sphericity of the samples of the wedge castings shows two independent trends. This means, mean sphericity wise, that the pore population of low hydrogen and low DAS can be distinguished by mean sphericity from all other samples, but the other two pore populations which were identified before (the low and high DAS samples with higher hydrogen content) are indistin-

guishable in the presented mean sphericity versus porosity plot. The presented results suggest that there is a fundamental difference between the pore nucleation and growth stage during solidification for low (0.04 ml / 100 g) and high (above 0.157 ml / 100 g) hydrogen levels with a relatively sharp turnover point.

If the mean sphericity (which is volume-weighted) is high, it means that the largest pores in those samples are also of high sphericity on average. The question arises how the largest pores up to high average porosity levels and at a significant volume can retain a highly spherical shape. In general, there seem to be two explanations for a high mean pore sphericity in a specimen. The first explanation for a high mean sphericity value is that small pores are formed. These small pores fit into the interdendritic spaces and are primarily in contact with the eutectic and of high sphericity to satisfy the Laplace-Young equation (as Felberbaum et al. (28) showed), which might have been the case for the identified medium to high hydrogen level (above 0.157 ml / 100 g), low DAS (up to 34 μm) population in Figure 0-4. The high cooling rates of these low DAS samples are thought to limit the hydrogen redistribution by diffusion in the melt and produce a large number of highly spherical, relatively small pores. The second possible explanation for high mean sphericity, even at low cooling rates and higher porosity levels, is an early pore formation of high sphericity pores. This formation is probably driven by extensive hydrogen redistribution, facilitated by a high hydrogen content and lower cooling rates of the melt. These pores have to nucleate before the dendrite coherency point to be able to push dendrites away to increase their room for further growth while retaining their highly spherical shape. As stated before, Murphy et al. (29) showed in experiments with an AlCu20 alloy that early nucleating pores, at a solid fraction of only 0.13, can push equiaxed dendritic crystals away. This way a significant amount of the total volume deficit due to solidification can be compensated in an early stage and only a few (or none at all) large pores can form in the final stage of solidification. A significant amount of porosity (up to 3.1 % in the presented data) seems to be able to form without much impingement of the largest pores. The second explanation seems more likely in case of the high hydrogen level (above 0.157 ml / 100 g), high DAS (above 83 μm) specimens.

0.3.3. Synopsis of wedge castings and industrial castings

Figure 0-6 shows the plot of the maximum envelope diameter versus porosity for the industrial castings and additionally the wedge castings. Colour indicates the DAS of the wedge samples. The industrial castings are shown as the two identified specimen populations: grey population (GP) and black population (BP), which were introduced in Section 0.3.1.1. The low DAS, low hydrogen wedge samples follow the

GP linear trend. The wedge samples of high DAS seem to be positioned slightly below the BP trend line, whereas the low DAS, high hydrogen wedge samples form a new fourth correction with the lowest sensitivity of the maximum envelope diameter to porosity. As discussed before, these last two specimen populations can be linked to a high or very high hydrogen level (especially in case of the lowest gradient population).

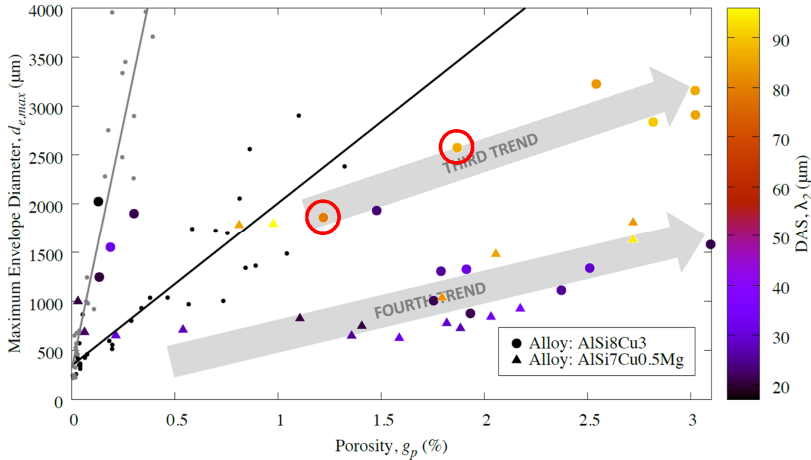


Figure 0-6: The maximum envelope diameter $d_{e,max}$ versus the average porosity g_p for all 96 conducted XCT scans of this work is shown. The industrial castings are shown as the grey and black population, as introduced in Section 0.3.1.1, marked by grey and black points and fitted by the grey and black linear functions. Additionally, the specimens of the wedge castings are shown with the DAS indicated by colour. Two red circles mark specimens that are of particular interest because they are of low hydrogen level (0.04 ml / 100 g) but do not show the drop in sphericity.

Only if the DAS is low (up to $\lambda_2 = 31 \mu\text{m}$), the low hydrogen samples of the wedge experiments follow the GP. For the other wedge samples, the DAS becomes the determining factor if a specimen is better described by the BP or rather a slightly lower third trend (high DAS samples) or if it is better described by a fourth, new, small-gradient correlation (low DAS).

One explanation could be that the samples following the GP fit curve, both the industrial castings and wedge samples, only show this strong sensitivity to increasing porosity up to a certain critical DAS. This threshold seems to be between the largest DAS value of the industrial casting samples of the GP, $\lambda_2 = 67 \mu\text{m}$, and the lower DAS

value of the before mentioned two wedge samples of low hydrogen, $\lambda_2 = 79 \mu\text{m}$ (marked by red circles in Figure 0-6). It seems plausible that if the dendritic structure becomes more coarse, the available space for pore growth in the last stages of solidification also become larger and thus a growing pore does not have to spread as strongly between the existing dendrites as for smaller DAS. Since the total volume deficit should change less than the available space between the dendrites, primarily the degree of pore-dendrite interaction would change. Without impingement, the dendrite interaction could cease quite abruptly and the driving force for the strong increase in maximum envelope diameter is lost. Moreover, sufficiently low cooling rates might lead to hydrogen precipitation, even at very low hydrogen levels. The sharp drop in solubility during solidification and very long solidification times are likely to lead extensive hydrogen redistribution and to nucleation or inflation events. The observed threshold behaviour is better explained by a nucleation than an inflation mechanism. Inflation should occur even below critical hydrogen levels and continuously. A steady change of the porosity type with increasing hydrogen level or solidification time would be the result. Instead, an abrupt morphology change is observed between the DAS values of $67 \mu\text{m}$ and $79 \mu\text{m}$ and, consequently, a nucleation mechanism seems more reasonable to operate.

A second characteristic threshold might explain the degree of pore-dendritic network interaction in case of the BP industrial samples and the higher hydrogen wedge samples. At medium hydrogen levels (probably the case for the BP samples) the sensitivity for the coarseness of the microstructure starts to get lost because now, for the first time, hydrogen-driven pores nucleate. In transition cases, both types of porosity (gas-driven and shrinkage-driven pores) might be present. If the pore number density is sufficiently high, they should be able to retain a high sphericity and show a low cooling rate sensitivity. Large pores, which can be expected at low solidification rates (hydrogen redistribution), might even start to push equiaxed dendrites during growth to avoid substantial impingement. It can be speculated that some of the wedge samples probably contained even more hydrogen than the industrial castings, based on the high hydrogen measurements. This would explain some deviation from the BP trend line (compare "THIRD TREND" in Figure 0-6). If on the other hand at high hydrogen levels the cooling rate is high (small DAS) the number density of hydrogen-induced pores increases and each pore becomes smaller; thus the pore-solid interaction becomes irrelevant for the final characteristic pore size.

Figure 0-7 shows the plot of mean sphericity versus average porosity, both, the industrial samples (here indicated as grey and black points) and the wedge samples, are shown. In the case of the wedge samples colour indicates the specimens' DAS.

One can see that the samples from the wedge castings which exhibit a low DAS, low porosity, and a low hydrogen level (as presented before) seem to follow the GP trend line which shows a sharp initial decrease of mean sphericity with increasing porosity. The majority of the wedge castings exhibit high mean sphericity at the same level as the industrial castings samples which follow the BP trend line. The black trend line seems able to describe the specimen behaviour for these samples up to 3.1 % porosity. Wedge specimens of large and small DAS are well described by the BP trend line throughout the whole porosity range. Two cases of particular interest are the samples marked by red circles. These specimens were previously marked in Figure 0-4, Figure 0-5, and Figure 0-6 and were discussed regarding their maximum envelope diameter and mean sphericity behaviour. Both show a large DAS of up to 86 μm , but they belong to the differently behaving low hydrogen samples of the wedge experiments (which follow the GP trend line).

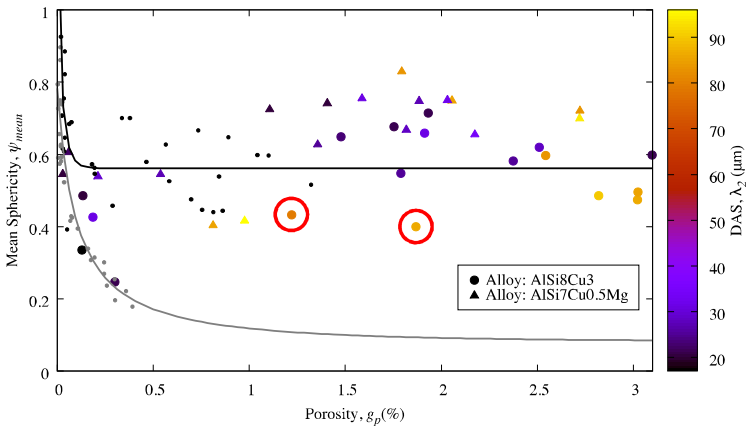


Figure 0-7: The plot of the mean sphericity ψ_{mean} versus the average porosity g_p . The industrial castings are shown as the grey and black population, as introduced in Section 0.3.1.1, marked by grey and black points and fitted by the grey and black functions. Additionally, the specimens of the wedge castings are shown with the DAS indicated by colour. Two red circles mark specimens that are of particular interest.

It is worth noting that the high porosity samples (close to the black fit function) do not seem to decrease in mean sphericity, which means that the largest pores are highly spherical up to porosity values of about 3.1 %. As an example, the wedge sample with the highest observed porosity level of 3.1 % should be mentioned. This sample exhibits a mean sphericity of 0.6, which is very close to the limiting value of

the BP trend line of 0.56, and at the same time a DAS of only 21 μm . Two explanations would account for this behaviour. First, pores in samples of high porosity, low DAS, and high mean sphericity form and grow rapidly and early before the dendritic network reaches dendrite coherency and equiaxed dendrite pushing seems unrealistic, or second, a high number density of hydrogen-induced pores, most of them small enough to avoid pore-dendrite impingement, form. In the case of the previously mentioned specimen showing 3.1 % porosity, the maximum envelope diameter is about 1500 μm . In aluminium foundry practice for grain refined Al-Si alloys (e.g. AlSi8), grain sizes between 500 to 1000 μm are typically observed, which means that a potential octahedra gap of 566 μm ($0.7 \times 800 \mu\text{m}$) should be available as a potential space for pore growth without significant impingement and that larger pores are likely to start to impinge with the solid network quite significantly. In this case, a drop in mean sphericity should be a consequence. For the previously mentioned sample with a maximum envelope diameter of about 1500 μm , this explanation seems not plausible; thus in case of larger maximum envelope diameters, the theory of dendrite pushing seems more likely. In cases where specimens show a lower porosity level, which goes along with a lower maximum envelope diameter, the second mechanism may also be feasible. Possibly, both mechanisms do occur and a transition from first to the second takes place, dependent on cooling rate. It might also be the case that in samples of high hydrogen level, pores always nucleate very fast and lead to a rearrangement of the crystalline solidifying structure. This rearrangement could decouple the pore shape from the total pore volume and the cooling rate.

The crankcase castings and the Na modified AlSi7Cu0.5Mg cylinder head castings form the experimental database for the black fit function. The hydrogen level of the high sphericity wedge experiment samples, which can also be described by the black fit function, gave readings from 0.157 to 0.380 ml / 100 g. All these samples show a high and constant mean sphericity over porosity. The thoroughly rotor degassed industrial cylinder heads cast from AlSi8Cu3(Sr) and AlSi7Cu0.5Mg(Sr), as well as the wedge casting samples showing a low DAS and a low hydrogen level of 0.04 ml / 100 g, show a strong and continued drop in mean sphericity over porosity. This finding suggests a turnover point for the hydrogen level between 0.04 and 0.157 ml / 100 g which in turn determines the characteristic sphericity behaviour of a sample. As outlined before, a very low cooling rate seems also to be able to pull a sample with low hydrogen content into the characteristic specimen regime that is described by high constant mean sphericity (turnover point between $\lambda_2 = 67$ and 79 μm).

0.4. Conclusions

In the industrial casting experiments, a wide range of process conditions was varied to investigate the effects on average porosity and pore size distributions in foundry practice. To cover a wide industrial application range, two alloys (AlSi8Cu3 and AlSi7Cu0.5Mg) were cast in two different industrial processes (Rotacast® and CPS). Since the XCT scanning resolution strongly affects the number density of pores in the evaluated specimens, a volume-weighted mean sphericity was chosen to enable comparative evaluations of the pore shape characteristics.

In general, the industrial data can be divided into two characteristic specimen populations. The first shows a high sensitivity of the maximum pore size regarding the average porosity level; the second one shows a lower sensitivity. Both correlations are linear correlations and show increasing maximum pore size with increasing porosity. The analysis of the characteristic pore shape in the form of the mean sphericity reveals significant differences between both specimen populations. Low sphericity pores dominate the high sensitivity population; high sphericity pores dominate the low sensitivity population. The argument is developed, that the pore nucleation stage is decisive for the formed characteristic pore morphology, in other words, early or late pore nucleation and growth relative to the progressively developing solid network.

The two identified specimen populations are independent of the alloy, process, modification or cooling rate, but the hypothesis of a hydrogen dependency is developed, which is then more closely examined in the laboratory wedge casting experiments.

In the wedge experiments, castings, which are capable of reproducing a microstructure gradient that can be found in the CPS process, were produced. All experimental conditions were adapted for the best comparison with the industrial castings. Additionally, the hydrogen content was manipulated by tablet treatments and measured by a state-of-the-art hydrogen measurement system (HYCAL).

The HYCAL system did not allow hydrogen control as accurately as anticipated. Two reasons for this behaviour were discussed, the tablet treatment itself, which might disturb the measurement system, and the degassing capability of the tablet treatment, which can be questioned based on the observed porosity development.

In separate evaluations of the XCT data from the wedge experiments and joint evaluations together with the data generated in the industrial casting experiments, the following further conclusion can be drawn. The previously introduced specimen population which shows a high sensitivity regarding the maximum pore size on average porosity is most likely correlated to low hydrogen contents. The second specimen population identified in the industrial casting experiments is probably of low

to medium hydrogen content and in some cases might be of a mixed shrinkage and gas-driven porosity type. Up to a characteristic dendrite arm spacing of 67 μm , no significant influence of cooling rate on both populations can be identified. For samples containing only a little hydrogen, between 67 and 79 μm DAS a shift from low sphericity, late-stage porosity, to higher sphericity, early-stage porosity seems to occur. By analysis of the wedge casting experiments, two additional pore populations can be identified and are improving the understanding of the connection between solidification rate and hydrogen level. The first newly identified population shows a slightly lower, the second newly identified population shows a much lower sensitivity of pore size to porosity compared to the industrial casting pore populations. These two new specimen populations are most likely correlated to high hydrogen levels and show a strong sensitivity to cooling rate. High cooling rates lead to the lowest sensitivity of pore size to porosity.

Figure 0-8 summarises the developed hypotheses on the development of microporosity based on the evaluation of the industrial casting experiments, together with the wedge casting experiments and all the available information.

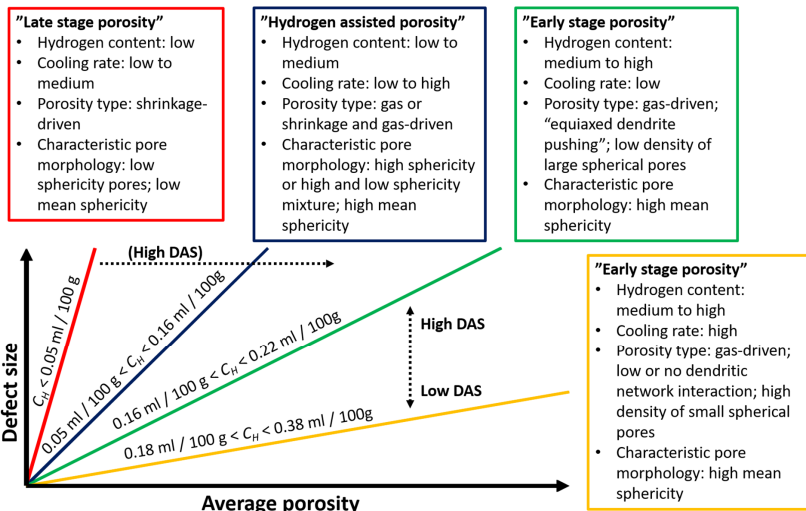


Figure 0-8: Schematic illustration of the results of the conducted experiments regarding the defect size of a micropore versus average porosity. The proposed mechanisms leading to the observed changes are indicated, as is the influence of the hydrogen content as well as the local cooling rate (by DAS).

The presented results improve the understanding of the correlation between aluminium alloy composition, solidification conditions, gas content, and the resulting pore size as well as morphology. The developed correlations will improve the capabilities of the Integrated Computational Materials Engineering (ICME) approach. These correlations are the first steps in a through process modelling framework which begins with the prediction of the microstructural features including the maximum pore size. All subsequent steps (e.g. heat treatment, machining and in-service performance) are based on this prediction, and thus it is of paramount importance for the fatigue proof design of new aluminium cast components.

1. Introduction

1.1. Aluminium history and cost

In 1808 Davy concentrated aluminium for the first time from its natural ore. He named it after the already well-known aluminium salt alum (double sulphate salts) (39). In 1825 Ørsted produced aluminium in his laboratory followed by Wöhler, a German scientist, a few years later. In 1855 St.-Claire Deville began with the small scale industrial production of aluminium. He used a chemical process and presented a slab of 97 % pure aluminium at the world exhibition in 1855. At that time aluminium had a price of about 130 £/kg, and so the use was limited. This changed after Hall in Ohio and Héroult in France supplanted the chemical process by the electrolysis process, which is in principle still used today. This process used the ability of cryolite, a sodium aluminium fluoride, to dissolve alumina above 900 °C. Despite the tremendous amount of electrical energy that was needed, the price of aluminium dropped to about 5.5 £/kg. In 1892 Bayer developed a process to extract alumina very cost-efficiently from Bauxite, which is a natural ore that contains up to about 50 % alumina. By this improvement and the opportunity to access relatively cheap energy, the aluminium price sank to about 0.5 £/kg. Today aluminium is an exchange-traded metal and its price is highly volatile. In 2005 the rate peaked at about 2 £/kg, in 2008, it dropped to about 0.8 £/kg, and today it is about 1.1 £/kg. Besides speculation, the economic demand and the production capacities, the energy consumption of aluminium production is a significant price trigger. The approximate energy content of one ton of aluminium is about 50×10^9 joule, which is up to three times the amount for steel (40).

Aluminium is a fascinating material in applications where a maximised ratio of Young's modulus to the square or cubic density is needed. These applications are first of all in the aerospace industry but more and more also in other transportation applications like lightweight vehicles. Due to the high corrosion resistance, the excellent thermal and electrical conductivity, the good formability and joining capabilities, aluminium is also favoured in many other applications like construction, packaging, and for electrical purposes.

1.2. Aluminium alloys

Pure aluminium is very soft. It has a tensile strength of about 17 MPa and an ultimate tensile strength of about 45 MPa. To improve the mechanical properties, one has to use alloying elements. There are two categories in which aluminium alloys are divided, the cast alloys and the wrought alloys (40). Cast alloys usually contain a higher amount of alloying element additions compared to wrought alloys because

these are not just used to increase the mechanical properties but also the castability. In Table 1-1 the denominations of the cast and wrought alloys are summarised. The first digit characterises the alloy's main alloying elements. For the high purity alloying systems of the 1XX.X and 1XXX series, the second, third, and in case of wrought alloys, the fourth digit stands for the purity level of the alloy. For the other systems digit two and three (cast alloy) and digit two, three, and four (wrought alloy) identify each particular alloy without an explicit systematic. Cast alloys also specify the product form by their last digit behind the comma. In the case of final shape casting zero is used. Sometimes a serial letter before the numerical code designates a modification of the original alloying composition.

Table 1-1: Aluminium Association alloy designation system

Cast alloys	Series	Wrought alloys	Series
Al ≥ 99.00 %	1XX.X	Al ≥ 99.00 %	1XXX
Cu	2XX.X	Cu	2XXX
Si + Cu or Mg	3XX.X	Mn	3XXX
Si	4XX.X	Si	4XXX
Mg	5XX.X	Mg	5XXX
Zn	7XX.X	Mg and Si	6XXX
Sn	8XX.X	Zn	7XXX
Other	9XX.X	Other	8XXX
Unused	6XX.X	Unused	9XXX

Both, cast alloys and wrought alloys can be categorised in heat-treatable alloys and non-heat treatable alloys. The first reaches its final mechanical properties only after a heat treatment, which produces finely dispersed precipitates. The second relies mainly on solid solution strengthening and work hardening to achieve the final mechanical properties. Usually, wrought alloys are further processed and by this processing many imperfections due to the prior casting (commonly DC casting) are healed. Typical process steps are rolling, stamping, forging or extrusion processes. For cast alloys, on the other hand, there is no further massive processing after the casting itself (apart from machining and heat treatment), and so all imperfections due to the solidification remain almost unaffected.

1.3. Casting defects

Due to the nature of casting and solidification, there are a variety of possible casting defects. They can be related to the melting process, the handling of the melt before casting, external materials (e.g. crucible material) or gases (e.g. atmosphere above the melt's surface) that are introduced into the melt, the filling process, the mould or the fundamental solidification process. A rough categorisation of the possible casting defects is given hereafter.

1.3.1. Macrosegregation

Macrosegregation describes the inhomogeneous solute distribution on a macroscopic scale after solidification of a casting. Elements that segregate strongly, like Cu in aluminium, enrich in the liquid during solidification. Convection of the liquid, redistribution of grains (movement of the solid) or stresses (e.g. thermal stresses) that push the liquid out of or into the mushy zone can lead to this type of defect. All efforts to prevent macrosegregation are aimed at controlling the flow of the liquid or movement of the solid (41).

1.3.2. Inclusions

Inclusions are particles or gas bubbles which are not originated from the melt itself but stem from external sources and which are introduced into the melt at different times of its processing. For high purity applications – like foil – impurities have to be avoided in any case. For typical cast applications, the harmfulness of inclusions depends on their size. If an inclusion is big enough to initiate a crack, it should be avoided. In some cases, inclusions like TiB_2 in aluminium are introduced on purpose to achieve an inoculation effect on the primary phase. Another kind of inclusion to be mentioned is the entrained gas defect. In the case of poor melt handling and turbulent mould filling, atmospheric air may be entrapped in smaller or bigger bubbles or in other words double oxide films - “bifilms” - as suggested by John Campbell (42). These gas-filled cavities tend to “heal” to some degree, but the entrapped oxygen and nitrogen is consumed with time by oxidation processes with the aluminium (or magnesium if available).

1.3.3. Stresses and distortion

Stresses occur during solidification if the solidification shrinkage or the thermal contraction during cooling cannot be compensated by liquid feeding or if thermal gradients lead to a non-uniform contraction in adjacent solidified areas. Both cases are practically always found in real castings. The stresses not only influence the heat extraction through the mould during solidification by gap formation (reduction of

heat transfer) or shrinkage on cores or mould structures (an increase of heat transfer) but they can also lead to segregation effects by sucking in or pushing out the liquid from the mushy zone. Hot tears in partly solidified regions or cold cracks in the fully solidified areas are major defects due to stress build-up (43). If the local shrinkage cannot be compensated by liquid feeding and the strength of the surface material is not sufficient, surface deformations are possible. Dimensional deviations of the casting, in general, are also a possible reason for the casting's rejection. Finally, residual stresses in the as-cast condition or after heat treatment can favourably or unfavourably be superimposed on application loads and thus improve or deteriorate fatigue properties.

1.3.4. Cavities and porosity

Holes in castings can occur on different size scales and due to many reasons. One source of a cavity type defect can be core gas that is generated during the degradation of binders in sand cores. If the gas pressure in the core exceeds the local pressure (metallostatic head) the possibility of core blows is given.

Macroporosity is often observable in regions of late/last solidification (hot spot). If an isolated volume of liquid metal is not macroscopically fed, the volume deficit due to the solidification shrinkage has to be compensated by the movement of the surface (see 1.3.3) or the formation of a cavity (porosity, hot tears). Depending on the size of the casting and the solidification paths, these hot spots can become macroscopically large, relative to the casting's dimensions, and the final cavities can be of the dimensions of cm. Depending on the solidification morphology the cavity volume may be dispersed or cohesive.

Finally, if substantial amounts of gas (e.g. H/N) are soluble in the liquid (e.g. Al/Fe) but not in the solid, gases in the liquid, which are rapidly rejected at the moment of phase transformation, increase the local driving force to form porosity.

1.3.5. Discontinuities in filling

Discontinuities in the filling process can lead to cold laps, misruns or nonfills. Cold laps are areas, in which new melt got in contact with already filled and partly solidified areas. The result is an insufficient interlinking between two or more melt volumes (showing reduced mechanical properties) and, in the case of reactive metals, nonbonded oxide layers.

Misruns and nonfills are related casting defects, which are characterised by not or partly filled mould areas. The reasons may be a low melt quality (high oxide content), low casting temperature, an interrupted filling, low melt velocity, insufficient venting, low mould temperature, effects of coatings, materials or cooling, casting

geometry (thin walls) or the alloy composition and therefore the solidification characteristic itself.

1.4. Porosity in aluminium and its alloys

Porosity is one of the most common defects in castings. Especially technical alloys (not pure metals, which tend to solidify with a planar solidification front) with a wide solidification range show the strong tendency to form porosity even in areas with a large thermal gradient and small solidification rate. As long as the solidification interface is not perfectly smooth and the aluminium's gas level is above its solid solubility, micropores most likely form. In cases of a very smooth solidification interface and early pore formation, for example, due to hydrogen dissipation, pores may float to the top of the casting.

Although tremendous effort has been made to understand pore nucleation in aluminium alloys, the exact mechanism is still not understood. In general, liquid (and solid) aluminium is always covered with an oxide layer, even at extremely low partial pressures of oxygen a thin (nanometres thick) film forms. During filling this film may be introduced into the melt due to surface turbulence, splashes, or other flow phenomena. Once gas from the atmosphere is introduced below the melt surface, it is contained by two oxide film. Because oxygen and nitrogen are almost insoluble in liquid aluminium (3×10^{-8} and 1×10^{-11} at the melting point respectively (44, 45)), both may only be consumed by reactions with the aluminium. This theory was introduced by John Campbell (42), and is called the "bifilm theory". These types of inclusions would be the perfect nuclei for pore formation because they already constitute a "pore" which has to be inflated or enlarged. There are two major factors which may lead to pore growth, solidification shrinkage and hydrogen precipitation. Nevertheless, there are publications which indicate pore nucleation even if the filling procedure happened very smoothly and the introduction of "bifilms" should be minimal. The bifilm theory is not undisputed, especially if applied as the universal underlying mechanism for every kind of pore formation.

The solidification shrinkage of Al-Si alloys leads to a volume deficit at the root of the dendritic solidification front. This volume deficit induces a pressure drop which in turn causes a feeding flow from areas with a higher pressure. In the literature, even negative liquid pressures (tension) of -200 kPa are described at the end of solidification (46). A typical pore which nucleated in the last stages of solidification is shown in Figure 1-1.

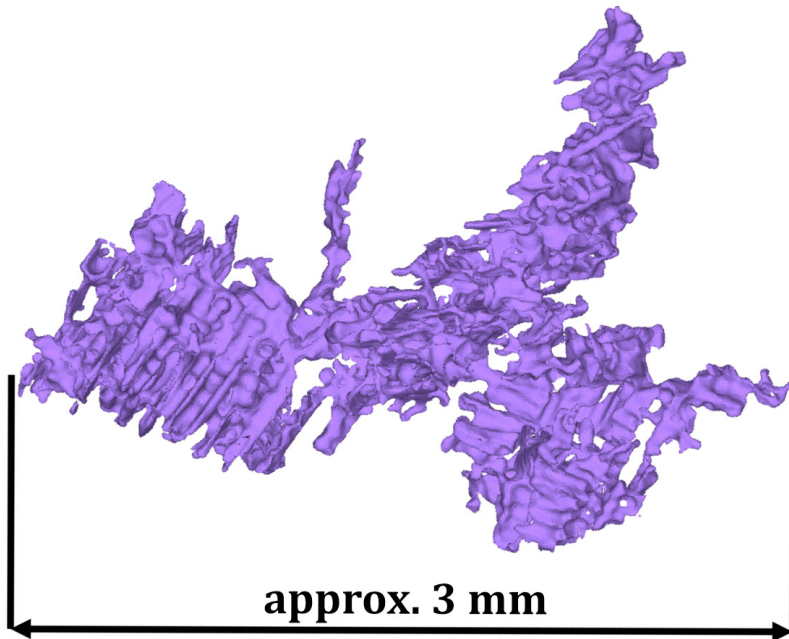


Figure 1-1: XCT-rendering of a pore which presumably formed in the late-stages of solidification. The dendritic morphology of the solid structure is visible on the pore's surface. The pore was found in a cylinder head camshaft bearing, cast in the Sr-modified alloy AlSi8Cu3. The total porosity of the specimen is $g_p = 0.358\%$.

Gas segregation by rejection from the solid during solidification may increase the local hydrogen level above the solubility limit of the melt. If a suitable nucleus is available, this hydrogen supersaturation can be released by pore formation and pore growth. The local volume deficit is almost instantaneously compensated. A typical pore which nucleated in an early-stage of solidification is displayed in Figure 1-2.

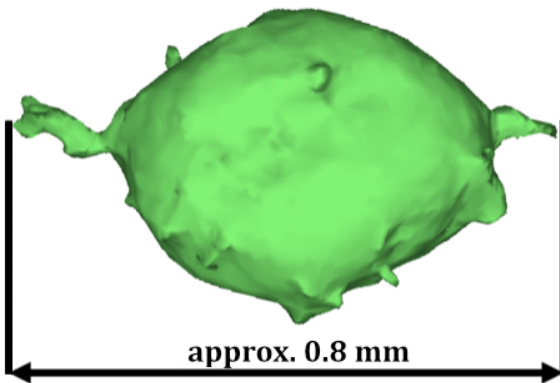


Figure 1-2: XCT-rendering of a pore which presumably formed in the initial stages of solidification. The dendritic morphology of the solid structure is not visible on the pore's surface. It shows a high sphericity, and small protrusions indicate a sucking in of liquid in the last stages of solidification. The pore was found in a cylinder head camshaft bearing, cast in the Na-modified alloy AlSi7Cu0.5Mg. The total porosity of the specimen is $g_p = 1.100\%$.

1.5. Objectives and outline

Simulation of the thermal field during casting processes is far advanced. The prediction of microporosity and additional information on the pore size distribution are still not reliable. Although numerous researchers worked on the problem of porosity prediction and modelling, no universally applicable model could be presented which satisfies all the demands of the casting industry for a fast and reliable defect prediction. Many parameters influence the final porosity characteristic. Morphology of the primary and eutectic phases, the permeability of the mushy zone, the gas content of the melt and changes in the interfacial energy due to chemical composition are only some of all the parameters which have to be considered. The most important aspects like the nucleation of pores in an aluminium melt and the related nucleation theories are yet to be understood and proven.

Advancements in the spatial ($< 0.1\ \mu\text{m}$) and temporal ($< 1\ \text{s}$) resolution capabilities of X-ray computed tomography (XCT) will push the limits of the current understanding in the coming years to a higher level. Nevertheless, even experimental XCT devices today facilitate new and insightful findings, for example, potential correlations between the amount of total porosity and the maximum defect sizes the pores

constitute. If the largest discontinuity in an aluminium cast volume is a pore, it is the limiting factor for the expected local fatigue life (1–6). Thus, the prediction of the pore size distribution for a given local amount of porosity is of paramount importance regarding the general usefulness of a porosity prediction. Each pore is essentially an existing crack which leads to a stress concentration dependent on the stress distribution during the casting's service and the orientation of the pore relative to the stresses. Crack propagation just has to start, which typically happens at the biggest, least favourably oriented pore close to the casting's surface. So far, no commercial casting software is available which allows the prediction of local defect sizes or fatigue properties in macroscopic castings within an industry-relevant period (< 24 hours). Central aspects of the porosity formation and development are not yet fully understood, and the computational power still limits the complexity of microstructure evolution simulations for macroscopic castings.

Because the characteristics of porosity (e.g. amount, morphology, or distribution) are influenced by most process parameters and additionally by the fundamentals of solidification itself, in section two of this work a thorough literature review is conducted to cover most relevant factors and to illustrate the multitude of aspects determining porosity in aluminium alloys. First, the fundamentals of the primary solidification are covered, followed by the solidification of eutectics, segregation, and the macroscopic freezing range of technical alloys. Next, the nucleation and growth of pores in aluminium are examined, followed by the multiple influential parameters determining porosity and its characteristics in Al-Si alloys. Finally, a short overview of existing modelling approaches on porosity is given.

In section three the conducted experiments and analysis methods are presented. First, basic qualitative experiments are described which were aimed to investigate the role of the very prominently discussed oxides or "bifilms" and their importance for nucleation, amount, and spatial distribution of porosity. Next, an extensive industrial, experimental program is presented, which was aimed at illuminating the effect of industrial solidification conditions on the local amount and distribution characteristics of microporosity. The applied analysis methods are presented. Finally, laboratory wedge experiments, conducted to investigate the roles of hydrogen and cooling rate on microporosity in Al-Si alloys, are mapped out.

In section four the experimental results from all three experiments are illustrated, contextualised and discussed. The role of oxides regarding porosity (and pore nucleation) is critically put into perspective, significant relations between the total amount of porosity, pore sizes distribution, and defect size are presented, and finally, the effect of the hydrogen content and cooling rate during the solidification of aluminium foundry alloys is outlined.

The conclusions of this work are afterwards summarised in section five and a proposal for, in the eyes of the author advisable, future work, as well as open questions, are presented in section six.

In this work, it was possible to develop equations which correlate the local amount of porosity with mean and maximum pore size as well as with mean and maximum absolute pore dimensions. Additionally, the development of the pore morphology could be described as a function of total porosity. The understanding of the influences of hydrogen, as well as cooling rate on the pore size distribution, could be advanced and quantified. The developed equations allow the prediction of porosity parameters which are highly relevant for fatigue behaviour. The presented results cover two standard cast alloys with significantly different Si and Cu contents and the two most commonly used types of eutectic modifier: Sr and Na. It was possible to capture the effect of hydrogen on the porosity characteristics in an industrially relevant range between 0.04 and 0.38 ml / 100 g.

2. Literature review

2.1. Fundamentals of solidification

2.1.1. Primary phase

2.1.1.1. Nucleation

A nucleation event is necessary to form the first solid nucleus in the liquid. The most idealised nucleation theory is the homogeneous nucleation. The downside of this theory is that its predictions are not observed in practice, and so the heterogeneous nucleation theory comes into the picture. Heterogeneous nucleation, together with its assumptions about the nucleation kinetics, can explain solidification as it is observed in practice. The principle is also applicable to other nucleation events like pore formation, and so it will be discussed in greater detail on the following pages.

Homogeneous nucleation

In the liquid melt, atoms are relatively free to move and change their spatial positions. Nevertheless, on a microscopic level, a short-range order is observable. This short-range order may form, just due to thermal fluctuation, small clusters with high atomistic order. These little clusters are not stable above the melting point but can become stable if the temperature falls below the melting point. To describe the thermodynamic difference of the liquid state and the state in which a solid cluster has been formed, one has to compare the energetic state of both conditions (the Gibbs free energy). The difference between both states is described by (47)

$$\Delta G = V_s \frac{G_s^m - G_l^m}{V^m} + A_{sl} \gamma_{sl} \quad \text{(Equation 1)}$$

where V_s and A_{sl} are the volume and surface of the cluster, $G_s^m - G_l^m \approx \Delta S_f^m \Delta T$, and ΔS_f^m is the molar entropy of fusion, $\rho \Delta S_f = \Delta S_f^m / V^m$, and γ_{sl} is the interfacial energy between the solid and liquid phases. Under the assumption of spherical clusters, one gets the equation

$$\Delta G = -\frac{4}{3} \pi r^3 \rho \Delta S_f \Delta T + 4 \pi r^2 \gamma_{sl} \quad \text{(Equation 2)}$$

where r is the spherical cluster radius and ΔT is a small undercooling.

Because for small r the first term representing the released energy due to solidification is smaller than the second term, representing the necessary energy to create new surface area, there is an energy barrier which can be described by (47)

$$r_c = \frac{2\gamma_{sl}}{\rho\Delta s_f\Delta T} \quad \text{(Equation 3)}$$

the critical radius for nucleation. Clusters that are smaller than this critical radius are not stable and are called embryos, clusters that are bigger than the critical radius are stable and called nuclei. The barrier associated with the critical radius is called homogeneous nucleation barrier ΔG_n^{homo} . By using the critical radius in (Equation 2), one gets

$$G_n^{homo} = \frac{4\pi\gamma_{sl}r_c^2}{3} = \frac{16\pi}{3} \frac{\gamma_{sl}^3}{(\rho\Delta s_f)^2\Delta T^2} \quad \text{(Equation 4)}$$

The surface, bulk and total free energy and the resulting homogeneous nucleation barrier for aluminium at an undercooling of 5 K are given in Figure 2-1.

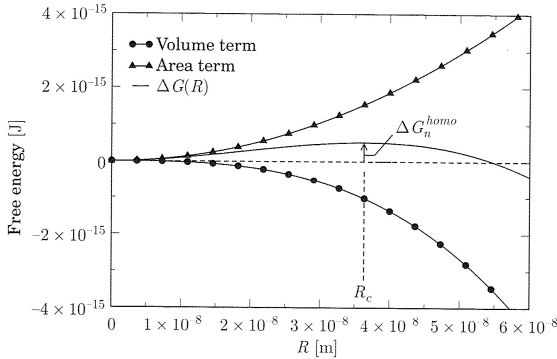


Figure 2-1:
Surface, bulk and
total free energy of
Al at 5 K
undercooling and
for a spherical
solid cluster (47)

Homogeneous nucleation rate

To calculate the rate of nucleation in the case of solidification, most models posit a thermally activated process, which means the energy of atoms follows a Maxwell-Boltzmann distribution. If n_l is the density of atoms in a liquid, n_N describes the density of clusters consisting of N atoms (47):

$$\frac{n_N}{n_l} = e^{\left(\frac{\Delta G(N)}{k_B T}\right)} \quad \text{(Equation 5)}$$

where k_B is the Boltzmann's constant. Under careful consideration (Equation 5) has some flaws and is, for the proposed purpose, not entirely correct, but good enough under the assumption of a very low density of clusters compared to the density of atoms in the liquid.

To calculate the nucleation density of clusters of the critical size one has to insert the homogeneous nucleation barrier ΔG_n^{homo} into (Equation 5) to obtain

$$\frac{n_c}{n_l} = e^{\left(\frac{\Delta G_n^{homo}}{k_B T}\right)} = e^{\left(\frac{16\pi}{3} \frac{\gamma_{sl}^3}{(\rho \Delta s_f \Delta T)^2 k_B T}\right)} \quad \text{(Equation 6)}$$

Furthermore, the rate at which a critical nucleus adds another atom to itself is proportional to the atomic vibration frequency ν_0 , and the probability of capturing the atom at the surface is given by p_c . The rate of formation of homogeneous nuclei I^{homo} is therefore provided by (47)

$$I^{homo} = \nu_0 p_c n_c = \nu_0 p_c n_l e^{\left(\frac{16\pi}{3} \frac{\gamma_{sl}^3}{(\rho \Delta s_f \Delta T)^2 k_B T}\right)} \quad \text{(Equation 7)}$$

If one calculates the time to nucleation of 1 nucleus for an undercooling of 100 K for 1 cm³ for Al, the homogeneous nucleation theory answers of more than 450,000 years ($p_c \approx 1$; $\nu_0 = 10^{13} \text{ s}^{-1}$ at T_f ; $n_l \approx 6 \times 10^{28} \text{ m}^{-3}$). This incubation time is inconsistent with experimental observations in which Al begins to solidify already a few Kelvin below its freezing point. The reason is the strong influence of the interfacial energy γ_{sl} (to the third power) to form new surface area in the melt. This recognition leads to the heterogeneous nucleation theory that will be discussed hereafter.

Heterogeneous nucleation

The nucleation on a foreign surface, which may be a particle, the mould, oxides or other inclusions added on purpose or not, is called heterogeneous nucleation. Figure 2-2 shows a solid droplet on a foreign surface, without the effects of gravity and under the assumption of isotropic surface energies. The summation of the forces parallel to the surface, which relate to the surface energies and the equilibrium contact angle θ , lead to the Laplace-Young equation (47)

$$\gamma_{fl} = \gamma_{fs} + \gamma_{sl} \cos \theta \quad \text{(Equation 8)}$$

where γ_{fl} is the surface energies between the foreign substrate and the liquid, γ_{fs} between the foreign substrate and the solid, and γ_{sl} between the solid and liquid phase.

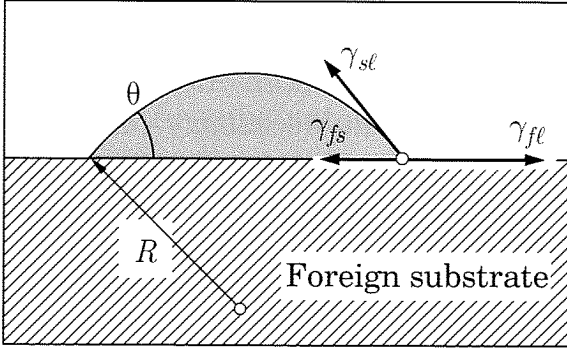


Figure 2-2:
Nucleation of a
hemispherical
droplet on a
foreign surface
(47)

If $0 \leq \theta \leq \pi/2$ one says that the solid “wets” the surface and forming a nucleus on the specific surface is energetically favourable. To calculate if a nucleus is stable, one has to sum up the single terms of Gibb's free energy. This approach happens analogously to the homogeneous nucleation described earlier.

$$\Delta G = -V_s \rho \Delta s_f \Delta T + A_{sl} \gamma_{sl} + A_{fs} (\gamma_{fs} - \gamma_{fl}) \quad \text{(Equation 9)}$$

The volume of the nucleus V_s , the surface of the solid-liquid interface A_{sl} and the surface of the substrate-solid interface A_{fs} can be derived for a spherical cap from geometry, and so the following equation follows (47)

$$\Delta G = \left(-\frac{4\pi r^3}{3} \rho \Delta s_f \Delta T + 4\pi r^2 \gamma_{sf} \right) f(\theta) \quad \text{(Equation 10)}$$

with the geometric factor

$$f(\theta) = \frac{3V_s}{4\pi r^3} = \frac{(2 + \cos \theta)(1 - \cos \theta)^2}{4} \quad \text{(Equation 11)}$$

If one compares (Equation 10) with (Equation 2) one can notice, that the now derived equation for heterogeneous nucleation is the same as for homogeneous nucleation apart from the geometry factor $f(\theta)$. The critical nucleation radius is therefore the same as for homogeneous nucleation (see (Equation 3)), and the heterogeneous nucleation energy is reduced by the factor $f(\theta)$.

$$G_n^{heter} = G_n^{homo} f(\theta) = \frac{16\pi}{3} \frac{\gamma_{sl}^3}{(\rho \Delta s_f)^2 \Delta T^2} f(\theta) \quad \text{(Equation 12)}$$

In the case of $\theta = \pi$, one finds $f(\theta) = 1$, which describes a perfectly spherical nucleus, non-wetting and therefore the conditions of homogeneous nucleation. If $\theta =$

One finds $f(\theta) = 0$, which describes perfect wetting, for example of an existing solid nucleus as substrate. This can be the case if, for example, due to dendrite fragmentation, nuclei of the same kind are available and the progressing solidification is not limited by nucleation but only by growth.

Heterogeneous nucleation rate

Now that not every atom in the melt is a potential nucleus, but there is a specific number given by the density of potent substrates in the melt, one has to adapt (Equation 7) for heterogeneous nucleation (47)

$$I^{heter} = v_0 p_c n_p e \left(\frac{16\pi}{3} \frac{\gamma_{sl}^3}{(\rho \Delta s_f \Delta T)^2 k_B T} f(\theta) \right) \quad \text{(Equation 13)}$$

Here n_p is the density of foreign nuclei in the melt. Figure 2-3 shows the time necessary to form one nucleus as a function of absolute temperature for aluminium with different values for θ , and in comparison, to homogeneous nucleation.

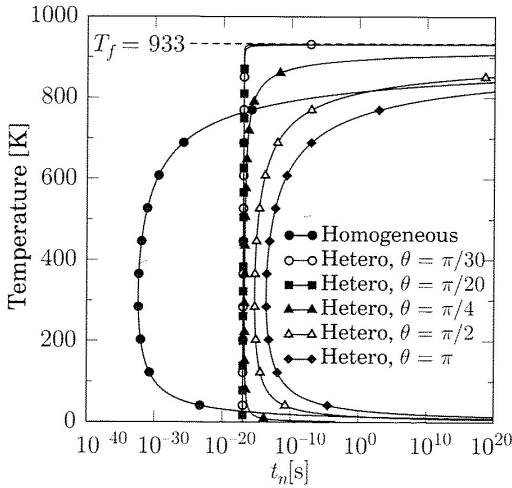


Figure 2-3: Time to nucleate one nucleus in an aluminium melt as a function of absolute temperature.

Homogeneous nucleation in comparison to heterogeneous nucleation with different values for θ (boundary conditions: $n_p = 10^9 m^{-3}$; $p_c \approx 1$; $v_0 = 10^{13} s^{-1}$ at T_f ; $n_i \approx 6 \times 10^{28} m^{-3}$) (47)

One can see that for reasonable undercooling in casting practice, heterogeneous nucleation always takes place much faster than homogeneous nucleation would (if the foreign substrate is a potent nucleus). However, the theory of heterogeneous nucleation has shortcomings. It cannot explain the well-observed fact that the number of

activated nuclei increases with increasing cooling, but rather predicts that all available nuclei are activated. Furthermore, the theory predicts solidification at an undercooling independent of the cooling rate, whereas reality shows that with increasing cooling rate the necessary undercooling to start solidification increases.

Athermal nucleation

To overcome the shortcomings of the previously introduced heterogeneous nucleation theory, the ‘‘Athermal Nucleation Theory’’ has to be introduced. The name is somewhat misleading as the main result is a nucleation rate depending on temperature, but it is, in contrast to heterogeneous nucleation, not dependent on the Maxwell-Boltzmann distribution but all available, potent nuclei are activated instantaneously.

If one considers a substrate of a circular shape, two interesting cases can be discussed. The first one is defined by $\gamma_{fs} + \gamma_{sl} < \gamma_{fl}$. In this case, there is no wetting angle θ which satisfies the Laplace-Young equation. It is even energetically favourable to substitute the substrate-liquid surface by two other surfaces, the substrate-solid, and solid-liquid surface. The equation describing the situation of the total free energy is given by (47)

$$\Delta G = -A_f \delta (\rho \Delta s_f) \Delta T + A_f (\gamma_{fs} + \gamma_{sl} - \gamma_{fl}) \quad \text{(Equation 14)}$$

Here A_f is the surface area of the foreign substrate and δ is the thickness of the solid layer. Under the previously given assumption that the second term gives a negative contribution to the total free energy, the interesting observation can be made that a nucleus can even be stable for negative undercooling (temperatures above the melting point). The equilibrium thickness δ can be calculated by differentiating (Equation 14) with respect to A_f and setting the result to zero

$$\delta = \frac{\gamma_{fs} + \gamma_{sl} - \gamma_{fl}}{\rho \Delta s_f \Delta T} \quad \text{(Equation 15)}$$

If the temperature now decreases towards the melting point, the undercooling increases towards zero $\Delta T \rightarrow 0$ and the equilibrium thickness δ increases too. At the melting point and if the surface area of the substrate A_f is large enough, the equilibrium thickness becomes undefined, and the nucleus size is governed by growth. If the surface area of the substrate is limited and the temperature drops below the melting point T_f the curvature of the nucleus’ surface has to increase to satisfy the Gibbs-Thomson equation which describes the equilibrium temperature of a curved surface of a pure substance. The curvature increases until the geometrically limited

radius $r = \phi/2$, where ϕ is the diameter of the substrate (disk), is reached. This is the case at the geometrically limited undercooling (47)

$$\Delta T_g = \frac{4\Gamma_{sl}}{\phi} \quad \text{(Equation 16)}$$

At this point, the further development of the nucleus is only governed by growth. Thus, the activation of the substrate particle is entirely controlled by its geometry and temperature.

If $\gamma_{fl} - \gamma_{sl} < \gamma_{fs} < \gamma_{fl} + \gamma_{sl}$, the case discussed previously for heterogeneous nucleation, nucleation could still take place in the now introduced way. Under the same assumption of a disk-shaped substrate of diameter ϕ , the critical radius for nucleation is given by (Equation 3) as previously derived for homogeneous and heterogeneous nucleation. But in the case of a limited size of a substrate, nucleation is only possible if $r_c \sin \theta < \phi/2$, which means that the spherical cap of the nucleus fits on the substrate. At the same time, it means that nucleation can only take place if the undercooling is high enough that $\phi \geq 2r_c \sin \theta$ is fulfilled. If nucleation now takes place, the embryo can grow until it reaches the edges of the substrate. At that point, the curvature has to grow, like discussed previously and only if the undercooling ΔT is bigger than the geometrically limited undercooling ΔT_g further growth is possible. Otherwise, the nucleus is stagnant, and growth is not possible. The various growth situations are summarized in Figure 2-4.

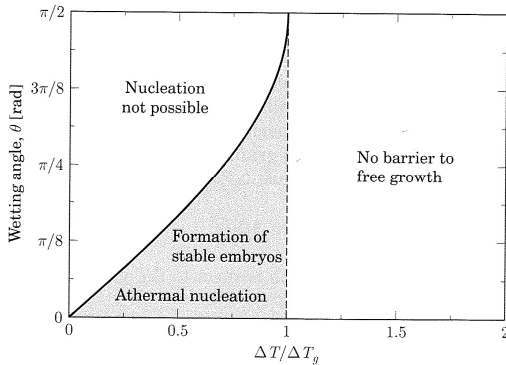


Figure 2-4: Nucleation on a foreign substrate as a function of wetting angle and normalised undercooling (47)

In real alloys, there is always not only one size of potential substrates but a distribution of sizes. The consequences of this matter are discussed now. If one assumes that the available substrates are well wetted, big enough to initiate heterogeneous

nucleation but small enough to limit growth until the geometrically defined undercooling ΔT_g is reached, we are discussing athermal nucleation, the grey marked area in Figure 2-4. Nucleation on these particles happens very rapidly if the undercooling for heterogeneous nucleation $\Delta T^{heter}(\phi)$ is reached. These nuclei grow up to the limit given by $\Delta T_g(\phi)$. The size and density of particles should now be described by a continuous distribution function Δn_i . Each particle is activated at a defined undercooling, so there is a continuous distribution of activated particles as a function of undercooling $dn/d(\Delta T)$. A physical distribution of particles can be described by a log-normal distribution, given by (47)

$$\frac{dn}{d\phi} = \frac{n_{max}}{\phi_\sigma \sqrt{2\pi} \phi} e^{-\frac{1}{2} \left(\frac{\ln \phi - \ln \phi_0}{\phi_\sigma} \right)^2} \quad \text{(Equation 17)}$$

where $\ln \phi_0$ is the mean value of the distribution and ϕ_σ is the standard deviation. With (Equation 16) one gets a distribution of the associated undercooling

$$\frac{dn}{d\Delta T} = \frac{n_{max}}{\Delta T_\sigma \sqrt{2\pi} \Delta T} e^{-\frac{1}{2} \left(\frac{\ln \Delta T - \ln \Delta T_0}{\Delta T_\sigma} \right)^2} \quad \text{(Equation 18)}$$

It can be shown and will be in the next chapter, that the distribution of particle size of inoculants can be correlated with the grain density.

2.1.1.2. Grain refinement

Often a fine grain structure is desired for production and later processing of metals. It ensures isotropic and good mechanical properties, reduces the tendency for hot tearing during casting and extends the alloy's ability for mass feeding. In general, there are two mechanisms that promote a fine and homogeneously grain distribution.

The first one is called inoculation which means the addition of foreign particles which promote the nucleation of the primary phase. Depending on the alloying system a broad variety of inoculants is used. For aluminium alloys, AlTi3B1 or AlTi5B1 is commonly used to achieve a grain refining effect. At the same time, additions of foreign particles can also deteriorate the mechanical properties and should, therefore, be used with a distinct purpose.

The second grain refining mechanism is achieved by vigorous agitation of the solidifying melt. This can be induced by ultrasound or electromagnetic steering and results in a local remelting, fragmentation and redistribution of dendrite arms. The small fragments can act as ideal nuclei without nucleation barrier.

Inoculation

As already mentioned above, for aluminium alloys, typical grain refiners are AlTi3B1 or AlTi5B1. In continuous casting processes, grain refiner is almost always used. For shape castings, grain refinement is often but not always used because of the possible detrimental effects. These can be observed in the form of a reduced eutectic modification due to reactions of Sr and B or the formation of sludge due to sedimentation of B rich phases (48).

In general, the foreign particle should provide at least one crystallographic plane that is close to the crystallographic properties of the phase that should be promoted to grow. The crystallographic relations of TiB₂, Al₃Ti, and Al are given in Figure 2-5. In some cases, there is an intermediate phase with a crystallographic structure close to both, the substrate particle and the phase which should be promoted to growth, necessary. The aim is to minimise the interfacial energy γ_{fs} and therefore the wetting angle θ .

This minimisation very efficiently takes place for Al₃Ti particles. Al₃Ti is tetragonal, but its c-axis is approximate twice its a-axis and thus can act as two stacked FCC cells with plane {112} corresponding to the {111} plane of FCC aluminium. At the same time, Al₃Ti is unstable in the melt if the total amount of Ti is below 0.15 wt%.

TiB₂ is a major compound of the introduced Ti-B master alloys and very stable in aluminium melts. Its capability to act as a primary nucleus for the aluminium phase is minimal due to its hexagonal crystallographic structure. Based on the research of Greer et al. (49, 50) Al₃Ti forms an epitaxial layer on basal planes [0001] of the hexagonal TiB₂ particles which in turn act as potent nucleation sites for primary aluminium. For this mechanism, excess Ti in the liquid is necessary for the Al₃Ti layer to form. After the heterogeneous nucleation of Al on the Al₃Ti substrate, which happens very fast if only minor undercooling is provided, athermal growth takes place until the critical geometric undercooling ΔT_g is reached, and free growth continues.

Some elements may interfere with this mechanism. First and foremost, there is silicon. Increasing Si content until 3 wt% reduces the grain size due to the restricted dendritic growth. After approximately 3 wt%, a Si "poisoning" of the TiB₂ particles can be observed. This means that instead of Al₃Ti, TiSi₂ forms and deactivates the potential nucleation site. A comparable process happens with Zr, which is commonly used to inhibit recovery, increase hardness as well as the recrystallisation temperature in wrought alloys, by the formation of Al₃Zr instead of Al₃Ti.

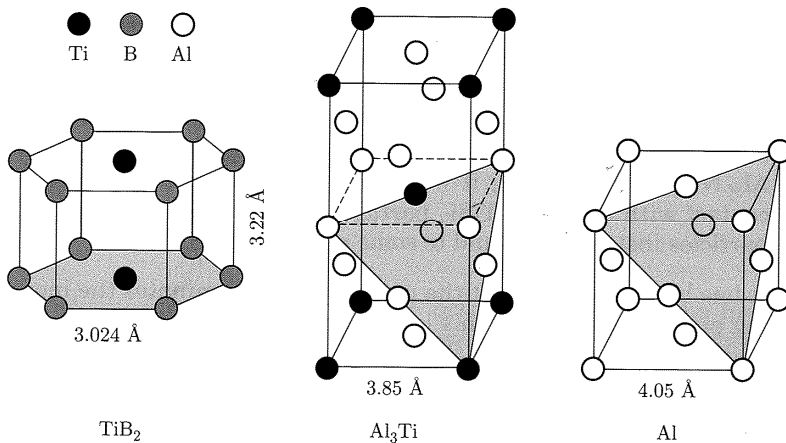


Figure 2-5: Crystallographic structures of TiB_2 , Al_3Ti , and Al (47)

Nucleation only takes place on the largest TiB_2 particles because these offer the lowest critical geometric undercooling ΔT_g . After the first nucleation sites are activated the continuous solidification process releases enough latent heat so that smaller embryos with higher ΔT_g are not activated anymore. This effect can be suppressed by higher cooling rates (due to the inertia of the heat transport) or a very narrow distribution of grain refining particles (due to the simultaneous activation of many particles). In industrial practice, only about 1 % (the largest) of all theoretically available particles introduced for the purpose of grain refinement is activated.

2.1.1.3. Dendritic growth

Once a stable nucleus exists, activated by sufficient undercooling from a spherical cap, the further development is governed by a mechanism of growth. This growth can be stable, but often becomes unstable and may lead to the formation of dendrites. Because dendrites formation, and the associated solidification phenomena, are essential for the conditions leading to pore formation, one has to understand the fundamental physics. Typically, one distinguishes between “free growth”, the growth of a single nucleus into the infinite pool of melt and “constrained growth”, the growth of many crystals which influence each other and under the external condition of a thermal gradient.

Free growth

Let us consider a spherical nucleus, larger than the critical radius, in an infinite pool of undercooled melt. Under these conditions, there are two reasons why a formerly perfect sphere becomes unstable and develops a non-spherical shape. The first is differences in the surface energy γ_{sl} of the crystallographic planes of the solid regarding the surrounding liquid. The second aspect is differences in the probability of atom attachment on the crystallographic planes. Both can, with varying importance, be summarized by a preferential growth direction of the crystal called anisotropy. The result may be a dendritic solidification characteristic like typical Al-Si alloys show. The FCC Al crystal, for example, shows a preference for the $\langle 100 \rangle$ direction, but still, the reason for the whole solidification characteristic is still the minimization of the total free energy. The larger the surface anisotropy is, the sharper the produced solid morphology becomes and finally one speaks of a faceted morphology for high anisotropy systems. The attachment of atoms plays, at least for most metals, only a minor role for the morphology characteristic. One observation led to a well-known rule of thumb that states that high anisotropy is often associated with a high entropy of fusion, namely

$$\frac{\Delta S_f^m}{R} > 2 \quad \text{(Equation 19)}$$

for faceted morphology and

$$\frac{\Delta S_f^m}{R} < 2 \quad \text{(Equation 20)}$$

for non-faceted morphology, respectively. Here ΔS_f^m is the molar entropy of fusion and R the ideal gas constant.

Surface anisotropy and the probability of atom attachment do not explain the observable changes of the solidification morphology due to changes in cooling rate or gradient. The actual shape of a growing solid nucleus is also controlled by diffusional transport. In 2D the surface energy can be described as a function of the azimuthal angle ϕ relative to a reference direction (47)

$$\gamma_{sl} = \gamma_{sl}^0 [1 + \varepsilon_n \cos(n\phi)] \quad \text{(Equation 21)}$$

where ε_n is the strength of anisotropy and n is the degree of symmetry (for example $n = 4$ for cubic symmetry). The surface stiffness in 2D is defined as (47)

$$\psi_{sl} = \gamma_{sl} + \frac{d^2 \gamma_{sl}}{d\phi^2} \quad \text{(Equation 22)}$$

If Ψ_{sl} becomes negative, the direction of growth is thermodynamically not allowed, and thus the crystallographic orientation cannot appear.

The Wulff construction can compute the equilibrium shape of the growing crystal, and the concept can be extended to 3D. The Wulff construction can also be used to derive the anisotropy of surface energy from experiments of small droplets of liquid.

Constrained growth

The previously introduced idea of free growth applies to equiaxed growth. In most practical applications, solidification starts from a mould wall and progresses into the undercooled melt as a solidification front. In this case, and for binary alloys, there is a thermal gradient $G_l^* > 0$, and a composition gradient $G_{cl}^* < 0$, one has to take into account. Under these conditions, experimental observation (51) shows, that the interface is only conditionally stable, depending on the thermal gradient G_l and the interface speed v^* . For low values of v^* one can observe a planar solidification front. Above a critical value, cells start to form, which are separated by grooves. These cells are of no particular crystallographic orientation and show a large radius. If the interface velocity is increased further, the grooves deepen, and the cell spacing increases until finally the transition to a dendritic solidification front with sharp tips, trunks and side branches whose orientations follow preferential growth directions are formed. The dendrites first develop at irregularities on the solidification front. The spacing between primary trunks is called the primary dendrite arm spacing λ_1 , and the spacing between the secondary branches is called the secondary dendrite arm spacing λ_2 , in this work abbreviated to DAS. The secondary dendrites often grow at a small angle to the preferential growth direction, at least if the anisotropy is low and the thermal gradient high. If various grains grow dendritically, they compete by growth velocity and only the most favourably oriented grains "survive". The surface energy anisotropy also plays a significant role in constrained growth and composition changes may alter the preferential growth direction. For example, for systems with very low surface energy anisotropy the seaweed structure is observable.

Length scale and pattern selection in constrained growth

To understand when and why a solidification interface becomes unstable, one has to take segregation in front of the interface into account. The local composition ahead of the interface can be described by (47)

$$C_l = C_0 \left(1 + \frac{1 - k_0}{k_0} e^{-\frac{v^* z}{D_l}} \right) \quad \text{(Equation 23)}$$

where z is the distance from the solid-liquid interface and C_0 is the nominal composition under the condition of a constant positive temperature gradient $G > 0$. The gradient in local composition in front of the solidification interface can be described by (47)

$$G_{Cl}^* = \left. \frac{dC_l}{dz} \right|_{z=0} = -\frac{C_0(1-k_0)v^*}{k_0D_l} = -\frac{\Delta C_0 v^*}{D_l} \quad \text{(Equation 24)}$$

where $\Delta C_0 = C_0(1-k_0)/k_0$ is the difference in composition between the liquid and the solid. In a linearized phase diagram, the liquidus temperature at any point in front of the solidification interface is given by (47)

$$T_{liq}(z) = T_f + m_l \Delta C_l(z) = T_{sol} + \Delta T_0 \left(1 - e^{-\frac{v^* z}{D_l}} \right) \quad \text{(Equation 25)}$$

where $\Delta T_0 = -m_l \Delta C_0 = T_{liq} - T_{sol}$ is the nominal freezing range. Chalmers (52) presented the explanation, that if the actual temperature $T_l(z)$ is greater than the local liquidus temperature $T_{liq}(z)$, then any possible perturbations on the solidification front would be unstable and remelt. Vice versa, if the local temperature $T_l(z) = T_{sol} + Gz$ is lower than liquidus temperature any perturbation would be stable and the planar solidification front therefore unstable. A stability condition can be derived from $T_l(z) \geq T_{liq}(z)$ which states (53)

$$G \geq m_l G_{Cl}^* = \frac{\Delta T_0 v^*}{D_l} \quad \text{(Equation 26)}$$

because $T_l(z=0) = T_{liq}(C_0/k_0) = T_{sol}(C_0)$. If the stability condition is not met, one speaks of constitutional supercooling because the melt is undercooling due to its constitution (or composition). The case is illustrated in Figure 2-6 which shows the situation of composition and temperature due to segregation ahead of a planar solidification front in case of unidirectional solidification of a binary alloy with constant velocity.

By performing a stability analysis and incorporating the surface energy one can derive the length scale of the microstructure.

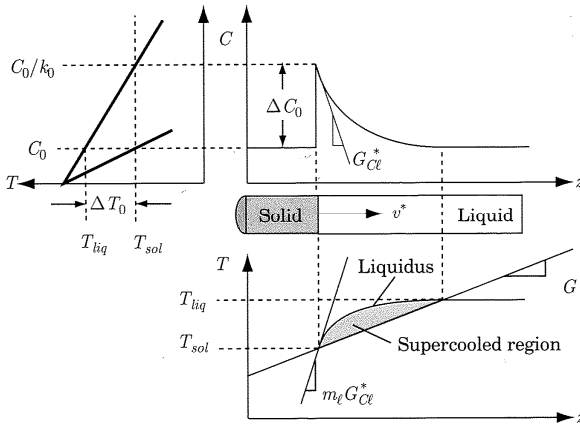


Figure 2-6: Sketch of the composition and temperature situation in front of a planar solidification front in a binary alloy under the condition of unidirectional solidification and constant growth velocity (47)

In the case of a planar solidification front of a binary alloy where the velocity of the solidification front v^* is equal to a controlled “pulling velocity”, v_p , set by the experimentally controlled solidification conditions and under further simplifying assumptions one can distinguish between three characteristic states:

1. A stable solidification front below the constitutional supercooling limit

$$v_p^c = \frac{GD_l}{\Delta T_0}$$
2. An unstable solidification front with various characteristic length scale which can be determined by stability analysis and which varies between a minimum wavelength λ_{min} and a maximum wavelength λ_{max} and is dependent on v_p . The destabilization by composition and the stabilization due to surface energy are the two driving forces in this characteristic state.
3. A stable planar solidification front above the absolute stability limit $v_p^a = (D_l \Delta T_0) / (k_0 \Gamma_{sl})$, where the wavelength decreases more slowly than $D_l / \Delta T_0$

A dendrite growing into an undercooled melt can be approximated as a “needle crystal”, a paraboloid growing in a shape-preserving manner and characterised by a tip radius R_{tip} . Under simplifying assumptions, a solution, called the Ivantsov solution, can be found, stating that for any given undercooling ΔT there is a family of solutions $v^* R_{tip} = const$. This solution is contradicted by experimental observations because for a given undercooling dendrites always grow with a reproducible velocity and tip radius. The problem is an oversimplification of the temperature condition for the solid. Ivantsov assumed an isothermal solid at T_f , independent of the

local curvature, which contradicts the Gibbs-Thomson condition. To derive a more physical solution for the problem one can include the surface energy anisotropy, which leads to no stable solution unless the surface energy has a non-zero anisotropy. This leads to a second solvability condition $R_{tip}^2 v^* = const$. Together both criteria lead to a unique tip shape and growth velocity for a given undercooling and therefore allow the application to real microstructures.

Lipton et al. (54) introduced a model, the so-called LGK model, which incorporates most of the essential physical phenomena and gives a unique pair of v^* and R_{tip} for a given undercooling or a pair of R_{tip} and ΔT for a given velocity (as in constrained growth). The model is only valid for small undercoolings and neglects the effect of attachment kinetics. Two equations were derived for ΔT (as a sum of thermal undercooling ΔT_T , solutal undercooling ΔT_C , and curvature undercooling ΔT_R) and R_{tip} (as an estimate based on linear stability analysis $R_{tip} \approx \lambda_{min}$) which have to be solved iteratively and are commonly used to determine the operating state for given solidification conditions. Nonetheless, to solve both equations for millions of grains in a computational simulation is very time-consuming. Because the effect of solutal undercooling ΔT_C dominates for alloys with a significant solute concentration, one can develop a simplified LGK model for small undercoolings of only a few Kelvin. This model neglects the influences of thermal undercooling and curvature undercooling and assumes solidification controlled by solute transport and yields a simple equation (47)

$$R_{tip}^2 v^* = - \frac{8\pi^2 \Gamma_{sl} D_l}{m_l C_0 (1 - k_0)} \quad \text{(Equation 27)}$$

Primary dendrite arm spacing under constrained growth

The competition in growth between the differently oriented dendrites leads to the primary dendrite arm spacing λ_1 . Again, a dendrite can be described by an approximation of an ellipsoid. The dendrite has a length a , a radius b , and a tip radius R_{tip} . The length of a dendrite under constrained growth is defined by the temperature gradient G and the freezing range

$$a = \frac{T_{tip} - T_{base}}{G} \quad \text{(Equation 28)}$$

where T_{base} is the temperature at the base of the dendrite. Two cases have to be distinguished. If the composition of the alloy C_0 is below the solubility of the primary phase and under equilibrium conditions, the freezing range ΔT_0 is given by

$$\Delta T_0 = T_{tip} - T_{base} \quad \text{(Equation 29)}$$

If the composition of the alloy lies above the solubility of the primary phase and under nonequilibrium conditions, the eutectic marks the end of solidification $T_{base} = T_{eut}$ and $\Delta T'_0 = T_{tip} - T_{eut}$, so the freezing range is defined by

$$a = \frac{\Delta T'_0}{G} \quad \text{(Equation 30)}$$

If one now assumes a hexagonal structure of the growing primary dendrites one can geometrically derive that (47)

$$b = \frac{\lambda_1}{\sqrt{3}} \quad \text{(Equation 31)}$$

The tip radius of the ellipsoid is given by (47)

$$R_{tip} = \frac{b^2}{a} = \frac{\lambda_1 G}{3\Delta T'_0} \quad \text{(Equation 32)}$$

Substituting the expression for R_{tip} form (Equation 27), assuming $\Delta T'_0 \approx \Delta T$ and solving for λ_1 yields

$$\lambda_1 = \left(-\frac{72\pi^2 \Gamma_{sl} D_t \Delta T_0}{k_0} \right)^{\frac{1}{4}} v^{*-\frac{1}{4}} G^{-\frac{1}{2}} \quad \text{(Equation 33)}$$

All quantities in (Equation 33) are known, and the primary dendrite arm spacing λ_1 is a measurable microstructural feature. Unfortunately, the commonly used and determined measurable quantities: cooling rate $|\dot{T}| = Gv^*$ and solidification time $t_f = \Delta T'_0/|\dot{T}|$ cannot be used directly to determine the primary dendrite arm spacing because both have different exponents.

Secondary dendrite arm spacing

In contrast to the primary dendrite arm spacing λ_1 , the secondary dendrite arm spacing λ_2 shows a good correlation between cooling rate $|\dot{T}|$ and solidification time t_f . It is readily available via metallographic measurement and therefore one of the most important microstructural features in casting practice. Moreover, pores forming in the late-stages of solidification are limited to the space moulded by the secondary dendrite arms and therefore their understanding and prediction are crucial to understanding the final morphology of microporosity.

Secondary dendrite arms form just a few tip radii behind the primary dendrite tip. They grow in length and width as long as the solute layer of the primary dendrites does not meet by thermal and solutal fluctuation. As soon as the solutal fields meet,

the growth of the larger dendrites takes place by the elimination of the smaller ones. This mechanism is called “coarsening” or Ostwald ripening and takes place until the root of the dendrite is reached. The phenomenon was first developed by Lifshitz and Slyozov (55) and by Wagner (56) and is therefore also called LSW theory. Kattamis and Flemings (57) developed a model to predict the final secondary arm spacing under the condition of a few simplifying assumptions. Two differently sized neighbouring secondary dendrite arms with a cylindrical shape in an isothermal field have the radii R (bigger arm) and r (smaller arm). The initial spacing between them is λ_2^0 . Both, the solid and liquid are in thermal equilibrium, and the solid phase of both arms has the same temperature but due to their different radii and the validity of the Gibbs-Thomson equation they have two different liquid compositions at the interface C_i^{*R} (bigger arm) and C_i^{*r} (smaller arm). The gradient in composition leads to a solute flux in the direction of the smaller arm, which has to dissolve to keep the equilibrium intact. This increases the composition gradient $C_i^{*R} - C_i^{*r}$ even further. If one assumes a linear gradient profile and a one-dimensional situation, Fick’s first law yields (57)

$$j = -D_l \frac{\delta C_l}{\delta x} \approx D_l \frac{C_i^{*R} - C_i^{*r}}{\lambda_2^0} \quad \text{(Equation 34)}$$

Equating both temperatures (of the big and small arm) and assuming a constant liquidus slope gives (47)

$$T_f + m_l C_i^{*R} - \frac{\Gamma_{sl}}{R} = T_f + m_l C_i^{*r} - \frac{\Gamma_{sl}}{r} \quad \text{(Equation 35)}$$

Solving (Equation 35) for $C_i^{*R} - C_i^{*r}$ and substituting in (Equation 34) yields the flux of solute dissolving the smaller dendrite arm

$$j = -\frac{D_l \Gamma_{sl}}{m_l \lambda_2^0} \left(\frac{1}{r} - \frac{1}{R} \right) \quad \text{(Equation 36)}$$

The interfacial flux balance takes, in this case, the form (47)

$$j = -C_i^{*r} (1 - k_0) \frac{dr}{dt} \quad \text{(Equation 37)}$$

Equating both fluxes and solving for dr/dt gives

$$\frac{dr}{dt} = \frac{D_l \Gamma_{sl}}{\lambda_2^0 m_l C_i^{*r} (1 - k_0)} \left(\frac{1}{r} - \frac{1}{R} \right) \quad \text{(Equation 38)}$$

(Equation 38) describes the radius change of the smaller dendrite arm over time. Three more assumptions are necessary to simplify the problem further. First, if $R \gg r$ one can assume R as constant and second, if the curvature undercooling is very

small, then $C_l^{*R} \approx C_l^{*r} \approx C_l$. Third, if the composition change of C_l from C_0 to C_{eut} is linear, one can calculate C_l^{*r} as a function of solidification time t_f

$$C_l^{*r} = C_0 + (C_{eut} - C_0) \frac{t}{t_f} \quad \text{(Equation 39)}$$

To determine the time needed for the smaller arm to dissolve completely $t_{r=0}$ one has to substitute (Equation 37) into (Equation 38), integrate over the radius from r_0 to 0 and over time from 0 to $t_{r=0}$ and rearrange the terms to get (47)

$$R^2 \lambda_2^0 = \left(\frac{1}{\frac{r_0}{R} + \ln \left(1 - \frac{r_0}{R} \right)} \right) \left(- \frac{\Gamma_{sl} D_l \ln \frac{C_l(t_{r=0})}{C_0}}{m_l (1 - k_0) (C_{eut} - C_0)} \right) t_f \quad \text{(Equation 40)}$$

where $C_l(t_{r=0})$ is the liquid composition at $t_r = 0$. At the time when the smaller arm has been totally dissolved, the initial secondary dendrite arm spacing has doubled. If one chooses the initial values $R = \lambda_2^0/2$ and $r_0/R = 0.5$, the time at which $\lambda_2 = 2\lambda_2^0$ is can be calculated by (47)

$$\lambda_2(t_{r=0}) = 5.5 \left(- \frac{\Gamma_{sl} D_l \ln \frac{C_l(t_{r=0})}{C_0}}{m_l (1 - k_0) (C_{eut} - C_0)} \right)^{\frac{1}{3}} t_{r=0}^{\frac{1}{3}} \quad \text{(Equation 41)}$$

If one extends (Equation 41) to the end of solidification with $t = t_f = \Delta T'_o / Gv^*$, one obtains

$$\lambda_2(t_f) = 5.5 \left(- \frac{\Gamma_{sl} D_l \ln \frac{C_{eut}}{C_0}}{m_l (1 - k_0) (C_{eut} - C_0)} \right)^{\frac{1}{3}} \left(\frac{\Delta T'_o}{Gv^*} \right)^{\frac{1}{3}} \quad \text{(Equation 42)}$$

2.1.2. Eutectics

Due to the growth of the primary phase and if $k_0 < 0$, the liquid composition of a binary alloy enriches. The liquid composition C_l might reach the eutectic composition C_{eut} . At this invariant point, a second phase β starts to form. From then on, the forming phase α rejects solute B, and the phase β rejects solute A. The exchange of solute happens via the liquid melt in front of the solidification front. Both, the $\alpha - l$ and $\beta - l$ interfaces are curved, and so the eutectic grows at an undercooling ΔT below the eutectic temperature T_{eut} . One distinguishes between different eutectic morphologies: regular, irregular, fibrous, lamellar, nodular, divorced and multi-component/multi-phase eutectics.

If one considers a binary hypoeutectic alloy of components A and B with a growing dendrite in a thermal gradient, the dendrite tip lies a little bit behind the isothermal liquidus line $T_{tip}^* < T_{liq}(C_0)$. The interdendritic liquid enriches with increasing distance from the dendrite tip. The eutectic growth starts when the liquid reaches (or comes close to) the eutectic composition and as mentioned above the undercooling ΔT reaches the nucleation undercooling for the β phase ΔT_n^β . This can be deduced from the linearized binary phase diagram in Figure 2-7 as

$$\Delta T_n^\beta = T_{liq}^\beta(C_l^{*\alpha}) - T_{liq}^\alpha(C_l^{*\alpha}) \quad \text{(Equation 43)}$$

where $T_{liq}^\beta(C_l^{*\alpha})$ is the liquidus temperature of phase β at the composition of the liquid phase at the interface with phase α and $T_{liq}^\alpha(C_l^{*\alpha})$ the liquidus temperature of phase α at the same composition, respectively.

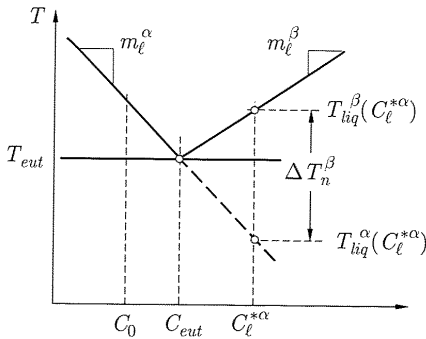


Figure 2-7: Undercooling at nucleation of a second phase in a hypoeutectic system (47)

If ΔT_n^β is big enough, the β phase will nucleate at the $\alpha - l$ interface. The nucleation and growth proceeds in a defined crystallographic relationship with the α phase, the β phase spreads and might become unstable forming “fingers” (58). Because of the concurrent continuous α growth, a natural sequence of both phases is created. If the eutectic solidification is characterized by the triple junctions of α , β , and l , one speaks of coupled growth. If both phases appear at the same temperature, one speaks of isothermal coupled growth. Because of the rejection of solute B and A by phases α and β respectively, lateral diffusion in the liquid is induced and reduces the minimum and maximum composition in front of both growing $s - l$ interfaces drastically. As the lamella spacing decreases, the lateral diffusion can increase. The final lamella spacing is determined by the diffusive transport of solute but also on the surface tensions of both $s - l$ interfaces.

Coupled eutectic growth morphology

As introduced before in chapter 2.1.1.3 on dendritic growth, the rule of thumb was stating that if the molar entropy of fusion divided by the ideal gas constant is bigger than $\Delta S_f^m / R > 2$, the growing phase shows a high interfacial anisotropy and is likely to solidify in a faceted manner. If the quotient is smaller than two, the phase solidifies non-faceted. If both growing phases in a binary eutectic solidify faceted, the triple junctions of $\alpha - \beta - l$ would appear to grow independently, and no coupled growth is possible. If one of both phases (α or β) solidifies faceted, the non-faceted phase can adjust its growth direction to the faceted phase. Under these conditions or if both phases are non-faceted, four eutectic morphologies can be distinguished. Dependent on the relation of the volume fractions g_α and g_β lamella or fibres are formed.

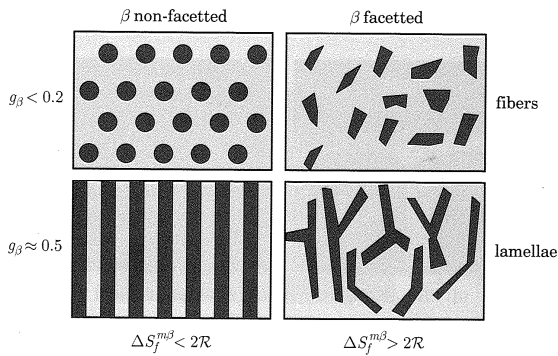


Figure 2-8: Observable eutectic morphology if the α phase solidifies non-faceted and the β phase solidifies faceted of non-faceted with changing volume fractions of β . The thermal gradient lies in the direction of the viewer (47)

In irregular eutectics, one of the phases solidifies faceted (see Figure 2-8 right side). The triple junctions can be maintained, and the non-faceted phase follows the needles or plates of the faceted phase. The faceted phase grows in defined directions possibly with the aid of defects like twins or screw dislocations. The Al-Si eutectic is a typical example of this morphology type.

In regular eutectics, both phases are non-faceted, which is typical for two metallic phases. The triple junctions can be maintained in almost any direction of growth although preferential directions may also be predominant. Typical examples in the aluminium system are Al-Cu or Al-Zn. Two crystallographically different phases tend to adjust their orientation according to a common preferential direction, fibres or lamella develop based on the minimisation of the interfacial energy $\gamma_{\alpha\beta}$. It can be shown that the transition between fibres and lamella occurs between $g_\beta \approx 0.28 - 0.38$.

Jackson and Hunt (59) developed in their analysis for regular lamellar eutectics with a periodic $\alpha - \beta$ lamellae spacing λ and relatively small solidification rates a correlation for the undercooling of the eutectic front

$$\Delta T = A_C \frac{v^* \lambda}{D_l} + \frac{A_R}{\lambda} \quad \text{(Equation 44)}$$

and for a given interface velocity v^* the undercooling shows a minimum which in turn is correlated with a lamella spacing

$$\lambda_{ext} = \sqrt{\frac{A_R D_l}{A_C v^*}} \quad \text{(Equation 45)}$$

A_R/A_C is a weighted average capillary length and D_l/v^* the thickness of the boundary layer ahead of the steady-state planar front. In (Equation 44) the first term of the right-hand side is proportional to the Péclet number $Pe = v^* \lambda / D_l$ and increases with increasing lamella spacing λ and velocity v^* . The second term is inversely proportional to λ with a coefficient proportional to the weighted sum of the Gibbs-Thomson coefficient of both phases. The function of undercooling ΔT versus lamella spacing λ is governed by two branches, a capillary branch, and a diffusive branch. At the minimum, both undercoolings, the solutal undercooling ΔT_C , and the average curvature undercooling ΔT_R are equal, and so λ_{ext} is simply the geometric mean of these two length scales. Notice that (Equation 45) is independent of the thermal gradient G . The analysis also allows an application to equiaxed growth but assumes in this case that the local undercooling is constant and the extremum corresponds to the maximum velocity of the eutectic. Jackson and Hunt also extended their theory to rod-like structures and Trivedi et al. (60) to rapid solidification.

In two dimensions (shown in experiments of very thin films), two mechanisms can be observed which allow the lamella spacing to adapt, following the change of interfacial velocity. If the eutectic interface velocity v^* decreases, lamellae can be eliminated by an overgrowth of another lamella. If v^* increases enough, the existing lamellae develop a negative curvature which increases the solute built up at these locations even further until a new lamella in the middle nucleates. It could be deduced from the theory of Jackson and Hunt, that this velocity increase is reached at $v_{new}^* = 4v_{old}^*$, but in reality, several mechanisms allow the lamella spacing to adjust to increased interfacial velocity.

Lamellae cannot grow below λ_{ext} due to elimination by overgrowth, but it is possible to some extent above λ_{ext} . To discuss this, it is convenient to introduce a dimensionless eutectic spacing $\Lambda = \lambda / \lambda_{ext}(v^*)$. In two dimensions, if $\Lambda > \Lambda_{2\lambda}$, the eutectic begins to oscillate (61). In this 2λ mode, the α phase has still a spacing of λ , but the β phase oscillates with 2λ . If $\Lambda > \Lambda_{tilt}$, the lamellae may tilt with a tilt angle

proportionally increasing with $\Lambda - \Lambda_{tilt}$. There are more mechanisms like 1λ oscillation, which have been observed (62), but in three dimensions there are even more mechanisms to accommodate for a velocity increase. For example, a lateral instability if $\Lambda > \Lambda_{crit}$, which has been observed in small Al-Cu specimens (63). Small fluctuations lead to perturbations on the lamellar phase, which grow parallel to the parent phase and detach from it eventually. In this case, the critical dimensionless lamella spacing has been observed to be in the region of approximately $\Lambda_{crit} \approx 1.2$. Another mechanism to reduce λ is the formation of a zigzag structure. It continuously develops with increasing speed v^* and reduces the average distance between the centres of the lamellae by the factor $\sin \theta$ with θ as the angle between the zigzag structure and the straight lamellar structure. In the case of big Λ , labyrinth-like structures were also observed (62).

Irregular eutectics

In irregular eutectics one of the phases grows faceted, it can only form along defined crystallographic directions. The Al-Si eutectic is a typical example in which the Si lamella typically form plates along the (111) planes. The faceted phase determines the growth of the eutectic, assisted by defects like twins or screw dislocations and the non-faceted phase follows. For the growth of the faceted phase, attachment kinetics may also play an important role. The Si plates in the Al-Si eutectic form assisted by twins with a typical spacing of 0.4–1 μm (at normal solidification conditions) and are typically interconnected to one eutectic nucleus.

The growth of the faceted Si phase can be affected in several ways. For one, the growth rate changes the growth morphology (modification can be achieved above approximately 1 mm/s). Additionally, active elements like Na, Sr, Ba and other rare earth elements cause a Si refinement and even a change to a non-faceted and fibrous morphology. The mechanism of eutectic modification is not entirely understood. Lu and Hellawell presented a theory assuming an enhancement of twinning of the Si phase by adsorption of elements with large atomic radii (64).

In case two faceted lamellae grow closer together, a similar process as in regular eutectics takes place (if $\Lambda < 1$). One lamella overgrows the other one. The result is a minimum spacing between the two lamellae after overgrowth λ_{min} . If two lamellae diverge $\Lambda > 1$, the non-faceted phase starts to build up solute in its centre. The local liquidus temperature is then reduced (if $m_l < 1$), the interface recedes in the temperature gradient, and at the spacing λ_{br} the driving force for the faceted phase is big enough to nucleate a new lamella. Thus, the range of lamella spacing for irregular eutectics can be in the range of $[\lambda_{min}, \lambda_{br}]$. If one assumes that λ_{min} and λ_{br} lie on the curve of the undercooling as a function of lamella spacing $\Delta T(\lambda)$ derived from the Jackson and Hunt theory, the average lamella spacing can be defined as (47)

$$\bar{\lambda} = \frac{\lambda_{min} + \lambda_{br}}{2} = \phi \lambda_{ext} \quad \text{(Equation 46)}$$

and the kinetics of growth for irregular eutectics can be described by (47)

$$\Delta T \bar{\lambda} = A_R (1 + \phi^2) \quad \text{(Equation 47)}$$

$$\Delta T = \left(\frac{1}{\phi} + \phi \right) \sqrt{\frac{A_R A_C}{D_l}} \sqrt{v} \quad \text{(Equation 48)}$$

$$\bar{\lambda}^2 v = \phi^2 \frac{A_R}{A_C} D_l \quad \text{(Equation 49)}$$

Note, that the eutectic front is no longer isothermal, because of its deep depressions due to solute build up between lamellae and thus the gradient G has to be considered.

Divorced eutectic

Under certain conditions in hypoeutectic alloys, a divorced eutectic can be observed. It is typical for some systems like Mg-Al and especially for moderate amounts of solute. In this case, there is a high volume fraction of primary phase before the eutectic composition is reached, and so the remaining liquid phase exists in the form of a thin liquid film or separated droplets. The small spatial dimensions in this late-stage of solidification make it hard for the eutectic phase to nucleate because a nucleation event has to take place in every separated liquid area. This way the eutectic solidification is delayed and the primary phase continues to grow. The result is a further increase in the nucleation undercooling. If the diffusion distance between the primary and secondary phase becomes equal or smaller than the space required for coupled growth, no gain of energy can be achieved by the formation of a triple junction. The second phase starts to grow independently of the primary phase, which also continued to grow. The result is a partially divorced or fully divorced eutectic.

Eutectic colonies

Under industry conditions, there are seldom cases in which binary compounds are used, and the morphological changes of the eutectic solidification can be significant if a third compound is involved. In the simplest case of a ternary system composed of three eutectic binary systems of compounds A-B, B-C and C-A, let's assume a eutectic composition of A and B with a low amount of C. If the composition cools down

to the monoinvariant line at which the liquid, α , and β phase are in equilibrium, further cooling starts the formation of the $\alpha - \beta$ eutectic. Both lamellae reject component C during growth. This would cause a solute build-up of C in front of the eutectic interface, comparable to the solidification of a planar front discussed in 2.1.1.3. The result is the same as discussed previously. The solidification front may become unstable and form eutectic cells or even dendrite, called eutectic colonies. The solute layer of C is superimposed by the diffusion of A and B. If the alloy has a composition of the 3-phase eutectic, the simultaneous growth of α , β , and γ is possible and 3-phase eutectic forms.

2.1.2.1. Coupled zone

Under industrial solidification conditions, the phases predicted by the phase diagram may not form as predicted. Nucleation and growth kinetics of phases play a significant role and may lead to the formation of a metastable phase rather than a stable. The coupled zone results from the competition between the primary phase and the eutectic morphology.

Under the assumption of a symmetric binary system of eutectic composition in which phases α and β solidify non-faceted, the eutectic composition should be approximately 50 % of α and β phase. If the alloy has a hypo- or hypereutectic composition, the amount of α respectively β phase formed during solidification should increase, dependent on the composition and cooling rate. If the composition is slightly hypereutectic and the solidification takes place at a low speed below the stability limit for the β -planar front $v^* < D_l G / \Delta T_{0\beta}$ with $\Delta T_{0\beta}$ as the solidification interval of β , the temperature at the $\beta - l$ interface is given by the β solidus line for C_0 as $T_{sol}^\beta(C_0) = T_{liq}^\beta(C_0/k_{0\beta})$. This temperature is lower than the eutectic temperature T_{eut} , and so the coupled eutectic is more likely to form with phase fractions of α and β given approximately by the lever rule. If the solidification is still slow and the composition is far from the eutectic composition, greater than the solubility limit of $C_0 \geq (1 - (1 - C_{eut})k_{0\beta})$, the solidus temperature is equal or higher than the eutectic temperature T_{eut} , and there is no advantage in the formation of a coupled eutectic solidification front. If the solidification velocity is larger and above the stability limit and the composition is in an intermediate range between the eutectic composition and the maximum solubility limit of phase β , the β phase morphology will change to dendritic. Now the temperature at the dendrite tip is given by $T_\beta^*(v^*) = T_{liq}^\beta(C_0) - \Delta T^\beta(v^*, C_0)$. The eutectic coupled growth starts at: $T_{eut}^*(v^*) = T_{eut} - \Delta T_{eut}(v^*, C_0)$ and both phases are competing at the highest temperature of formation, because $T_{eut}^*(v^*)$ is monotonically decreasing with v^* whereas $T_\beta^*(v^*)$

exhibits a maximum. The increase in $T_{\beta}^*(v^*)$ is associated with the change from planar to cellular to dendritic solidification morphology. The decline after the peak is attributed to reasons discussed earlier in 2.1.1.3. One can distinguish three characteristic regions in directional solidification because the microstructure that forms at the highest temperature forms first. For low interfacial velocities, the temperature of the eutectic formation lies above the temperature for β phase formation $T_{eut}^*(v^*) > T_{\beta}^*(v^*)$. The result is a coupled eutectic growth. At intermediate interfacial velocities $T_{\beta}^*(v^*) > T_{eut}^*(v^*)$ the β dendrites grow, followed by the interdendritic eutectic. At high interfacial velocities, again $T_{eut}^*(v^*) > T_{\beta}^*(v^*)$, so a fully coupled eutectic morphology forms before the β dendrites can form. If the first and third region is marked in the phase diagram, this area can be called the coupled zone.

If the β phase solidifies faceted in a eutectic system, the irregular phase forms slower than the regular one. For faceted phases, attachment kinetic can play a significant role and slow the growth down. Moreover, the often-observable plates, rather than needles, also contribute to more gradual solidification. The result can be, that $T_{\beta}^*(v^*)$ shows a faster increase and after the maximum a more pronounced decrease. At high cooling rates, this can cause that the α phase becomes the leading phase, followed by the formation of the coupled eutectic. This solidification type can be added to the already described solidification morphologies for regular eutectic, explained above. This means that four regions can be distinguished and the coupled zone becomes skewed towards the faceted phase. Kurz and Fischer fitted the growth kinetics under the assumption of a faceted α phase and a non-faceted β phase and deduced an equation for the nucleation undercooling $\Delta T^{\alpha,\beta}$

$$\Delta T^{\alpha,\beta} = \frac{GD_l}{v^*} + A^{\alpha,\beta}\sqrt{v^*} \quad \text{(Equation 50)}$$

where A^{α} and A^{β} are adjustable parameters. The growth of the eutectic is similar to (Equation 49) but takes the thermal gradient G into account

$$\Delta T^{eut} = A^{eut} \sqrt{\frac{v^*}{G}} \quad \text{(Equation 51)}$$

The theory of the (skewed) coupled zone of the Al-Si eutectic explains the observations of the formed microstructure at different cooling rates. In Figure 2-9 an Al-Si eutectic has been solidified with low (a) and high (b) cooling rate.

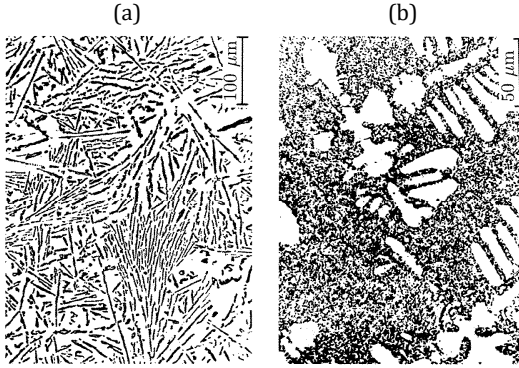


Figure 2-9:
Microstructure of two
eutectic Al-Si alloys,
solidified at low (a) and
high (b) cooling rate
(65)

The low solidification rate leads to a fully coupled eutectic microstructure. The high solidification rate leads to the formation of primary (non-faceted) α -Al phase, followed by the growth of coupled eutectic.

2.1.3. Segregation

Segregation develops during solidification due to solute rejection from the solid and solute diffusion in the liquid and solid. The transport of solute in the liquid and of heat in the liquid and solid are in most cases sufficiently fast to be considered uniform at the scale of the microstructure. The transport of solute in the solid can vary significantly depending on the solidification conditions.

The simplest case which can be considered is the one-dimensional microsegregation of a binary alloy. Under the assumption of a two-dimensional periodic array of dendrites with secondary dendrite arm spacing λ_2 and a length L , two components, a constant density of the liquid ρ_l and solid ρ_s and constant thermal properties of the solid and liquid, the governing equations for heat and solute transport in a unit cell are (47):

$$\frac{\partial T}{\partial t} = \alpha \left(\frac{\partial^2 T}{\partial x^2} + \frac{\partial^2 T}{\partial z^2} \right) \quad \text{(Equation 52)}$$

$$\frac{\partial C_l}{\partial t} = D_l \left(\frac{\partial^2 C_l}{\partial x^2} + \frac{\partial^2 C_l}{\partial z^2} \right) \quad \text{(Equation 53)}$$

$$\frac{\partial C_s}{\partial t} = D_s \left(\frac{\partial^2 C_s}{\partial x^2} + \frac{\partial^2 C_s}{\partial z^2} \right) \quad \text{(Equation 54)}$$

By introducing the scaled variables

$$\xi = \frac{x}{\lambda_2/2} \quad \zeta = \frac{z}{L} \quad \tau = \frac{t}{t_f} \quad \text{(Equation 55)}$$

where t_f is the solidification time, one gets

$$\frac{\partial T}{\partial \tau} = \frac{4\alpha t_f}{\lambda_2^2} \left(\frac{\partial^2 T}{\partial \xi^2} + \frac{\lambda_2^2}{L^2} \frac{\partial^2 T}{\partial \zeta^2} \right) \approx Fo_T \frac{\partial^2 T}{\partial \xi^2} \quad \text{(Equation 56)}$$

$$\frac{\partial C_l}{\partial \tau} = \frac{4D_l t_f}{\lambda_2^2} \left(\frac{\partial^2 C_l}{\partial \xi^2} + \frac{\lambda_2^2}{L^2} \frac{\partial^2 C_l}{\partial \zeta^2} \right) \approx Fo_l \frac{\partial^2 C_l}{\partial \xi^2} \quad \text{(Equation 57)}$$

$$\frac{\partial C_s}{\partial \tau} = \frac{4D_s t_f}{\lambda_2^2} \left(\frac{\partial^2 C_s}{\partial \xi^2} + \frac{\lambda_2^2}{L^2} \frac{\partial^2 C_s}{\partial \zeta^2} \right) \approx Fo_s \frac{\partial^2 C_s}{\partial \xi^2} \quad \text{(Equation 58)}$$

If $\lambda_2 \ll L$ the problem reduces to one-dimensional. The dimensionless groups in the equations are the Fourier numbers, which represent the ratio of the local solidification time t_f to the characteristic time for heat and solute transport. The equations can be further developed if the experimental correlation between λ_2 and t_f is introduced. For aluminium alloys between solidification times of $0.1 \text{ s} < t_f < 10^7 \text{ s}$ the dendrite arm spacing is well described by (47)

$$\lambda_2 = \left(10^{-5} \text{ m s}^{-\frac{1}{3}} \right) t_f^{\frac{1}{3}} \quad \text{(Equation 59)}$$

For typical values of α , D_l and D_s and solidification times between $0.1 \text{ s} < t_f < 10^7 \text{ s}$ for aluminium alloy the evaluation of the Fourier numbers shows that $Fo_T \gg 1$ and $Fo_l \gg 1$. If one rewrite (Equation 56) and (Equation 57), neglecting the terms that are small compared to unity, one gets

$$\frac{\partial^2 T}{\partial \xi^2} \approx 0 \quad \text{(Equation 60)}$$

$$\frac{\partial^2 C_l}{\partial \xi^2} \approx 0 \quad \text{(Equation 61)}$$

The solution of the two equations with the boundary conditions $\xi = 0, 1$ gives $T = T(t)$ and $C_l = C_l(t)$, meaning that temperature and liquid composition has no spatial dependency and may only vary in time. There are two cases to be distinguished for the solid composition. If $t_f > 1000 \text{ s}$ both sides of (Equation 58) are of comparable order and diffusion in the solid must be considered. This is called back diffusion. Under typical casting conditions $t_f < 1000 \text{ s} \Rightarrow Fo_s \ll 1$, the composition does not change with time in the solid and diffusion can be neglected. The result of the scaling analysis has been first introduced by Gulliver(66) and Scheil(67). The Gulliver-Scheil equation can be deduced from the developed concepts under a few assumptions. There is a solute balance over the unit cell, the density of the solid and liquid are constant and equal, the unit cell is a closed system, the liquid composition in the unit cell is equal to the liquid composition at the solid-liquid interface (perfect

mixing), there is a thermodynamic equilibrium at the interface (i.e. $C_s^* = k_0 C_l^*$), and diffusion in the solid can be neglected ($D_s = 0$). This way one gets the Gulliver-Scheil equation (47):

$$C_l^* = C_0 g_l^{k_0-1} \quad \text{(Equation 62)}$$

The segregation profile in the solid is obtained by $C_s^* = k_0 C_l^*$. For the liquid fraction regarding temperature under the assumption that the liquidus curve is a straight line ($T = T_f + m_l C_l$) follows

$$g_s = 1 - g_l = 1 - \left(\frac{T - T_f}{T_{liq} - T_f} \right)^{\frac{1}{k_0-1}} \quad \text{(Equation 63)}$$

At low cooling rates ($Fo_s \gg 1$) the solid composition is almost independent of the spatial position, and the lever rule is describing the solidification better. At high cooling rates ($Fo_s \ll 1$) the other extreme, the Gulliver-Scheil equation, describes the solidification situation best. For intermediate cooling rates ($Fo_s \approx 1$) diffusion in the solid needs to be considered. Models which consider back-diffusion have to take the effect of time and scale into account. This is why Brody and Flemings(68) developed a model which is based on the Fourier number in the solid Fo_s

$$g_s(T, Fo_s) = \frac{1}{1 - 2k_0 Fo_s} \left[1 - \left(\frac{T - T_f}{T_{liq} - T_f} \right)^{\frac{1-2k_0 Fo_s}{k_0-1}} \right] \quad \text{(Equation 64)}$$

$$C_s^*(g_s) = k_0 C_0 [1 - (1 - 2k_0 Fo_s) g_s]^{\frac{k_0-1}{1-2k_0 Fo_s}} \quad \text{(Equation 65)}$$

Clyne and Kurz(69) further developed Brody and Fleming's model by replacing Fo_s by a function $f(Fo_s)$:

$$f(Fo_s) = Fo_s \left(1 - e^{-\frac{1}{Fo_s}} \right) - 0.5 e^{-\frac{1}{2Fo_s}} \quad \text{(Equation 66)}$$

The advantage of this substitution is that not only the Scheil approximation is retrieved if $Fo_s \rightarrow 0$ but also the lever rule if $Fo_s \rightarrow \infty$.

2.1.4. Freezing range

2.1.4.1. Mushy zone

Pure metals solidify without a solidification interval, which is also the case for high purity aluminium, which solidifies with a planar solidification front. Alloyed aluminium has a solidification interval, which means that during solidification there are both phases, the liquid and the solid, stable in the same region. How this region is

structured depends for typical aluminium cast alloys mainly on the quotient of the gradient G to the growth rate v^* and the number of nuclei in the melt. For a low G/v^* ratio and sufficient nuclei in the melt, the typical growth morphology is equiaxed dendritic. If there are less potent nuclei in the melt, the solidification morphology may switch to a columnar dendritic front. The equiaxed dendritic structure is the most common one, for example, if typical foundry alloys with a medium silicon content of around 6 to 8 wt% are cast into sand moulds. Examples of all three solidification morphology types are shown in Figure 2-10.

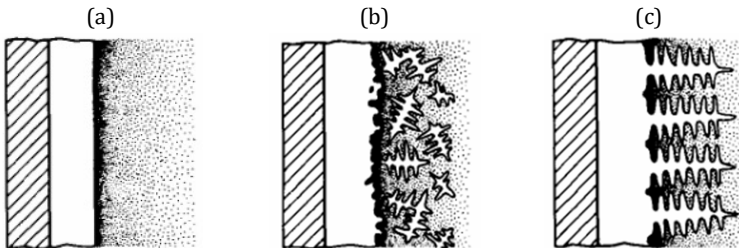


Figure 2-10: (a) Planar solidification front of pure or rapidly cooled metals, (b) equiaxed dendritic solidification front, (c) columnar dendritic solidification front (70)

For sand castings, due to the low thermal conductivity of the mould material, this state of partly liquid partly solid may stretch through the entire casting and thus is responsible for the critical processes taking place in the last stages of solidification. If the solidification progresses from the mould to the inner areas of the casting one speaks of an exogenous solidification type, if the growth of nuclei floating in the melt is dominant one speaks of endogenous solidification.

In the equilibrium state of a binary alloy, the connection between the solidified volume g_s and the temperature T is given by the binary phase diagram, as is the actual composition of the solid C_s or liquid phase C_l . A phase diagram depicts the equilibrium state at a given constant pressure which is usually standard pressure (100.000 Pa). A simple phase diagram for a binary alloy is shown in Figure 2-11. Phase diagrams of the most relevant systems for this thesis, Al-Cu, and Al-Si, are shown in Figure 2-12.

2.1.4.2. Feeding mechanisms

Five feeding mechanisms are typically distinguished. Liquid feeding, mass feeding, interdendritic feeding, burst feeding, and solid feeding. They all arise from the need for mass transport to compensate for solidification shrinkage and cooling contraction. Figure 2-13 illustrates the different zones in a directional solidification situation. The mechanisms can co-occur, depending on alloy composition and solidification conditions.

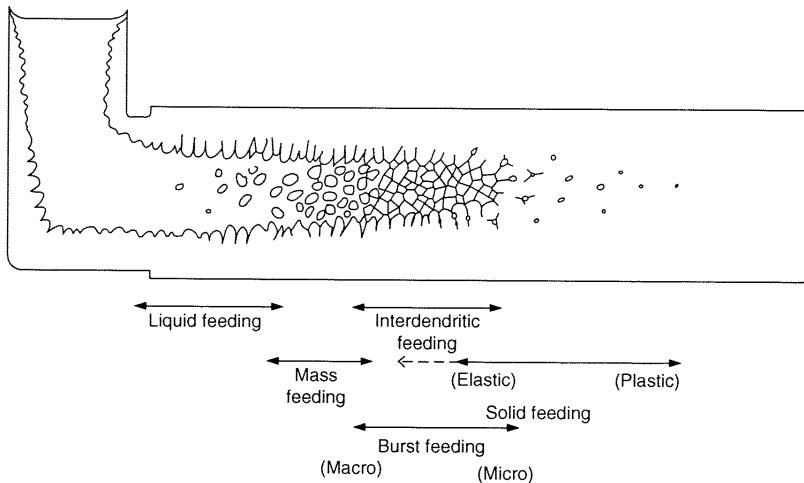


Figure 2-13: Illustration of the five feeding mechanisms of an alloy showing a solidification interval. A chill on the right generates directional solidification towards the feeder (42)

Liquid feeding is the flow of liquid melt, induced by the pressure difference. It is the most important feeding mechanism for pure metals and eutectics (substances which solidify with a smooth solid-liquid interface). The lower the viscosity of the melt, the less pressure difference is necessary for a certain feeding flow. Skin freezing alloys may develop an extended shrinkage pipe from the feeder into the casting. Long-freezing range alloys will form a dendritic network that is eventually “sucked empty” by liquid feeding. A result is a form of interdendritic feeding (42).

The formation of equiaxed dendrites in Al-Si foundry alloys and the pressure gradient induced flow of this so-called “slurry”, marks the mass feeding. With increas-

ing solid fraction the overall viscosity increases as well, and a larger pressure gradient is necessary to induce the feeding flow. In thin sections, where only a few grains (e.g. 2 or 3) are formed, mass feeding is unlikely to occur. The movement of the grains is too limited by the contact to the mould wall. In thicker sections, this feeding mechanism may play an important role to compensate for the local volume deficit. Campbell proposes the ratio of “casting section thickness” divided by “average grain size” as an important criterion for the occurrence which is, in turn, one of four major mechanisms influenced by grain refinement which reduces porosity (42).

Mass feeding continues until the dendrite coherency point is reached (73, 74). As solidification progresses, the dendrites impinge on each other, reach the maximum packaging density, and the movement of the solid phase is ceasing. The liquid phase now just flows through the mushy network, which is called interdendritic feeding. This type of feeding is crucial for the formation of porosity (42, 75). If the metallostatic pressure is not large enough to induce sufficient flow through the mush zone, pores form to release the pressure difference. The flow resistance of the solid dendrite network depends on the length, tortuosity and specific surface area of the channels. It is reduced by a shorter mushy zone, smaller globular primary grains, and a eutectic solidification which does not block the feeding paths. The pressure drop in the mushy zone is discussed in more detail in Section 2.2.1.2.

If the solid dendritic network cannot stand the pressure difference induced forces, it can collapse. This process is called burst feeding (42, 76). There is strong circumstantial evidence for burst feeding. If it occurs, it may further decrease the feedability of the mushy zone by blocking feeding paths with dendrite fragments (74, 76). The risk of burst feeding increases sharply if the stresses in the mushy zone increase faster than the strength of the network. After pore formation took place, burst feeding is unlikely because the necessary stresses are already released (76).

If the stresses associated with the pressure drop exceed the yield strength of the solid material (e.g. the surface of the casting), it may yield and compensate the volume deficit by plastic deformation, which is called solid feeding.

2.2. Porosity

Porosity is one of the most severe defects in aluminium castings. Especially microporosity prevents the application of aluminium cast components in certain areas like the aerospace industry. Micropores, as by definition small voids of the micrometre scale, may nucleate cracks and thus limit the fatigue life in service.

Two main contributions can be made out as causes for micropores, “shrinkage” and “gas”. Both types will be roughly characterized in this paragraph. The first contribution is the lack of feeding of the volume deficit in the mushy zone. Due to the density difference between the liquid and solid phase $\rho_l < \rho_s$, the local solidification necessitates a constant liquid flow in the direction of the solidification front. Alloys, which exhibit a long freezing range with a dense dendritic mushy zone hinder this feeding flow and generate a pressure drop. If the drop in liquid pressure is sufficient, a pore may be nucleated and instantaneously compensate most of the accumulated volume deficit. This type of porosity is often referred to as “shrinkage porosity” although it will be shown later that both types of porosity can be described by the same governing equations. Thus, a distinction in the stage during which pores nucleate seems more reasonable. The second contribution is soluble gases in the melt, in the case of aluminium primarily hydrogen. Hydrogen diffuses into existing voids and inflates pores to spherical bubbles which are often referred to as “gas porosity”. The rejection of hydrogen from the solid, which has a much lower solubility than the liquid, and the segregation during the progressing solidification, are the leading causes to reach the necessary hydrogen levels for precipitation to start. The sources of hydrogen are reactions with water or a surface reaction with the surrounding atmosphere (and the containing water vapour). The result is the formation of alumina (aluminium oxide) and dissolved atomic hydrogen. If the hydrogen level is sufficiently high, pores can nucleate early in solidification before a highly developed dendritic network is established.

In casting practice, typically both contributing factors are involved to varying degrees, and so a differentiation in the pore formation stage is reasonable. Early-stage porosity is primarily driven by hydrogen and can be characterised by high sphericity of the pores associated with the sufficiently available space. Late-stage porosity is characterised by its tortuous form/low sphericity caused by impingement of the pores and the dendritic network. The time of formation is very late, often associated with the formation of the eutectic, which can be, depending on the alloy composition, very dense. For example, alloys containing high amounts of Cu form the high-density eutectic Al_2Cu and have an extended solidification interval, which means a high feeding demand to compensate the associated solidification shrinkage and concomitantly a large pressure drop due to the enlarged mushy zone. The two-dimensional appearance of this kind of pores is small, for example from metallographic sectioning; nevertheless, the three-dimensional pore size can be quite the opposite. The first who observed pore formation in-situ were Lee and Hunt(77) by x-ray radiography experiments with Al-Cu alloys. Today, by the application of high quality and high-intensity x-rays available in synchrotron facilities, spatial ($< 1 \mu\text{m}$) and

temporal (< 1 s) resolutions sufficient to capture in-situ pore formation are available.

2.2.1. Nucleation and growth of pores

2.2.1.1. Fundamental equations

The basis for the definition of the fundamental equations describing the phenomena related to pore formation in the mushy zone is a Representative Volume Element (RVE), consisting of liquid, solid, and pores with

$$g_s + g_l + g_p = 1 \quad \text{(Equation 69)}$$

The average mass conservation equation is given by (78)

$$\frac{\partial \langle \rho \rangle}{\partial t} + \nabla \langle \rho \mathbf{v} \rangle = 0 \quad \text{(Equation 70)}$$

where $\langle \rho \rangle$ is the average density of all phases in the RVE

$$\langle \rho \rangle = \rho_s g_s + \rho_l g_l + \rho_p g_p \quad \text{(Equation 71)}$$

The only relevant gas in solution of aluminium is hydrogen. Because its density is much lower compared to the solid or liquid phase, (Equation 71) can be written as

$$\langle \rho_0 \rangle(T) = \frac{\rho_s g_s + \rho_l g_l}{g_s + g_l} \quad \text{(Equation 72)}$$

where $\langle \rho_0 \rangle(T)$ is the pore-free density. From (Equation 69), (Equation 71), and (Equation 72) it follows

$$\langle \rho \rangle = \langle \rho_0 \rangle (1 - g_p) \approx \langle \rho_0 \rangle - \rho_l g_p \quad \text{(Equation 73)}$$

By neglecting the transport of gases, the mean mass flux $\langle \rho \mathbf{v} \rangle$ can be written as

$$\langle \rho \mathbf{v} \rangle = \rho_l g_l \langle \mathbf{v} \rangle_l + \rho_s g_s \langle \mathbf{v} \rangle_s \quad \text{(Equation 74)}$$

where $\langle \mathbf{v} \rangle_l$ and $\langle \mathbf{v} \rangle_s$ are the intrinsic velocities of the respective phases. From (Equation 70), (Equation 73), (Equation 74), and by neglecting the term $g_p (\partial \rho_l / \partial t)$ because it is much smaller than the other, it can be followed (47)

$$\frac{\partial \langle \rho_0 \rangle}{\partial t} - \rho_l \frac{\partial g_p}{\partial t} + \nabla (\rho_l g_l \langle \mathbf{v} \rangle_l) + \nabla (\rho_s g_s \langle \mathbf{v} \rangle_s) = 0 \quad \text{(Equation 75)}$$

In (Equation 75) the first term represents the solidification shrinkage due to solidification, which can be compensated by pore formation, the second term, or by interdendritic feeding of the liquid, the third term. Theoretically also the deformation of the solid can compensate the solidification shrinkage, the fourth term, but this phenomenon is primarily associated with hot tearing, which is beyond the scope of this work.

2.2.1.2. Pressure drop in the mushy zone

As the solidification progresses, the solid network of dendrites gets denser and more complex. Dendrites meet and form a solid interconnected structure. Nevertheless, there has to be a liquid feeding flow due to the volume deficit between liquid and solid. Due to the ripening of the dendrites, the channels of liquid melt in between get thinner and thinner. As a result, the resistance against the liquid feeding flow increases and so does the pressure drop between the still liquid areas and the fully solidified. This phenomenon was first described by Darcy (79). In 1856 Dalmont published a monograph of the French engineer as part of the *Librairie des Corps Imperiaux des Ponts et Chaussees et des Mines*. Before, Darcy had worked for several years on the modernisation and enlargement of the waterworks of Dijon. This task demanded a filter system for a defined quantity of water per day. Because Darcy did not find any available design guidelines to determine the flow rate through a given filter bed of sand, he made his experimental observations. He derived the equation:

$$q = \frac{-K(h_2 - h_1)}{l} \quad \text{(Equation 76)}$$

in which q is the volume of water crossing unit area in unit time, l is the thickness of the sand and h_1 and h_2 the heights above a reference level of water in equivalent water manometers placed above and below the sand. K is a proportionality factor. The equation became known as Darcy's law, and it plays the same role in the conduction of fluids through porous media as Ohm's law in the condition of electricity or Fourier's law in the condition of heat.

Under the circumstances of the liquid feeding flow through the dendritic network in an RVE, Darcy's law translates to

$$\langle \mathbf{v}_l \rangle = g_l \langle \mathbf{v} \rangle_l = -\frac{K}{\mu_l} (\nabla p_l - \rho_l \mathbf{g}) \quad \text{(Equation 77)}$$

where p_l is the pressure in the liquid and \mathbf{g} is the gravity vector. Nielsen et al. (80) showed for Al-Cu alloys that the permeability K could be well described by the solid fraction g_s and with the Carman-Kozeny relationship

$$K = \frac{(1 - g_s)^3}{5(S_V^{sl})^2} \quad \text{(Equation 78)}$$

with the ratio of the solid-liquid area relative to the considered volume S_V^{sl} , which can, in turn, be approximated by (81)

$$S_V^{sl} \approx 6 \frac{g_s}{\lambda_2} \quad \text{(Equation 79)}$$

By combining (Equation 75) and (Equation 77) and neglecting the contraction of the solid phase one gets

$$\nabla \left[\rho_l \frac{K}{\mu_l} (\nabla p_l - \rho_l \mathbf{g}) \right] + \rho_l \frac{\partial g_p}{\partial t} = \frac{\partial \langle \rho_0 \rangle}{\partial t} \quad \text{(Equation 80)}$$

To solve (Equation 80) one needs further information on the segregation and precipitation of gases, the gas mass balance equation (in the case of aluminium for hydrogen).

2.2.1.3. Al-H phase diagram

The Al-H system can be well described by a regular solution model (82). The Gibbs free energy of each phase i (with $i = s, \text{ or } l$) can then be described by (83)

$$G_i^m = \underbrace{X_A G_{Ai}^0 + X_B G_{Bi}^0}_{G_{ideal}} + \underbrace{\Omega X_A X_B}_{\Delta H_{mix}^m} + \underbrace{\mathcal{R}T(X_A \ln X_A + X_B \ln X_B)}_{-T\Delta S_{mix}} \quad \text{(Equation 81)}$$

with the molar fractions of the components X_A and X_B , the interaction parameter for the enthalpy of mixing Ω , the ideal gas constant \mathcal{R} and the entropy of mixing ΔS_{mix} . In Figure 2-14 Qiu et al. (82) used this approach under the assumption that hydrogen is an ideal gas and deduced an Al-H phase diagram and the respective Arrhenius plot (both at 1 atm). The necessary parameters were deduced from experiments. The dotted line in Figure 2-14(a) represents the solubility of hydrogen in liquid or solid aluminium. Experimentally, this solubility corresponds to solid or liquid aluminium in equilibrium with a hydrogen reservoir at 1 atm pressure.

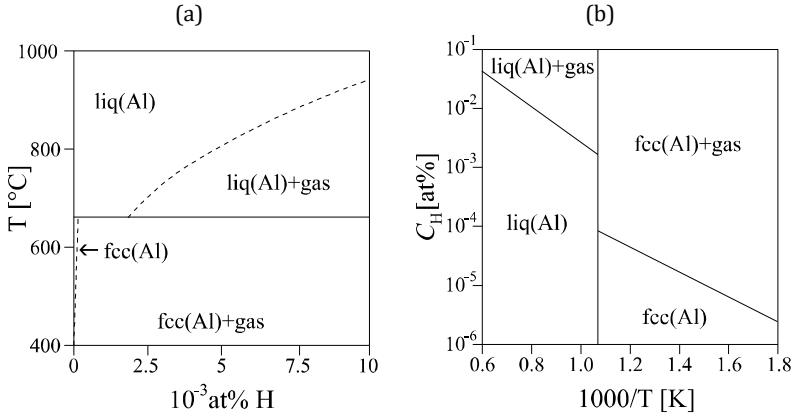
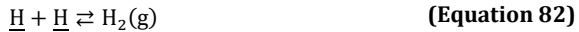


Figure 2-14: Al-H phase diagram (a) and Arrhenius plot of the Al-H diagram (b), both at 1 atm (82)

2.2.1.4. Hydrogen solubility

The equilibrium between hydrogen in solution and gaseous hydrogen follows the reaction



where $\underline{\text{H}}$ is the atomic hydrogen in solution in aluminium. In equilibrium, the vaporisation of hydrogen in solution equals the dissolution of gaseous hydrogen in the melt. For the equilibrium, the equilibrium constant \mathcal{K} is given by (84)

$$\mathcal{K} = \frac{\text{activity of the products}}{\text{activity of the reactants}} \quad \text{(Equation 83)}$$

For gases in equilibrium, the activity of component A is defined as the product of its partial pressure p_A with its fugacity coefficient ϕ_A . For the equilibrium in solution, the activity of component A is given by the product of the molar fraction X_A and its activity coefficient f_A^o (84). Under the assumption that hydrogen is an ideal gas, the equilibrium reaction constant can be calculated to

$$\mathcal{K} = \frac{\frac{p_g}{p_0}}{a_{\text{Hl}}^2} \quad \text{(Equation 84)}$$

with p_g instead of p_{H_2} and the sum of all partial pressures equal to p_0 . From the equilibrium reaction constant, the change of Gibbs free energy of the reaction given by (Equation 82) can be described by

$$\Delta G^m = -\mathcal{R}T \ln \mathcal{K} \quad \text{(Equation 85)}$$

Because hydrogen is present in a diluted solution, one can apply Henry's law, and the activity is given by $a_{Hl} = f_H^o X_H^{eq}$. It can be concluded that

$$\Delta G^m = \Delta H^m - T\Delta S^m = -\mathcal{R}T \ln \mathcal{K} = -\mathcal{R}T \ln \left(\frac{\frac{p_g}{p_0}}{(f_H^o X_H^{eq})^2} \right) \quad \text{(Equation 86)}$$

or

$$\frac{p_g}{p_0} = (f_H^o X_H^{eq})^2 e^{\left(\frac{\Delta H^m}{\mathcal{R}T}\right)} e^{\left(\frac{\Delta S^m}{\mathcal{R}}\right)} \quad \text{(Equation 87)}$$

with ΔH^m as the enthalpy of dissolution and ΔS^m as the entropy of dissolution. Finally, one gets Sievert's law, stating that the amount of dissolved gas in solution is proportional to the square root of the diatomic gas partial pressure

$$X_H^{eq} = \frac{1}{\sqrt{A_{H_2}}} e^{\left(\frac{\Delta H^m}{2\mathcal{R}T}\right)} \sqrt{\frac{p_g}{p_0}} \quad \text{(Equation 88)}$$

with

$$A_{H_2} = e^{\left(\frac{\Delta S^m}{\mathcal{R}}\right)} (f_H^o)^2 \quad \text{(Equation 89)}$$

Sigworth and Engh (85) determined a temperature-dependent reaction constant for H in pure aluminium. From this data ΔH^m and ΔS^m can be deduced.

For binary Al-H alloys with only moderate amounts of H (a few ppm), the fugacity coefficient can be assumed to be unity. If multiple alloying elements are present in the melt, they may alter the solubility of H significantly. Here the use of an adapted interaction coefficient is common, which was first introduced by Wagner (86) and later refined for aluminium alloys by Sigworth and Engh (85). The interaction coefficient is based on a Taylor series expansion of the excess Gibbs free energy of solution of the respective element. Hydrogen can be described by

$$f_{Hl} = f_{Hl}^o 10^c \quad \text{(Equation 90)}$$

with

$$c = \sum_{B=1}^{N_s} (e_H^B C_{Bl} + r_H^B (C_{Bl})^2) \quad \text{(Equation 91)}$$

where e_H^B and r_H^B are the first- and second-order interaction coefficients of the element B (e.g. Cu) in solution and the gas. N_s is the total number of elements in solution. Figure 2-15 shows the solubility of hydrogen as a function of Cu content and temperature ($p_{H_2}/p_0 = 0.1$). As can be seen, the solubility of hydrogen is significantly reduced with increasing Cu content.

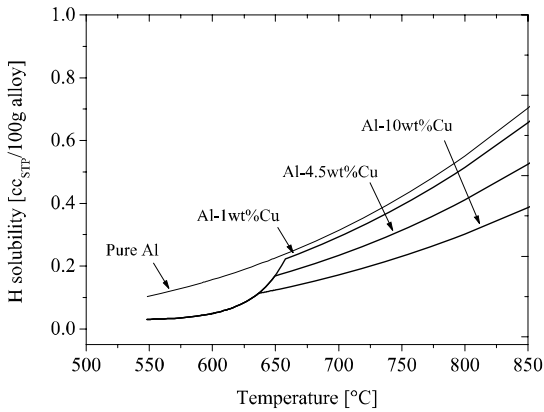


Figure 2-15: Influence of the copper content on the solubility of hydrogen for the partial pressure of $p_{H_2}/p_0 = 0.1$ (71)

The partition coefficient of pure aluminium commonly expresses the solubility of hydrogen in the solid

$$X_{HS}^{eq} = k_{0H} X_{Hl}^{eq} \quad \text{(Equation 92)}$$

with a partition coefficient for hydrogen in aluminium of approximately $k_{0H} = 0.07$ (87).

2.2.1.5. Pore morphology

With the above introduced fundamental equations, the moment in which pore nucleation becomes (theoretically) possible can be determined. Assuming total mixing of hydrogen in the liquid (lever rule) and a situation before any pores have formed, the equilibrium saturation composition is given by (47)

$$C_{HI}^{eq} = \frac{\langle \rho_0 \rangle C_{H0}}{g_s \rho_s k_{oH} + g_l \rho_l} \quad \text{(Equation 93)}$$

and if pores have already formed by (47)

$$\langle \rho_0 \rangle C_{H0} = [g_s \rho_s k_{oH} + (1 - g_s) \rho_l] C_{HI}^{eq} + 2 \frac{g_p p_g}{RT} \quad \text{(Equation 94)}$$

So far, the pressure in the pore is not known. Pore nucleation does not instantaneously take place if $C_{HI} > C_{HI}^{eq}$ because an overpressure due to curvature has to be accounted for. It is given by the Laplace-Young equation as

$$\Delta p = 2\gamma_{lg}\bar{\kappa} \quad \text{(Equation 95)}$$

where

$$\bar{\kappa} = \frac{1}{2} \left(\frac{1}{R_1} + \frac{1}{R_2} \right) \quad \text{(Equation 96)}$$

$\bar{\kappa}$ is the local mean curvature, which is defined by the two local principal radii R_1 and R_2 . Thus, the pressure in a pore, surrounded by liquid melt is

$$p_p = p_l + 2 \frac{\gamma_{lg}}{R_p} \quad \text{(Equation 97)}$$

with R_p as the pore radius (the local mean curvature of a sphere is $1/R$). The composition of the gas inside of the pore is still given by Sievert's law, see (Equation 88). Therefore, small pores show a huge overpressure due to curvature and need a high hydrogen oversaturation or low liquid pressures of the melt to nucleate. The necessary supersaturation for pore nucleation is given by

$$\Delta C_{H0} = C_{HI}^{eq}(p_g, T) - C_{HI}^{eq}(p_l, T) \quad \text{(Equation 98)}$$

Some porosity models define the necessary condition for pore formation this way.

If a pore has been formed, two factors determine its growth: curvature and hydrogen diffusion to the pore. As long as a pore is fully surrounded by liquid, it takes on the shape of a sphere. The relationship between the pore fraction and the pore number density is then given by

$$g_p = n \frac{4}{3} \pi R_p^3 \quad \text{(Equation 99)}$$

with the pore number density n .

If the pore grows in the interdendritic mush, it has to adapt to the shape of the surrounding solid phase. By combining (Equation 94) and (Equation 95), one can deduce:

$$\langle \rho_0 \rangle C_{H0} = [g_s \rho_s k_{oH} + (1 - g_s) \rho_l] C_{HI}^{eq} + 2 \frac{g_p}{RT} (p_l + 2\gamma_{lg} \bar{\kappa}) \quad \text{(Equation 100)}$$

Pores forming and growing in the late-stages of solidification show a very complex shape, and therefore their local mean curvature has to be estimated as a function of the solid fraction g_s . A commonly applied approach is described by Pequet et al. (88), who assume a constant pore radius until a certain volume fraction of spherical pores is reached and then deploy a function $\bar{\kappa}(g_s, \lambda_2)$. Couturier et al. (46) developed an equation which describes the pore radius as a function of the solid fraction under the assumption of a pore growing in a regular array of cylinders. The resulting radius is then normalized by the secondary dendrite arm spacing or the grain size.

2.2.1.6. Pore nucleation

The nucleation of pores in the liquid phase can be described analogous to the nucleation of a solid nucleus in the liquid (see Chapter 2.1.1.1). The nucleation barrier can be deduced from the volumetric energy and surface energy. Thus, for a spherical pore with radius R_p , the change in Gibbs free energy is described by (47)

$$\Delta G = \left(-\frac{4\pi R_p^3}{3} \Delta G_V + 4\pi R_p^2 \gamma_{lg} \right) f(\theta) \quad \text{(Equation 101)}$$

with $\Delta G_V = p_g - p_l$ and where $f(\theta)$ is the geometric factor reflecting the wettability of a substrate in heterogeneous nucleation ($f(\theta) = 1$ for homogeneous nucleation). In homogeneous nucleation for typical liquid-gas surface energies in aluminium of $\gamma_{lg} \approx 1 \text{ Jm}^{-2}$ and pore radii in the order of nanometres, overpressures in the order of GPa are necessary to nucleate a pore. These values are unrealistic (42) and consequently heterogeneous nucleation or inflation of an already existing cavity are the only realistic theories.

Since the 1990s, research was done on the nucleation of porosity via X-ray temperature gradient stage technique (XTGS) (89). By observation of individual pores and extrapolation to the pore size “zero”, Lee and Hunt tried to determine the time during solidification at which nucleation occurred. Unwetted or unfavourably wetted inclusions or the oxide skin of aluminium melt are discussed to be potential nucleation sites (90).

Heterogeneous pore nucleation

Analog to the solidification of the solid, substrates facilitate the nucleation of pores. The potency of a substrate can be described by the wetting angle θ , which satisfies the Young-Dupré equation. In heterogeneous nucleation, the maximum number of nuclei is also reached almost immediately (and is therefore also called instantaneous nucleation) (47).

Figure 2-16 shows a sequence of three X-ray radiographs depicting the early-stage pore formation associated with hydrogen condensation in an aluminium alloy with 30 wt% Cu (91). The specimen is 200 μm thick and solidifies in a vertical thermal gradient. Because the absorption of the X-rays is proportional to the atomic number of the elements, dark areas are Cu rich as are bright areas mark the primary aluminium dendrites or pores. The thin horizontal line marks the eutectic solidification front. Because the solidification interval ΔT is only about 10 K, the feeding of the solidification shrinkage is relatively easy, and all observed porosity is mainly driven by hydrogen supersaturation.

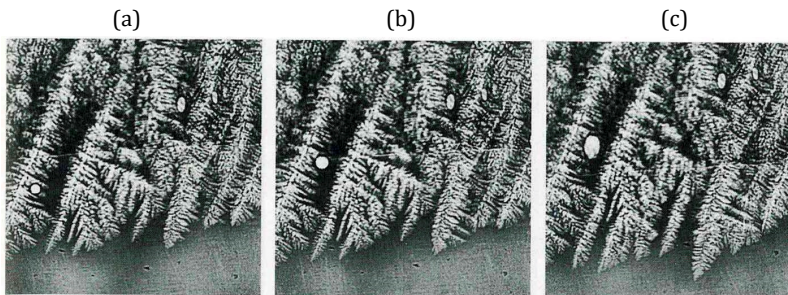


Figure 2-16: Growth sequence (a–c) of hydrogen-induced porosity in an Al-30 wt% Cu alloy (91)

The concentration on the pore on the left shows its trapping in the dendrites (Figure 2-16(a)) and transportation towards the eutectic front (Figure 2-16(b)). When the pore passes the eutectic front, it elongates (Figure 2-16(c)). All the while there is a steady pore growth observable. Frames analysed before the sequence starts, show that the bubble stems from the mould surface and is probably an entrapped air bubble.

In experiments with an AlCu20 alloy and low cooling rates of 0.084 K/s, Murphy et al. (29) showed nucleation of pores at a low solid fraction of 0.13 (see Figure 2-17). In these experiments, the nucleated and growing pores can push the equiaxed crystals away to increase the available room for further pore growth. The growing pores can remain highly spherical during this growth.

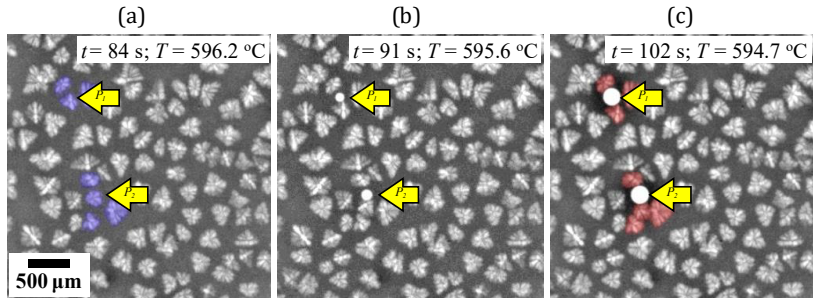


Figure 2-17: X-ray sequence of the solidification of an AlCu20 alloy with a low cooling rate of 0.084 K/s. Arrows indicate the location of pore one and two nucleating and growing. Note that the pores can push the blue marked dendrites to increase the available space for further pore growth (29).

Just before pore nucleation, the pushed dendrites are marked in blue (Figure 2-17(a)). As the pores grow they can retain a highly spherical shape and push the equiaxed dendrite crystals even further ((b) and (c)).

Late-stage porosity nucleates deep in the mushy zone at high solid fractions. The nucleation may be associated with the eutectic solidification and normally alloys with a long solidification interval (especially in the last stages of solidification) are more prone to this type of porosity than short freezing range alloys. Figure 2-18 shows the solidification sequence captures via X-ray tomography of an Al-10 wt% Cu specimen. The cylindrical specimen is only contained by its oxide skin, has a diameter of approximately 1 mm and a length of approximately 2–3 mm.

Already in the first image Figure 2-18(a), some porosity is observable, which is probably an old oxide. When the solidification progresses, the surface contracts to compensate some of the volume deficit. Simultaneously the dendritic structure becomes more prominent, and the contrast increases by enrichment of the liquid with Cu and one more pore forms (see Figure 2-18(b)). In the last picture Figure 2-18(c) a Cu rich eutectic formed and more pores are visible. These are probably not independent pores, but part of one big tortuous pore.

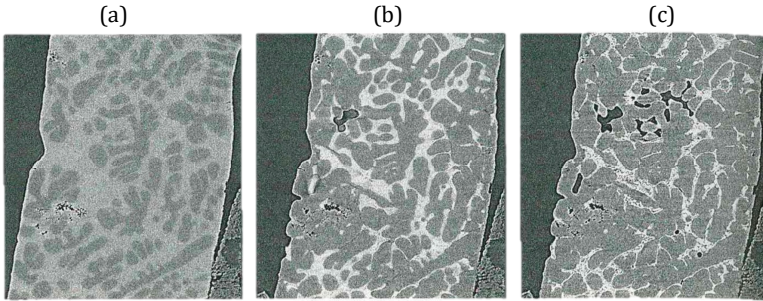


Figure 2-18: Solidification sequence (a-c) obtained from X-ray tomography of an Al-10 wt% Cu alloy (47)

2.2.1.7. Gas diffusion and pore growth

If pores already exist in the melt, they are ideal locations for hydrogen dissolution. Hydrogen diffuses relatively fast in the aluminium melt ($D_{IH} \approx 10^{-7} \text{m}^2 \text{s}^{-1}$ at the melting point (87)), but if the pore growth is limited by hydrogen diffusion or not depends on the Fourier number of diffusion

$$Fo_D = \frac{D_{IH} t_f}{L^2} \quad \text{(Equation 102)}$$

where L is half of the distance between pores. If the pore number density n and the solidification time t_f are low, Fo_D is also small and diffusion-controlled pore growth is predominant. Both approaches, lever rule without diffusion-controlled growth (88, 92, 93) and diffusion-controlled growth (33, 77) have been used for multiple models.

Models, which incorporate hydrogen diffusion, need to model the pore-liquid area because the hydrogen diffuses 2.5 times faster in the liquid than the solid phase (33, 94). Nonetheless, Felberbaum (71) showed that at high solid fractions the hydrogen diffusion through the solid phase also needs to be considered and developed an approach which is based on the effective medium theory (95).

Diffusion takes place as long as the chemical potential μ is equilibrated in all phases. The flux of atoms J_A (of species A) is locally proportional to the gradient of the chemical potential $\nabla\mu_A$.

$$J_A = -M_A C_A \nabla\mu_A \quad \text{(Equation 103)}$$

where M_A is the mobility coefficient of A. J_A from Fick's first law is proportional to the local gradient of concentration, which is a simplification of the stated relationship. By (Equation 103) and the Gibbs-Duhem relationship and by introducing the molar volume $V_M = X_A/C_A$, one can deduce (83)

$$J_A = -M_A \frac{X_A}{V_M} \frac{\mathcal{R}T}{X_A} \left(1 + \frac{d \ln f_A}{d \ln X_A} \right) \nabla X_A \quad \text{(Equation 104)}$$

By the comparison of Fick's first law and (Equation 104), one gets the relationship between the diffusion coefficient of A (D_A) and the mobility coefficient

$$D_A = M_A \mathcal{R}T \left(1 + \frac{d \ln f_A}{d \ln X_A} \right) \quad \text{(Equation 105)}$$

For a dilute solution, like in the Al-H system, $X_H \rightarrow 0$ and $f_H = a_H/X_H \approx \text{const}$ (Henry's law) and so the term in brackets in (Equation 105) goes towards 1. It follows

$$D_H = M_H \mathcal{R}T \quad \text{(Equation 106)}$$

To solve the diffusion equation for a heterogeneous material, the chemical potential at the interface between the phases has to be continuous. Thus, Fick's first law has to be generalised for the RVE

$$J_A = -M_H X_H \nabla \mu_H \quad \text{(Equation 107)}$$

(Equation 103) equals (Equation 107) if divided by the molar volume V_M . Fick's second law can be adapted the same way

$$\frac{\partial X_H}{\partial t} = -\nabla J_A = \nabla(-M_H X_H \Delta \mu_H) \quad \text{(Equation 108)}$$

2.2.2. Porosity in Al-Si alloys

2.2.2.1. Grain size and grain refinement

The morphology of the dendritic structure is mainly controlled by the Si content of the aluminium alloy. A transition of equiaxed dendrites from globular to orthogonal can be observed if the silicon content increases from low to medium (e.g. 7 wt% Si in cast alloys) levels (96). The grain size of the primary aluminium decreases until 3 wt%, then it increases again (97).

Two mechanisms determine the grain size in aluminium cast alloys, the potency of the nuclei and the constitutional undercooling in front of the solidification front.

The potency of different grain refiners was examined by Easton and StJohn (98). Two parameters can characterise the constitutional undercooling. The growth restriction factor Q and the supercooling parameter P

$$Q = m_l C_0 (k_0 - 1) \quad \text{(Equation 109)}$$

$$P = \frac{m_l C_0 (k_0 - 1)}{k_0} \quad \text{(Equation 110)}$$

where m_l is the gradient of the liquidus line, C_0 is the initial solute concentration, and k_0 is the equilibrium partition coefficient. Q corresponds to the initial rate of formation of a constitutional undercooled zone. P corresponds to the “amount” of constitutional undercooling (98). Shorter times available to develop a sufficient undercooling (high Q) means shorter times for grain growth and thus smaller grain size.

Grain refinement in Al-Si alloys by additions of Al-Ti or Al-Ti-B master alloys is done to produce a fine equiaxed grain structure. The reasons are multifold and described by Tøndel (99). Amongst other reasons, grain refinement is used to produce better product properties. Dahle investigated the effect of grain refinement on the fluidity of aluminium alloys and was able to show a significant improvement (100).

The grain refinement effect on porosity is not well established. Fang and Granger (101) investigated the effect of cooling rate on porosity in directionally solidified AlSi7Mg and were able to show a pore volume fraction reduction if the alloy was grain refined. Dahle (102) studied the effect of grain refinement on the alloys AlSi7Mg and AlSi11Mg. For the first, he showed a porosity reduction by grain refinement, for the latter the effect was not verifiable. He explained the effect by a delayed dendrite coherency and thus, extended mass feeding and shorter inter-dendritic feeding. Because of the more efficient mass feeding, the total amount of porosity is reduced. Another explanation is given by Fang and Granger (101) who compared experimental results with gas-driven modelling results. They found a strong correlation between the dendrite arm spacing and the porosity level. In their work, they presented the theory that a refined primary grain may affect the porosity level similarly as the dendrite arm spacing. Ghomashchi (103) investigated the formation of AlSiTi, which forms as flakes or blocks in an early-stage during solidification. The blocky morphology is dominating at higher Ti levels and lower cooling rates during solidification, while the reverse is true for the flake morphology. It was hypothesised that the phase might deteriorate the permeability of the mush zone and thus increase porosity, but in general, more research on the topic is needed.

2.2.2.2. Shrinkage

Molten metals (in general) take up more space than solidified metals. The difference (shrinkage) is caused by a change of the atomic arrangement. Where liquid metals show a random close-packed atomic structure, solid metals exhibit a regular crystalline atomic array with higher density. The highest density crystals are cubic close-packed structures (face-centred-cubic – fcc or hexagonal close-packed – hcp). These two show the biggest difference between the liquid and solid state and thus the largest solidification shrinkage. Aluminium is one of these (fcc) and contracts 7.14 vol% on solidification (42). In general, metal contracts with three different rates when cooled from liquid to solid state. Figure 2-19 shows these three stages schematically.

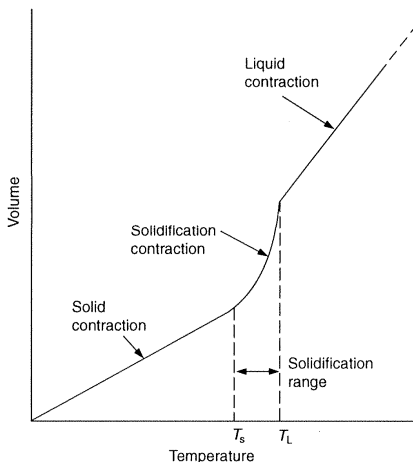


Figure 2-19: The three characteristic shrinkage regimes of solidifying metal. From high to low temperature: liquid contraction, solidification contraction, and solid contraction (42)

The first contraction during cooling from the liquid state to room temperature is the thermal contraction of the liquid. It is an almost linear volume reduction as a function of temperature. Usually, the liquid contraction is not a problem during casting because the local volume deficit is immediately compensated. Extra material flows to the cooling areas, and a slight drop in the feeder may be observed.

The second characteristic regime is the solidification contraction which occurs at the freezing point. In the case of alloys with a solidification interval (solidification range), the solidification contraction can be observed between the liquidus temperature T_L and the solidus temperature T_s . This phenomenon may cause problems.

First, the solidification contraction is compensated by the movement of liquid and solid but in the later (final) stages “shrinkage porosity” may form as a result.

The third and final regime is the shrinkage of the solid (“solid contraction”). As the cooling progresses, the solid is often not free to contract but confined by the mould or other already solidified parts. The result is almost always that the casting is a little bigger than the “free contraction” would suggest (plastic deformation). Additionally, defects like hot tearing or cold cracks may be introduced (42) as well as residual stresses may deform the casting.

Under ideal conditions (totally clean melt without nuclei), the shrinkage cannot be compensated by pore formation. If one compares the tensile strength of liquid metal, which is in the range of -1000 to -10000 MPa, with the tensile strength of the solid, it becomes clear that collapse has to occur by plastic or creep flow. Even if separated hot spots may still be partly feedable through a mushy semi-solid network, the pressure drop might become sufficiently high (42).

2.2.2.3. Hydrogen effect

Many studies were conducted on the effect of hydrogen on the porosity level of Al-Si foundry alloys (101, 104–107). Fang and Granger (101) investigated the alloy A356 at three different cooling rates and three hydrogen levels. Their results showed a significant porosity increase with increasing hydrogen content. The effect was enhanced at low cooling rates. Their porosity model, which neglects the influence of shrinkage and is based on hydrogen dissipation and the effect of surface tension, suggested that there is a critical hydrogen level below which no gas porosity is created. Furthermore, higher cooling rates lead to smaller pore radii. These findings agreed with their experimental comparisons. In modelling work done by Carlson et al. (33) who not only took into account the effect of shrinkage-induced feeding flow and pressure variations but also finite-rate hydrogen diffusion, Carlson et al. were able to show that the finite-rate diffusion is actually limiting the amount of hydrogen-related porosity in their model (and in compared samples). This limitation was, in fact, the only way to explain and model the, in experiments observed, reduction in porosity with increasing cooling rates at high hydrogen content conditions. Sigworth and Cáceres (108) researched on hydrogen macrosegregation and its influences on porosity formation. They investigated five different Al-Si alloys (with varying Cu, Mg, and Fe contents) but concluded that macrosegregation of hydrogen has no significant impact on porosity. Instead, long solidification times generate a coarse microstructure, which in turn enlarges the confining space of the primary aluminium for growing pores.

2.2.2.4. Cooling rate and thermal gradient

Tiedje et al. (109) analysed the relationship between local solidification conditions and porosity in Al-Si castings. The solidification morphology of the primary Al phase and the Al-Si eutectic are determined by the local thermal gradient, the local cooling rate, and the nuclei density. The solid morphology, in turn, has a significant influence on the permeability and the pore morphology. In general, three characteristic zones in a casting can be distinguished (83). The first outer zone is a so-called “chill zone”. It can be characterised by a high thermal gradient and fine globular and densely packed primary grains. Tiedje et al. (109) observed small pores and a low porosity level. The second zone is called “columnar zone”, and the thermal gradient and cooling rate are lower. Columnar grains grow in the opposite direction of the heat flow, and the resulting feedability is characterised as low. The observed porosity level is higher, and the pore shape is elongated, as the primary and eutectic grain structure requires. In the inner areas of a casting, the third zone, the “equiaxed zone”, can be found. The thermal gradient is small, and big equiaxed grains are predominant. The pores tend to be dispersed, round, and larger. If and to what extent these three zones are present in castings depends strongly on the chemical composition, the solidification conditions, modification and grain refinement. This third zone may also be identified as a hot spot, as a zone of the last solidification. Depending on the geometric conditions of the casting and the amount of volume deficit that is localised in this area (see also the growth of the eutectic phase and effect of Sr or Na on the eutectic solidification in Section 2.2.2.7), macroscopically sized pores (of a couple of cm in size) may form.

Two more characteristic morphological transitions can be distinguished in aluminium castings. The first is the so-called “columnar-to-equiaxed transition” (CET), where dendrites no longer grow columnar but equiaxed growth begins to dominate. There has been done quite some work on the influences on the CET (28, 83, 110–114) with the result that local temperature gradient, local cooling rate, and nuclei density are the key parameters. The second transition is the “dense-packed to free growth transition” (DFT). Close to the mould wall in castings, the eutectic cells grow presumably in a densely packed structure (planar like). Eutectic nuclei are activated simultaneously and in proximity. Deeper into the casting, the eutectic cells become larger and more spherical. The growth is presumed to be relatively free. The DFT has been observed by Tiedje et al. (109) for Na and Sr-modified, but not for unmodified Al-Si alloys. For AlSi7 and AlSi12, they found only very small pores below the casting surfaces and the DFT if the melt was modified. Both Sr-modified alloys showed the highest area fraction and density and the lowest roundness of pores between the DFT and CET. These pores follow the elongated shape of the primary

aluminium crystals which grow parallel to the heat flow. Below the CET pores were found to be rounder, especially for the alloy AlSi12. An intense heat extraction or Na-modification lead to a concentration of porosity in this area. The authors presume that porosity is pushed into the region of the last solidification. In general, Tiedje et al. found the pores at the junctions of the eutectic cells. If there was a significant amount of primary phase, it affected the resulting pore shape and reduced the pore roundness.

Lee and Hunt (77) used an X-ray temperature gradient stage to observe the effects of solidification velocity v and thermal gradient G on pore formation. The experimental condition was a controlled directional solidification for which it was shown, that inadequate feeding due to shrinkage was not the driving force for pore formation. They used Al alloys with relatively high Cu contents (10 wt% Cu and more) to achieve sufficient X-ray contrast. The solidification velocity v had the strongest effect on porosity characteristics. An increase of v leads to a decrease of the effective pore size, the maximum pore length, and the total amount of porosity. Concurrently the pore number density increased. The results are reasonable in the case of diffusion-limited gas-induced porosity formation. Additionally, they showed that the local thermal gradient G was able to subsidize the solidification velocity v and that the solidification time t_f as a transformation of v and G as a single predictor is sufficient to describe the porosity characteristic under the observed conditions.

2.2.2.5. Inclusions and bifilms

Campbell (42) calculated the necessary pressure of hydrogen bubbles for homogeneous nucleation in an aluminium melt. He came to the result of 3.14×10^9 Pa, which is unrealistic to occur in reality. For heterogeneous nucleation, he estimates a necessary pressure of 3.65×10^7 Pa, which is still highly unlikely to develop during solidification. He proposes another mechanism, which does not rely on nucleation, but on already existing cavities in the melt. The so-called double oxide films or "bifilms". By turbulence, melt surface disturbance or any other mechanism introducing surface oxide into the melt, it folds on itself and retains a small amount of gas (atmosphere above the melt). This bifilm is proposed to be an already existing "crack" in the melt, which only has to be inflated by gas dissipation or low melt pressure. Dispinar and Campbell (115, 116) introduce the bifilm index, the total length of the maximum dimension of all pores, measured after solidification in the reduced pressure test on the sectioned surface. This index is meant to capture the melt's potential to form porosity, and by the authors' assessment, is more relevant than the hydrogen level.

Raiszadeh and Griffiths (117, 118) tried to show in their experiments, that hydrogen can penetrate the oxide film or bifilms due to disturbances induced by deformation. They propose inflation of bifilms by hydrogen and thus the creation of gas porosity. Dispinar and Campbell try to prove in reduced pressure tests (RPT) that bifilm free melts, even if they contain the necessary high hydrogen (119) levels, are not able to form gas pores.

Nyahumwa et al. (120, 121) researched the deactivation or healing of double oxide films by bonding, with the result that these bifilms are no longer available as nuclei for pore formation. Some other work seems to support their theory (119, 122–124). Raiszadeh and Griffiths concluded from their research that first oxygen would be consumed by oxidation of Al or Mg, then nitrogen is reacting to form nitrides. Only then they judge oxide film bonding may be possible. They also calculate, based on experimental results of an artificially produced pore filled with oxygen and nitrogen, which is consumed by time by reaction with the surrounding aluminium, that a typically anticipated oxide defect would be deflated after only a few seconds (117, 118). If hydrogen is present in the melt, the deflation process of a bifilm may be extended significantly though. Aryafar, Raiszadeh, and Shalbazadeh come to the same conclusion (119). The second complementary mechanism to “heal” the double oxide film is a bonding due to atomic rearrangements. Najafzadeh-Bakhtiarani and Raiszadeh observed bifilm deactivation in commercial purity alloys after 5 h (123). They explained the bonding with the transformation of $\gamma\text{-Al}_2\text{O}_3$ to $\alpha\text{-Al}_2\text{O}_3$. For Al-Mg alloys Aryafar et al. (119) observed bifilm deactivation. In this case, their mechanism hypothesis is the transformation of Al_2O_3 to the spinel MgAl_2O_4 and finally to MgO. In any case, some gas phase in the form of Ar would remain in the bifilm due to its inert character (125).

Campbell (42) hypothesised that for Al-Si-Mg alloy the Mg level greatly determines the bifilm’s ability to heal itself. He stated that for low Mg levels below 0.1 wt% the oxide film is mostly alumina and thus very unlikely to bond. Mg levels above 1.0 wt% would lead to a MgO oxide layer which is also very stable and unlikely to bond. Only in the intermediate range of 0.1–1.0 wt% Mg the alumina film would absorb Mg and convert the oxide to a spinel structure. In this case, some bonding of the bifilm surfaces could be expected due to the significant differences in the lattice structure and the associated diffusion processes. Additionally, Campbell suggests that some mechanical bonding due to the surface roughness of both alumina surfaces might take place and that healing of bifilms happens faster for “young” oxide films than for “old” oxide films. Huang et al. observed “fused together” bifilms which they detached by ultrasound from samples. They also conclude a bonding mechanism due to the formation of a MgAl_2O_4 spinel.

Once a bifilm is “healed” by bonding, Campbell (42) suggests that the nucleation site is no longer available for example for gas bubble formation but also shrinkage-induced micropores.

2.2.2.6. Effect of Si

Al-Si alloys dominate the casting applications; they make up about 85 % of all cast aluminium (126). Si improves the castability by reducing the coefficient of thermal expansion. Moreover, it expands during eutectic solidification and compensates some of the volume deficit (127), and improves the fluidity because of its high latent heat of fusion (128). The solidification interval is reduced up to the eutectic concentration. Si additions increase the strength and reduce the ductility (128). If silicon increases the amount of porosity, is debated. Some publications are indicating a porosity increase (129); others are suggesting a decrease in porosity (130). Some results point out a porosity maximum between 4 wt% (131) and 7 wt% (132, 133). Probably, the Si content only becomes relevant for the porosity in combination with other alloying elements, modification, and cooling conditions. Because of the beneficial properties discussed above, eutectic melt should have good feeding properties (high latent heat), but the morphology and formation of the eutectic phase can also block feeding channels and by the release of latent heat reduce the local thermal gradient. A sufficient thermal gradient is necessary to induce the feeding flow. The effect of Si modification by Na or Sr on porosity is discussed in Section 2.2.2.7.

2.2.2.7. Sr and Na modification

Unmodified Al-Si eutectic grows faceted in needles or flakes by the so-called “twin plane re-entrant edge mechanism” (134). The most common element to modify the eutectic morphology is Sr, but Na and Sb are also used. Sr and Na change the eutectic morphology from faceted acicular flakes to fibrous rods. Sb refines the Si flakes. An improvement of the mechanical properties, especially of the elongation at fracture is achieved (135). A side effect of modification is often an increased porosity level compared to unmodified alloys (101, 136–142). Sr modification also alters the pore distribution and morphology. Where in unmodified industrial Al-Si alloys pores are typically concentrated in the hot spot, Sr leads to a dispersed porosity throughout the casting (138–144). The effect of increased porosity level can even outweigh the benefits on the mechanical properties (145).

Some theories state that Sr and Na might increase the hydrogen level of the aluminium melt (136). Contradicting publications concluded that both modifiers do not change the gas content of the melt (32, 146). The turbulent reaction associated with the introduction of Na into the melt might cause a gas absorption (32). It was

described by Thiel (31) and has been observed in experiments by Mulazimoglu et al. (32) that Na additions can modify the structure of the aluminium oxide layer and deteriorate its impermeability. The result might be an increased hydrogen pick-up from the atmosphere.

It was proposed that the modifiers reduce the surface energy of the melt and thus the pore nucleation barrier, which causes more porosity (145, 147). Still, the extent of the surface tension reduction is under discussion, and diverging results were found in experiments (101, 148).

Modification might also introduce oxides into the melt (149, 150). These oxides might act as nuclei for pore formation (151).

Emadi and Gruzleski (147) showed that Sr additions to modify the eutectic Si increase the volumetric shrinkage of A356 aluminium and Argo and Gruzleski (139) proposed an explanation that by modification, and the accompanying suppression of the eutectic temperature, the mushy zone length is extended. As a consequence, the feeding of the solidification shrinkage becomes more difficult. Fuoco et al. (137) could not support this theory. They did experiments with an adapted Si-content to mirror the solidification range extension associated with Sr modification. The effect on porosity was not comparable to Sr additions. The solidification range alone seems not responsible for the change in the porosity distribution.

Dinnis et al. (152) showed that the changes in porosity amount and distribution are primarily related to a modification of the eutectic solidification morphology. Two concepts to explain modification by a changed solidification morphology are discussed. The first is a change in the growth of the eutectic phase. It is proposed that modification changes the Si growth from the so-called "formation and propagation of twin-plane re-entrant edges" to an "impurity induced twinning" mechanism (64). The impurity induced twinning mechanism is proposed to go along with a considerable increase in twin density, and consequently lead to the formation of fibrous Si. However, recent publications could not find significant differences in twinning density between fibrous Si (Ba, Ca) and a refined flake (Y, Yb) morphology and the authors instead suggest that an effect of modifying elements on eutectic growth kinetics and nucleation frequency has to be considered. An increased twinning density as the impurity induced twinning theory suggests seems not sufficient (153). The second concept to explain the Si modification is based on a changed nucleation behaviour. The increased eutectic undercooling is taken as proof for this hypothesis (154, 155). A conventional explanation is that the eutectic nucleates on AlP particles (127, 154, 156, 157). Between AlP particles and Si, the lattice mismatch is only approximately 0.2 %.

Three criteria determine the ability of epitaxial growth of one phase on another (158):

1. The crystallographic planes in contact have to have the same symmetry and comparable lattice parameters.
2. Both crystals have to be the same type of chemical bond.
3. If ionic crystals grow epitaxial on each other, the alternating order of positively and negatively charged ions has to be maintained.

Although criteria three is not met in the case of AlP and Si, AlP is characterised as a potent nucleus. Na and Sr modification are supposed to alter the eutectic nucleation behaviour by deactivating the AlP particles, which may happen by the formation of P and Sr or Na containing particles or by forming a Sr or Na containing layer on AlP particles (159, 160).

Modification of the eutectic Si can also be achieved if Mg-containing alloys are superheated to 850–900 °C for a sufficient amount of time (161). An explanation for this phenomenon is the solution of solid phases, which act as nuclei for the eutectic phase as well as a homogenization of the Mg in the melt. The same heat treatment also leads to a morphological change of the Fe intermetallics and seems to support the nucleation associated changes observed by modification.

Eutectic solidification morphologies

By electron backscattered diffraction (EBSD) one can reveal the orientation relationship between primary Al and eutectic Al. In Figure 2-20 the three proposed types for unmodified, Sr, or Na-modified eutectic nucleation and growth are shown. In high purity aluminium with Sr additions up to 150 ppm or above 500 ppm, epitaxial growth of eutectic Al on primary Al can be observed. In commercial purity aluminium alloys, no crystallographic orientation relationship is detectable. The conclusion is that in the case of commercial purity alloy, which is Sr or Na-modified, the nucleation of the eutectic aluminium happens independently from the primary aluminium (143, 162–169). Na modification leads to eutectic nucleation close to the mould wall and a eutectic growth opposite to the heat flow (Figure 2-20(a)) (167).

The nucleation and growth rate in unmodified alloys is up to one magnitude higher than in Sr-modified ones (159, 170). In Sr-modified alloys ((Figure 2-20(c)) the eutectic grows spherically from independent nucleation sites into the interdendritic liquid (159, 162–166, 170) and hence may block feeding paths and deteriorate the mushy zone permeability (152). Dahle et al. (143) and Argo and Gruzleski (139) observed an increase in porosity with Sr additions between 50 and 200 ppm.

The eutectic growth rate, which is proportional to the undercooling, may also change the eutectic morphology. Less potent nuclei in a modified alloy lead to a bigger eutectic grain size, which means a smaller eutectic-liquid interface and higher growth velocity. A higher growth velocity generates a refinement of the Si and in the case of very high growth speed, produce a flake to fibre transition. Modified eutectic grains grow with a smooth interface (162, 164–166, 168). By influencing the permeability of the melt, modification changes the amount of porosity (142–144, 170, 171). In the case of Sr modification, there is typically no eutectic growth from the mould wall. Dahle et al. (143) proposed that this destabilises the casting's surface and leads to the, in casting practice frequently observed, surface slumping. An alternative explanatory approach is that the reduced feedability results in a higher pressure drop which in turn results in surface collapsing.

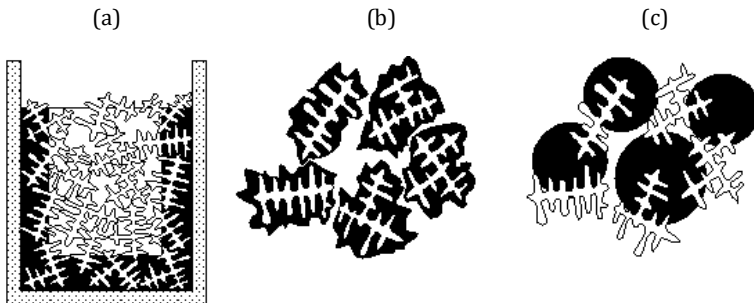


Figure 2-20: Proposed growth of the eutectic phase (black). For modification with Na opposite to the heat flow (a) and in the case of Sr modification independent of the primary aluminium (b). Unmodified growth leads to eutectic nucleates on the primary aluminium crystals (c) (162)

Unmodified alloys (Figure 2-20(b)) show a eutectic growth in the direction of heat flux (162, 163, 165, 166), with little sensitivity to it. Nucleation and growth can simultaneously progress from the mould wall and the dendrite tips into the melt (162, 166). Pores were found close to the last regions of solidification where eutectic grains meet and form a liquid pocket (144, 172). Because the unmodified eutectic morphology shows a high complexity (caused by the faceted Si), the pore morphology also shows a microscopically irregular surface. The eutectic growth from the dendrite tips (143) into the interdendritic liquid happens only after the primary dendrite is surrounded and thus feeding paths stay open longer, compared to Sr-modified alloys. The eutectic formation throughout the casting may also stabilise

the casting's surface; therefore no surface slumping is typically observed for unmodified alloys (143).

Na modified eutectic tends to grow from the mould wall if the heat extraction and thus the undercooling is sufficient (140, 155, 159, 173, 174). Eutectic cells grow opposite to the heat flux, and the amount of solute segregation determines the interface stability (167, 168). By growing from the mould wall to the hot spot, the porosity is concentrated and often a macroscopic pore forms. Analog to unmodified alloys, there is typically no surface slumping observable, which may be associated with the previously discussed growth mode.

Figure 2-21 show experimental results by Dahle et al. which show the cross-section of a hot spot area of a permanent mould AlSi10 alloy which was unmodified (a), Sr-modified (b), and Na-modified (c). (d) to (f) illustrate the associated observed eutectic growth behaviour.

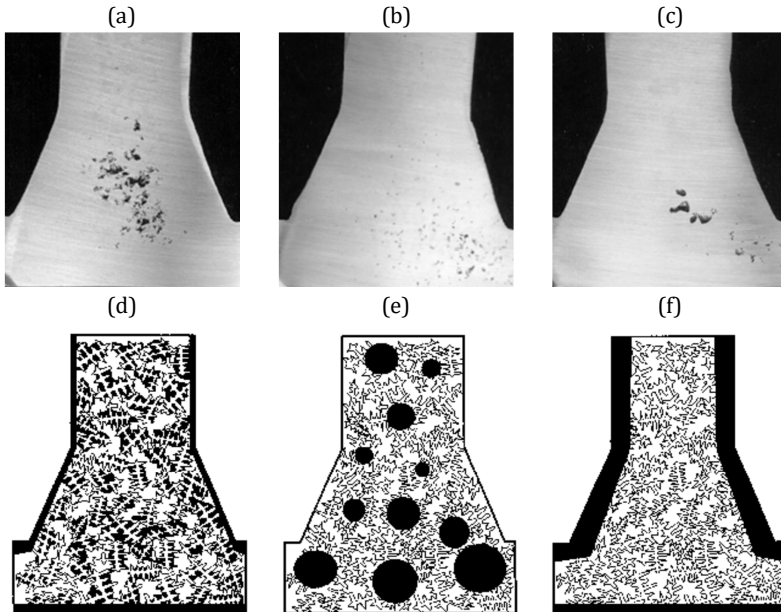


Figure 2-21 Cross sections of the hot spot area of permanent mould AlSi10 test castings. (a) shows an unmodified sample, (b) the Sr-modified alloy, and (c) a Na-modified one. The in (a) to (c) observable porosity distribution can be explained by the corresponding illustrations (d) to (f) which show the eutectic growth (black) during solidification (143).

The figure illustrates and summarises the importance of the eutectic solidification, and thus its modification, for the porosity distribution in aluminium castings.

Eutectic mushy zone

The segregation in front of the eutectic front determines its stability. Heiberg et al. (9, 114) propose that by increased segregation of individual elements like Cu, Mg, and Fe, the constitutional undercooling is increased, and a columnar-to-equiaxed-transition associated with the formation of a eutectic mushy zone takes place. The Al-Si reaction is not isothermal anymore but exhibits a solidification interval. Hunt (113) states that equiaxed growth is facilitated by a shallow thermal gradient, high growth rates, and a large number of nuclei. If the growth rate is low, the efficiency of the nuclei is decisive; if the growth rate is high, the number of nuclei is crucial. Flood and Hunt (155) suggest that modification poisons the nuclei (e.g. AlP), which are pushed in ahead of the eutectic, which stabilised a smooth interface. Other nuclei may be activated instead (144, 160). A smooth interface was only found in unmodified and high purity Sr-modified alloys, whereas Heiberg et al. found a eutectic mushy zone in a technical alloy (A356) (114).

The mechanism of Sr-modification and the formation of a eutectic mushy zone is probably not only one, but a combination of constitutional undercooling and nuclei poisoning (114). To provide sufficient nuclei for the eutectic solidification has the potential to reduce the eutectic grain size, increase the permeability of the mush zone and reduce the porosity level. Smaller grains go along with shorter and less tortuous feeding paths. Additionally, the size of liquid pockets and thus the pore size can be reduced (16).

2.2.2.8. Effect of Cu and Mg

Segregation of Cu and Mg during the primary and eutectic solidification destabilises the eutectic front and leads to the formation of a eutectic mushy zone (9). If by segregation sufficiently high solute levels are reached, Cu or Mg-rich intermetallics form. In the case of eutectic modification, Cu and Mg reduce its effectiveness (10–15), and bigger eutectic grains are the consequence which in turn lead to bigger liquid pools and larger pores (16).

Cu is typically added as an alloying element to increase the strength (especially after heat treatment), improve the hardness and machinability. Cu decreases the liquidus temperature of the primary aluminium phase, as is the solidus temperature decreased. Because the latter decreases stronger than the first, the solidification interval is increased. A longer mushy zone and lower permeability are the consequence. The formation of Al₂Cu is typically one of the last phases to form during

solidification (175). There are two major effects of Cu content on porosity. The first is that the Al_2Cu phase develops very late when the dendritic network is well developed and compensation of the significant solidification shrinkage of 8.4 % (176). The second reason is the extended mushy zone and the associated deteriorated permeability. The Cu phase forms as a fine Al- Al_2Cu eutectic (which consists of about 24 wt% Cu) or as a blocky phase (which contains about 40 wt% Cu). The conditions of formation are unclear. Some work indicates that $\beta\text{-Al}_5\text{FeSi}$ phases affects the blocky morphology formation along with some influence of Sr-modification (11–13). The lattice mismatch of Al_2Cu and $\beta\text{-Al}_5\text{FeSi}$ is minor so that epitaxial growth may be possible (127).

Cárceles et al. (177) observed a strong porosity increase in Al-Si cast alloys if the Cu content exceeded 0.2 wt% (the specimen were cast in small graphite crucibles). Edwards et al.'s (130) work confirm the previous observation and show an increase in porosity level for alloys of the Al-Si-Mg-Cu system (cast in sand moulds) from 1–4 wt% Cu. They explain their findings with the significant volumetric shrinkage and a reduced hydrogen solubility with increasing Cu content in liquid aluminium (178).

Mg in Al-Si-Cu alloys is added to improve the material's strength by precipitation hardening. Additions above 0.2 wt% lead to the formation of a ternary eutectic (Al-Si- Mg_2Si). Typically, it forms after the formation of the Al-Si eutectic and before the Al_2Cu phase (179). The effect of Mg additions on the porosity level is not well established. Mg increases the hydrogen solubility of aluminium melt (178) and slightly the fluidity (175). Some publications show a minor porosity decrease in the interaction with Ti grain refiners and Sr-modification (17, 180). In experiments with an Al-Si-Cu-Mg alloy Gowri and Samuel (175) observe a shift of the Cu-phase formation temperature to lower values, if the Mg content is increased from 0.06 to 0.50 wt%. The increase in Mg content might lead to a porosity increase due to a reduced feedability in the late solidification stage.

2.2.2.9. Fe intermetallics

Typically, Fe is an impurity introduced into recycled alloys. One exception where Fe is added or used on purpose is for high pressure die casting alloys to reduce the tendency to die soldering. An increased Fe content leads to the formation of Fe intermetallics. For typical cooling conditions in the foundry practice, $\beta\text{-Al}_5\text{FeSi}$ is the predominant and most critical phase. Very high cooling rates promote the formation of $\alpha\text{-Al}_8\text{Fe}_2\text{Si}$, characterised as “Chinese script” morphology. $\beta\text{-Al}_5\text{FeSi}$ has a stoichiometrically sharp composition and solves only minimal amounts of Cu, Mg, and Mn (127, 179, 181, 182). How detrimental $\beta\text{-Al}_5\text{FeSi}$ is, depends on when it forms in the

solidification sequence. In general, it is hard and brittle, has a flake or plate-like morphology and low bonding strength to the matrix (18). Mascré (183) identified a critical Fe content for β -Fe formation, dependent on cooling rate, eutectic modification, Mn level, and Si content. Figure 2-22 shows a simplified ternary Al-Si-Fe phase diagram. As can be seen, by the liquidus lines for AlSi9, the solidification sequence is given by the Fe content. If the Si and Fe content are sufficiently high, β -Fe forms after the primary Al phase but before the Al-Si- β -Al₅FeSi eutectic. In this case, the Fe intermetallics become very extensive, and the primary Al phase mostly limits their size. Numerous research shows a very detrimental effect in this case (19–21, 183, 184).

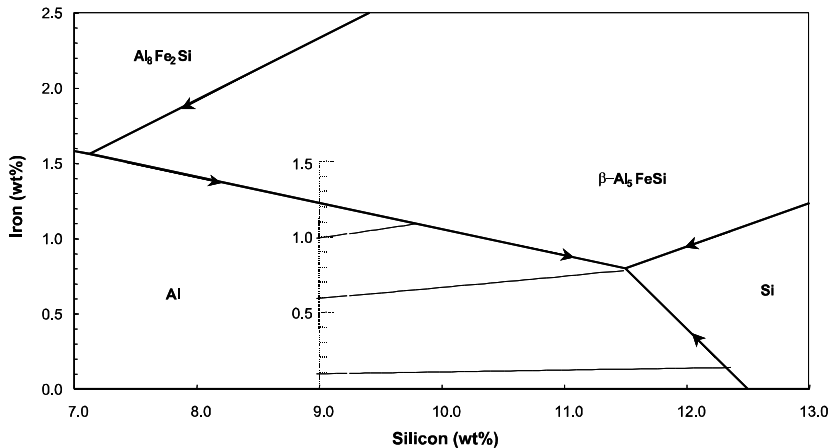


Figure 2-22: Simplified ternary Al-Si-Fe phase diagram. The lines show the liquid composition of an AlSi9 alloy with 1 wt% (supercritical), 0.6 wt% (critical) and 0.1 wt% (subcritical) Fe (27).

Additions of Sr or Na to modify the eutectic Si can also shift the eutectic coupled zone to higher Si levels. As a result, the Al-Si forms later at higher Si content, and Fe has more time to segregate and reach the critical level for β -Fe formation. This way modification can lead to or increase the Fe intermetallic volume fraction.

β -Al₅FeSi is often associated with porosity in Al-cast alloys. There are multiple convincing explanations about the underlying mechanisms (17, 22–24, 140, 183, 185, 186). One proposed mechanism is the blockage of feeding paths by the plate-

like morphology of the β -Al₅FeSi phases, which leads to more porosity (183). Another theory assumes that the β -Fe intermetallics are potent nuclei for pores (17). It was reported that Fe intermetallics nucleate at non-wetted oxide film (187, 188), as are these possible nucleation sites for pores (149, 150, 189), but a connection between the Fe intermetallics and pore nucleation is not yet established. The nucleation of β -Fe was also associated with impurities (190) or ALP particles (191, 192).

Taylor et al. (186, 193–195) did extensive research on the influence of the Fe content on the porosity level. They found a minimum in porosity that shifted depending on the Si level from 0.4 wt% Fe for an AlSi5Cu1 to 0.7 wt% Fe for an AlSi10Cu1. They explained their observation with a change in the solidification sequence to β -Al₅FeSi formation before the Al-Si eutectic formation and introduced three critical Fe contents: A subcritical Fe content $C_{Fe} < Fe_{crit}$, a critical Fe content $C_{Fe} = Fe_{crit}$, and a supercritical Fe content $C_{Fe} > Fe_{crit}$. In the subcritical state, the Al-Si eutectic forms before the β -Al₅FeSi. At the critical condition the ternary eutectic Al-Si and β -Al₅FeSi is formed simultaneously and at the supercritical condition β -Al₅FeSi forms before the Al-Si eutectic. Taylor et al. found in specimens with supercritical Fe content big β -Al₅FeSi plates and they concluded that big unfeedable liquid pockets are formed which result in extended pores. In subcritical specimen, first, the Al-Si eutectic forms and the size of the Fe intermetallics is limited. Under (near) critical conditions, the β -Al₅FeSi forms in small flakes as part of a ternary eutectic reaction. Because of Taylor et al. but also other researchers (22, 196, 197) assume Si nucleation on β -Al₅FeSi particles, the critical Fe content is associated with an efficient refinement of the eutectic and a porosity minimum, due to high permeability. Shankar et al. (197) even state that β -Al₅FeSi nucleation is possible at an Fe content below 0.1 wt% due to segregation, but this hypothesis is controversial because they do not take segregation of Si, Mg, Cu, etc. into account. The lattice difference between β -Fe and Si is bigger than between Al and typical Ti-based grain refiners or Si and ALP, but nucleation may be possible. If the orientation relationship $(210)_{\beta} || (200)_{Si}$ is compared, the lattice mismatch is only 0.77 % (186), which indicates the possibility of Si nucleation on β -Fe particles.

Otte's research (140) builds upon the work of Taylor. He also tried to understand the effect of Fe in Al alloys on porosity formation. In experiments with an AlSi9Cu3 with 0.6 wt% Fe, cast into the same experimental mould Taylor used, he did not find a porosity minimum. The amount of porosity increased slightly but continuously with increasing Fe content. He observed big connected pores if the Fe content exceeded Fe_{crit} . Moreover, experiments with sub- and supercritical Fe content and constant thermal gradient showed different solidification behaviour. In sub- and critical alloys β -Al₅FeSi and the Al-Si eutectic formed at high solid fractions approximately

in the same mushy zone region. On the other hand, in supercritical alloys the β - Al_5FeSi formed at low solid fractions and reduced the permeability (140). There is a difference that may explain the different observations, which is the Cu level. Dinnis et al. (198) found a different behaviour for Cu-less and Cu-containing alloys. The latter exhibits a porosity minimum at a critical Fe content. Nevertheless, Taylor's observed porosity minimum is controversially discussed. Iwahori et al. (23) did find a porosity increase in AlSi7Cu3 if a critical Fe content is reached but were not able to substantiate a porosity minimum. To an equivalent conclusion come Edwards et al. (130) in their experiments with the lower thermal gradient of sand castings. Wang et al. (199, 200) observed in recent synchrotron observations, pore growth around Fe intermetallics. Synchrotron observations also confirm this finding by Puncreobutr et al. (201). Both conclude a reduced solid-gas interfacial energy. Wang et al. further argued that the Fe-rich intermetallics also reduce the local hydrogen diffusion capabilities by impeding the diffusion across the plates. Besides the Cu level and the associated changes in solidifying microstructure, the gas level, and solidification rate are the most important aspects regarding the effect of the Fe level on porosity formation.

2.2.2.10. Mn effect on porosity

In aluminium alloys, Manganese is primarily used to neutralise the detrimental effect of an increased Fe content (18). A second reason is the formation of phases to increase the high-temperature mechanical properties. Mn additions lead to the formation of α - $\text{Al}_{15}(\text{Fe},\text{Mn})_3\text{Si}_2$, a cubic phase exhibiting an equiaxed structure that tends to form dendrites with "Chinese-script" morphology (18). The morphological differences are believed to neutralise the detrimental effect of the β - Al_5FeSi platelets (202).

If Mn is present in an alloy with a supercritical Fe content, the solidification sequence is changed. Instead of forming β - Al_5FeSi platelets after the primary aluminium, the α - $\text{Al}_{15}(\text{Fe},\text{Mn})_3\text{Si}_2$ phase is formed. Subsequently α - $\text{Al}_{15}(\text{Fe},\text{Mn})_3\text{Si}_2$ and β - Al_5FeSi and finally α -Fe, β -Fe, and Al-Si eutectic may form. α - $\text{Al}_{15}(\text{Fe},\text{Mn})_3\text{Si}_2$ even forms at low cooling rates which are often predominant in the foundry practice (179). There are three options to avoid the formation of β -Fe. First, a high cooling rate. Second, the addition of Mn. Third, superheating of the melt before casting.

Numerous researchers showed that Mn additions reduce the amount of porosity in Fe containing aluminium cast alloys (17, 19–26). Villeneuve et al. (25) observed in his research with the alloy AlSi6Cu4 , comparable porosity levels at 1.4 wt% Fe and 0.5 wt% Mn and 0.37 wt% Fe in conjunction with 0.05 wt% Mn. He explained

the beneficial effect of $\alpha\text{-Al}_{15}(\text{Fe,Mn})_3\text{Si}$ with an easier feedability, which is a controversial theory. Fundamental research on the subject was also done by Iwahori et al. (23). Their experimental set up was a sand mould plate casting with a central hot spot and a varying feeder size. In the experiments with an AlSi7Cu3 with 1.15 wt% Fe, Mn additions of 0.2–0.3 wt% reduced the necessary feeder size to produce porosity-free castings. Higher Mn additions had no additional effect. For Mn levels higher than 0.3 wt%, they observed almost exclusively $\alpha\text{-Fe}$. Mn additions of about 0.2 wt% led to a microstructure with equal amounts of $\alpha\text{-Fe}$ and $\beta\text{-Fe}$. Additions lower than 0.1 wt% resulted in the formation of only $\beta\text{-Fe}$. Their explanation for the reduced amount of porosity is a delayed formation of liquid pockets, which cannot be fed, thus an increase of the respective critical solid fraction. Dinnis (27) investigated the effect of Fe on porosity and found a reduced nucleation frequency of the Al-Si eutectic with increasing Fe content. Mn additions increased the nucleation frequency again. Crepeau (20) evaluated some publications on the effect of porosity reduction of Fe containing alloys by Mn additions. He was not able to extract a well-substantiated explanation of the mechanism.

Lastly, Mn additions do not generally lead to beneficial mechanical properties. Even if the formation of $\beta\text{-Fe}$ is suppressed, high amounts of $\alpha\text{-Fe}$ impair the alloy's ductility (19) and large quantities of $\alpha\text{-Al}_{15}(\text{Fe,Mn})_3\text{Si}$ can cause sedimentation problems (203).

2.2.2.11. Surface tension

The surface tension of aluminium counteracts the nucleation and growth of pores. The pore nucleation can be suppressed or shifted to a later stage during solidification (see Chapters 2.2.1.6 and 2.2.1.7). Anson et al. (148) investigated the effect of hydrogen content on the surface tension of modified and unmodified A356 and found no significant influence. Emadi and Gruzleski (147) investigated the impact of Sr and Na on the surface tension. Their results indicate a significant surface tension reduction, which may contribute to the increased porosity level of modified aluminium alloys. Nevertheless, they also find an increased volumetric shrinkage due to the Sr and Na additions, which might also increase the amount of porosity. Schmitz et al. (204) measured an increase of surface tension with increasing Cu levels in Al melt. Because Cu segregates strongly in aluminium, this effect may be relevant for the local conditions at pore formation. In the late-stages of solidification, even Cu levels close to the eutectic composition of approx. 33 wt% can be reached.

The effect of Mg on the surface tension of aluminium alloys was investigated by Korol'kov (205), who found that Mg additions up to 1 wt% reduce the surface tension sharply (approx. up to 24 %), but further additions only lead to a marginal decrease.

Sigworth and Wang (206) discussed the effect of surface tension on the feeding efficiency of feeders. As long as the melt in the feeder is below the coherency point feeding works by liquid and solid transport. Once the dendrites form a network (coherency) feeding becomes more difficult because the liquid melt is still transported but has to pull away from the solid dendrite skeleton forming new surface area. A schematic illustration is shown in Figure 2-23.

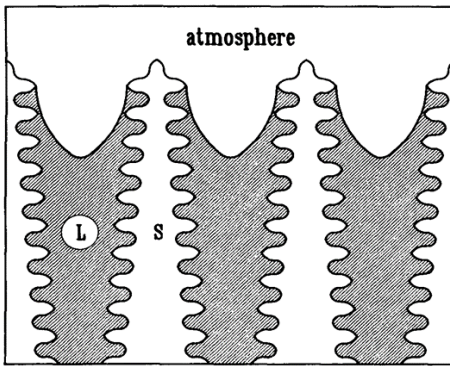


Figure 2-23: Schematic illustration of the melt surface pulling away from the feeder surface, forming new surface area (206)

Two surface tension effects have to be overcome. First, the liquid capillary and second, the formation of a new interfacial area between solid dendrites and the atmosphere. Because the liquid is pinned at the tips of the dendrites a curvature of the liquid is formed. Under the assumption of half-sphere surfaces of primary dendrite spacing diameter Sigworth and Wang estimate the necessary pressure in aluminium sand casting to 0.2 to 0.3 atm at a fraction liquid of 0.5. This estimate may even be conservative because the interdendritic openings are probably of smaller size.

Once the capillary force is overcome, the liquid will flow away from the dendrite tips, and the new solid-atmosphere surface will form. By calculating the energy balance over a volume element with its surface area normal to the flow of liquid, the necessary pressure drop to form new surface area can be estimated (206):

$$\Delta P = (\sigma_{sa} - \sigma_{sl})S_d = -\sigma_{la} \cos(\theta S_d) \quad \text{(Equation 111)}$$

where σ_{sa} , σ_{sl} , and σ_{la} are the surface tension between solid and atmosphere, solid and liquid, and liquid and atmosphere, respectively. θ is the three-phase contact angle, and S_d is the specific surface area of the dendrites. For an estimated contact angle of 135° and a specific surface area of $8/\lambda_1$ (minimum area of a spherical film around the average grain) Sigworth and Wang calculate a pressure drop of 0.25 atm. By putting both surface tension effects together, they estimate a pressure drop of at least half an atmosphere (probably more) once the feeding region shows coherency.

The same consideration was discussed and investigated by Liu et al. (207) who used borneol-paraffin mixtures as a dendritic substitute substance. Their observations show a reduction of the liquid feeding flow predicted by Darcy's law by two orders of magnitude, and since the surface tensions of metals are typically more than ten times greater than in this reference system, the effect might even be stronger. Liu et al. conclude that capillary pressure is one of the most important factors in porosity formation once the free surface of the feeding area has reached coherency.

Two important conclusions can be drawn from the presented argument. First, that the effect of grain refinement on the point of coherency might also positively influence the porosity formation and second, surface tension changes due to changes in the chemical composition (e.g. Cu variations or Sr additions) may play an important role by indirectly changing the feeding efficiency of the riser.

Finally, one has to keep in mind that aluminium, especially under a stationary condition, immediately forms an alumina layer in contact with the atmosphere. This surface alumina layer bears all the tension applied to the surface of the aluminium melt and has an ultimate tensile strength of two to three times the surface tension of liquid aluminium. The surface tension of the liquid in contact with the solid alumina layer also contributes a little to the total surface strength, but the contribution is estimated to be small. Moreover, the thickness of the oxide layer increases by further oxidation processes with time, therefore increasing its strength (42).

2.2.3. Modelling of porosity

2.2.3.1. Analytical models

Many volume-averaging approaches used for porosity prediction today, which try to determine the moment in solidification when the local pressure facilitates pore formation are based on the one-dimensional analytic developments by Piwonka and Flemings from 1966. They are the first to model pore formation incorporating solidification shrinkage and gas dissolution. For a constant solidification rate and a constant thermal gradient, they made three central assumptions. First, the mushy

zone consists of n tubes with n as the reciprocal of the primary dendrite arm spacing. Second, a tortuosity factor accounts for the discrepancy between the straight tubes and the tortuous feeding paths in reality. Third, the flow in the tubes is laminar and described by the Hagen-Poiseuille's solution. Comparisons with experimental results showed an underprediction of the amount of porosity. As a consequence, they introduced a fourth critical assumption, the effect of gas in solution (following the lever rule) and the pressure in the pores described by Laplace-Young's equation. The model results now delivered reasonable porosity predictions.

2.2.3.2. Criterion functions

In the 1950ies criterion functions were developed to predict centreline shrinkage porosity in steel plate castings. Many criteria were developed, but the Niyama criterion is probably the most popular and widely used one. It is based on physical reasoning, which separates it from most of the other criteria.

The mass balance requires a feeding flow perpendicular to the direction of solidification.

$$v_l = -\beta v^* \quad \text{(Equation 112)}$$

where v^* is the solidification front velocity, and β is the solidification contraction. (Equation 112) is also valid for steady-state columnar solidification of dendrites under the assumption of $\rho_s = \text{const.}$ and $\rho_l = \text{const.}$ Under this condition the microscopic velocity of the liquid phase $\langle v \rangle_l$ in the mushy zone is uniform, and the superficial velocity $\langle v_l \rangle = g_l \langle v \rangle_l$ varies proportionally to the mass flow. Niyama derived from this fundamental relationship, together with Darcy's law (see Chapter 2.2.1.2), the pressure drop in the mushy zone from the dendrite trip ($x = 0$) to a point $x(T)$ into the mushy zone up to the solid fraction $g_s = 1$ as

$$\Delta p = p_l(T_{liq}) - p_l(T) = \frac{\beta \mu_l v_T}{G} \int_{g_l}^1 \frac{g_l}{K(g_l)} \frac{dT}{dg_l} dg_l \quad \text{(Equation 113)}$$

where v_T is the isothermal velocity. Because v_T is difficult to measure, Niyama replaced it by $-\dot{T}/G$ which makes the pressure drop proportional to $|\dot{T}|/G^2$. Experiments with steel cylinders with various diameters showed that shrinkage porosity was observable if $N_y = G/\sqrt{|\dot{T}|} < 1\sqrt{\text{K min}^{-1}\text{m}^{-1}}$. It seems reasonable that higher isothermal velocities go along with higher interdendritic feeding velocities and hence a higher pressure drop. Also, a larger thermal gradient means a shorter mushy zone and thus easier feeding of the solidification shrinkage. The criterion

was specifically developed for steel and does not incorporate gas associated porosity in any way. Moreover, critical Niyama values vary between material, alloy, process, and casting geometry. Carlson tried to overcome the latter limitations by developing a dimensionless Niyama criterion (208). They integrated (Equation 113) using measured or calculated fraction solid curves $g_s(T)$.

2.2.3.3. Numerical models

In 1985 Kubo and Pehlke (209) developed the first two-dimensional numerical model for porosity prediction. They assumed development of the solid fraction determined by the Scheil approximation and a liquid velocity given by Darcy's law and the conservation of masses. First, they calculated the solidified volume fraction, which has to be compensated, then they determined the necessary feeding flux to make up for the volume deficit and the associated pressure drop. They assumed pore nuclei with an initial diameter in the order of the secondary dendrite arm spacing and a pore pressure satisfying the Laplace-Young equation. When the pressure in the pores exceeded a critical pressure, pores were nucleated, and growth was determined by Sievert's law. Their assumption of nucleation at the solid-liquid interface is questionable because the wetting between the solid and its liquid is usually excellent and thus nucleation at the solid-liquid interface unlikely. Nevertheless, many of their ideas can be found in subsequently developed models. Although many researchers tried to advance the prediction of microporosity by numerical models, three research groups should be highlighted due to their contributions to the field.

The first is Lee who published, together with Hunt in 1997 (210), a paper where they observed pore nucleation in an Al-Cu alloy. They used an X-ray temperature gradient stage for their experiments and deduced a two-dimensional model which neglects the pressure drop due to solidification but considered the diffusion of hydrogen in a continuum diffusion model. Pore nucleation was implemented as a stochastic model (77), similar to a cellular automaton describing solid nucleation in an undercooled melt, where each nucleus has a different nucleation potential (211). The correlation between predicted and measured pore growth was satisfying. In 2004 Lee et al. published a paper on a multiscale model of the solidification of Al-Si-Cu alloys, incorporating microsegregation and microporosity formation (96). A commercial software package was used to solve the energy, momentum, and continuity equations to provide the heat and momentum equations. The solid fraction was calculated by a combined cellular automaton and finite differences model. The grain growth was estimated by the KGT model (213), and the solid-liquid interface was traced by a Gandin and Rappaz' technique (211). Pore nucleation was modelled by the finite difference solution of the diffusion of hydrogen, and the locations of pore nucleation were stochastically distributed. The impingement of the pores with

the solid was incorporated, and the volume deficit due to shrinkage was taken into account. For the effective diffusion coefficient and the curvature restriction law, they used empirical correlations (214). The local solubility is only considered rudimentary.

The second research group is led by Beckermann. 2007, Carlson et al. published a volume-averaged model of finite-rate diffusion hydrogen controlled pore growth (33). They coupled the gas species conservation equation with the feeding flow, and the pressure field and showed that the pore growth is dependent on the hydrogen supersaturation of the melt and microstructure parameters. Carlson et al. were the first to model diffusion-controlled pore growth in three dimensions. Again, only gas transport via the liquid-pore interface was taken into account and impingement was modelled by the correlation developed by Péquet et al. (88). In 2017 Khalajzadeh et al. presented a unified gas and shrinkage model based on the dimensionless Niyama model (208) discussed above. By solution of the local point equations, the model extends and generalises the existing model and incorporates the effect of gas in solution. By making a pore-centric approach, the temporal evolution of the pore radius is calculated as a function of cooling rate, thermal gradient, gas diffusion, and shrinkage.

The third research group is led by Rappaz. In 2002, Péquet et al. presented a three-dimensional microporosity model based on Darcy's equation for the feeding flow and pressure drop and microsegregation of hydrogen (88). They were the first to couple microporosity, macroporosity, and pipe-shrinkage. To calculate the pressure drop in the mushy zone, they developed a dynamic mesh refinement technique to solve the governing equations of pore formation and growth only in the region of interest. Couturier et al. (46, 92, 215) extended the porosity model to a multi-gas multi-component model and implemented a simple but efficient impingement description by assuming a perfectly non-wetting pore growing in a square lattice of regular cylinders. A drawback of this model is that it does not take the effect of hydrogen diffusion into account.

3. Experimental procedure

3.1. Preliminary castings experiments

The goal of this experiment was to study the effect of Mg content and melt treatment, i.e., oxide content of the melt and holding time before solidification, on porosity amount and its characteristic distribution. The Mg effect was investigated at three targeted Mg levels: <0.05 wt%, 0.25 wt%, and 0.5 wt%. Two experimental sets were conducted. For the first one, the base composition of the used alloy EN AB-46000, as well as the composition after the addition of approximately 0.5 wt% Mg and after Sr addition, is shown in Table 3-1, Table 3-2 and Table 3-3, respectively. The second experimental set was done with the alloy EN AB-46000 with a Mg addition of approximately 0.25 wt% and no Sr addition. The composition is given in Table 3-4.

Table 3-1: Composition of the base alloy “EN AB-46000”, determined by a spark spectrometer (first experimental set)

	Si	Cu	Mg	Ti	B	Sr	Na	Mn
Unit	%	%	%	%	ppm	ppm	ppm	%
Mean	9.0	3.0	0.07	0.03	10	<1	<1	0.24
	Fe	P	Sb	Bi	Ca	Li	Cd	Zn
Unit	%	ppm	ppm	ppm	ppm	ppm	ppm	%
Mean	0.74	10	-	45	<0.1	<1	<3	0.92
	Ni	Cr	Pb	Sn	V	Zr	Al	Mn/Fe
Unit	%	%	%	%	%	%	%	-
Mean	0.03	0.02	0.07	0.02	0.01	0.01	85.88	0.32

Table 3-2: Composition of the alloy “EN AB-46000” after Mg addition, determined by a spark spectrometer (first experimental set)

	Si	Cu	Mg	Ti	B	Sr	Na	Mn
Unit	%	%	%	%	ppm	ppm	ppm	%
Mean	9.1	3.0	0.60	0.03	11	<1	<1	0.29
	Fe	P	Sb	Bi	Ca	Li	Cd	Zn
Unit	%	ppm	ppm	ppm	ppm	ppm	ppm	%
Mean	0.83	10	-	54	<0.1	<1	<3	0.92
	Ni	Cr	Pb	Sn	V	Zr	Al	Mn/Fe
Unit	%	%	%	%	%	%	%	-
Mean	0.03	0.03	0.07	0.02	0.01	0.01	85.11	0.34

Table 3-3: Composition of the alloy “EN AB-46000” after Mg and Sr addition, determined by a spark spectrometer (first experimental set)

	Si	Cu	Mg	Ti	B	Sr	Na	Mn
Unit	%	%	%	%	ppm	ppm	ppm	%
Mean	9.2	3.0	0.55	0.02	11	110	<1	0.29
	Fe	P	Sb	Bi	Ca	Li	Cd	Zn
Unit	%	ppm	ppm	ppm	ppm	ppm	ppm	%
Mean	0.82	12	-	51	<0.1	<1	<3	0.91
	Ni	Cr	Pb	Sn	V	Zr	Al	Mn/Fe
Unit	%	%	%	%	%	%	%	-
Mean	0.03	0.03	0.07	0.02	0.01	0.01	85.07	0.36

For the first experimental set, the alloy was not grain refined and only in the last experiment of the first experimental set Sr-modified. A batch of about 3 kg aluminium was heated up to 760 °C (+- 10 °C), and sequentially cast into small silica ceramic cups. The cups were preheated to remove any moisture and to suppress solidification. After the cups were filled as tranquil as possible, some were held at 750 °C for 2 to 30 min in a heating furnace and afterwards partly manipulated and then solidified under ambient conditions. The goal of the holding process was to “heal” existing oxide films, if possible. After that, the manipulation was supposed to introduce new oxides into the aluminium and observe the influence on the porosity characteristic after solidification. To achieve this introduction of new oxides, four

kinds of manipulations were applied and are depicted in Figure 3-1. In total 23 castings were made.

Table 3-4: Composition of the alloy “EN AB-46000”, determined by a spark spectrometer (second experimental set)

	Si	Cu	Mg	Ti	B	Sr	Na	Mn
Unit	%	%	%	%	ppm	ppm	ppm	%
Mean	10.1	2.1	0.25	0.02	9	<1	<1	0.19
	Fe	P	Sb	Bi	Ca	Li	Cd	Zn
Unit	%	ppm	ppm	ppm	ppm	ppm	ppm	%
Mean	0.91	<10	<30	40	<1	<1	<1	0.68
	Ni	Cr	Pb	Sn	V	Zr	Al	Mn/Fe
Unit	%	%	%	%	%	%	%	-
Mean	0.03	0.01	0.04	0.05	0.01	0.01	85.55	0.21

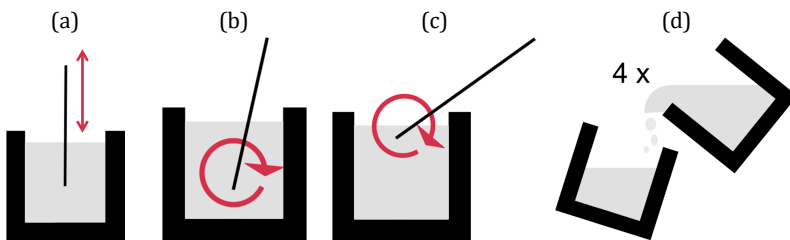


Figure 3-1: Schematic pictures of the chosen melt manipulations: (a) “surface dip”, (b) “stirring”, (c) “surface stir”, and (d) “four times decanting”

For the second experimental set, the same amount of aluminium was heated to 675 °C (+ 5 °C). The same cups were filled as tranquil as possible, some were held in a heating furnace at 680 °C for various times, and afterwards, some were manipulated by “stirring” or “four times decanting” (compare Figure 3-1(b) and (d), respectively). After the manipulation, some samples were solidified without disturbance at ambient temperature; others were quenched by introducing a copper rod into the specimen’s surface. In the second experimental set 16 castings were made. An overview of all variances of the first and second experimental set can be found in Table 3-5 and Table 3-6, respectively. The geometric measures are displayed in Figure 3-2 and Figure 3-3, respectively.

Table 3-5: Variations of the first experimental set with composition, holding time and manipulation

Specimen number	Mg level / Sr addition	Holding time (min)	Manipulation
1	Low Mg level (see Table 3-1)	0	None
2		2	
3		5	
4		15	Surface stir
5			
6			
7			
8			
9			
10			
11		30	None
12	Medium Mg level (see Table 3-2)	0	None
13		2	
14		5	
15		15	Surface stir
16			
17			
18			
19			
20			
21			
22		30	None
23	0		

Table 3-6: Variations of the second experimental set (holding time and manipulation)

Specimen number	Holding time (min)	Manipulation
1	0	None
2		
3		
4	15	Four times decanting
5		
6		
7		
8	0	Stirring
9		
10		
11	15	None
12		
13		
14		
15		
16	15	Four times decanting
16		
		Stirring

Both solidification processes were simulated with MAGMASOFT® to assess the overall solidification time and to estimate the position of the region of the last solidification. The chosen material datasets are from the standard MAGMASOFT® database as are the selected heat transfer coefficients. Details can be found in Table 3-7. A copper rod was submerged in the second experimental set to achieve a controlled quenching from the top region and to shift the material volume of the last solidification to the centre of the specimen. This shift of the hot spot was done to exclude the effect of feeding from the upper sample region from the overall porosity distribution.

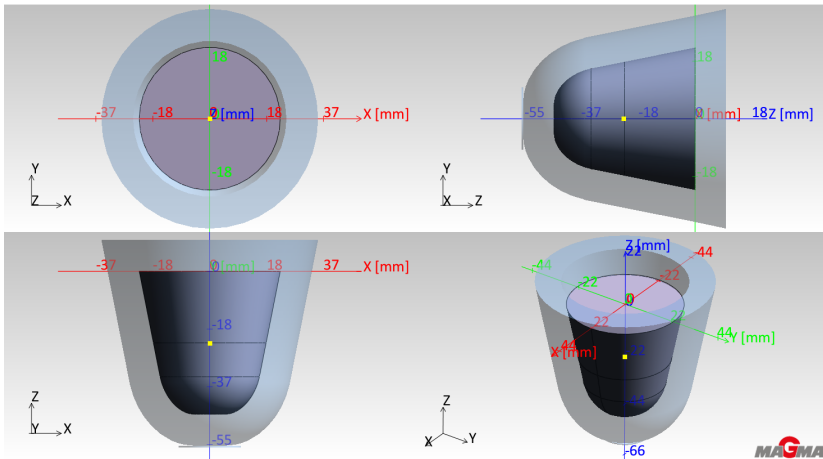


Figure 3-2: MAGMASOFT® geometry perspective of the unquenched experimental setup: melt (grey), cup (light blue transparent), floor (light blue thin transparent disk)

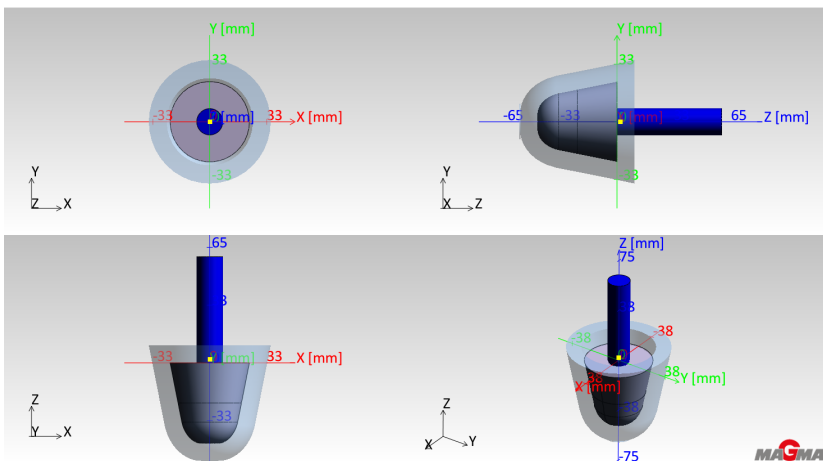


Figure 3-3: MAGMASOFT® geometry perspective of the quenched experimental setup: melt (grey), cup (light blue transparent), a copper rod extending 5 mm into the melt (dark blue), floor (light blue thin transparent disk)

Each specimen was cut through the middle by a water-cooled circular saw, to produce an A and B specimen. Only the A sample was processed further. The specimens were first ground on a laboratory grinding machine (Presi Mecapol P310 VV) by grinding paper of the grits 220 and 800 with water and afterwards polished in three steps on a laboratory grinding and polishing machine (Struers Tegramin 30) with diamond suspensions with 9, 3 and 1 μm polishing particles (disk Allegro/largo with 9 μm diamond suspension, disk Dac with 3 μm diamond suspension and disk Nap with 1 μm diamond suspension).

The images of the specimen surfaces were taken on a commercial optical scanner with a resolution of 600 dpi.

Table 3-7: Table of the chosen material datasets and heat transfer coefficients (HTCs) for the simulation of the quenched and not quenched preliminary castings

Component	Dataset	HTC
Melt	MAGMASOFT® standard dataset: AlSi9Cu3-Sand (adapted to "long freezing range") @ 750 °C	To cup: MAGMASOFT® standard HTC (temperature-dependent): AlSi9Cu3-mold To Chill: constant HTC of 7000 W/(m ² K)
Cup	MAGMASOFT® standard dataset: Graphit @ 750 °C	To melt: MAGMASOFT® standard HTC (temperature-dependent): AlSi9Cu3-mold To floor: constant HTC of 1000 W/(m ² K)
Chill	MAGMASOFT® standard dataset: Copper @ 20 °C	To melt: constant HTC of 7000 W/(m ² K)
Floor	User defined dataset: Al2O3 (adapted to infinite heat capacity) @ 20 °C	To cup: constant HTC of 1000 W/(m ² K)

3.2. Industrial castings

Two engine components were cast to characterise porosity amount and characteristics under industry conditions. These castings are representative of a broad range of aluminium cast components and cover, due to the use of a permanent mould process as well as a sand casting process, a wide range of solidification rates. The used alloys are typical for applications in the powertrain and chassis. In summary, four characteristic cast alloy – cast part combinations were produced: First, AlSi8Cu3, Sr-modified, cylinder head. Second, AlSi8Cu3, Sr-modified, crankcase. Third, AlSi7Cu0.5Mg, Sr-modified, cylinder head. Fourth, AlSi7Cu0.5Mg, Na-modified, cylinder head. The geometric measures of both castings, cylinder head and crankcase, are given in Figure 3-4.

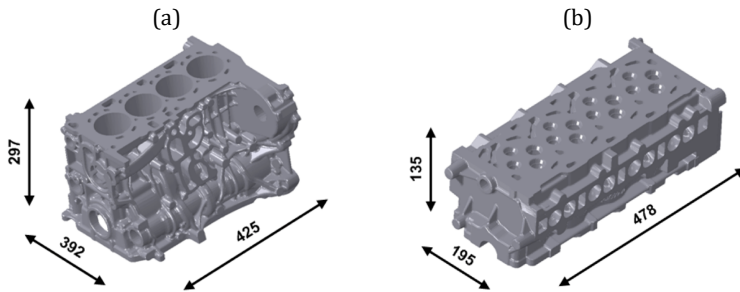


Figure 3-4: Geometric measures of the two industrial castings used for the specimen extraction and analysis: (a) crankcase and (b) cylinder head (dimensions are given in mm) (216)

In total sixty XCT samples were extracted from the four characteristic cast part/cast alloy combinations. Table 3-8 gives an overview of the produced castings and the extracted XCT samples.

Table 3-8: List of the four characteristic cast part/alloy combinations and the extracted XCT samples

Cast part	Alloy	Modification	Position	Number of XCT samples
Cylinder head	AlSi7Cu0.5Mg	Sr	Fire deck	5
			Camshaft bearing	5
			Tween deck	5
	AlSi8Cu3	Sr	Fire deck	5
			Camshaft bearing	5
			Tween deck	5
	AlSi7Cu0.5Mg	Na	Fire deck	5
			Camshaft bearing	5
			Tween deck	5
Crankcase	AlSi8Cu3	Sr	Bridge	5
			Stud bolt	5
			Bearing bracket	5

Due to space limitations, not all sixty XCT-specimens can be presented and discussed in this work. Eight representative samples were selected due to their representativeness for the observed porosity characteristics and are given in Table 3-9. The samples cover the observed range in the porosity of the conducted experiments and the two characteristically different pore morphologies; both are discussed in Section 4.2.

Table 3-9: List of eight selected XCT-specimens, which are representative of the general observations of the sample analysis and which are discussed in detail in Section 4.2. The extraction positions for the crankcase and cylinder head are shown in Figure 3-5 and Figure 3-7, respectively.

Specimen	Cast part	Position	Alloy	Modification	Spatial XCT Resolution (μm)
1	Crankcase	Bridge	AlSi8Cu3	Sr	3
2	Cylinder head	Camshaft bearing	AlSi7Cu0.5Mg	Sr	3
3	Cylinder head	Tween deck	AlSi8Cu3	Sr	8
4	Cylinder head	Fire deck	AlSi7Cu0.5Mg	Na	3
5	Cylinder head	Camshaft bearing	AlSi8Cu3	Sr	8
6	Cylinder head	Tween deck	AlSi7Cu0.5Mg	Na	8
7	Crankcase	Stud	AlSi8Cu3	Sr	8
8	Cylinder head	Fire deck	AlSi7Cu0.5Mg	Na	3

3.2.1. Crankcase

NEMAK Dillingen produced the crankcases in the CPS (core package system) process (217). Directly after filling, the casting is “rolled-over” (rotation by 180°) to enable natural solidification from the bottom (last filled region) to the feeder (first filled region). After solidification, the crankcase is heat treated.

The casting is a four-cylinder crankcase. Test castings for this thesis were extracted from the series production process. Additionally, castings with thermocouples at predefined specimen positions were cast. The aim was to cover a wide range of local solidification rates. Three areas were selected for this purpose: bridge

(between two chills forming the cylinder contour), bearing bracket and stud bolt. At the specimen locations, average cooling rates of approximately 0.1 K/s to 8 K/s were measured between the liquidus and the solidus temperature. The specimen extraction positions are shown in Figure 3-5.

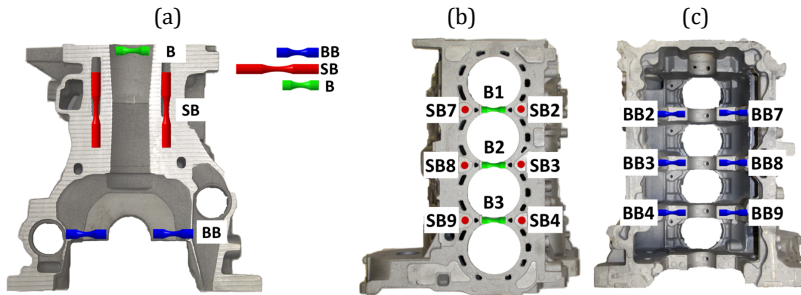


Figure 3-5: Locations of the specimen extraction positions within the crankcase casting in the sectioned (a), top (b), and bottom view (c): bridge “B”, bearing bracket “BB”, and stud bolt “SB” (216)

A reduced pressure test was done to determine the density index of the melt. All castings were Al-Ti-B grain refined (1.5 kg/t AlTi5B1) and Sr-modified. The composition after the addition of grain refiner and the eutectic modifier is shown in Table 3-10. The alloy will be named as AlSi8Cu3 from here on.

Table 3-10: Composition of the alloy “AlSi8Cu3” used for the crankcase, determined by a spark spectrometer

	Si	Cu	Mg	Ti	B	Sr	Na	Mn
Unit	%	%	%	%	ppm	ppm	ppm	%
Mean	8,0	2,9	0,2	0,16	7,6	140	-	0,4
	Fe	P	Sb	Bi	Ca	Li	Cd	Zn
Unit	%	ppm	ppm	ppm	ppm	ppm	ppm	%
Mean	0,6	-	-	-	-	-	-	-
	Ni	Cr	Pb	Sn	V	Zr	Al	Mn/Fe
Unit	%	%	%	%	%	%	%	-
Mean	-	-	-	-	-	-	86,91	0,7

From the castings, five specimens per position were mechanically extracted and machined to a rotating bending specimen. Depending on the available space, three specimen sizes have been used (Figure 3-6).

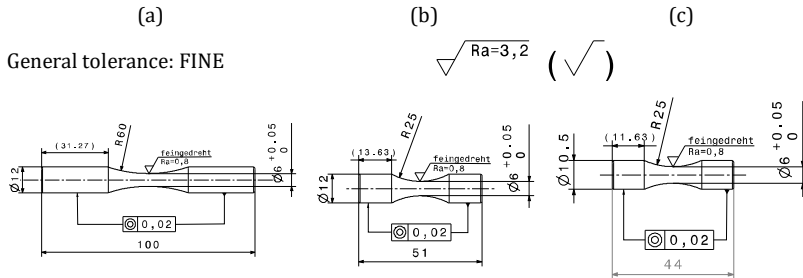


Figure 3-6: Rotating bending specimen, (a) RP01a - stud bolt, (b) RP02 - bearing bracket, (c) RP03 - bridge

These samples were later analysed by X-ray computed tomography (XCT). Additionally, metallographic specimens were extracted, ground, polished and etched and the secondary dendrite arm spacing was determined.

3.2.2. Cylinder head

The cylinder head was produced by NEMAK Linz in the Rotacast® process (217, 218). This process offers excellent flexibility and is used to generate high-quality castings. By active cooling of specific areas of the mould, local microstructural properties can be controlled and the process time can be reduced. The castings are heat treated to T5 or T6 condition.

All produced castings were made under series production conditions. Two alloys were cast, one only Sr-modified the other Sr and Na-modified. The alloy AlSi8Cu3(Sr) (see Table 3-11) and the primary alloy “AlSi7Cu0.5Mg” with its composition given in Table 3-12 (Sr-modified) and Table 3-13 (Na-modified). Three specimen locations were selected: fire deck, tween deck, and camshaft bearing. At the specimen locations, average cooling rates of approximately 0.1 K/s to 3.5 K/s were measured between the liquidus and the solidus temperature. The specimen extraction positions are shown in Figure 3-7.

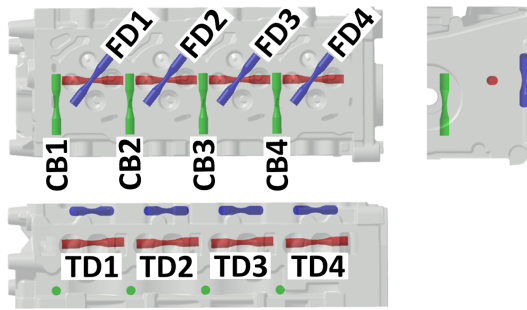


Figure 3-7: Locations of the specimen extraction positions within the cylinder head casting: fire deck “FD”, camshaft bearing “CB”, and tween deck “TD” (216)

Both alloys were cast at 710 °C. A considerable difference between both processes lay in the cooling concept. Whilst the die of the AlSi7Cu0.5Mg is permanently cooled (water cooling of the fire deck, jet cooling close to the fire deck, and inlet mould), the AlSi8Cu3 die was only cooled during preparation and the beginning of the solidification. The effect is a lower solidification rate of the latter castings.

Table 3-11: Composition of the alloy “AlSi8Cu3(Sr)”, Sr-modified, used for the cylinder head, determined by a spark spectrometer

	Si	Cu	Mg	Ti	B	Sr	Na	Mn
Unit	%	%	%	%	ppm	ppm	ppm	%
Mean	8.5	3.3	0.35	0.10	6	200	3	0.26
	Fe	P	Sb	Bi	Ca	Li	Cd	Zn
Unit	%	ppm	ppm	ppm	ppm	ppm	ppm	%
Mean	0.4	2	-	-	-	-	-	-
	Ni	Cr	Pb	Sn	V	Zr	Al	Mn/Fe
Unit	%	%	%	%	%	%	%	-
Mean	-	-	-	-	-	-	86.52	0.6

Table 3-12: Composition of the alloy “AlSi7Cu0.5Mg(Sr)”, Sr-modified, used for the cylinder head, determined by a spark spectrometer

	Si	Cu	Mg	Ti	B	Sr	Na	Mn
Unit	%	%	%	%	ppm	ppm	ppm	%
Amount	6.7	0.55	0.35	0.12	3	220	15	0.06
	Fe	P	Sb	Bi	Ca	Li	Cd	Zn
Unit	%	ppm	ppm	ppm	ppm	ppm	ppm	%
Amount	0.11	5	-	-	-	-	-	-
	Ni	Cr	Pb	Sn	V	Zr	Al	Mn/Fe
Unit	%	%	%	%	%	%	%	-
Amount	-	-	-	-	-	-	92.12	0.6

During both casting processes, two castings with thermocouples at the specimen positions were produced. From the castings, five specimens per position were mechanically extracted. This means from the AlSi8Cu3(Sr), the AlSi7Cu0.5Mg(Sr), and the AlSi7Cu0.5Mg(Na) fifteen samples each. These were machined to rotation bending specimen with the dimensions given in Figure 3-8.

Table 3-13: Composition of the alloy “AlSi7Cu0.5Mg” Na-modified, used for the cylinder head, determined by a spark spectrometer

	Si	Cu	Mg	Ti	B	Sr	Na	Mn
Unit	%	%	%	%	ppm	ppm	ppm	%
Amount	6.9	0.58	0.31	0.11	3	5	59	0.01
	Fe	P	Sb	Bi	Ca	Li	Cd	Zn
Unit	%	ppm	ppm	ppm	ppm	ppm	ppm	%
Amount	0.16	7	-	-	-	-	-	-
	Ni	Cr	Pb	Sn	V	Zr	Al	Mn/Fe
Unit	%	%	%	%	%	%	%	-
Amount	-	-	-	-	-	-	91.87	0.1

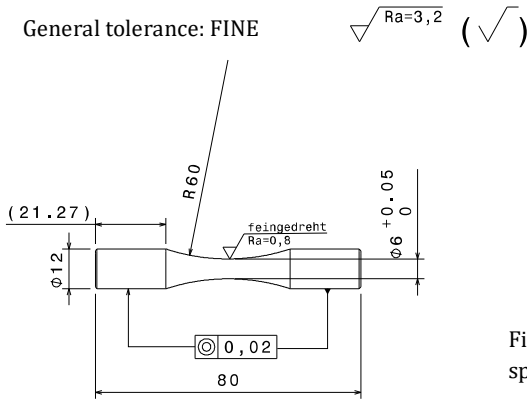


Figure 3-8: Rotating bending specimen RP01b

These specimens were analysed by XCT. Additionally, metallographic specimens were extracted, ground, polished and etched and the secondary dendrite arm spacing was determined.

3.3. Wedge casting experiments

Twelve wedge castings were cast to characterise average porosity amount and pore size characteristics under laboratory conditions. The layout of the sand mould with the wedge casting, chill, filter, and casting system is displayed in Figure 3-9. The geometric measures of the wedge itself are shown in Figure 3-10. The wedge casting was developed by Nematik Dillingen GmbH (Germany) to reproduce microstructures representative of the earlier introduced industrial castings. A chill block is located in the thinnest steps of the wedge, to achieve the high cooling rates associated with chills in the industrial process. Additional to the local solidification rate, two parameters were introduced: the quantitative hydrogen content of the aluminium melt and its density index.

For density index determination the reduced pressure test (219) was used. About 200 g of aluminium is poured into each of two thin wall steel crucibles. One is solidified under atmospheric pressure, the other at the reduced pressure of 80 mbar. The density index is calculated by

$$DI = \frac{\rho_{atm} - \rho_{red}}{\rho_{atm}} 100 \quad \text{(Equation 114)}$$

with the specimen's density solidified at atmospheric pressure ρ_{atm} and the specimen's density solidified at reduced pressure ρ_{red} , both determined by the Archimedes Principle.

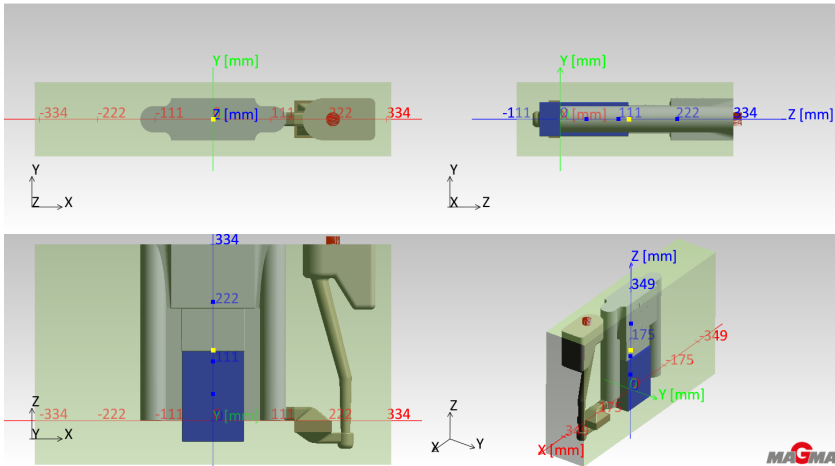


Figure 3-9: MAGMASOFT® geometry perspective of the experimental setup: melt (grey), sand mould (light green transparent), iron chill (dark blue), ceramic filter (dark brown) and pouring basin/gating system (light brown). The experimental set up was developed by Nematik Dillingen GmbH (Germany).

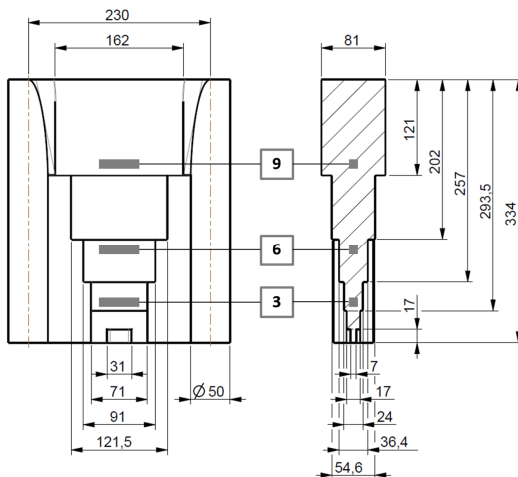


Figure 3-10: Geometric measures of the casting produced in the wedge experiment. The wedge specimens were extracted at the wedge wedge positions 3, 6, and 9, which are located 50.6, 111.9, and 224 mm from the wedge bottom (dimensions given in mm)

Two TiB_2 grain refined and Sr-modified AlSi8Cu3 and AlSi7Cu0.5Mg alloys were cast. The goal was to mimic the solidification conditions of the industrial castings

but under simplified geometric conditions. The exact chemical composition of both alloys is given in Table 3-14 and

Table 3-15, respectively. The Composition was chosen as close to the chemical analysis of the industrial castings in chapter 2 as available.

The wedge casting had a volume of approximately 3915 cm³ (without casting system) and was cast in approximately 20 s. The pouring temperature of the AlSi8Cu3 and the AlSi7Cu0.5Mg alloy was 700 °C (±5 °C) and 715 °C (±5 °C), respectively. A ceramic filter was used to prevent the flow of old oxides into the wedge. The hydrogen level of the aluminium melt was modified by either addition of HYDRAL 40® (to increase the hydrogen content) or NITRAL 10® tablets (to reduce the hydrogen content). Further details on the procedure of de- or up-gassing with the aforementioned tablets can be found in Section 3.4. 15 min before casting 1,5 kg AlTi5B1 master alloy per ton and 100 ppm Sr (by AlSr10 master alloy) were added. Just before casting a sample for chemical analysis and a hydrogen measurement was taken. The hydrogen level was determined by an HYPAL® hydrogen analyser system (see Section 3.5 for further details). Two wedges were cast directly after another under the same conditions. Directly after casting the step castings, the reduced pressure test to determine the density index was conducted.

Table 3-14: Composition of the alloy “AlSi8Cu3” Sr-modified, used for the wedge castings, determined by a spark spectrometer

	Si	Cu	Mg	Ti	B	Sr	Na	Mn
Unit	%	%	%	%	ppm	ppm	ppm	%
Amount	7.9	3.0	0.25	0.12	-	200	<1	0.30
	Fe	P	Sb	Bi	Ca	Li	Cd	Zn
Unit	%	ppm	ppm	ppm	ppm	ppm	ppm	%
Amount	0.41	-	-	-	-	-	-	0.66
	Ni	Cr	Pb	Sn	V	Zr	Al	Mn/Fe
Unit	%	%	%	%	%	%	%	-
Amount	0.03	0.02	0.02	0.01	-	-	87.20	0.73

Table 3-15: Composition of the alloy “AlSi7Cu0.5Mg” Sr-modified, used for the wedge castings, determined by a spark spectrometer

	Si	Cu	Mg	Ti	B	Sr	Na	Mn
Unit	%	%	%	%	ppm	ppm	ppm	%
Amount	6.8	0.76	0.33	0.12	-	100	<1	0.08
	Fe	P	Sb	Bi	Ca	Li	Cd	Zn
Unit	%	ppm	ppm	ppm	ppm	ppm	ppm	%
Amount	0.11	-	-	-	-	-	-	0.04
	Ni	Cr	Pb	Sn	V	Zr	Al	Mn/Fe
Unit	%	%	%	%	%	%	%	-
Amount	0.01	<0.01	<0.01	<0.01	-	-	91.67	0.75

Each wedge casting has ten predefined sample positions from 1 (highest cooling rate) to 10 (lowest cooling rate). In wedge positions 3, 6, and 9, rotation bending specimen were extracted (see Figure 3-6(a)). These specimens (in total 36) were scanned by XCT (further details on the XCT procedure can be found in Section 3.6). In the same wedge positions (3, 6, and 9) metallographic samples were prepared. A complete overview of the produced wedge castings and extracted specimens is given in Table 3-16.

Table 3-16: Complete list of the produced AlSi8Cu3 wedge castings and the extracted specimens

Alloy	Targeted hydrogen level	Wedge casting number	Wedge position	Local cooling rate	Wedge specimen number
AlSi8Cu3	Low	1	3	High	1
			6	Medium	2
			9	Low	3
		2	3	High	4
			6	Medium	5
			9	Low	6
	Medium	3	3	High	7
			6	Medium	8
			9	Low	9
		4	3	High	10

Experimental procedure

	High	5	6	Medium	11	
			9	Low	12	
			3	High	13	
		6	6	Medium	14	
			9	Low	15	
			3	High	16	
	AlSi7Cu0.5Mg	Medium	7	6	Medium	17
				9	Low	18
				3	High	19
			8	6	Medium	20
				9	Low	21
				3	High	22
Low		9	6	Medium	23	
			9	Low	24	
			3	High	25	
		10	6	Medium	26	
			9	Low	27	
			3	High	28	
High	11	6	Medium	29		
		9	Low	30		
		3	High	31		
	12	6	Medium	32		
		9	Low	33		
		3	High	34		
			6	Medium	35	
			9	Low	36	

3.4. HYDRAL 40® and NITRAL 10® tablets

HYDRAL 40® is a hydrogen up-gassing tablet for aluminium alloys distributed by FOSECO®. It is typically used in permanent mould casting and low pressure die casting of aluminium alloys. Its function of up-gassing is provided by the release of a defined amount of hydrogen during the reaction with the melt in the submerged

state. The HYDRAL 40® tablet is placed on the melt surface and submerged with a plunging bell. The release of gas is most active in the first couple of minutes, and the melt treatment is finished after the gas generation has ceased. Before casting, the melt surface has to be cleaned of generated dross and is immediately ready for pouring. If multiple tablets are added, the alloy composition has to be readjusted due to significant burn off of Sr and Mg.

NITRAL 10® is a degassing tablet distributed by FOSECO®. It is used to increase the melt cleanliness and decrease the hydrogen content of aluminium melt. Typical applications are the sand-, die-, and high pressure die casting processes. It should not be used in alloys sensitive to minor Na additions. NITRAL 10®'s function is provided by releasing Nitrogen while reacting with the melt in the submerged state. The tablet is placed on the melt surface and submerged with a plunging bell. In a strong reaction, Nitrogen is released, and fragments of burned off tablets are washed to the melt surface. The melt treatment is finished when no more gas is generated. After the treatment, dross has to be removed, and the melt should settle for a couple of minutes. If an extensive amount (3 or more) tablets are added, the alloy's composition should be readjusted due to burn off of Sr and Mg. In the case of a grain refined alloy, new grain refinement should be done.

3.5. HYPAL® hydrogen measurement system

The HYPAL® measurement system provides quantitative hydrogen and temperature measurement in liquid aluminium. The system was used to perform spot measurements prior to casting. The HYPAL® probes are calibrated before shipping and require no on-site calibration. The HYPAL® is a battery-powered device which is automatically detecting if a stable hydrogen measurement is achieved and logs up to 5 days of continuous measurement. The condition of the HYPAL® probe is monitored continuously, and the user is informed if the probe has reached its end of life. Before the measurement, the HYPAL® is adjusted to the alloy composition and by that to the specific alloy's hydrogen solubility. The reproducibility of the analysis is given as ± 0.01 ml/100 g or 3 %, whichever is greater. By purging the probe with nitrogen (N₂ or Ar are possible), the reading can be refreshed. Further advantages of the purging procedure are the removal of moisture in the porous probe tip, and the prolongation of the probe service life by avoiding condensation of high vapour pressure elements (e.g. Sn) in the probe tip. Figure 3-11 shows a schematic illustration of the measurement set-up.

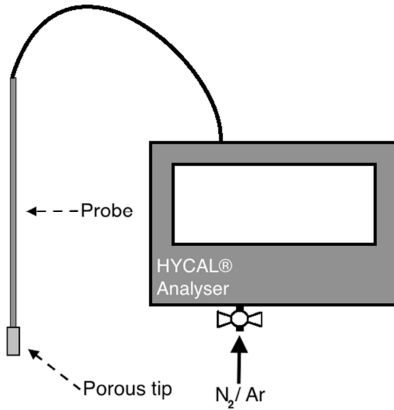


Figure 3-11: HYCAL® measurement set-up. The probe can be purged by Nitrogen or Argon to refresh the hydrogen reading

The HYCAL® unit utilises a ceramic $\text{CaZrO}_3\text{-In}$ proton conductor. The tip also contains a thermocouple. When immersed in the liquid aluminium, a porous ceramic can absorb and conduct H^+ protons to the measurement chamber. In the chamber, the hydrogen protons recombine to H_2 , and partial pressure in thermodynamic equilibrium with the aluminium melt is established. Between the measurement chamber and a solid-state reference electrode (which known H content), the $\text{CaZrO}_3\text{-In}$ proton conductor enables the measurement of an electrical potential, proportional to the hydrogen partial pressure in the measurement chamber. The following equation established the described correlation

$$U = \frac{RT}{2F} \ln \frac{p_{\text{H}_2}^{\text{ref}}}{p_{\text{H}_2}^{\text{meas}}} \quad \text{(Equation 115)}$$

where U is the measured electrical potential between the inner and outer surface of the ceramic proton conductor, R is the ideal gas constant, T the absolute temperature, F the Faraday's constant, $p_{\text{H}_2}^{\text{ref}}$ the known reference hydrogen partial pressure, and $p_{\text{H}_2}^{\text{meas}}$ the hydrogen partial pressure in the measurement chamber. Via Sievert's law, the last quantity is correlated to the hydrogen content of the aluminium melt. The measurement is moderated by the hydrogen solubility of the melt (by alloy composition and temperature). Figure 3-12 shows the schematic design of the HYCAL® probe tip.

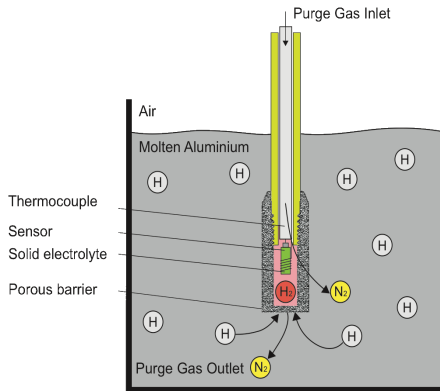



Figure 3-12: Schematic sketch of the HYCAL® hydrogen measurement probe tip (220)

3.6. X-ray tomography

A total of 96 specimens from crankcases, cylinder heads, and wedge castings were scanned with a GE nanotom m micro-XCT system at the Material Centre Leoben Forschungs GmbH, Leoben, Austria. The specifications of the XCT are given in Table 3-17. The used X-ray tube is a 10-180 kV nano focus tube with internal cooling and a diamond window target. The detector is a DX500L (300 x 240 mm), 3000 x 2400 pixels resolution, 1.5 x IMR and 10,000:1 dynamic range. For each industrial casting (crankcase, cylinder head) and for each alloy and variation of modification (AlSi8Cu3(Sr), AlSi7Cu0.5Mg(Sr) and AlSi7Cu0.5Mg(Na)) five specimens per position (three positions per casting) were scanned. In the case of the laboratory wedge castings, two specimens per position (three positions per wedge) were analysed. A voxel size of 3, 5, and 8 μm was used, depending on the size of the anticipated microstructural fineness. The voxel size is the edge length in x, y, and z of a cube-shaped voxel, the three-dimensional equivalent to a two-dimensional pixel. The specimens had the shape of rotating bending specimen with a minimum diameter of 6 mm, a radius of 60 mm or 25 mm. The scan's height lay between 5.4 mm (3 μm voxel size) and 15.5 mm (8 μm voxel size). The effectively scanned volume lies therefore between approximately 144 mm³ and 477 mm³ respectively (arithmetic means of all scans).

The scanned data was divided into pore volume and dense material, which was done by a self-determined consistent threshold value on the upper border of an acceptable threshold range. The resolution of the resulting pore volumes has been artificially increased by a digital superresolution image technique (7). Adjacent pores were “merged” and analysed as one bigger pore if a certain distance to pore size threshold was met or exceeded (8).

Table 3-17: Technical details about the micro XCT used for the analysis of the samples.

GE Nanotom M	
Scanning principle	3D XCT
X-ray tubes	10-180 kV nano focus with internal tube cooling and diamond window target
Detectors & virtual detector axis "IMR"	DX500L (300 x 240 mm), 3000 x 2400 pixel 1.5 x IMR, 10,000:1 dynamic
Scanning volume & sample weight	Diameter: 240 mm, height: 250 mm, 3 kg
No. of axes & manipulator type	5 (R, Y, Z, XD, ZD) granite-based
Cabinet dimension (W x H x D) & weight	1980 x 2100 x 2180 mm, 1.9 t

3.7. Analysis of XCT-Data

After XCT data processing, the data analysis was conducted. The total pore volume V_p in each scan was defined as

$$V_p = \sum_N v_{p,i} \quad \text{(Equation 116)}$$

where N is the total number of pores in the scan and $v_{p,i}$ is the volume of each pore. The total porosity was defined as

$$g_p = \frac{V_p}{V_0} 100\% \quad \text{(Equation 117)}$$

where V_0 is the total volume of the scan. Each pore was described by the equivalent spherical diameter of a volume equivalent sphere $d_{s,i}$

$$d_{s,i} = \sqrt[3]{\frac{6v_{p,i}}{\pi}} \quad \text{(Equation 118)}$$

and the biggest equivalent spherical diameter was defined as $d_{s,max}$. Analog to d_s and $d_{s,max}$ the diameter of the convex pore envelope was described by d_e , and

$d_{e,max}$. The envelope is equivalent to the sometimes used maximum Feret's diameter. Both quantities, d_s and d_e , are illustrated in Figure 3-13.

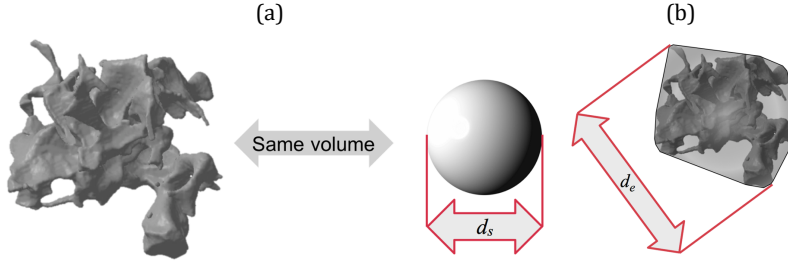


Figure 3-13: Illustration of the equivalent spherical diameter d_s (a) and the equivalent envelope diameter d_e (b) (224)

A volume-weighted mean diameter was used to characterise the pore distribution's mean. The same procedure was applied for the distribution of the envelope diameters. Both are defined by

$$d_{s,mean} = \frac{\sum_N (v_{p,i} d_{s,i})}{\sum_N v_{p,i}} \quad \text{(Equation 119)}$$

$$d_{e,mean} = \frac{\sum_N (v_{p,i} d_{e,i})}{\sum_N v_{p,i}} \quad \text{(Equation 120)}$$

where $d_{s,i}$ and $d_{e,i}$ are the spherical and envelope diameters for a given pore i . The morphology of a pore was described by its sphericity which is defined by

$$\psi_i = \frac{\pi^{\frac{1}{3}} (6v_{p,i})^{\frac{2}{3}}}{s_i} \quad \text{(Equation 121)}$$

where s_i is the pore's surface area. If the calculation of the sphericity was not possible (in case the surface area s_i was not determinable) or if the calculated value was unreasonable ($\psi_i > 1$), it was excluded from the analysis. Especially at the lower resolution limit of the XCT-scan, the determination of the pore surface was not possible or very inaccurate. The mean sphericity was introduced to describe the prevailing pore morphology in each specimen. Analog to $d_{s,mean}$ and $d_{e,mean}$, a volume-weighted mean sphericity ψ_{mean} was introduced and proved itself to be insensitive to the influences of resolution and small pore detection accuracy

$$\psi_{mean} = \frac{\sum_N (v_{p,i} \psi_i)}{\sum_N v_{p,i}} \quad \text{(Equation 122)}$$

4. Results and discussion

4.1. Preliminary casting experiments

The goal of the preliminary laboratory casting experiments is to investigate the effect of young oxides on the amount, as well as the distribution and morphology of porosity in an aluminium cast alloy. Based on the theory presented by Campbell (42), the ability of the melt to “heal” young oxides depending on Mg content is also investigated. To examine the differences that may be induced by a directed solidification from the bottom to the top of the sample or an isolated hot spot region in the centre of the samples, two experimental sets are conducted.

4.1.1. First experimental set

In the first experimental set, 23 castings were produced. Figure 4-1 shows a selection of representative samples which were not manipulated after filling and which were allowed to solidify directly (Figure 4-1(a)), or after 15 min (b), or 30 min (c) at 750 °C in a holding furnace.

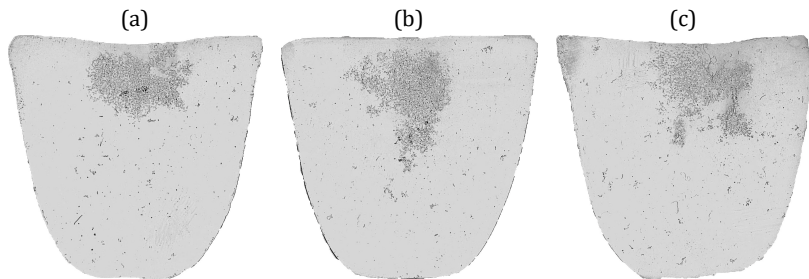


Figure 4-1: Micrographs of polished samples 1 (a), 4 (b), and 11 (c) of the first set of 23 cup samples. All samples were filled as tranquil as possible and contained less than 0.1 wt% of Mg. (a) was allowed to solidify directly after filling, (b) was held for 15 min, (c) for 30 min at 750 °C before solidification under ambient conditions.

All samples show approximately the same qualitative amount of total porosity and quite similar porosity distribution. At the top of the specimens, a hot spot leads to the formation of a spongelike, high porosity, region. The rest of the samples shows an even distribution of small to medium-sized pores.

All three samples are from the experiments conducted with the low Mg containing alloy (below 0.1 wt%), and thus oxide film “healing” due to the formation of a MgAl_2O_4 spinel is not expected even after long holding times (42, 119, 123).

Figure 4-2 shows selected samples produced with the same experimental procedure as the previously shown samples. The only difference is an increased Mg content of approximately 0.6 wt%. In general, the amount of total porosity, based on the visual impression, increased. There is less porosity concentrated in the upper hot spot region and more porosity evenly distributed over the sectioned sample surface. The distributed porosity itself appears to be tortuous, but the individual pores seem not to be connected. Each pore seems to be the result of a local isolated porosity nucleation event. In summary, there are no significant differences between all three samples shown in Figure 4-2. The missing concentrated porosity in the hot spot region in specimen 22 (Figure 4-2(c)) is not consistently observable with increased holding time.

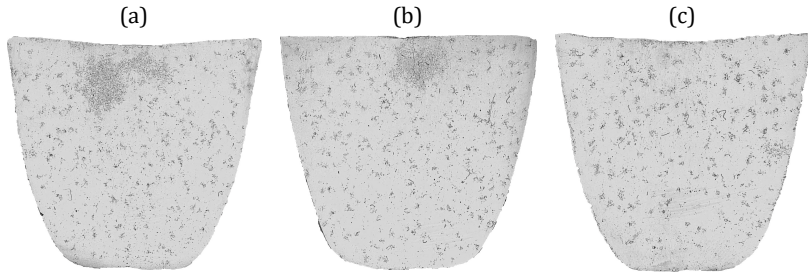


Figure 4-2: Micrographs of polished samples 12 (a), 15 (b), and 22 (c) of the first set of 23 cup samples. All samples were filled as tranquil as possible and contained approximately 0.6 wt% of Mg. (a) was allowed to solidify directly after filling, (b) was held for 15 min, (c) for 30 min at 750 °C before solidification under ambient conditions.

In contrast to the expected behaviour based on the hypothesis presented by Ar-yafar et al. (119) and Campbell (42) of an increased ability to heal existing nucleation sites due to the formation of a MgAl_2O_4 spinel in this composition range, no such trend is apparent. Moreover, there are no significant observable differences in all three samples presented in Figure 4-2. This could be the case because 15 or even 30 min holding time is not sufficient to consume all available gases trapped in the bi-film, although experimental results of Raiszadeh and Griffiths suggest the possibility to consume the oxygen and nitrogen within seconds (117). A delayed deflation of a pore can be caused by an elevated hydrogen content of the melt, yet there is no indication of the typically observed porosity with high sphericity. If the samples in Figure 4-1 and Figure 4-2 are compared further, it is not possible by visual impression to conclusively answer if the increased Mg content leads to an overall increase or decrease of total porosity. It is apparent that the Mg addition produced a more

dispersed porosity, which is less concentrated in the region of last solidification (hot spot).

Figure 4-3 shows another set of three selected samples. All were cast with the low Mg containing alloy, held for 15 min after tranquil filling at 750 °C and then manipulated before solidification under ambient conditions. The three types of manipulation were stirring at the surface to introduce fresh oxides (Figure 4-3(a)), manipulation by pushing a steel rod to the bottom of the crucible (Figure 4-3(b)), and four times decanting from one crucible to another (Figure 4-3(c)). Samples (a) and (c) seem to show a slight increase porosity level, compared to sample (b) and compared to all three specimens presented in Figure 4-1 of the same alloy with no manipulation. The vigorous stirring of the sample surface (a) and the multiple decanting processes (c) might have introduced a high number of fresh oxides. The qualitative differences are small, considering the presumably massive amount of fresh oxides inside of the melt before solidification. In principle, one would expect a profoundly different porosity level, based on the “bifilm theory” presented by Campbell (42). All freshly introduced oxide films should be ideal nucleation sites for pore growth.

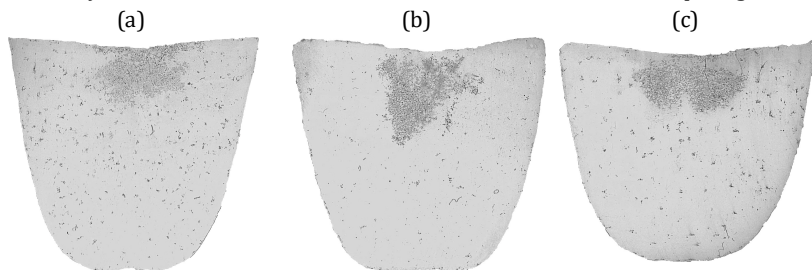


Figure 4-3: Micrographs of polished samples 5 (a), 8 (b), and 9 (c) of the first set of 23 cup samples. All samples were filled as tranquil as possible and then held at 750 °C for 15 min. The Mg level is lower than 0.1 wt%. Before solidification (a) was stirred at the surface to introduce fresh oxides, (b) was manipulated by pushing a steel rod to the bottom of the crucible, and (c) was decanted four times from one crucible to another.

In Figure 4-4 the same manipulation processes were applied as in the samples presented in Figure 4-3, but with the alloy containing approximately 0.6 wt% Mg. As with the previously displayed samples in Figure 4-1 and Figure 4-2, the higher Mg level leads to a qualitatively increased amount of porosity of the specimens presented in Figure 4-4 compared to the samples shown in Figure 4-3. The effect of the three different types of manipulation, note that (a) and (c) should contain a significant amount of fresh oxides, are masked by the in general higher porosity

level. All three samples show about the same amount of porosity and are hardly distinguishable from the three (not manipulated, but also 0.6 wt% Mg containing) samples shown in Figure 4-2.

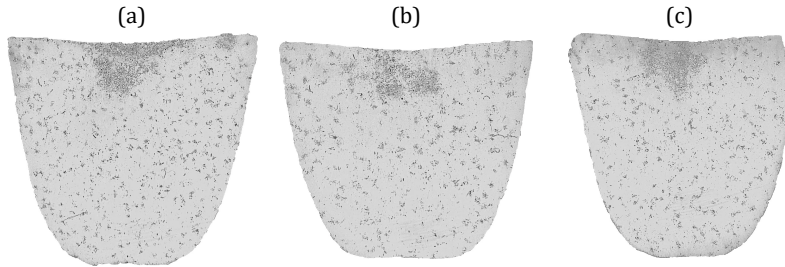


Figure 4-4: Micrographs of polished samples 16 (a), 19 (b), and 20 (c) of the first set of 23 cup samples. All samples were filled as tranquil as possible and then held at 750 °C for 15 min. The Mg level is approximately 0.6 wt%. Before solidification (a) was stirred at the surface to introduce fresh oxides, (b) was manipulated by pushing a steel rod to the bottom of the crucible, and (c) was decanted four times from one crucible to another.

The higher Mg level of the samples presented in Figure 4-2 and Figure 4-4 seems to have increased the total porosity, especially compared to the introduction of young oxides into the melt by unfavourable melt handling (or the introduction on purpose as shown in Figure 4-3 and Figure 4-4). Some of the observed change due to Mg addition might be associated with a changed porosity distribution within the sample (less porosity in the hot spot region and more distributed porosity), some may originate from a higher porosity level in general. There are a couple of possible explanations for this development. First, the width of the solidification interval increased, or second, the local permeability of the mushy zone was reduced, or third, the local melt viscosity in the last stages of solidification increased. Fourth, the spatial growth behaviour of the Si eutectic became less directional, less determined by the general thermal gradient over the sample or the increased Mg level destabilised the eutectic front. Fifth, the Mg addition could have reduced the local surface tension of the melt and thus promoted pore formation. Sixth, the formation of a MgAl_2O_4 spinel did not occur or did not “heal” a theoretical “bifilm”. It might even have facilitated pore nucleation. Even the hydrogen level in the melt might have changed.

By calculations of the solidification of EN46000, with and without Mg addition of approx. 0.5 wt%, by the commercial software package JMatPro® (which can calculate thermomechanical and thermophysical material properties), some of the explanations above were illuminated. A Mg addition of about 0.5 wt% reduces the

solidus temperature about two degrees but also lowers the liquidus temperature to the same approximate amount. The solidification interval thus does not change according to these calculations. The probably more important terminal freezing range between a solid fraction of 85 % and 95 % (TFR_{85-95}) does not change, or rather between 95 % and 98 % (TFR_{95-98}) is even reduced by two degrees. Because a long terminal freezing range is associated with unfavourable feeding conditions in the critical last stage of solidification, a changed solidification interval or local permeability due to the mushy zone length cannot be substantiated based on these thermophysical calculations. Research by Gowri and Samuel (175) states that more and lower sphericity pores at higher Mg levels are to be expected due to a delayed formation of the Al_2Cu phase. In their experiments with varying Mg contents in an Al-Si-Cu-Mg alloy, they were able to measure a shift to lower formation temperatures of the Cu-phase at higher Mg levels. A lower formation temperature of the Cu-phase is associated with a farther progressed solidification (higher fraction solid) which should also be linked to a reduced feedability and higher tortuosity of the remaining liquid melt pools. Their general observation agrees with the thermophysical calculations, which predict a decrease of the Al_2Cu phase formation temperature by about 11 degrees for 0.5 wt% Mg addition. Though the presented terminal freezing ranges do not indicate an extended mushy zone at the end of solidification, the shift to lower formation temperatures of the Al_2Cu phase and the associated high solidification shrinkage of 8.4 % (176), may still explain some of the higher and more disperse porosity.

The JMatPro® calculations of the liquid viscosity two degrees above solidus temperature predicts that the Mg addition increases the dynamic viscosity only about 1.15 %, a rather small change compared to the significant differences in porosity distribution (note that JMatPro® considers the segregation of elements during solidification).

Segregation of Mg during primary and eutectic solidification is known to destabilise the eutectic front and thus lead to an extended eutectic mushy zone (9), which in turn may lead to the porosity increase due to more isolated liquid pockets which are also less feedable.

The predicted change in surface tension by JMatPro® is below 1 %, but there is contradicting research (205) which states that Mg additions up to 1 wt% reduce the surface tension of aluminium sharply (approx. up to 24 %). A significant reduction in surface tension should facilitate pore formation and thus might play a role in the explanation of the presented results.

Mg increases the hydrogen solubility of liquid aluminium (178), which may also lead to more hydrogen-induced porosity and delay a “healing” process of introduced

oxides. Although the hydrogen in the experimental set up was not controlled, the visual impression of the pores does not suggest gas supersaturation as a main driving force in the conducted experiments. The specimens with the lower porosity level (which are also the ones with the lower Mg level) seem to exhibit higher qualitative pore sphericity than the pores present in the specimens cast with the higher Mg level.

The potential effect of a MgAl_2O_4 spinel formation that “heals” an existing bifilm defect, will be discussed after the presentation of the second experimental set in Section 4.1.2. The more complex eutectic mushy zone in combination with the delayed formation of the Al_2Cu phase, seem most likely to be responsible for the observed general porosity trend.

4.1.2. Second experimental set

To reduce the influence of feeding from the top specimen region on the overall porosity distribution and to validate the findings presented above under the condition of an isolated hot spot region in the centre of the casting, in the second set of experiments the samples were quenched from the top by inserting a cold copper rod (as can be readily noticed in Figure 4-5 and Figure 4-6 in the specimens’ top regions). In the second experimental set, the alloy EN 46000 was cast as well. There are deviations in Si and Cu content (about one percent more Si and one percent less copper) in comparison to the first experimental set. For a detailed overview Table 3-1, Table 3-2, Table 3-3 (first experimental set) can be compared to Table 3-4 (second experimental set). The Mg level of the latter lies with 0.25 wt% approximately in the middle between the low and high Mg level of the first experimental set.

The fundamental observation presented in Section 4.1.1 remains valid for the second experimental set. The fact, that the region of the last solidification was, as intended, shifted into the middle of the casting, did not fundamentally change the qualitative amount of porosity of the whole casting. If the total amount of porosity is compared to the first experimental set, it can be placed in about the middle between the low and high Mg castings (compare Figure 4-5 with Figure 4-1 and Figure 4-2 and compare Figure 4-6 with Figure 4-3 and Figure 4-4). Considering that the Mg content in the second experimental set of 0.25 wt% lies in the intermediate region between the 0.07 and 0.60 wt% of the first set, this observation seems to be plausible. The same explanations which are given in Section 4.1.1 hold in case of an isolated hot spot region. The most plausible explanation for the increased porosity level due to Mg addition are still the following. First, a destabilisation of the eutectic solidification front and formation of a eutectic mushy zone, which goes along with a reduced local permeability with larger and more frequent occurrence of liquid un-

feedable pockets. Second, the delayed formation of the Al_2Cu phase and the associated high solidification contraction increases the need for liquid feeding in the final solidification stage, which in turn leads to higher porosity levels.

As in the first experimental set, the vigorous stirring (see Figure 4-5(a)) and decanting (see Figure 4-5(b)) just before solidification seem to have the effect of increasing porosity. Comparisons of Figure 4-1 versus Figure 4-3 and Figure 4-2 versus Figure 4-4 show a clear trend. By qualitative evaluation, Mg additions from 0.07 wt% to 0.60 wt% lead to a stronger increase in porosity, than the introduction of fresh oxides just before solidification did. A general distortion of the observations made in the first experimental set by feeding from the mushy top region can be excluded by the results from this second experimental set.

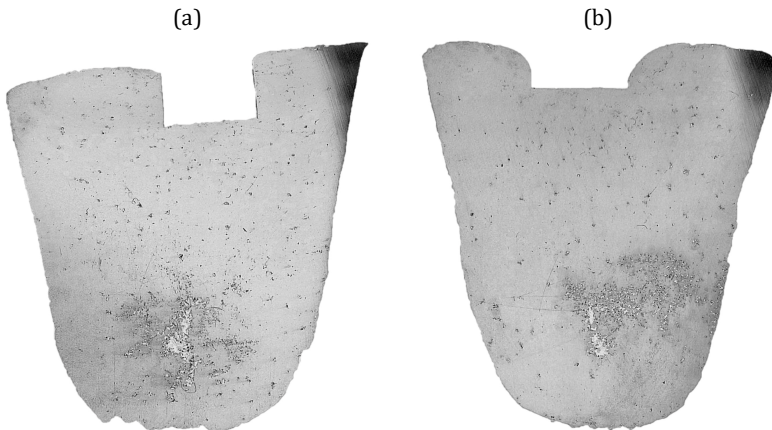


Figure 4-5: Micrographs of polished samples 9 (a) and 4 (b) of the second set of 16 cup samples, containing approx. 0.25 wt% Mg. Both samples were filled as tranquil as possible. Specimen (a) was allowed to solidify directly after filling, sample (b) was held at 680 °C for 15 min in a heat treatment furnace and then also solidified under ambient conditions. During solidification, both were quenched from the top with an introduced copper rod.

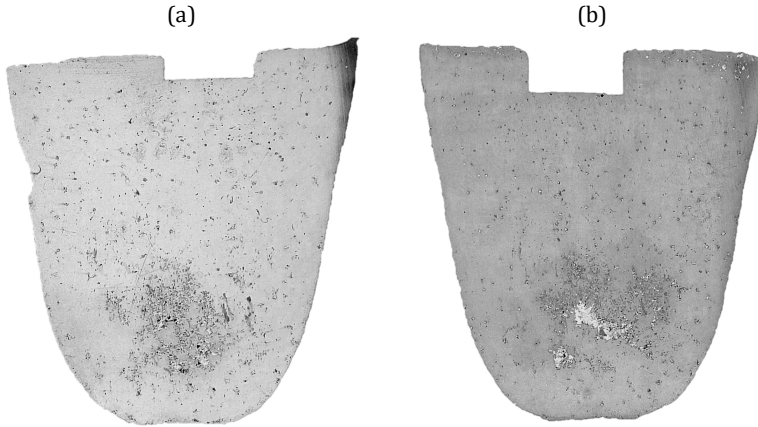


Figure 4-6: Micrographs of polished samples 14 (a) and 15 (b) of the second set of 16 cup samples, containing approx. 0.25 wt% Mg. Both samples were filled as tranquil as possible and held at 680 °C for 15 min in a heat treatment furnace. Before solidification under ambient conditions, (a) was stirred vigorously and (b) was decanted four times to introduce new oxides. During solidification, both were quenched from the top with an introduced copper rod.

These results put the crucial importance of bifilms on porosity as Campbell (221) suggests into perspective. In the examined alloy system and under the given solidification conditions, young oxides affect porosity, but it is superimposed by a stronger composition effect of Mg. The theory presented by Campbell (42) of an increased ability of bifilm healing in the intermediate range of Mg levels (around 0.5 wt%) by MgAl_2O_4 spinel formation, is not supported by the results. There are three explanations regarding the bifilm theory which may explain the experimental results that the porosity level does not decrease but instead increases with increasing Mg level. First, the holding times in the first experimental set without manipulation and medium Mg level (see Figure 4-2) were not sufficiently long to facilitate bifilm healing, or second, hydrogen in solution prevented and delayed the healing as proposed by Raiszadeh and Griffiths (117, 118) as well as by Aryafar, Raiszadeh, and Shalbafzadeh (119). Third, bifilms as unbonded double oxide films may not be the only possible pore nucleation site, and thus more research regarding the exact nucleation process of pores during solidification of aluminium alloys is necessary. The conclusion from these experiments is that the fundamentals of solidification on

porosity nucleation, amount, distribution, and morphology are of paramount importance to be understood and a limited focus only on oxide films falls short of explaining the phenomenon altogether.

4.1.3. Summary

Two sets of preliminary casting experiments were conducted to investigate the effect of young oxides on the amount, distribution and morphology of porosity in aluminium cast alloys.

In contrast to the expectation, no healing effect of oxides by the formation of a Mg spinel is observed. A holding time of 30 min prior to solidification does not change the porosity characteristics. The Mg addition to the cast alloy EN AB-46000 leads to a more dispersed, less in the hot spot concentrated, spatial porosity distribution.

The sample manipulations in the form of vigorous stirring of the sample (in the bulk or at the surface) or the multiple decanting before solidification to introduce young oxides, lead to a slight porosity increase. This increase is found to be relatively small, especially compared to the porosity increase due to Mg addition. The effect of oxide introduction was effectively “cover-up” by the chemical composition effect.

The most likely explanation for the observed behaviour is a shift of the Al_2Cu formation to lower temperatures and a destabilisation of the eutectic front. The latter being associated with the extension of the width of the eutectic mushy zone and the formation of more isolated liquid pockets which are also less feedable. Possibly, a reduction of the melt's surface tension due to Mg addition can also contribute to a promoted pore nucleation.

The second experimental set, in which the region of the last solidification was shifted from the top of the sample to its centre, does not lead to different conclusions. On the contrary, the level of Mg continues to be more relevant for the porosity characteristics than the melt manipulation and thus the availability of young oxides during solidification. A general distortion of the presented results by unhindered feeding from the top specimen region can be excluded based on the finding from the second experimental set.

The paramount importance of “bifilms” and oxides, in general, is put into perspective by the presented results and it becomes clear that more research is needed to understand the pore nucleation mechanism better.

4.2. Industrial castings

To investigate porosity in general and the pore distribution characteristics more specifically, industrial castings of the alloys AlSi8Cu3 and AlSi7Cu0.5Mg are produced. The aim is to examine the effect of chemical composition, eutectic modifier, and casting process on average porosity, pore distribution, and pore morphology. The two eutectic modifier Sr and Na are used, and the two industrial casting processes CPS (core package system, as a sand mould process) and Rotacast® (as a permanent mould process) are applied. If possible, predictions of the characteristic measures mean and maximum pore volume, as well as mean and maximum pore size, should be developed. The industrial process is chosen because of its high reproducibility and representativeness of many other comparable aluminium cast products in the powertrain.

A total of sixty XCT specimen were analysed (see Table 3-8). These sixty samples stem from four experimental sets (AlSi8Cu3, Sr-modified, cylinder head; AlSi8Cu3, Sr-modified, crankcase; AlSi7Cu0.5Mg, Sr-modified, cylinder head; AlSi7Cu0.5Mg, Na-modified, cylinder head). In each set, three sample positions were analysed and five samples per position were taken. Table 4-1 gives an overview of the minimum and maximum values of the characteristic quantities used to describe the pore distributions.

Table 4-1: Summary of the minimum and maximum characteristic quantities of the industrial castings representing the pore distribution characteristic (the DAS was determined as specified by VDG specification P220 (222))

	DAS, λ_2 (μm)	Porosity, g_p (%)	Spherical Mean Diameter, $d_{s,mean}$ (μm)	
Min	17	0.003	13	
Max	78	1.322	466	
	Maximum Spherical Diameter, $d_{s,max}$ (μm)	Envelope Mean Diameter, $d_{e,mean}$ (μm)	Maximum Envelope Diameter, $d_{e,max}$ [μm]	Mean Sphericity, φ_{mean}
Min	51	87	218	0.18
Max	813	2505	3961	0.93

As can be seen from the λ_2 values, the castings cover a broad range of cooling rate. The total amount of porosity also varies significantly, and the associated maximum envelope diameter is even at the lowest observed porosity levels still of an order of size ($> 200 \mu\text{m}$) that is potentially relevant for the fatigue properties of the material.

It was shown in the literature [2–6, 223] that if a micropore constitutes the largest defect, it is the limiting factor for the fatigue performance of the part.

4.2.1. Porosity distribution

In Figure 4-7 the distribution of total porosity g_p in bins of the equivalent spherical diameter d_s is shown. Eight characteristic specimens, already introduced in Table 3-9 and part of the sixty XCT measurements performed on the industrial castings, were selected to show four different types of porosity distribution. In Figure 4-8 an overview is given for these four characteristic pore volume distribution types for each characteristic experimental set. The type of distribution (maximum in the smallest size bins, maximum in the medium-sized bins, maximum in the biggest bins, and bi-modal pore volume distribution) was assigned by visual impression. In Figure 4-7(a) a distribution with a maximum in the lower third of the bins is displayed. The biggest bin contains roughly 25 % of the total porosity. Cylinder head specimens cast in AlSi7Cu0.5Mg(Sr) with a low porosity level below approximately 0.03 % show this type of distribution (compare Figure 4-8(a)). If the porosity rises above approximate 0.03 %, the distribution shifts to a centric distribution like shown in Figure 4-7(b), (e), and (g). The same behaviour is displayed by the specimens of the crankcase cast in AlSi8Cu3(Sr) (Figure 4-8(b)), but the shift from a distribution with its maximum in the small bins to a distribution which is more centric occurs at a porosity level between approximately 0.1 % and 0.3 %. Figure 4-7(d) shows a bimodal porosity distribution with two maxima, one in the lowest quarter, the other in the upper third. This kind of distribution was only observed in three castings and only for the AlSi7Cu0.5Mg(Na) cylinder heads with approximately 0.2 % porosity. Specimens with less than approximately 0.1 % porosity show a centric or low bins maximum distribution. Specimens with more than approximately 0.3 % porosity show a distribution with its maximum in the higher bins (compare Figure 4-8(c)). So, the bimodal distribution may be a transition between specimen with very low and higher porosity levels. Figure 4-7(f) and (h) display a maximum in the upper third of the bins, which is typical for AlSi7Cu0.5Mg(Na) cylinder heads with medium and high amounts of porosity. For the AlSi8Cu3 cylinder head alloy, the behaviour is not as clear as for the other alloys. Up to approximately 0.26 % porosity, a distribution may have its maximum in the low bins or a centric distribution. Above 0.26 % porosity, the centric porosity distribution dominates (see Figure 4-8(d)). Figure 4-7(c) belongs to this experimental set but cannot be categorised with absolute certainty.

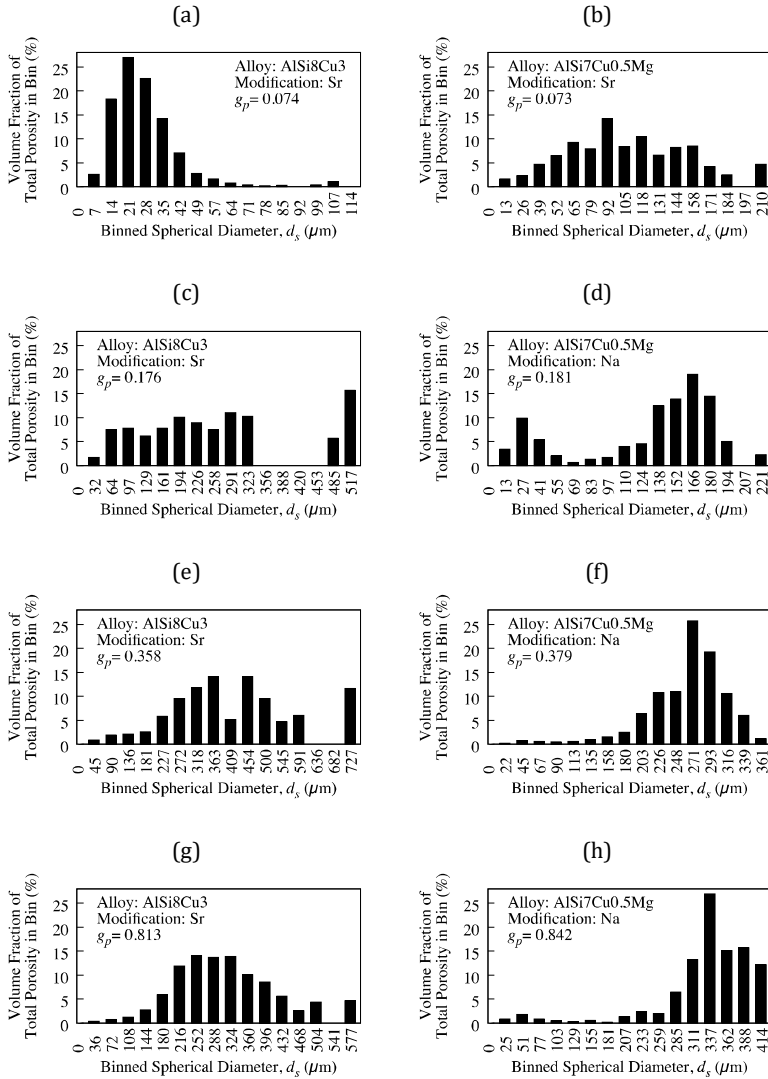


Figure 4-7: Histograms of the pore size distribution showing the volume fraction of the total porosity in spherical diameter bins for specimens 1–8 in (a)–(h) (224)

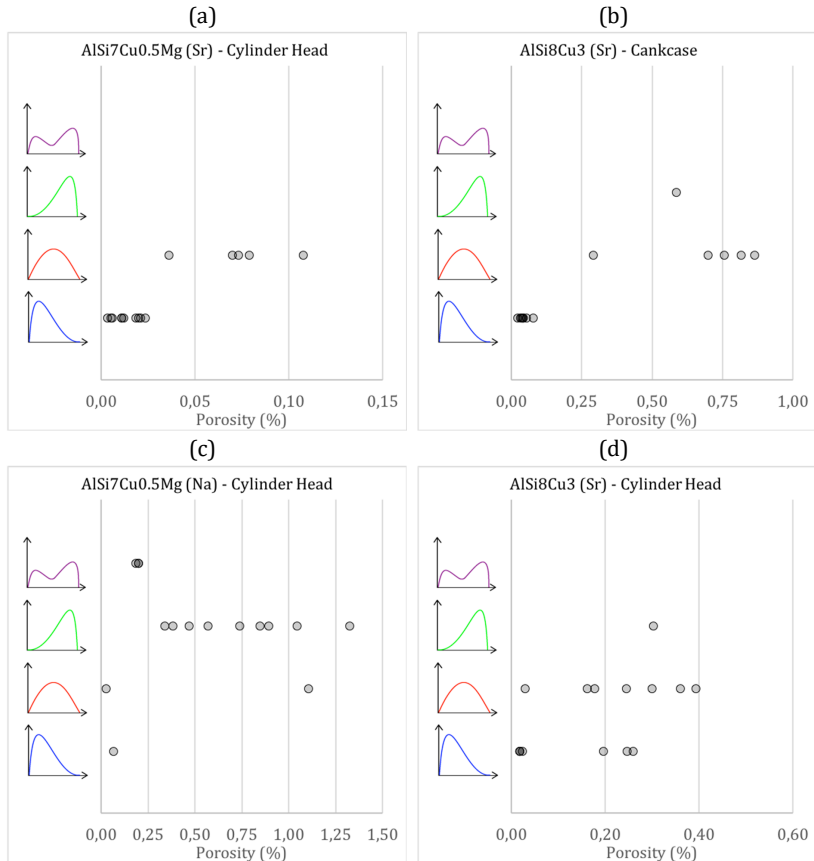


Figure 4-8: Categorization of the pore volume distribution of each of the sixty XCT specimens into four categories by the visual distribution impression. The samples are presented within their experimental set: (a) AlSi7Cu0.5Mg, Sr-modified, cylinder head; (b) AlSi8Cu3, Sr, crankcase; (c) AlSi7Cu0.5Mg, Na-modified, cylinder head; and (d) AlSi8Cu3, Sr-modified, cylinder head.

For the Sr-modified specimens with a low amount of porosity, the major pore volume is distributed in the smallest or medium-sized pores. Especially for the lowest porosity levels for each experimental set, a porosity distribution with a maximum in the smallest bins can be observed most often, which may indicate a high density of liquid pockets or a large thermal gradient (and thus large differences in the size

of liquid pockets) in the last stages of solidification. The effect of eutectic grain size as the last solidification reaction and the correlation between the size of the liquid pool, pore size, and the effect of the local thermal gradient was presented and discussed at length by McDonald et al. (16). The fundamental idea is likely applicable to vice versa. If a pore size distribution with a high number of small pores can be observed, a high number density of isolated liquid pockets had to be present in the final stages of solidification, which means that the porosity distribution should be a direct link to the isolated pockets of liquid melt (assuming only shrinkage-related porosity). Nevertheless, according to McDonald et al., a large thermal gradient should also be associated with a large size gradient of the liquid pools. If this size gradient is large enough, it may be able to prevent the pocket isolation all together or at least reduce it significantly.

For the high Cu alloy the threshold for which the transition to the centric porosity distribution can be observed shifts to higher porosity levels, which may indicate that Cu increases the nuclei density for porosity during solidification or destabilises the eutectic solidification which leads to many liquid pools. It was described by Heiberg et al. (9) that Cu additions could destabilise the eutectic solidification front and promote the formation of a eutectic mushy zone. Additionally, Cu extends the solidification interval and thus the mushy zone, which probably deteriorates the permeability. Furthermore, the Al_2Cu phase, which forms at the end of solidification (175), has a significant solidification shrinkage of approximately 8.4 % (176). All these effects seem to support the present findings of porosity behaviour.

A bimodal porosity distribution was only observed in Na modified cylinder head with low Cu content and a relatively low porosity content. In the present findings, Na modification led to a high number of small pores if the porosity level was relatively low. The low amount of porosity was presumably associated with a large thermal gradient and minimal hydrogen absorption from the atmosphere. Even though Na is reported to increase the eutectic cell size significantly (16), a strong thermal gradient may enable long local feeding and very late isolation of liquid pools by a changed macroscopic eutectic growth behaviour.

Dahle et al. (143) showed for Na-modified permanent mould test castings that the eutectic solidification takes place from the mould wall in the direction of the local thermal hot spot (opposite to the thermal gradient). The growth front is expected to be relatively flat with very little dispersed microporosity forming in this stage because interdendritic feeding is relatively easy. Only later, once the eutectic enclosed an isolated partly liquid area, could concentrated pore nucleates. The second population of bigger pores in the bimodal porosity distribution probably nucleated early during solidification due to hydrogen dispersion, but only to a limited extent. The final solidification shrinkage in the mushy zone led to many very small pores.

The Na-modified experimental sets with medium and high porosity levels show a porosity distribution with a maximum in the largest (upper third) bin of the pores. Even if the thermal gradient favoured a short mushy zone, significant hydrogen absorption during the casting procedure might have occurred (31, 32). The result would be an early and continued nucleation and growth of pores (relatively spherical), which compensate a significant amount of the total solidification shrinkage. Consequently, the amount of porosity leading to very small pores in the final stages of solidification is limited. It is important to emphasise that this behaviour may be caused by a fundamentally different driving force for pore formation (hydrogen supersaturation) and thus the previously presented argument of a correlation between the size of the liquid isolated melt pockets and the porosity distribution is most probably not or at least not fully applicable in these cases.

4.2.2. Spherical and envelope diameter versus average porosity

The analysis of the XCT data showed that the scanning resolution strongly affects the number density of pores at the lower resolution limit. Therefore, a volume-weighted approach was chosen. This way the evaluated results are almost independent of the spatial resolution of the XCT scan (for 3 μm and 8 μm). Concurrently, the volume-weighted approach weighs the big pores, which determine the fatigue behaviour of the cast part, highest and so the displayed result parameters are of high significance for potential later use in fatigue life predictions. In Figure 4-9 the plot of the spherical mean diameter $d_{s,mean}$ versus the average porosity g_p is shown. All sixty XCT scans are plotted.

In general, a v-shape of the data can be observed. Based on this observation, the data is divided into two characteristic specimen populations. First, the grey population (from here on called GP), consisting of the experimental sets AlSi8Cu3(Sr) cylinder head and AlSi7Cu0.5Mg(Sr) cylinder head, marked by grey points. The alloys have a significant difference in their Cu contents, but both are produced in the same process (cylinder head in the Rotacast® process). Second, the black population (from here on called BP), consisting of the experimental sets AlSi8Cu3(Sr) crankcase and AlSi7Cu0.5Mg(Na) cylinder head, marked by black points. The composition differences are again the same, but additionally, the eutectic modifier and the casting process differ (AlSi8Cu3(Sr) cast in CPS and AlSi7Cu0.5Mg(Na) cast in Rotacast®).

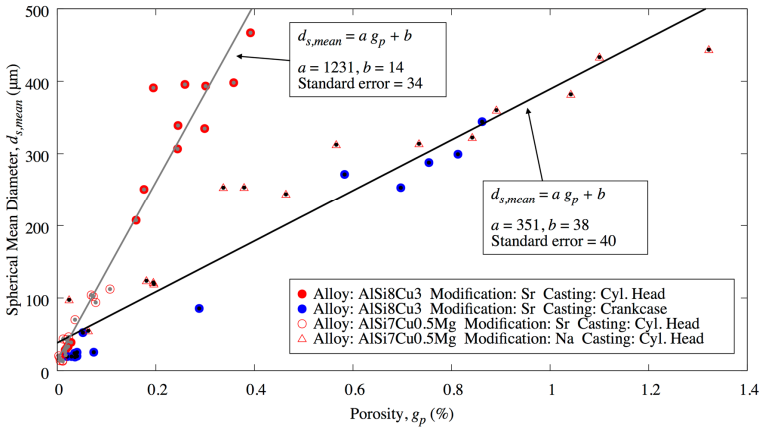


Figure 4-9: Plot of the spherical mean diameter $d_{s,mean}$ versus the average porosity g_p . Two populations are recognisable, the grey population (GP) marked by grey points and fitted by the grey line, and the black population (BP) marked by black points and fitted by the black line (224).

Both populations are fitted by a linear fit function of the respective colour. For the GP the fit function is

$$d_{s,mean} = 1231g_p + 14 \quad \text{(Equation 123)}$$

and for the BP the function is given by

$$d_{s,mean} = 351g_p + 38 \quad \text{(Equation 124)}$$

The slope of the GP is much steeper than the slope of the BP. Although both populations show comparable maximum values of $d_{s,mean}$ (GP: 467 μm ; BP: 444 μm), the maxima are reached at clearly different porosity levels (GP: 0.392 %; BP: 1.322 %). Both BP consists of alloys represent specimen with low and high porosity values. In the case of the GP, only the AlSi8Cu3(Sr) shows this behaviour and the AlSi7Cu0.5Mg(Sr) is only represented with low porosity specimens.

In Figure 4-10 the plot of the maximum spherical diameter $d_{s,max}$ versus the average porosity g_p is displayed. As in Figure 4-9, data is divided into the two characteristic populations GP and BP. Two linear correlations describe the behaviours of the populations well. The GP can be described by

$$d_{s,max} = 2070g_p + 68 \quad \text{(Equation 125)}$$

and BP by

$$d_{s,max} = 517g_p + 107 \quad \text{(Equation 126)}$$

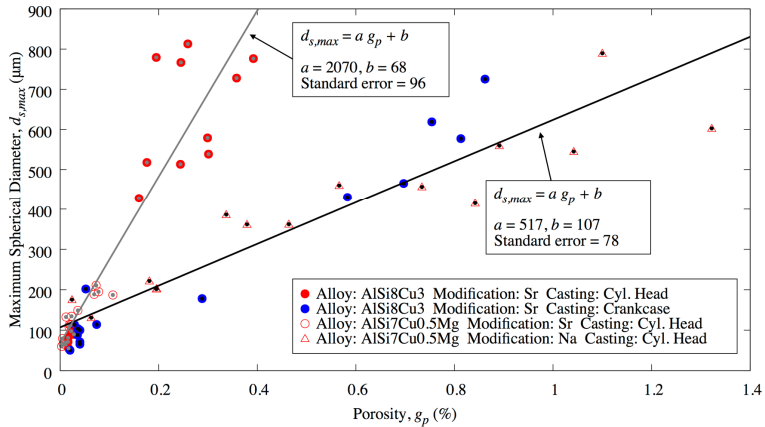


Figure 4-10: Plot of the maximum spherical diameter $d_{s,max}$ versus the average porosity g_p . Two populations are recognisable, the grey population (GP) marked by grey points and fitted by the grey line, and the black population (BP) marked by black points and fitted by the black line [224].

An essential difference between the two plots is that the latter depicts the single maximum value of each specimen. This value is directly correlated to the volume of the single largest pore (by volume). No weighting is applied in Figure 4-10. Again, the maximum values of the GP and the BP are comparable (GP: 813 μm ; GP: 789 μm) but reached at very different porosity levels (GP: 0.259 %; GP: 1.1 %).

In Figure 4-11 the envelope mean diameter $d_{e,mean}$ is plotted against the average porosity g_p , comparable to Figure 4-9. As in both figures above, the GP and BP are clearly distinguishable. Nevertheless, there are differences which should be pointed out. In Figure 4-11 the maximum values of $d_{e,mean}$ of both populations show differences by almost factor two (GP: 2505 μm ; BP: 1426 μm). In general, the measures evaluating the envelope instead of the pore volume are significantly larger, which hints to a pore shape which is quite aspherical, especially for the GP.

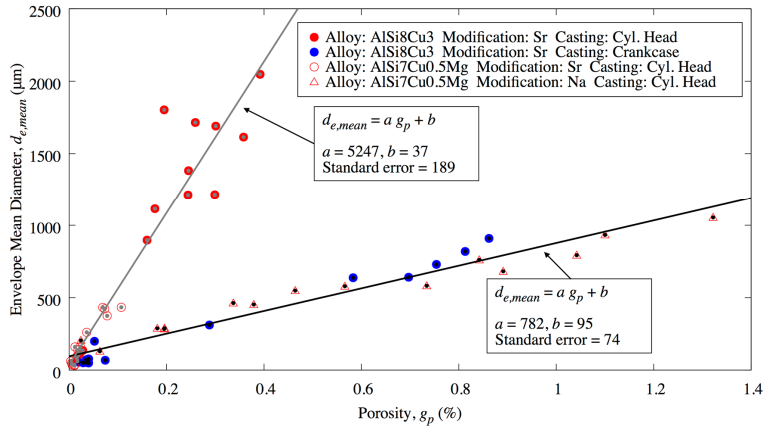


Figure 4-11: Plot of the envelope mean diameter $d_{e,mean}$ versus the average porosity g_p . Two populations are recognisable, the grey population (GP) marked by grey points and fitted by the grey line, and the black population (BP) marked by black points and fitted by the black line (224).

Both specimen populations are again fitted by linear functions quite well. For the GP the fit function is given by

$$d_{e,mean} = 5247g_p + 37 \quad \text{(Equation 127)}$$

and for the BP

$$d_{e,mean} = 782g_p + 95 \quad \text{(Equation 128)}$$

Finally, in Figure 4-12 the plot of the maximum envelope diameter $d_{e,max}$ versus the average porosity g_p is shown. As in all three Figure above, the GP shows a much steeper slope than the BP. This means in all four cases the GP is far more sensitive to changes in porosity than the BP. The maximum envelope diameter $d_{e,max}$ is a direct measure of the defect size in the casting and therefore of high relevance for the prediction of defect size.

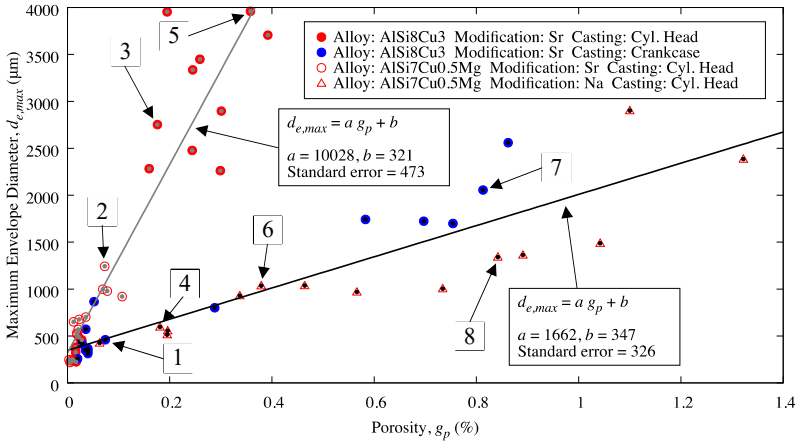


Figure 4-12: Plot of the maximum envelope diameter $d_{e,max}$ versus the average porosity g_p . Two populations are recognisable, the grey population (GP) marked by grey points and fitted by the grey line, and the black population (BP) marked by black points and fitted by the black line (224).

A linear fit is applied to both populations giving

$$d_{e,max} = 10028g_p + 321 \quad \text{(Equation 129)}$$

for the GP and

$$d_{e,max} = 1662g_p + 347 \quad \text{(Equation 130)}$$

for the BP. Note, especially for the GP, the large values for $d_{e,max}$ of almost 4 mm even at relatively low porosity levels of approximately 0.2 %. Additionally, in Figure 4-12 eight specimens are marked for more detailed analysis in the following chapters. The specimens 2, 3, and 5 of the GP and 1, 4, and 6 of the BP have been selected for their comparable porosity level (roughly 0.1 %, 0.2 %, and 0.4 %). They are used in Chapter 4.2.4 to explain significant pore morphological differences. Specimens 7 and 8 are of the BP and also show a comparable porosity level (roughly 0.8 %), yet both exhibit interesting morphological differences which are discussed later.

It is remarkable that in all four previously presented figures and the respective quantities ($d_{s,mean}$, $d_{s,max}$, $d_{e,mean}$ and $d_{e,max}$), two clearly distinguishable trends

are observable. Especially above approximately 0.1 % porosity, the differences become evident. It is noteworthy that both specimen populations consist of both alloys. The BP consists of two production processes and Sr and Na-modified castings. This means that there are significant differences in Cu content (approximately 2.5 wt%) and moderate differences in Si content (approximately 1 wt%) in each specimen population. It can be concluded that the composition differences are not directly responsible for the two observable porosity trends. The only significant characteristic is the increased maximum porosity level of the AlSi8Cu3(Sr) relative to the AlSi7Cu0.5Mg(Sr) for the GP.

The higher porosity level of the first alloy can be explained by several mechanisms. Cu destabilises the eutectic solidification front and leads to a eutectic mushy zone (9). The result is a reduced permeability and earlier pore formation. Moreover Cu, in conjunction with Sr-modification, increases the eutectic cell sizes and thus the size of the liquid pockets which cannot be fed at the end of solidification (10–16). Finally, Cu enlarges the solidification interval (which in turn reduces the feedability at the end of solidification), and the Al₂Cu phase shows a significant volumetric shrinkage of approx. 8.4 vol %, which is difficult to compensate.

Another difference between both alloys is the Fe content. The secondary alloy AlSi8Cu3(Sr) contains approximately 0.3 wt% more Fe compared to the primary alloy AlSi7Cu0.5Mg(Sr). Nevertheless, both alloys contain enough Mn to ensure a favourable formation of α -Al₁₅(Fe,Mn)₃Si₂ instead of β -Al₅FeSi (both show a Mn/Fe ratio of approximately 0.65) and thus to eliminate most of the detrimental effects associated with β -Fe formation (17–26). Villeneuve et al. (24) observed the same amount of porosity in experiments with AlSi6Cu4, once cast with 1.4 wt% Fe and 0.5 wt% Mn and once with 0.37 wt% Fe and 0.05 wt% Mn. Iwahori et al. (23) found for AlSi7Cu3 with 1.15 wt% Fe a reduction in porosity for Mn additions from 0.2 to 0.3 wt% and Dinnis (27) was able to show that the reduces Al-Si nucleation frequency due to Fe additions was again increased after Mn additions. Why only the GP seems to be affected by the differences in Cu content will be discussed in Section 4.2.4, after the porosity morphological differences are presented.

4.2.3. Maximum versus mean diameters

In Figure 4-13 the maximum spherical diameter $d_{s,max}$ is plotted against the spherical mean diameter $d_{s,mean}$. All sixty XCT specimens of the industrial castings are displayed. The data are fitted by a linear function given by

$$d_{s,max} = 1.58d_{s,mean} + 45 \quad \text{(Equation 131)}$$

The variability and scatter increase with increasing average porosity g_p . In contrast to Figure 4-9 to Figure 4-12 all data points can be fitted with one single linear function, and no distinction in two specimen populations is necessary.

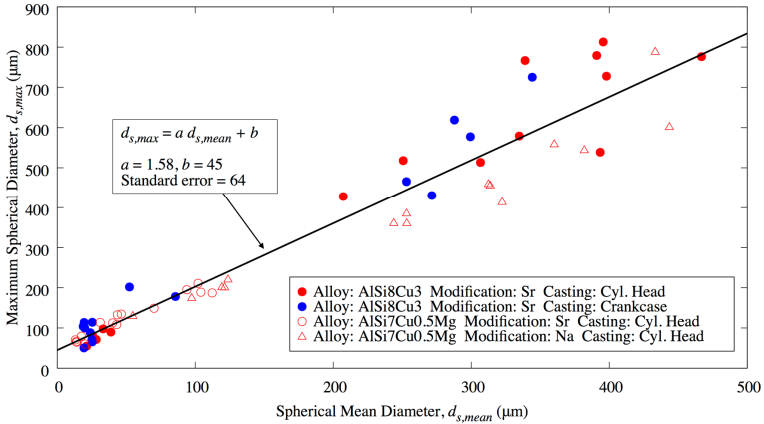


Figure 4-13: Plot of the maximum spherical diameter $d_{s,max}$ versus the spherical mean diameter $d_{s,mean}$. All sixty specimens are plotted. The data is linearly fitted and the result marked by the black line (224).

In Figure 4-14 the plot of the maximum envelope diameter versus the envelope mean diameter is shown. Like in Figure 4-13 all available data is plotted and fitted linearly by

$$d_{e,max} = 1.97d_{e,mean} + 213 \quad \text{(Equation 132)}$$

Again, the quality of the correlation decreases with increasing average porosity level.

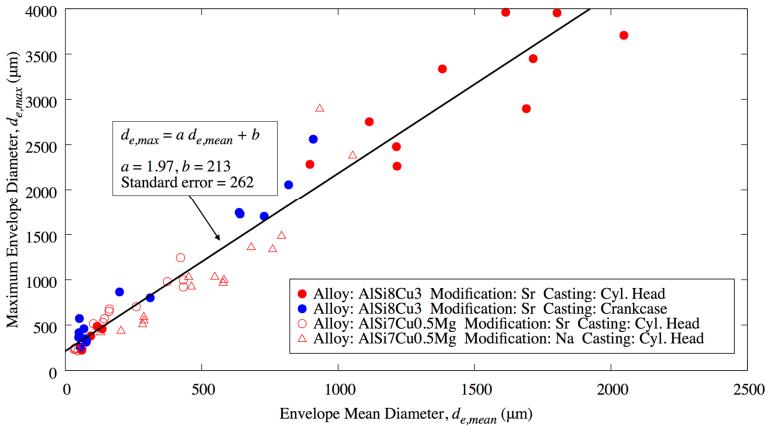


Figure 4-14: Plot of the maximum envelope diameter $d_{e,max}$ versus the envelope mean diameter $d_{e,mean}$. All sixty specimens are plotted. The data is linearly fitted and the result marked by the black line (224).

It is surprising that for all sixty specimens the respective spherical and envelope mean diameter can be linearly correlated with the maximum spherical and envelope mean diameter. The four displayed experimental sets show a significant difference in alloy composition, eutectic modifier, and casting process. This means that if the mean diameter of a pore distribution can be predicted, the prediction of the maximum diameter is (in the limits of the studied parameter field) also possible. Especially the maximum envelope diameter $d_{e,max}$ is of highest significance for the prediction of fatigue properties because it is a measure which indicates the size of the largest defect (225, 226). The presented connection between mean pore volume and maximum pore volume as well as mean pore size and maximum pore size also suggests that the general porosity distribution is behaving similarly for both alloys, both eutectic modifiers and different solidification rates. Keeping in mind the marked effect of Sr or Na modification on solidification morphology and thus on porosity distribution (see Section 2.2.2.7) and the expected differences in pore nucleation stage due to hydrogen precipitation (see Section 2.2.2.3) or shrinkage-driven porosity (see Section 2.2.2.2), the observed trend is remarkable. Although the exact pore size number density distribution cannot be evaluated in this work because the XCT scan resolution was not sufficient to resolve the smallest pores, it seems possible that porosity in comparable aluminium cast alloys always follows a similar type of size distribution.

4.2.4. Pore morphology

Eight characteristic XCT specimens from the industrial castings were selected to discuss the characteristic differences between the observed pore morphologies. Specimens 1 to 8 are marked in Figure 4-12, and their characteristic measures are given in Table 4-2. As stated in Section 4.2.2, specimen pairs 1 and 2, 3 and 4, 5 and 6, and 7 and 8 were selected for their comparable porosity level of 0.1 %, 0.2 %, 0.4 %, and 0.8 %. Although each pair is of a comparable porosity level, specimens 2, 3, and 5 are members of the GP and specimens 1, 4, 6, 7, and 8 are members of the BP. Both show indicative morphological differences.

Specimen 1 (Figure 4-15(a)) exhibits an average porosity of 0.074 %. The pores are very small and of high sphericity. Much of the porosity is located in tiny pores at the XCT resolution limit (approximately 50 % up to equivalent spherical pore diameter of 21 μm). Specimen 2 (Figure 4-15(b)) also exhibits a very low porosity level of only 0.073 %, but the visual impression of this porosity is relatively high (also due to the two-dimensional visualisation of the three-dimensional porosity). The pores are very tortuous and have a relatively large surface area. Even at this low porosity level, the maximum envelope is $d_{e,max} = 1242 \mu\text{m}$. Although both samples show approximately the same amount of porosity, the spatial distribution is significantly different. The difference can also be understood by the already discussed porosity distribution histograms for specimens 1 and 2 (Figure 4-7(a) and (b)).

The appearance of specimen 3 (Figure 4-16(a)) is comparable to specimen 2 (Figure 4-15(b)), but there are pores of higher tortuosity with larger relative surface area due to the higher level of average porosity. Specimen 4 (Figure 4-15(c)) exhibits pores which are not tortuous, but rather round and have a low surface area compared to their volume. Moreover, there are many tiny pores close to the resolution limit of the XCT scan. These can be linked to the low maximum of the porosity distribution histogram presented in Figure 4-7(d). It is noteworthy that although both specimens contain roughly the same amount of porosity, the maximum envelope diameter is dramatically different by more than a factor of 4.5 (specimen 3: $d_{e,max} = 2753 \mu\text{m}$; specimen 4: $d_{e,max} = 593 \mu\text{m}$).

Table 4-2: List of selected XCT specimens with key measurement and porosity data (the DAS was determined as specified by VDG specification P220 (222))

Specimen	Cast part	Position	Alloy	Modification	Spatial XCT Reso- lution (μm)	DAS (μm)
1	Crankcase	Bridge	AlSi8Cu3	Sr	3	17
2	Cylinder head	Camshaft bearing	AlSi7Cu0.5Mg	Sr	3	67
3	Cylinder head	Tween deck	AlSi8Cu3	Sr	8	54
4	Cylinder head	Fire deck	AlSi7Cu0.5Mg	Na	3	30
5	Cylinder head	Camshaft bearing	AlSi8Cu3	Sr	8	58
6	Cylinder head	Tween deck	AlSi7Cu0.5Mg	Na	8	56
7	Crankcase	Stud	AlSi8Cu3	Sr	8	78
8	Cylinder head	Fire deck	AlSi7Cu0.5Mg	Na	3	30

Specimen	Porosity, g_p (%)	Spherical Mean Di- ameter, $d_{s,mean}$ (μm)	Maximum Spherical Di- ameter, $d_{s,max}$ (μm)	Envelope Mean Di- ameter, $d_{e,mean}$ (μm)	Maximum Envelope Diameter, $d_{e,max}$ (μm)	Mean Spheric- ity, ϕ_{mean}
1	0,074	25	114	68	460	0,69
2	0,073	102	211	422	1242	0,43
3	0,176	251	518	1114	2753	0,31
4	0,181	124	222	288	596	0,57
5	0,358	398	728	1614	3961	0,22
6	0,379	253	362	452	1035	0,70
7	0,813	299	577	818	2056	0,44
8	0,842	322	415	760	1341	0,54

(a) (b)

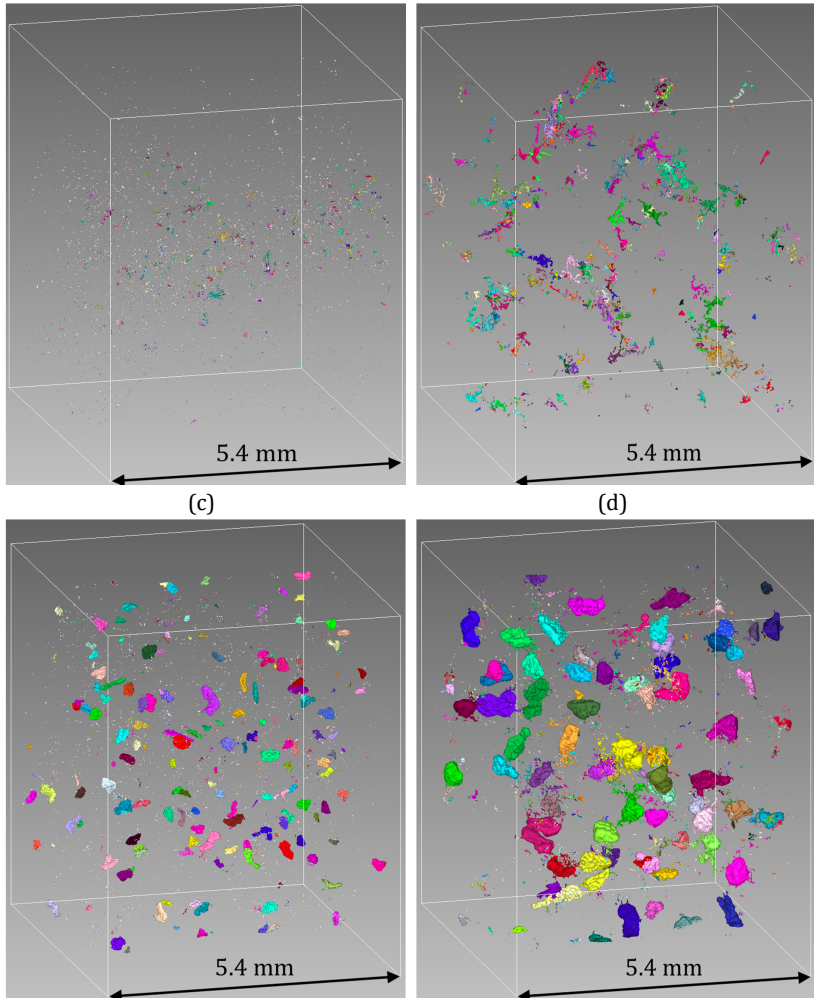


Figure 4-15: Selected XCT-scans performed with 3 μm spatial resolution: (a) Sample 1, crankcase, bridge, AlSi8Cu3(Sr) , $\lambda_2 = 17 \mu\text{m}$, $g_p = 0.074 \%$; (b) Sample 2, cylinder head, camshaft bearing, AlSi7Cu0.5Mg(Sr) , $\lambda_2 = 67 \mu\text{m}$, $g_p = 0.073 \%$; (c) Sample 4, cylinder head, firedeck, AlSi7Cu0.5Mg(Na) , $\lambda_2 = 30 \mu\text{m}$, $g_p = 0.181 \%$; (d) Sample 8, cylinder head, fire deck, AlSi7Cu0.5Mg(Na) , $\lambda_2 = 30 \mu\text{m}$, $g_p = 0.842 \%$ (224)

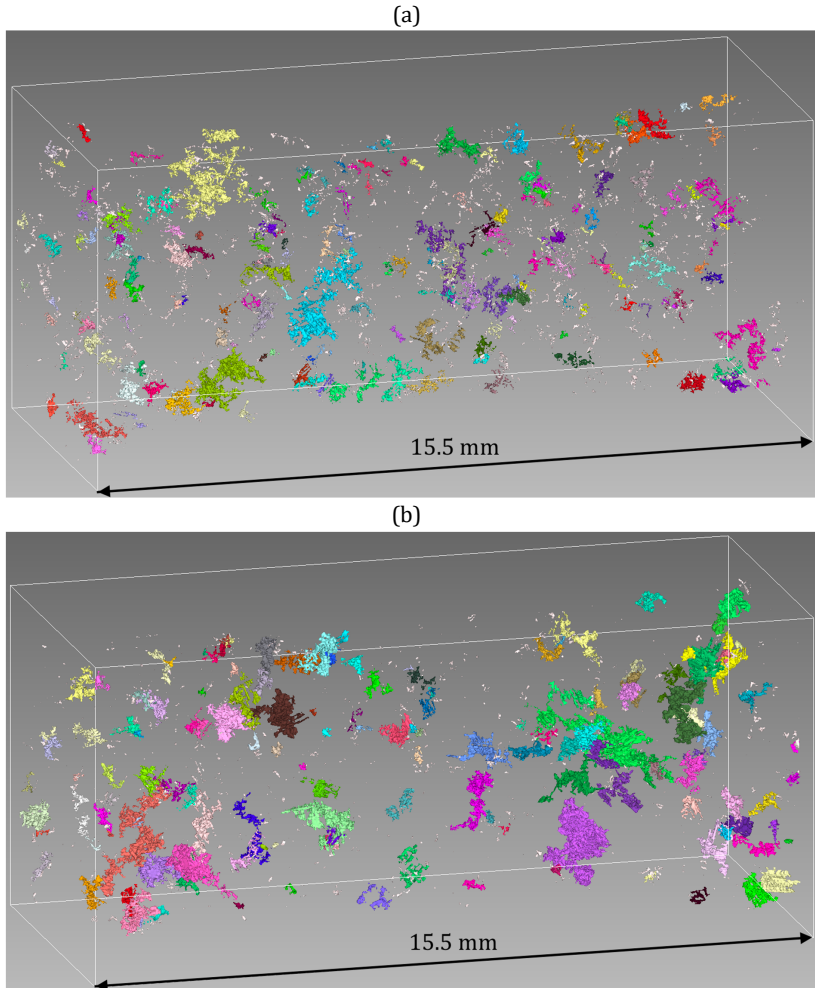


Figure 4-16: Selected XCT-scans performed with $8\ \mu\text{m}$ spatial resolution: (a) Sample 3, cylinder head, tween deck, AlSi8Cu3(Sr) , $\lambda_2 = 54\ \mu\text{m}$, $g_p = 0.176\ \%$; (b) Sample 5, cylinder head, camshaft bearing, AlSi8Cu3(Sr) , $\lambda_2 = 58\ \mu\text{m}$, $g_p = 0.358\ \%$ (224)

The trend described so far is continues if specimens 5 (Figure 4-16(b)) and 6 (Figure 4-17(a)) are compared. Both show an average porosity of approximately 0.37 % and are comparable in their pore characteristic to specimens 3 and 4, respectively. Note that both specimens show a DAS of around 57 μm , but are different regarding their pore characteristic. Pores in specimen 5 are almost plate-like and of highest tortuosity. Specimen 6 shows many high sphericity pores and although both specimens contain approximately the same amount of porosity the maximum envelope diameter differs by almost factor four (specimen 5: $d_{e,max} = 3961 \mu\text{m}$; specimen 6: $d_{e,max} = 1037 \mu\text{m}$).

Specimens 2, 3, and 5 of the GP and specimens 1, 4, and 6 of the BP were presented in order of increasing average porosity. Specimens 7 and 8 (see Figure 4-17(b) and Figure 4-15(d)) again are of a higher porosity level of approximately 0.83 %, but both are members of the BP. The GP does not contain specimen with a porosity level this high. Nevertheless, both specimens show significant pore morphological differences. Specimen 8 is comparable to the other specimen showing primarily high sphericity pores (specimens 4 and 6). Due to the even higher porosity level, the pores are even bigger. Because the microstructure is relatively fine at the same time ($\lambda_2 = 30 \mu\text{m}$), there has been significant impingement of the pore with the surrounding dendrites, and as a result, the pores' surfaces shows the primary aluminium's structure. To form pores of this size, despite the high cooling rates associated with a low DAS, the pores had to form early during solidification. They may even have pushed equiaxed dendrites away to enable their growth to their final size. Specimen 7 shows very distinct features of the crankcase cast in the AlSi8Cu3(Sr) alloy. Specimens with 0.583 % porosity or more show this kind of pore morphology. It is characterised by a mixture of smaller high sphericity pores and bigger tortuous pores, which might be slightly more voluminous than the pores observed in specimens 2, 3, and 5. Only the tortuous pores show clear signs of impingement with the primary aluminium phase. The pore nucleation sequence which produced this type of morphology may be a two-stage process, in which first pore nucleation happens early at a lower solid fraction, but the driving force (probable hydrogen in solution) is not very big. After this first nucleation event, the solidification progresses until a well-developed dendritic network procures liquid pools of the melt which are separated and cannot be fed anymore. Now a second pore nucleation sequence starts and the tortuous pore population nucleates and grows to the final tortuous pore shape. Specimens of this experimental set with 0.288 % porosity or lower do not show this dualistic pore characteristic but only tortuous porosity. It may be an indication that the necessary driving force (probably the necessary hydrogen level) was not reached for early-stage pore nucleation, which means there is probably a

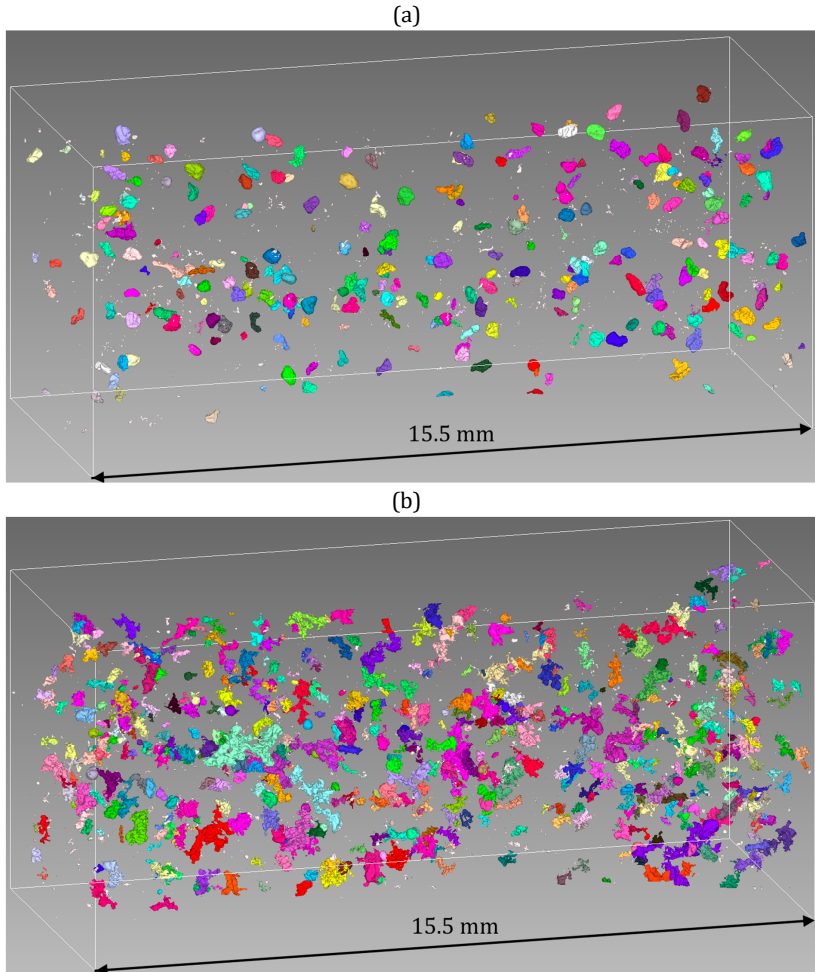


Figure 4-17: Selected XCT-scans performed with $8\ \mu\text{m}$ spatial resolution: (a) Sample 6, cylinder head, tween deck, AlSi7Cu0.5Mg(Na) , $\lambda_2 = 56\ \mu\text{m}$, $g_p = 0.379\ \%$; (b) Sample 7, crankcase, stud, AlSi8Cu3(Sr) , $\lambda_2 = 78\ \mu\text{m}$, $g_p = 0.813\ \%$ (224)

threshold value between 0.288 % and 0.583 % average porosity which determines if “hydrogen porosity” is formed or not. The exact threshold value cannot be determined because there are no crankcase specimens between these two characteristic porosity levels. It should be noted that none of the specimens in the present work showed any signs of a preferential pore shape or an inhomogeneous pore distribution in the evaluation XCT scan volume.

The morphology analysis explains the observed differences between the GP and the BP. Specimens 4, 6, and 8 show pores which had to nucleate early during solidification, so the pores were able to grow to a spherical shape. Concurrently, one can see that the increasing average porosity level and the concomitant increasing pore size leads to an increase of impingement between pore and primary aluminium phase, especially in specimen 8. The dominant driving force in these cases is probably an increased hydrogen level of the melt. All these samples represent the Na-modified experimental set. It is reported in the literature by Thiele (31) and has been observed in experiments by Mulazimoglu et al. (32) that Na additions change the structure of the oxide layer on the aluminium surface and increase its permeability for hydrogen from the atmosphere. The mixed porosity characteristic of the experimental set of the crankcase cast in AlSi8Cu3(Sr) alloy (see Figure 4-17(b)) is probably also related to an elevated hydrogen level, due to the melt handling and melt transfer processes. Although a threshold value seems to exist (between 0.288 % and 0.583 % average porosity) below which no early-stage pores nucleate. The hypothesis that the hydrogen in liquid solution is primarily responsible for the observed pore morphological differences cannot be proven based on the above-presented results. The lack of quantitative hydrogen measurements during the industrial trials does not allow any conclusion on this matter. The extensively rotary degassed experimental sets AlSi8Cu3(Sr) and AlSi7Cu0.5Mg(Sr), both cast in the cylinder head Rotacast® process, do not show any signs of early-stage pore nucleation. In these two cases, it seems plausible to assume that pore nucleation starts very late during solidification and pores have to grow into the well-developed dendritic aluminium phase to increase their volume.

Just as Fang and Granger (101) and further research showed (101, 104–107), there is a clear correlation of an increased porosity with increasing hydrogen level. The amount of porosity increases with lower solidification rate. Fang and Granger also developed a porosity model which is based only on hydrogen dissipation and surface tension (no shrinkage) and were able to show the observed effect of lower solidification rate. The present results can not directly confirm the effect of solidification rate, but there are indications for a comparable mechanism. Since the experimental sets AlSi8Cu3(Sr) and AlSi7Cu0.5Mg(Sr), both cast in the cylinder

head, were well degassed, these two are not considered for evaluation. The AlSi7Cu0.5Mg(Na) crankcase is probably strongly affected by hydrogen pickup, but this uptake probably took place during a more extended period during the crankcase production and was not quantitatively monitored. Consequently, not all produced castings had the same hydrogen content. Therefore, the AlSi8Cu3(Sr) crankcase castings are evaluated more closely. Before the start of the pouring and production sequence, the density index was determined to be 2.4. This value is relatively low, and suggest reasonably low to medium hydrogen levels (42). Nevertheless, there is no direct correlation to the quantitative hydrogen level possible and melt cleanliness is also an important parameter for this quality control method (227). The CPS process shows high reproducibility and is fully automated as a running mass production casting process. Thus, it is assumed that all castings were poured with approximately the same hydrogen content. If the DAS and porosity level are evaluated, one finds 18 μm and 0.046 % in the bridge, 26 μm and 0.085 % in the bearing bracket and 78 μm and 0.742 % in the stud bolt. There is a big "gap" in solidification rate between bridge respectively bearing bracket and stud bolt, but the general trend confirms the presented correlation of solidification rate and porosity level in literature.

Fang and Granger's porosity model (101) also predicts a hydrogen threshold value, below which no gas-induced porosity can form. In the present work, this threshold can also be placed in the region between 0.288 % and 0.583 % porosity for the AlSi8Cu3(Sr) crankcase specimen. As discussed before, it seems reasonable that a certain hydrogen supersaturation has to be reached, before a gas pore can form. Once a hydrogen-induced pore has formed, Carlson et al. (33) show in their model of finite-rate diffusion-limited porosity growth (which also takes into account that the solid reduces the effective hydrogen diffusion to the pore) that porosity is sharply reduced by increasing cooling rate. Carson et al.'s prediction compares well to experimental data, which means that the amount of hydrogen porosity is most probably limited by the time available for hydrogen to diffuse to the pore, and if this time is not available the hydrogen is trapped in solid solution of the aluminium crystal. As stated before, this general trend can be confirmed by the porosity versus DAS trend for the AlSi8Cu3(Sr) crankcase castings presented in this work.

4.2.5. Sphericity

The mean sphericity φ_{mean} is calculated for every specimen to quantify the pore morphological observations made in Section 4.2.4. It is shown in Figure 4-18 plotted against the average porosity g_p . Pores for which the determination of the surface area or the pore volume was not possible, or which were calculated to have a mean sphericity higher than unity, were excluded from the data. This unphysical behaviour is primarily observed for small pores if the algorithm for the surface and volume determination stops working properly due to XCT scan resolution limits. As in Figure 4-9–Figure 4-12, the four experimental sets are divided into the same two characteristic populations, the GP, and the BP. For both, a correlation with three constants is developed. For the GP the function is given by

$$\psi_{mean} = \frac{0.08}{1 - 0.9e^{-1.09g_p}} \quad \text{(Equation 133)}$$

and for the BP by

$$\psi_{mean} = \frac{0.56}{1 - 0.59e^{-29.94g_p}} \quad \text{(Equation 134)}$$

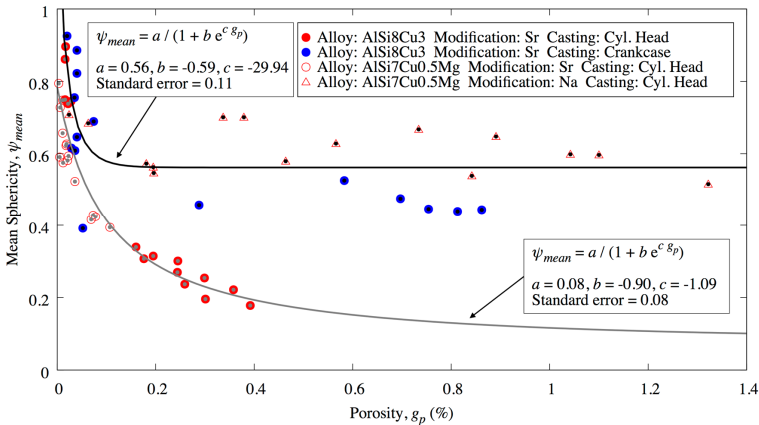


Figure 4-18: Plot of the mean sphericity versus the porosity. Grey points mark the points considered in the grey population correlation; black points are used in the black population correlation. The sphericity of the black-marked specimens approaches 0.56 at higher porosity values. The sphericity of the grey-marked specimen behaves differently and approaches a lower value of 0.08 as porosity increases (224).

The BP fits the experimental results of the AlSi8Cu3(Sr) crankcase and AlSi7Cu0.5Mg(Na) cylinder head. Specimens 1, 4, 6, 7 and 8 are members of this population. At 0.01 % porosity, the function runs towards the limit unity. Above 0.2 % porosity, the sphericity becomes constant at 0.56. The grey curve fits the specimens of the experimental sets AlSi8Cu3(Sr) cylinder head and AlSi7Cu0.5Mg(Sr) cylinder head. Specimens 2, 3, and 5 are members of this population. If the porosity runs towards 0, the sphericity runs towards 0.8. For the maximum porosity of about 0.4 % in this population, the sphericity drops to 0.2, and theoretically to the constant value of 0.08.

Both functions show high sphericity values at low average porosity levels. The BP keeps a high sphericity even at high porosity, which demonstrates that even large pores like in specimens 4 (Figure 4-15(c)), 6 (Figure 4-17(a)), and 8 (Figure 4-15(d)) exhibit a highly spherical shape. The mean sphericity values of the AlSi8Cu3(Sr) crankcase are slightly lower compared to the AlSi7Cu0.5Mg(Na) cylinder head specimens, which means the limiting value of the first would be slightly lower compared to the second. This observation is consistent with the dualistic porosity character (Figure 4-17(b)), of the AlSi8Cu3(Sr) crankcase as described before. The mean sphericity of the GP continuously decreases with increasing porosity. The pores are only able to grow into the solid dendritic network, and their surface area increases more strongly than that of a volume equivalent sphere.

The observed pore morphology presented before in Section 4.2.4 is well described by the presented Figure 4-18. In specimens with low porosity, the pores have enough space to grow, and impingement between pores and the solid phase hardly takes place. Moreover, these pores are primarily in contact with the eutectic phase, which is the only possible conclusion if impingement is not dominant. Felberbaum et al. (28) show that pores which are in contact with the eutectic show positive mean curvatures to satisfy the Laplace-Young equation, which is in agreement with the presented results. In general, for very small pores the driving force to minimise the surface energy results in highly spherical pores. This effect becomes less dominant the bigger a pore becomes. For both populations, the sphericity decreases with increasing porosity, which can be explained by an increasing pore-solid impingement. The effect is limited in case of the presumably gas-induced porosity due to its earlier nucleation, so impingement happens later and only if the hydrogen level is sufficiently high (BP). As Murphy et al. showed (29) in solidification experiments with a grain-refined AlCu20 alloy at low cooling rates, these spherical pores may even be able to push equiaxed crystals away to increase their individual space to grow unhindered while maintaining their spherical shape. The result is a relatively constant mean sphericity even at high average porosity levels. The observed behaviour also corresponds to the work of Puncreobutr et al. (30) with an in-situ observation of

the growth of an individual pore. They observed a pore's growth and found a sphericity drop from about 0.83 to 0.6 between nucleation and a pore volume of 0.025 mm³ ($d_s = 363 \mu\text{m}$). Afterwards, the sphericity was observed to be constant at 0.6 up to a pore volume of and 0.054 mm³ ($d_s = 469 \mu\text{m}$). This pore size is equivalent to a medium-sized high sphericity pore in the present work and is very close to the constant sphericity of 0.56 for the BP for specimens of 0.2 % porosity or more. Moreover, the initial sphericity value in Puncreobutr et al.'s work of 0.83 corresponds well with the limiting value of the GP of 0.8 if the grey fit function is extrapolated towards zero. Probably, the high mean sphericity values of the AlSi8Cu3(Sr) crankcase specimens are also associated with an increased hydrogen level, which might be introduced by the production process (CPS). The level of the average porosity is the key factor for both specimen populations, which determines the mean sphericity. Nevertheless, g_p itself may be primarily affected by the chemical composition, eutectic modification, Fe-phases or solidification rate.

4.2.6. Prediction of the pore size distribution

It was shown in Chapter 4.2.2 that there are linear correlations between average porosity g_p and the four introduced characteristic measures $d_{s,mean}$, $d_{s,max}$, $d_{e,mean}$, $d_{e,max}$ for both identified specimen populations (GP, BP). In Chapters 4.2.4 and 4.2.5, it was shown that there are fundamental pore morphological differences which distinguish both populations. This chapter aims to demonstrate that the characteristic measures can be calculated by the average porosity and the mean sphericity. If this is true, it is a strong indication that the mean sphericity and average porosity are key parameters for predicting the pore size distribution. Functions based on these two parameters were developed and are presented in the following section. In the plots, the blue diagonal line indicates ideal agreement between the prediction and measurement. The given standard error is used to assess the quality of the respective prediction.

In Figure 4-19 the plot of the calculated spherical mean diameter versus the measured spherical mean diameter is shown. The function which has been used is given by

$$d_{s,mean}^{cal} = \frac{g_p \psi_{mean}}{-5.48 \times 10^{-4} + 9.78 \times 10^{-4} g_p + 1.92 \times 10^{-3} \psi_{mean}} \quad \text{(Equation 135)}$$

Prediction and measurement correlate well, which means the spherical mean diameter is not only correlated with the average porosity (as shown in Section 4.2.2), but also with the pore morphology, represented by the mean sphericity. By usage of ψ_{mean} it is possible to collapse both trend lines describing the GP and BP behaviour in Figure 4-9.

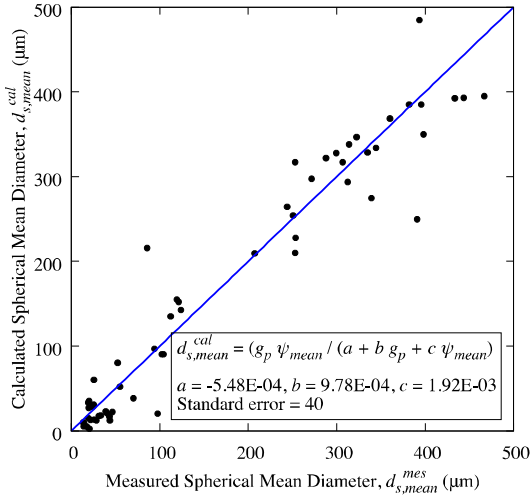


Figure 4-19: Plot of the calculated spherical mean diameter versus the measured spherical mean diameter (224).

Analogously, in Figure 4-20 the calculated maximum spherical diameter is plotted against the measured maximum spherical diameter. Again, a good correlation is apparent. The used function for calculating the maximum spherical diameter is given by

$$d_{s,max}^{cal} = 908 + 748g_p - 2289\psi_{mean} - 262g_p^2 + 1530\psi_{mean}^2 \quad \text{(Equation 136)}$$

It was possible to collapse both linear trend lines shown in Figure 4-10. The scatter between prediction and measurement increases with increasing pore size.

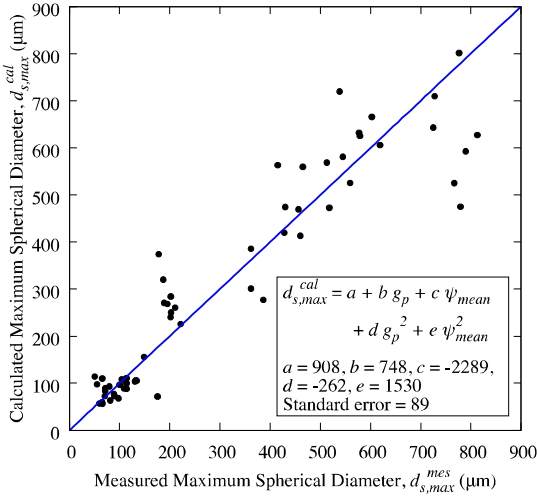


Figure 4-20: Plot of the calculated maximum spherical diameter versus the measured maximum spherical diameter (224).

In Figure 4-21 the calculated envelope diameter is plotted against the measured envelope diameter. The function to calculate the characteristic measure is given by

$$d_{e,mean}^{cal} = 2819 + 924g_p - 7902\psi_{mean} - 247g_p^2 + 5533\psi_{mean}^2 \quad \text{(Equation 137)}$$

Again, the correlation is good and of comparable quality as the two correlations presented before. The pore morphology, described by the parameter mean sphericity, is the critical parameter to predict the envelope mean diameter.

Finally, in Figure 4-22 the calculated maximum envelope diameter is plotted versus the calculated envelope diameter. The applied function is

$$d_{e,max}^{cal} = 5726 + 1109g_p - 14721\psi_{mean} + 212g_p^2 + 9835\psi_{mean}^2 \quad \text{(Equation 138)}$$

The quality of the correlation is good, and it was possible to collapse both trend lines of the GP and the BP (see Figure 4-12).

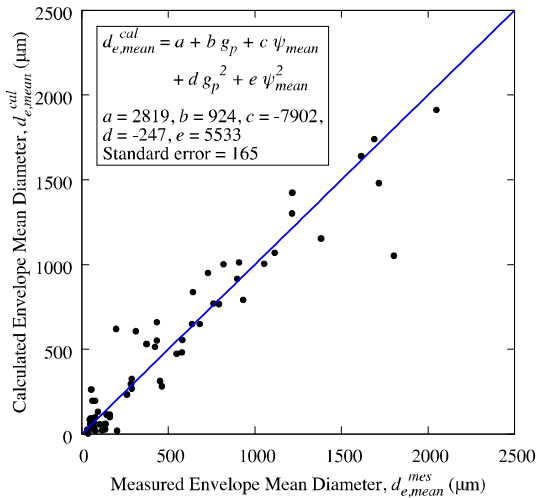


Figure 4-21: Plot of the calculated envelope mean diameter versus the measured envelope mean diameter (224).

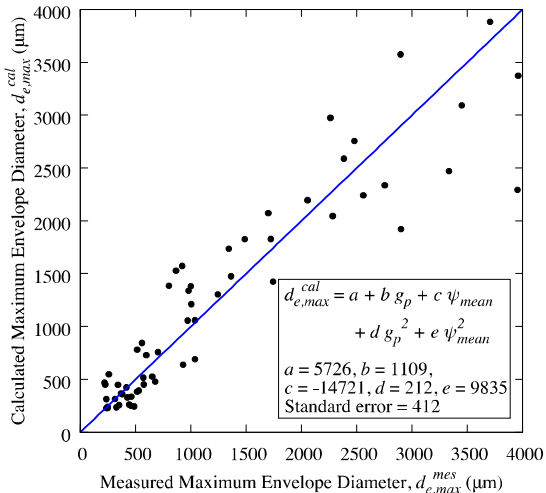


Figure 4-22: Plot of the calculated maximum envelope diameter versus the measured maximum envelope diameter (224).

For the analysed alloying system and under the condition that the local amount of average porosity and the mean sphericity is known (by measurement of perdition), all four characteristic quantities describing the pore size distribution can be calculated with reasonable accuracy. The four quantities describe the distribution

mean ($d_{s,mean}$ and $d_{e,mean}$) as well as the distribution maximum ($d_{s,max}$ and $d_{e,max}$) regarding the pore volume and the spatial pore dimensions, respectively. A critical parameter which is missing until this point is the connection between the hydrogen level of the melt and the mean sphericity of a given specimen. It might even be possible to predict the mean sphericity based on the gas content but to establish this link further experiments are needed.

The maximum defect size is the most important parameter determining the fatigue life behaviour of aluminium cast parts (1–6). A simple correlation is presented to predict this crucial parameter of microporosity.

4.2.7. Summary

A total of 60 XCT specimens were analysed from two industrial aluminium castings. The whole span of typical solidification ranges of an industrial permanent mould, as well as sand mould process, were covered. Two alloys, AlSi8Cu3 and AlSi7Cu0.5Mg, were cast, two different eutectic modifiers were used and two castings, a cylinder head and a crankcase were produced. From each casting specimens from three positions of different solidification time were extracted, scanned, and evaluated.

In the case of the AlSi7Cu0.5Mg(Sr) cylinder head castings with a very low amount of porosity, most of the specimen's porosity is comprised of the smallest pores. For higher porosity samples, the majority of the porosity is located in the medium-sized pores. The AlSi8Cu3(Sr) crankcase castings show similar behaviour, but the transition between both characteristic distributions is shifted to slightly higher porosity values. The AlSi7Cu0.5Mg(Na) cylinder head castings show a transition stage in pore volume distribution. Low porosity samples show a porosity distribution with its maximum in the smallest or medium-sized pore size bins. Higher porosity specimens have their distribution maximum in the largest bins. In-between a bimodal porosity distribution can be observed for some specimens. The observation suggests that the volume deficit can, to a large extent, be compensated by early formation of pores which continue to grow. The driving force to nucleate small pores in the final stage of solidification is sharply reduced. The results further suggest a destabilisation of the eutectic front with increasing Cu additions and thus an increased number of liquid, unfeedable melt pools at the end of solidification.

The XCT scanning resolution strongly affects the number density in the evaluations. Therefore, a volume-weighted approach is chosen, which allows the direct comparison of sample characteristics, almost independently of scanning resolution.

In general, maximum pore volume and size, as well as mean pore volume and size can be divided into two characteristically different experimental groups. The first shows a much stronger sensitivity of the pore distribution characteristics to the

general porosity level than the other. This separation into two specimen groups is independent of the alloy, modification, or process type. Moreover, a linear correlation between the mean pore volume and the maximum pore volume as well as the mean pore dimensions and the maximum pore dimensions is established, which enables the prediction of one of the two characteristic values if the other is known. Especially the maximum pore dimension in a certain cast alloy volume is of the highest value for the fatigue proof design of cyclically loaded components.

An analysis of the pore morphology reveals significant differences in pore shape. In samples of the first specimen group, highly tortuous pores dominate. These can be, relative to the total porosity of the specimen, very large. In samples of the second specimen group, it is shown that pores of higher sphericity dominate, especially at higher porosity levels. The AlSi8Cu3(Sr) crankcase castings show a special behaviour, a tortuous and spherical porosity characteristic, which points at a two-stage (early and late-stage) pore nucleation mechanism. In summary, the hydrogen level of each sample seems most likely to determine which characteristic porosity behaviour can be observed.

The two identified experimental specimen groups can also be divided by their sphericity-porosity characteristic. The first, more sensitive, probably shrinkage-related specimen group, shows a continuous drop in mean sphericity from a high sphericity value with increasing porosity to about 0.2 at 0.4 % porosity. The second, probably hydrogen-related population, also drops from a high sphericity value but to a constant sphericity value of 0.56. This mean sphericity trend is kept up to the highest observed porosity levels of about 1.3 %. This observation confirms the pore-morphological observations.

Finally, the four characteristic pore-distribution measures are predicted based on the average porosity and the mean sphericity of each specimen. This prediction works with good accuracy as it is tested against the experimental data. A missing key parameter is a possible link between the hydrogen level of a sample and its mean sphericity. The mean sphericity seems to be a central porosity characteristic which could be used to determine the general behaviour of the porosity-pore distribution characteristic.

Since the maximum defect size, one of the predicted measures, is of paramount importance for the development of new fatigue-resistant cast components, the presented findings have the potential to improve the design process significantly.

4.3. Wedge casting experiments

Based on the findings presented in Section 4.2 on the results of the industrial castings, the wedge casting experiments are conducted. The aim is to investigate the

effect of hydrogen on the amount of porosity as well as the pore distribution in the form of the previously introduced characteristic measures. In the controlled environment of an experimental foundry, twelve wedge castings were produced, which were developed to reproduce the microstructures of the industrial castings as closely as possible. Two alloys were cast, the AlSi8Cu3 and the AlSi7Cu0.5Mg, both Sr-modified and grain refined and as close to the chemical composition of the alloys used in the industrial castings as possible.

A total of 36 XCT specimen were analysed. Table 4-3 gives an overview of the minimum and maximum values of the characteristic quantities used to describe the pore distributions.

Table 4-3 Summary of the minimum and maximum characteristic quantities of the wedge castings representing the pore distribution characteristic (the DAS was determined as specified by VDG specification P220 (222))

	DAS, λ_2 (μm)	Porosity, g_p (%)	Spherical Mean Diameter, $d_{s,mean}$ (μm)	
Min	17	0.029	69	
Max	96	3.097	948	
	Maximum Spherical Diameter, $d_{s,max}$ (μm)	Envelope Mean Diameter, $d_{e,mean}$ (μm)	Maximum Envelope Diameter, $d_{e,max}$ [μm]	Mean Sphericity, ϕ_{mean}
Min	142	172	632	0.25
Max	1220	1967	3224	0.83

As can be seen from the λ_2 values, the castings cover a broad range of cooling rates. The total amount of porosity also varies significantly. The smallest maximum envelope diameter of all specimens of the wedge castings is 632 μm and therefore still large enough to represent a highly fatigue relevant defect (2–6, 223).

4.3.1. Hydrogen adjustment and measurement

As described in Section 3.3, two experimental sets of wedge castings were produced with the alloys AlSi8Cu3 and AlSi7Cu0.5Mg. Both are very similar to the alloys used in the industrial castings and were supplied by the industrial foundry where the castings shown in the previous section were produced. The goal was to produce wedge castings with controlled variations in hydrogen content (three levels for each alloy) and investigate the effects on the local amount of porosity as well as the pore size distribution characteristics. Figure 4-23 shows an overview of the first experimental set conducted with the alloy AlSi8Cu3 (see Section 3.3 for detailed chemical

analysis). Six wedge castings were produced, where two castings were poured at a certain experimental condition. Additionally, quantitative hydrogen measurements by the HYCAL measurement system were conducted. During the first experimental set four RPT tests, comprised of four RPT sample pairs were produced. The RPT samples were taken directly after the wedges were poured (the third RPT sample pair was taken in between the wedges 3 and 4 and wedges 5 and 6). Figure 4-24 and Figure 4-25 show the four sectioned RPT samples solidified under atmospheric pressure (a, c) and the four sectioned RPT samples (b, d) solidified at reduced pressure. Additionally, Figure 4-24 and Figure 4-25 give the density index determined for each sample pair (a, b) and (c, d).

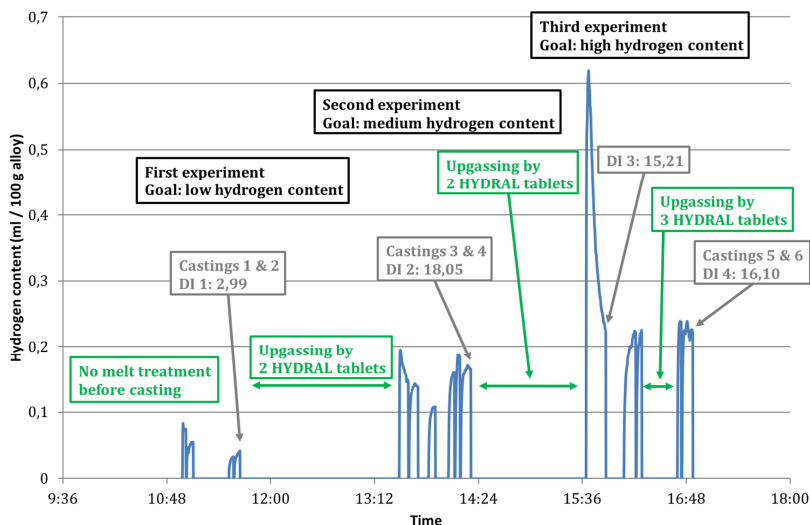


Figure 4-23: Overview of the experimental procedure of the first experimental set conducted with AlSi8Cu3. The HYCAL hydrogen measurement is plotted over time. The melt treatment procedures are indicated, as are the wedge castings and the RPT tests by DI. The goal was to produce three different hydrogen levels, a low one below 0.1 ml / 100 g Al, a medium one of approximately 0.2 ml / 100 g Al, and a high one of approximately 0.3 ml / 100 g Al.

The first two wedges 1 and 2 (indicated by “First experiment” in Figure 4-23) were cast without any addition or removal of hydrogen by tablet treatment. The quantitative hydrogen measurement by the HYCAL system gave a reading of 0.040 ml / 100 g Al. The density index of the RPT sample (DI 1) was found to be 2.99 (see

Figure 4-24(a, b)). The first sectioned RPT sample of DI 1 solidified at ambient pressure (Figure 4-24(a)) shows very little distributed porosity and some tortuous concentrated porosity in the hot spot region, in total 2.55 %. Its top surface is flat. The sample of DI 1 which solidified at reduced pressure (Figure 4-24(b)) displays distributed tortuous pores except for the material in the edge area of the sectioned surface. The RPT sample has a flat surface, which indicates a low hydrogen level. After the addition of 2 HYDRAL 40® tablets, the hydrogen reading increased to 0.165 ml / 100 g Al and the density index of DI 2 increased to 18.05 (Figure 4-24(c, d)). The second set of RPT samples (DI 2) show significantly different porosity behaviour compared to the first set. The sectioned sample which solidified under atmospheric pressure (Figure 4-24(c)) exhibits dispersed isolated pores throughout the sample, in total 3.27 % porosity. The pores do not seem to be connected but are individual pores of high volume to surface ratio. The sample's surface is flat. The sample which solidified at reduced pressure (Figure 4-24(d)) displays significantly larger pores. These large pores are distributed throughout the sample, and the dendritic structure becomes recognisable on the inside of the sectioned pores. In between the large pores, many small, tortuous pores are visible. The overall visual impression of the material between the large pores is almost sponge-like, in any case highly porous. The sample's top surface solidified in a "mushroom" shape. After the addition of two more HYDRAL 40® tablets, the third set of RPT samples (DI 3) was taken (Figure 4-25(a, b)). The hydrogen level was measured but was judged to be too low to cast the next wedge castings. The RPT sample of DI 3 which solidified at ambient pressure (Figure 4-25(a)) shows a comparable qualitative porosity characteristic as the previous sample of DI 2 (Figure 4-24(c)) and in total 4.36 % porosity. The sample of DI 3 which solidified at reduced pressure (Figure 4-25(b)) again shows a porosity characteristic comparable to the previous sample (DI 2) which solidified at reduced pressure (Figure 4-24(d)). The density index yielded 15.21. Finally, in the last experiment of the first experimental set another three HYDRAL 40® tablets were added to increase the hydrogen level even further. The HYCAL system gave a reading of 0.224 ml / 100 g Al and the density index of DI 4 was determined to be 16.10 (Figure 4-25(c, d)). Again, the visual impression of the sectioned fourth pair of RPT samples (Figure 4-25(c, d)) is comparable to the second (Figure 4-24(c, d)) and third (Figure 4-25(a, b)), possibly the amount of distributed tortuous pores in the areas between the large pores may be slightly higher. The fourth RPT sample (DI 4) which solidified under atmospheric pressure contained 2.91 % porosity.

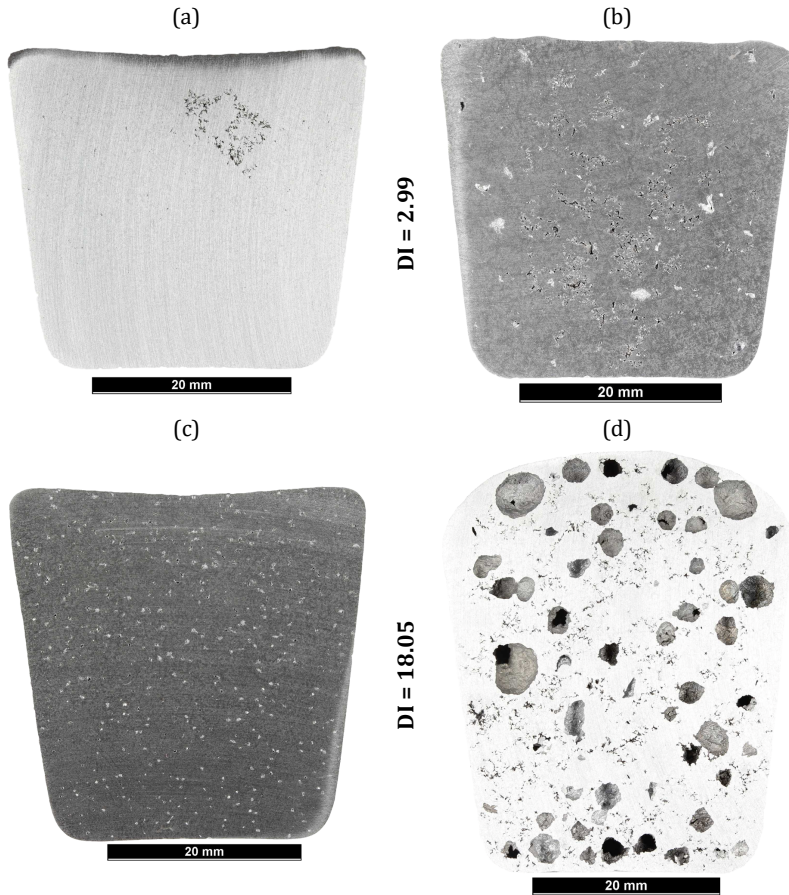


Figure 4-24: Sectioned reduced pressure test (RPT) sample pairs DI 1 and DI 2 of the first experimental set. RPT sample pair DI 1: (a) solidified under atmospheric pressure ($g_p = 2.55\%$) and (b) at reduced pressure. The density index (DI) of sample pair DI 1 is 2.99. RPT sample pair DI 2: (c) solidified under atmospheric pressure ($g_p = 3.27\%$) and (b) at reduced pressure. The density index of sample pair DI 2 is 18.05.

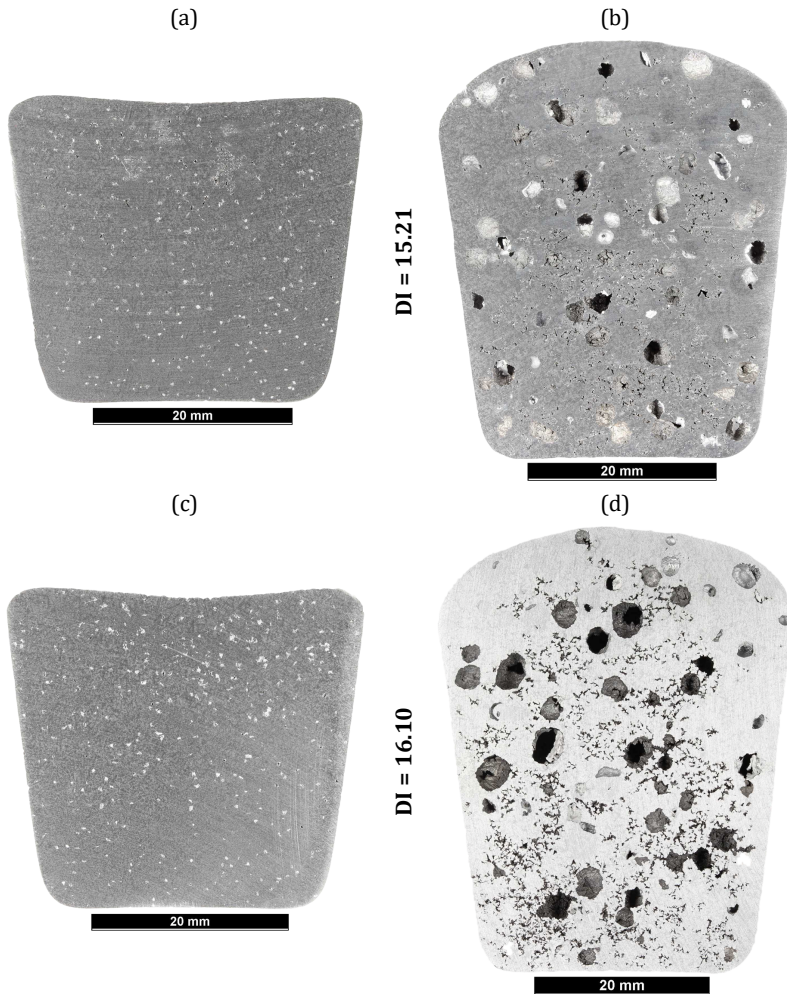


Figure 4-25: Sectioned reduced pressure test (RPT) sample pairs DI 3 and DI 4 of the first experimental set. RPT sample pair DI 3: (a) solidified under atmospheric pressure ($g_p = 4.36\%$) and (b) at reduced pressure. The density index of sample pair DI 3 is 15.21. RPT sample pair DI 4: (c) solidified under atmospheric pressure ($g_p = 2.91\%$) and (d) at reduced pressure. The density index of sample pair DI 4 is 16.10.

As can be seen from the HYCAL measurements throughout the whole experimental set, the measurement is not as reproducible as was expected based on the technical information provided by Mr Henson from EMC, the supplier company of the HYCAL system (228). The HYCAL system should give highly reproducible hydrogen readings in consecutive measurements. In-between each measurement the reading can be refreshed by inert gas purging. After a specific time to reach an equilibrium partial pressure in the probe the same hydrogen level should be measured. This lack of reproducibility may be caused by the melt treatment by tablets itself. After the experiments, Mr Henson confirmed similar reproducibility problems of the HYCAL system if tablets are used (228). During the addition of a HYDRAL 40® tablet, a strong chemical reaction is releasing hydrogen. The released gas bubbles are relatively large, which might impede an effective upgassing process because the bubble surface in contact to the melt is relatively small. Moreover, the chemical reaction burns off elements like Mg and Sr. Chemical analysis samples taken directly before casting each batch of wedges showed a change in Mg level from 0.26 to 0.24 to 0.20 wt% and a change in Sr level from 0.018 to 0.021 to 0.007 wt% (note that about 100 ppm of Sr were always added after tablet treatment and before chemical analysis and casting). Although the changes in Mg concentration are not substantial, since magnesium increases the hydrogen solubility of the molten aluminium (178), the change might be significant for the hydrogen measurement (which was calibrated to the chemical composition at the start of the experiment). Korol'kov (205) showed a pronounced decrease of the surface tension of aluminium (approx. up to 24 %) for Mg additions up to 1 wt%. Moreover, changes in the Sr level might also lead to a change in surface tension, as proposed by some publications (145, 147) but contradicted by others (101, 148). If and how a change in surface tension could affect the HYCAL measurement is not clear at this point. Besides, the permeability of the oxide skin, which might be changed due to an altered Sr level (145, 147), could also play a role in a dynamic hydrogen measurement and reduce or extend the time for a constant, reliable reading.

The first pair of RPT samples DI 1 (Figure 4-24(a, b)) is clearly distinguishable from the following three pairs DI 2 to 4 (Figure 4-24(c, d) and Figure 4-25(a-d)). The relatively low density index of the first experiment (DI 1) is consistent with the low hydrogen reading by the HYCAL device. Following the major increase of the density index and change in RPT sample appearance after the first HYDRAL 40® addition, further upgassing by HYDRAL 40® tablets made no significant difference to the density index and the appearance of the RPT samples. From DI 2 (Figure 4-24(c, d)) to DI 3 (Figure 4-25(a, b)), the density index even decreased from 18.05 to 15.21 although two tablets were added in between both tests. After the immersion of another three HYDRAL 40® tablets, the density index of the fourth RPT test (DI 4) again

increases to 16.10 (Figure 4-25(c, d)). The flat sample surface of DI 1, which solidified at reduced pressure (Figure 4-24(b)), and the “mushroom” top shape of DI 2 to 4, which solidified at reduced pressure (Figure 4-24(d) and Figure 4-25(b, d)), are consistent with observations by Campbell (42) that increasing hydrogen levels yield a continuously increasing pore fraction in RPT samples. Assuming a gas-pressure-pore-volume relationship following the ideal gas law, the porosity in the RPT sample, which solidifies at reduced pressure doubles if the amount of hydrogen in solution is doubled or the pressure is reduced by half. Unlike in Campbell’s observations, there is not a continuous change in density index, which may be because only two characteristic hydrogen levels were achieved (three were originally intended). This contradicts the general trend of the HYCAL readings, which show a change in hydrogen level from 0.040 to 0.165 ml / 100 g Al after the first melt treatment (2 HYDRAL 40® tablets) and from 0.165 and 0.224 ml / 100 g Al after the second treatment (in total 5 HYDRAL 40® tablets). A possible explanation for this behaviour is that the RPT and thus the density index is not capable of resolving very high hydrogen levels above a certain value. This explanation is consistent with observations from foundry practice of bubbles escaping from the surface of high hydrogen RPT samples while solidifying at reduced pressure. This escape of hydrogen must result in a loss of available gas to inflate the specimen even further; thus, the “density index” method reaches its limits. Another possible explanation could be that the introduction of hydrogen becomes less and less efficient or not even feasible by HYDRAL 40® tablets. Although the exact level of the hydrogen partial pressure in the released reaction gases is unknown and thus the equilibrium hydrogen level achievable by tablet additions cannot be determined (by Sievert’s law, see (Equation 83)), it can be assumed that the pickup of hydrogen is reduced as the hydrogen level rises. This decrease in upgassing efficiency must be the case since the hydrogen pickup is the balance of the vaporisation of hydrogen in solution and the dissolution of gaseous hydrogen in the melt, with the first term increasing during the up-gassing process. The observable reaction during HYDRAL 40® tablet treatment can be described by a very strong initial release of gas after submersion. This strong initial reaction is reduced within a couple of minutes, whereafter a relatively constant stream of gas is still released up to 10 to 15 minutes. Throughout the treatment process, the released gas bubbles appear relatively large, which would mean that the available surface for hydrogen transfer from gas to the melt is limited. After the reaction, the remainder of the burned off tablet floats to the melt surface and can be removed as a whole. The amount of dross produced, which has to be removed afterwards, is very limited.

In the second experimental set, another six wedge castings were produced. The alloy AlSi7Cu0.5Mg was cast, also as close as possible to the chemical analysis of the industrial casting experiments. In Figure 4-26 the development of the HYPAL measurement during the experimental procedure of the second experimental set is shown. In contrast to the first experimental set where the hydrogen level was only raised by HYDRAL 40® tablets, the second experimental set started with a targeted medium hydrogen level of about 0.2 ml / 100 g Al. Next, a low hydrogen level (target <0.1 ml / 100 g Al) for the second experiment was intended by degassing with the immersion of NITRAL 10® tablets. The last experiment of the second set of experiments involved raising the hydrogen content to a high level above 0.3 ml / 100 g Al.

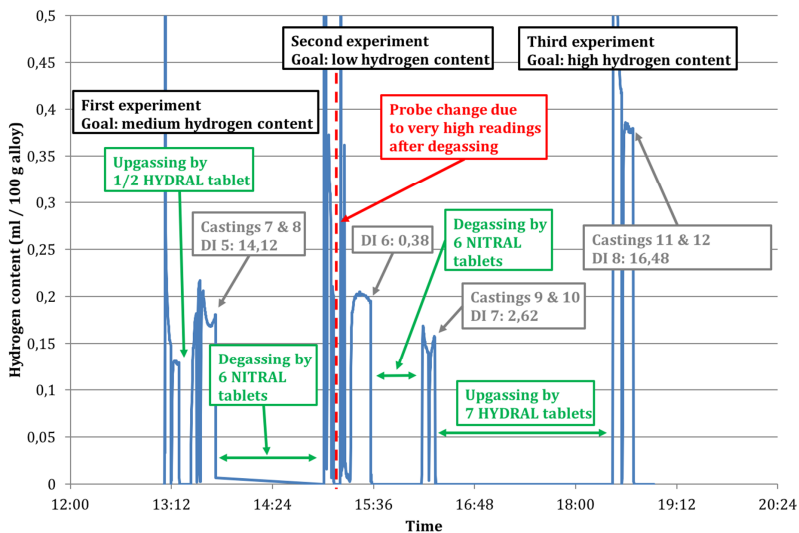


Figure 4-26: Overview of the experimental procedure of the second experimental set conducted with AlSi7Cu0.5Mg. The HYPAL hydrogen measurement is plotted over time. The melt treatment procedures are indicated, as are the wedge castings and the RPT tests DI 5 to DI 8. The goal was to produce three different hydrogen levels, a low one below 0.1 ml / 100 g Al, a medium one of approximately 0.2 ml / 100 g Al, and a high one of approximately 0.3 ml / 100 g Al.

RPT test (DI 5 to 8) were done four times during the second experimental set. The sectioned RPT samples and the resulting density index are shown in Figure 4-27 and Figure 4-28. DI 5 (Figure 4-27(a, b)), DI 7 (Figure 4-28(a, b)), and DI 8 (Figure 4-28(c, d)) were done directly after each pair of wedge castings were poured.

(Figure 4-27(c, d)) was done after the first two wedge castings of the second experimental set, the immersion of six NITRAL 10[®] tablets and the change of the HYCAL probe.

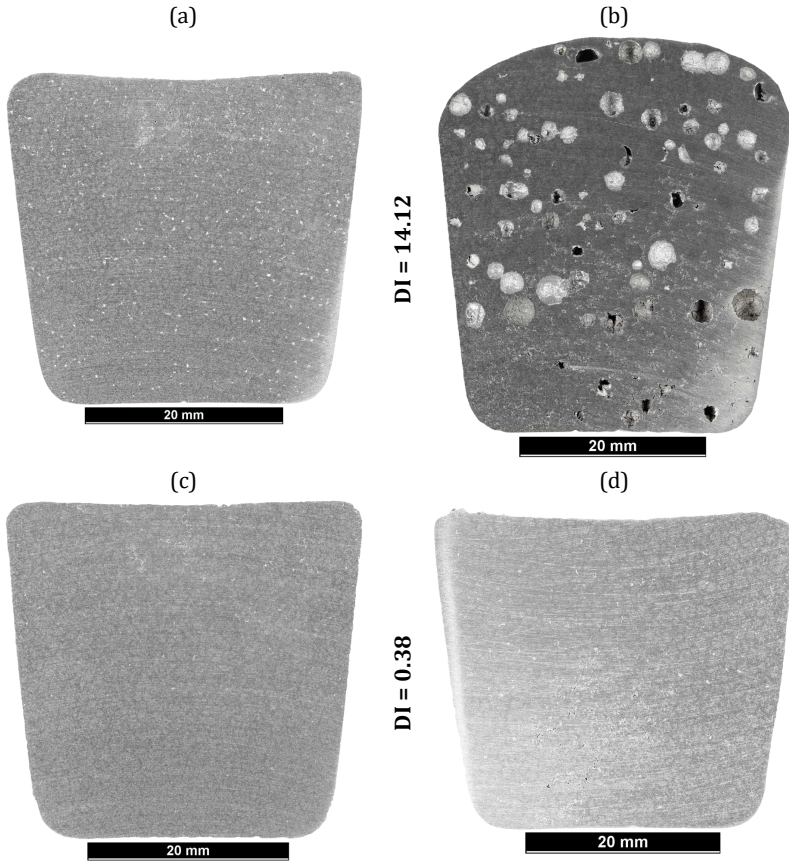


Figure 4-27: Sectioned reduced pressure test (RPT) sample pairs (DI 5 and 6) of the second experimental set. RPT sample pair DI 5: (a) solidified under atmospheric pressure ($g_p = 2.96\%$) and (b) at reduced pressure. The density index of DI 5 is of 14.12. RPT sample pair DI 6: (c) solidified under atmospheric pressure ($g_p = 1.48\%$) and (d) at reduced pressure. The density index of DI 6 is 0.38.

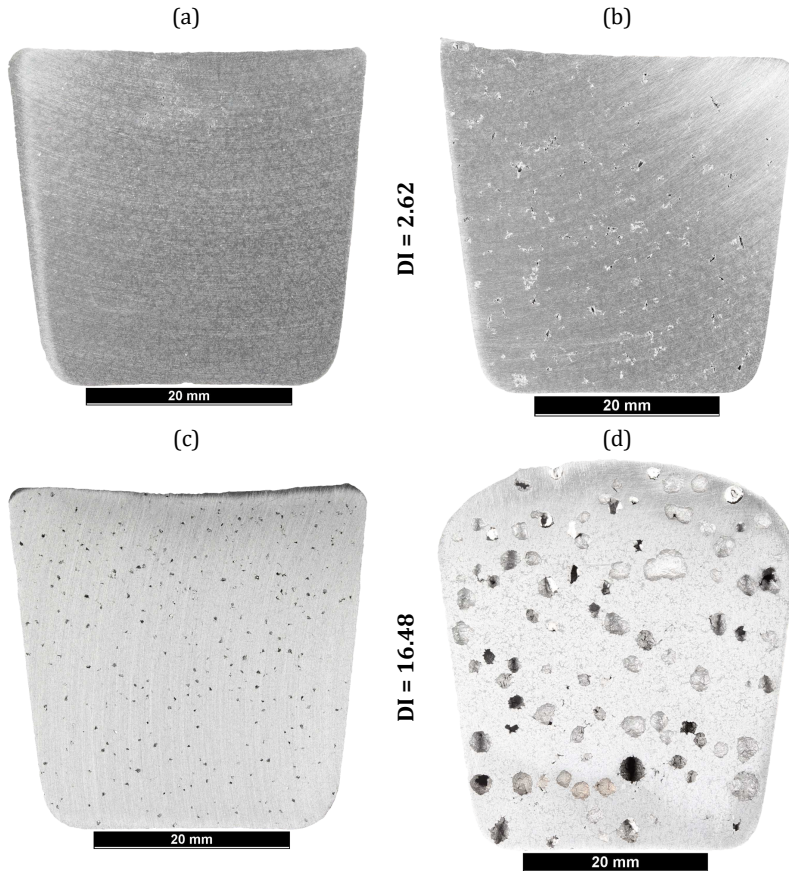


Figure 4-28: Sectioned reduced pressure test (RPT) sample pairs (DI 7 and 8) of the second experimental set. RPT sample pair DI 7: (a) solidified under atmospheric pressure ($g_p = 1.11\%$) and (b) at reduced pressure. The density index of DI 7 is 2.62. RPT sample pair DI 8: (c) solidified under atmospheric pressure ($g_p = 3.33\%$) and (d) at reduced pressure. The density index of DI 8 is 16.48.

As can be seen in Figure 4-26, before the first two wedge castings 7 and 8 of this set up were poured, the hydrogen level was raised by the addition of half a HYDRAL 40® tablet. This means that no untreated (in terms of no tablet additions) wedge castings were produced in the second experimental set. After the melt treatment, the hydrogen content was determined to be 0.179 ml / 100 g Al. The RPT test DI 5

resulted in a density index of 14.12. The sample which solidified at ambient pressure (Figure 4-27(a)) displays finely dispersed small pores which seem mostly isolated and with high sphericity. The sample's top surface is flat. The sample which solidified at reduced pressure (Figure 4-27(b)) shows the typical features of an RPT sample of elevated hydrogen level. Large spherical pores dominate the sectioned RPT specimen. Small, tortuous pores are present between the large spherical pores, and the specimen's top surface has a pronounced "mushroom" shape. Six NITRAL 10® tablets were added to reduce the hydrogen content for the second experiment. Since the HYCAL readings were not reproducible afterwards (large fluctuations in measurement were observable, and finally a first realistic reading of 0.2 ml / 100 g Al was measured) the HYCAL probe was replaced, and an RPT test (DI 6) was done. The density index was found to be 0.38, which is very low, and consistent with the visual impression of the second pair of sectioned RPT samples shown in Figure 4-27(c, d). The sample which solidified at ambient pressure (Figure 4-27(c)) showed hardly any visual porosity and the specimen which solidified at reduced pressure only had a small number of distributed pores and some tortuous pores in the centre of the sample. The surface of the RPT sample DI 6 was flat with no indication of a "mushroom" shape in accordance with the low hydrogen level expected from the density index. Because the pursued hydrogen level by HYCAL measurement was not achieved so far, six more NITRAL 10® tablets were immersed in the melt. A hydrogen reading of 0.157 ml / 100 g Al was measured and wedges nine and ten were poured although the targeted hydrogen level of approximately 0.1 ml / 100 g Al by HYCAL measurement was not reached. The RPT measurement (DI 7) conducted directly after casting yielded a density index of 2.62. Note that the density index increased from 0.38 to 2.62 despite the immersion of 6 more NITRAL 10® tablets. The DI 7 sample which solidified at ambient pressure (Figure 4-28(a)) is hardly distinguishable from the RPT sample DI 6 which solidified at ambient pressure (Figure 4-27(c)). The DI 7 sample which solidified at reduced pressure (Figure 4-28(b)) clearly shows more pores which are relatively tortuous but evenly distributed across the cross-section than the DI 6 sample which solidified at reduced pressure (Figure 4-27(d)). However, the top surface of the RPT sample DI 7 which solidified at reduced pressure (Figure 4-28(b)) does not indicate a hydrogen increase, compared to the RTP specimen DI 6 which solidified at reduced pressure (Figure 4-27(d)). Finally, to produce a high hydrogen level above 0.3 ml / 100 g Al, seven HYDRAL 40® tablets were added. The HYCAL system yielded 0.380 ml / 100 g Al and the RPT test DI 8 a density index of 16.48. The DI 8 specimen pair (Figure 4-28(c, d)) is comparable to DI 5 (Figure 4-27(a, b)). Both samples of DI 8, the sample which solidified at ambient pressure, as well as the sample which solidified at

reduced pressure show similar characteristics as the DI 5 specimen pair. The DI 8 RPT sample which solidified under atmospheric pressure (Figure 4-28(c)) shows an evenly distributed high number of small high sphericity pores with a flat sample top surface. The DI 8 RPT sample which solidified at reduced pressure (Figure 4-28(d)) shows a significant number of huge pores with many small tortuous pores in the material in-between and a pronounced “mushroom” shape. A comparison of the porosity, determined by Archimedes Principle, shows a slight increase in porosity in the DI 8 atmospheric pressure RPT sample (Figure 4-28(c)) compared to the respective DI 5 sample (Figure 4-27(a)), so there is some indication for the significantly higher hydrogen level measurement obtained by HYCAL.

The second set of experiments showed problems with the control of the hydrogen content via tablet additions and its measurement with the HYCAL system even more than in case of the first experimental set. There is an apparent discrepancy between the HYCAL measurement and the RPT measurement before and after the first NITRAL 10® treatment (DI 5 and 6). While the HYCAL reading is almost unchanged after the tablet treatment, the density index is drastically reduced (from 14.12 in Figure 4-27(a, b) to 0.38 in Figure 4-27(c, d)). In principle, there are two explanations which would explain the observed behaviour.

The first is that the NITRAL 10® tablet was not capable of removing substantial amounts of hydrogen from the melt because its degassing capability is limited. The reaction produces relatively large bubbles (estimated by visual impression of the reaction during melt treatment), and so the gas surface area in contact with the melt is much lower than in case of a well-adjusted rotary degassing procedure. Additionally, the generated turbulent gas release increases the melt area in contact with the atmosphere and thus might also facilitate the pickup of new hydrogen. At some point, a balance between hydrogen removal and pickup will most likely limit the degassing procedure. In this case, there is the question of why the density index dropped from 14.12 to 0.38. Besides the removal of hydrogen in solution, the NITRAL 10® tablets would also be expected to provide a cleaning effect on the aluminium melt. Released bubbles are thought to carry oxides or other non-metallic inclusions to the melt surface for later removal. In the light of the “bifilm” theory, presented by Campbell (42), the thorough removal of double oxide films in the aluminium melt should result, even at high hydrogen levels, in a pore-free solidification. Without the already existing gas pore, in the form of a folded and a submerged double oxide film, Campbell calculates the necessary internal pressure for pore nucleation to be 3.14×10^9 Pa in case of homogeneous nucleation or 3.65×10^7 Pa in case of heterogeneous nucleation. Even the latter being very high and unlikely to occur during solidification. Dispinar and Campbell (119) try to prove in experiments with RPT samples that this is indeed the case and that no porosity will form in clean

melts, even at high hydrogen levels. Raiszadeh and Griffiths (117, 118) tried to show in their experiments, that hydrogen can penetrate the oxide film or bifilms due to disturbances induced by deformation. They propose inflation of bifilms by hydrogen and thus the creation of gas porosity. Since the bifilm theory in general and more specifically the type of nuclei facilitating pore formation in aluminium alloys is not conclusively proven and understood, this argument cannot be closed at this point. Nevertheless, it was one of the conclusions of the preliminary experimental castings (see Section 4.1) that young oxides play a role in porosity formation and distribution, but it is not the most important or dominant factor. It was shown that, for example, slight changes in the chemical composition can effectively “mask” the changes due to the addition of young oxides into the melt.

The second explanation is that the NITRAL 10[®] treatment indeed removed a significant amount of hydrogen from the melt, but the HYCAL system was not showing the change. Note, that a change in density index from 14.12 (DI 5) to 0.38 (DI 6) after the first addition of 6 NITRAL 10[®] tablets is quite significant (from Figure 4-27(a, b) to Figure 4-27(c, d)). By personal discussion with Mr Henson of the HYCAL supplier company, the measurement of the hydrogen level might have been disturbed by the tablet treatment, thus explaining the observed inaccuracies of the hydrogen measurement. Note the very high hydrogen readings after the first NITRAL 10[®] additions which led to the decision to change the measurement probe for the following experimental procedure. If indeed the hydrogen level was significantly reduced, it would explain the low density index and agree with Campbell’s observations (42). Interestingly, after the addition of another 6 NITRAL 10[®] tablets, the density index (of DI 7) rose to 2.62 (Figure 4-28(a, b)). Although the DI 6 and DI 7 samples which solidified at ambient pressure are very similar (compare Figure 4-27(c) and Figure 4-28(a)), the respective specimens which solidified at reduced pressure are not (compare Figure 4-27(d) and Figure 4-28(b)). The one which was taken after the second tablet treatment (DI 7) and solidified at reduced pressure (Figure 4-28(b)) is more porous than the comparable DI 6 RPT sample before the tablet submersion (Figure 4-27(d)). Neither an inaccurate measurement of hydrogen by the HYCAL device (the level even dropped approximately 0.05 ml / 100 g Al from approx. 0.2 to 0.15 ml / 100 g Al) nor an inefficient degassing procedure would have suggested this development. In the light of the experienced strong metal-NITRAL 10[®] tablet reaction, a possible explanation could be that the uptake of hydrogen due to the intense reaction was overcompensating the degassing by bubble transport. Thus, as described before, the degassing capabilities of the NITRAL 10[®] tablet might have been reached after the first melt treatment. Another aspect could also be that the second NITRAL 10[®] treatment also introduced more impurities than it removed and

pore nucleation once more became easier than after the first melt treatment. Some indications of a higher particle inclusion content were found on micrographs of the specific wedge castings. The author was able to observe a significant amount of dross formation after each NITRAL 10® addition. The tablet disintegrated during the reaction, and a large amount of dross was formed. The final upgassing procedure to a high hydrogen level above 0.3 ml / 100 g Al worked as intended by HYDRAL 40® treatment and the HYCAL reading is plausible relative to the last density index measurement and the sectioned samples of DI 8 (Figure 4-28(c, d)).

Although the melt was treated multiple times by NITRAL 10® and HYDRAL 40® between RPT sample sets DI 5 (Figure 4-27(a, b)) and DI 8 (Figure 4-28(c, d)), both samples pairs show little difference in the observable porosity characteristics. Both samples (DI 5 and 8) which solidified under atmospheric pressure show a finely dispersed porosity of high qualitative sphericity. Both samples which solidified at reduced pressure show approximately the same mushroom shape, number and size of large inflated pores and a fine tortuous porosity in-between. This comparable porosity characteristics in the sectioned RPT samples is curious, since if the melt treatment by tablets added or removed active nuclei for porosity formation, it does not clearly show in the density index between DI 5 and 8. If indeed the HYCAL measurement worked adequately and there is a significant change in hydrogen content between the beginning and end of the second experimental set, then the tablet treatment might have deactivated or removed nuclei from the melt, and therefore the porosity characteristics and the density index hardly changed. Based on Dispinar's and Campbell's theory (119), a cleaner melt should show more resistance towards pore formation, and in extremely clean melts the nucleation should be suppressed entirely. Nevertheless, it was shown in Section 4.1 that the melt cleanliness is not necessarily the most critical factor controlling the porosity amount and the porosity distribution. In the previously presented preliminary laboratory castings, the introduction of young oxides into the melt did increase the qualitative amount of porosity, but not as much as a Mg addition did. The melt cleanliness effect on porosity was covered up by small Mg additions. Thus it seems questionable if the observed changes in the presented RPT tests conducted during the wedge castings are primarily linked to a change in melt cleanliness (in the form of a number of inclusions or bifilms or their potency to nucleate pores). Based on the results presented in this section, it seems just as likely that the tablet treatment, which caused small changes in the alloy's composition (loss of Mg and Sr) or interference with the HYCAL system, led to the presented results. This aspect is further discussed based on the development of the pore morphology presented in Section 4.3.4.

4.3.2. Spherical diameter and envelope diameter versus average porosity

The same XCT data analyses as used for the industrial castings are applied to obtain the spherical mean diameter ($d_{s,mean}$) and the maximum spherical diameter ($d_{s,max}$), as well as the envelope mean diameter ($d_{e,mean}$) and the maximum envelope diameter ($d_{e,max}$), versus total porosity for the wedge castings. The characteristic mean values are volume-weighted as described in Section 3.7, the chapter on the analysis of the XCT data. Two important, influential factors were varied in the wedge castings. First, the hydrogen level determined by quantitative HYCAL hydrogen measurements and indicated by the density index measurements from reduced pressure tests. Second, the cooling rate by producing a wedge casting and extracting samples at different wedge thicknesses. The local cooling rate of each specimen is represented by the secondary dendrite arm spacing, here just called DAS.

In Figure 4-29 the spherical mean diameter ($d_{s,mean}$) is plotted three times versus average porosity (g_p). All 36 XCT samples are shown. In Figure 4-29(a) the colour of each point represents the quantitative hydrogen content determined by the HYCAL system. In Figure 4-29(b) the colour of each point represents the determined density index from the reduced pressure test samples and in Figure 4-29(c) the colour represents the secondary dendrite arm spacing of each sample. In general, two presumed trends are distinguishable. The first trend is comprised of the samples which show a low sensitivity (low gradient) of the spherical mean diameter with porosity. The second, less apparent, trend consists of samples which show a higher sensitivity to porosity and follow a higher gradient. On both presumed trend lines, both alloys are represented without any apparent preference for one or the other. In the lower left corner of Figure 4-29(a) and Figure 4-29(b) there are only samples with low to medium hydrogen level (0.04 and 0.157 ml / 100 g) or low density indexes (2.62 and 2.99). The distinction between a low density index and a high density index in Figure 4-29(b) is more evident than in case of the low and high hydrogen levels (Figure 4-29(a)). Above a porosity level of approximately 1.9 %, only specimens with a medium to high hydrogen content or high density index are present. Although all specimens below 1 % of porosity show a hydrogen level up to 0.157 ml / 100 g (lower-left corner of Figure 4-29(a)), there are samples exhibiting a hydrogen level of 0.165 ml / 100 g and exhibiting up to 3 % of porosity. There is a slight tendency towards higher hydrogen levels for the high porosity samples following the low

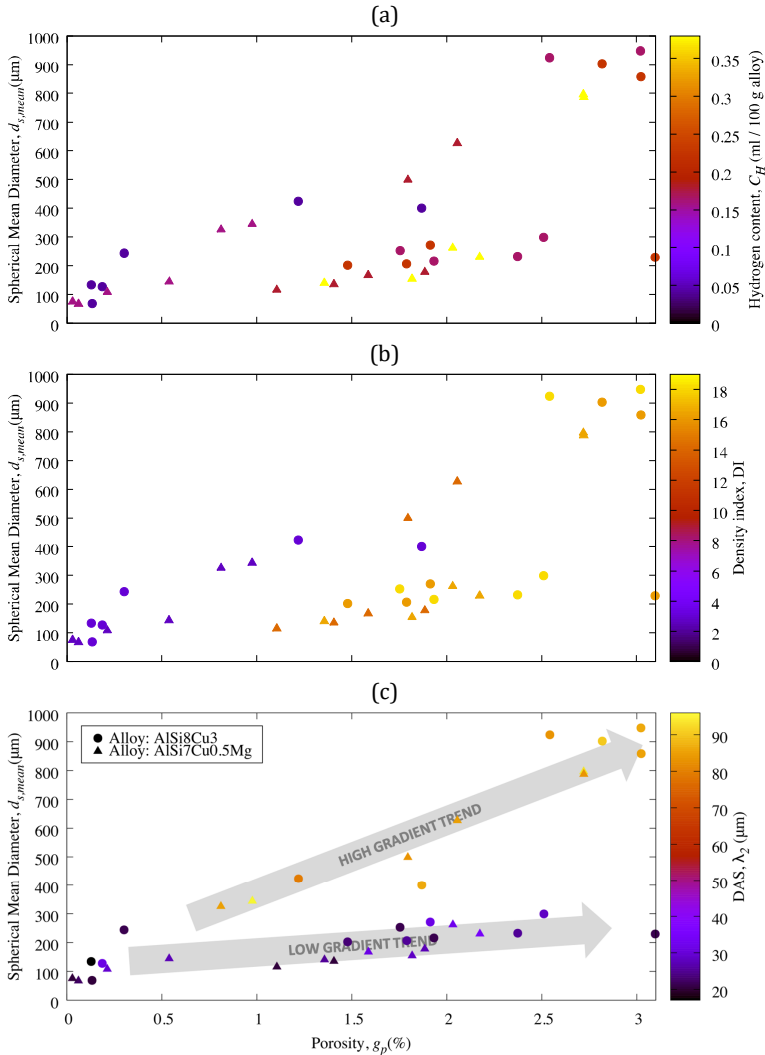


Figure 4-29: Plot of the spherical mean diameter $d_{s,mean}$ versus the average porosity g_p . The hydrogen content (a), density index (b), and DAS (c) are colour-coded. Two presumable trends are indicated in (c).

gradient trend. In Figure 4-29(c) the distinction between specimens with a low dendrite arm spacing below 34 μm and above is obvious. All specimens in Figure 4-29(c), which follow the first presumed trend line with the lower spherical mean diameter to porosity gradient, exhibit a DAS between 17 μm and 34 μm . All specimens following the second presumed trend line with the higher spherical mean diameter to porosity gradient show a DAS between 79 and 96 μm .

In Figure 4-30 the maximum spherical diameter ($d_{s,max}$) is plotted three times versus the average porosity (g_p) for each XCT specimen. As in Figure 4-29, in Figure 4-30(a, b, c) the colours indicate the hydrogen content, the density index, and the dendrite arm spacing for each specimen, respectively. The maximum spherical diameter represents the volume equivalent diameter of the largest (by volume) pore in a given sample. In general, Figure 4-30(a) shows an increasing maximum spherical diameter with increasing porosity. In contrast to Figure 4-29(a) only one general trend in behaviour is apparent. The scatter in maximum spherical diameter continuously increases with increasing porosity. There is only a slight indication that the hydrogen level influences the porosity level. In the lower-left corner below approximately 1 % porosity only samples with a maximum hydrogen content of 0.157 ml / 100 g or lower are located. There is no apparent tendency at higher porosity levels that a low or high maximum spherical diameter is linked to a high or low hydrogen level. In Figure 4-30(b) the plot of the maximum spherical diameter versus porosity with the indication of the density index by colour leads to similar general observations as Figure 4-30(a). The differences in density index are again more distinct than the differences in the hydrogen content; thus, a clear tendency towards lower porosity and smaller maximum spherical diameters with lower density index becomes apparent. As in Figure 4-29(c), Figure 4-30(c) shows the most apparent distinction between specimens of all three plots presented in Figure 4-30. Again, two general trends become evident. The samples with a DAS below 34 μm show a relationship between maximum spherical diameter and porosity with a lower gradient than the samples with larger DAS. A clear separation between both specimen populations (low gradient and higher gradient) is possible.

In Figure 4-31 the envelope mean diameter is plotted three times versus average porosity. As in the two previous plots the colour in Figure 4-31(a, b, c) indicates hydrogen content, density index, and dendrite arm spacing, respectively. The general trend is an increase in envelope mean diameter with increasing porosity. Unlike in Figure 4-29 and Figure 4-30, in Figure 4-31 three (not two) trend lines, one with a lower gradient, one with a medium gradient, and one with a very high gradient only formed by the samples of below 0.5 % porosity are apparent. Especially if

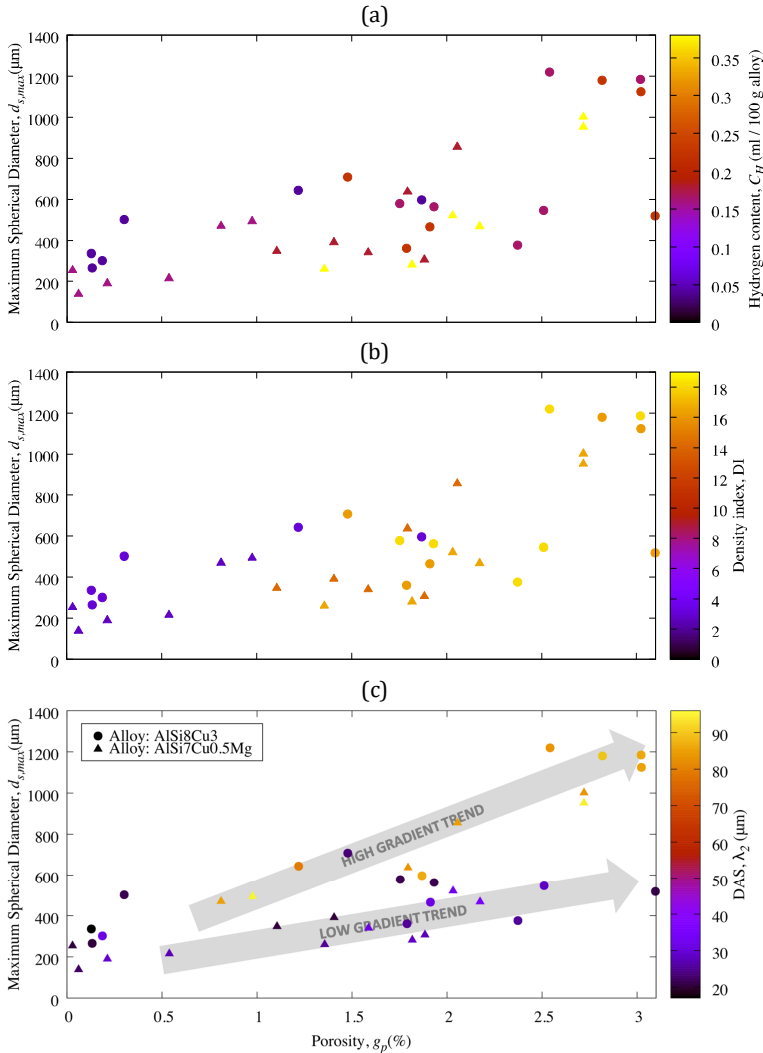


Figure 4-30: Plot of the maximum spherical diameter $d_{s,max}$ versus the average porosity g_p . The hydrogen content (a), density index (b), and DAS (c) are colour-coded. Two presumable trends are indicated in (c).

Figure 4-31(c), where the DAS is indicated by colour, is examined, one can see the separation between samples of low and high DAS. The low DAS, low porosity samples are harder to distinguish from the other two presumed trend lines. As in Figure 4-29, in Figure 4-31 the scatter of the samples in the population following the low gradient relationship does not seem to increase significantly at higher porosity levels. In general, similar observations can be made for the envelope mean diameter as for the spherical mean diameter versus porosity plot. The hydrogen content (only weakly) and the density index show an indication of being low in samples which are also low in average porosity (below 1.9 %). Again, the distinction is more pronounced in case of the density index than the hydrogen content. A clear separation of the specimen population showing the lower gradient and the population showing the larger gradient is once more indicated by Figure 4-31(c) meaning by dendrite arm spacing. It is noteworthy that the third specimen trend population with the highest gradient is entirely comprised of low hydrogen level, low DAS samples.

Figure 4-32 shows three plots of the maximum envelope diameter $d_{e,max}$ versus the average porosity level (g_p) for each XCT specimen. The colour in Figure 4-32(a, b, c) indicates hydrogen content, density index, and dendrite arm spacing, respectively. As in Figure 4-31, there is a general increase in maximum envelope diameter with increasing porosity level. Again, three specimen populations seem distinguishable. In the low porosity region ($g_p < 0.5$ %) there is a very steep increase of maximum envelope diameter with porosity. Although the identification of this high gradient specimen populations might seem somewhat questionable based on Figure 4-32, figures presented in Section 4.3.6 will identify this population as a separate individual group. These samples are all low in hydrogen level, density index and dendrite arm spacing. Mind that two samples of 0.04 ml / 100 g in hydrogen, marked by red circles in Figure 4-32(c), show much more porosity ($g_p = 1.22$ % and 1.87 %) than all the other samples of the lowest hydrogen level and which do not follow the high gradient trend. Nevertheless, the previously introduced distinction is correct, since these samples are also very different in DAS ($\lambda_2 = 79$ μm and 86 μm) and in this regard separated from the other samples ($\lambda_2 = 17$ –31 μm). The second specimen trend is characterised by a medium gradient and comprised of samples of larger DAS ($\lambda_2 \geq 83$ μm). The hydrogen level of these samples is mostly in the medium range of the wedge casting experiments ($C_H = 0.157$ – 0.224 ml / 100 g). The third presumable trend consists of the low DAS samples ($\lambda_2 \leq 34$ μm), with medium to high hydrogen content ($C_H = 0.157$ – 0.380 ml / 100 g). These samples only show a slow increase of the maximum envelope diameter with increasing porosity level.

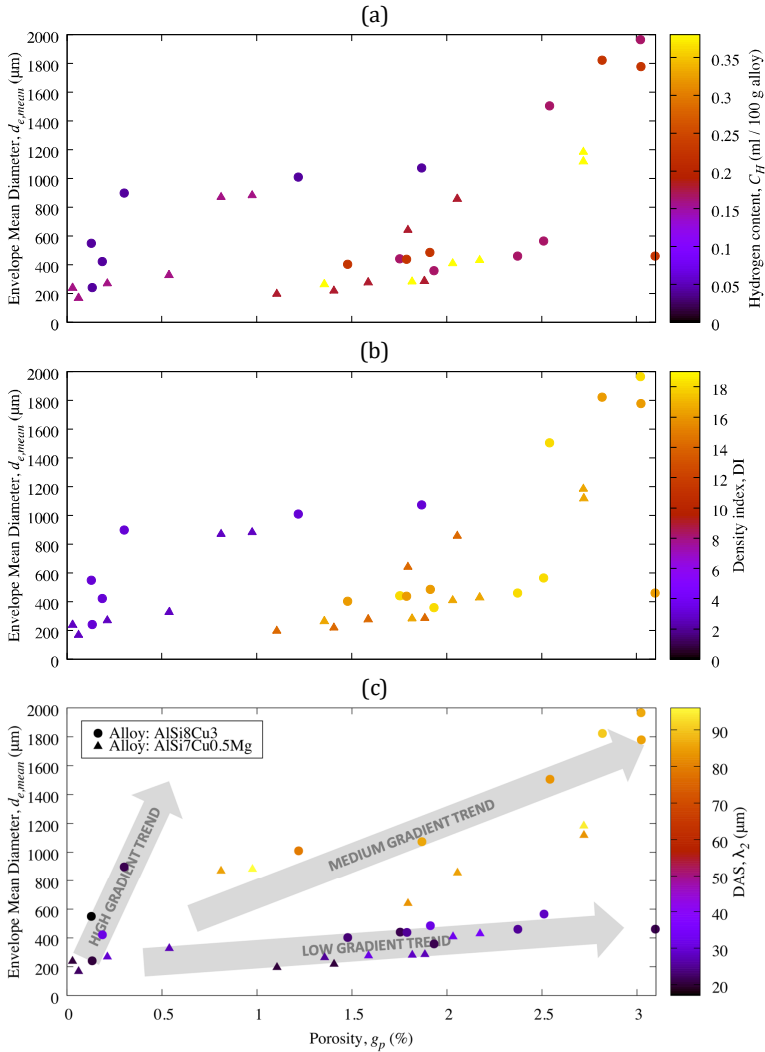


Figure 4-31: Plot of the envelope mean diameter $d_{e,mean}$ versus the average porosity g_p . The hydrogen content (a), density index (b), and DAS (c) are colour-coded. Three presumable trends are indicated in (c).

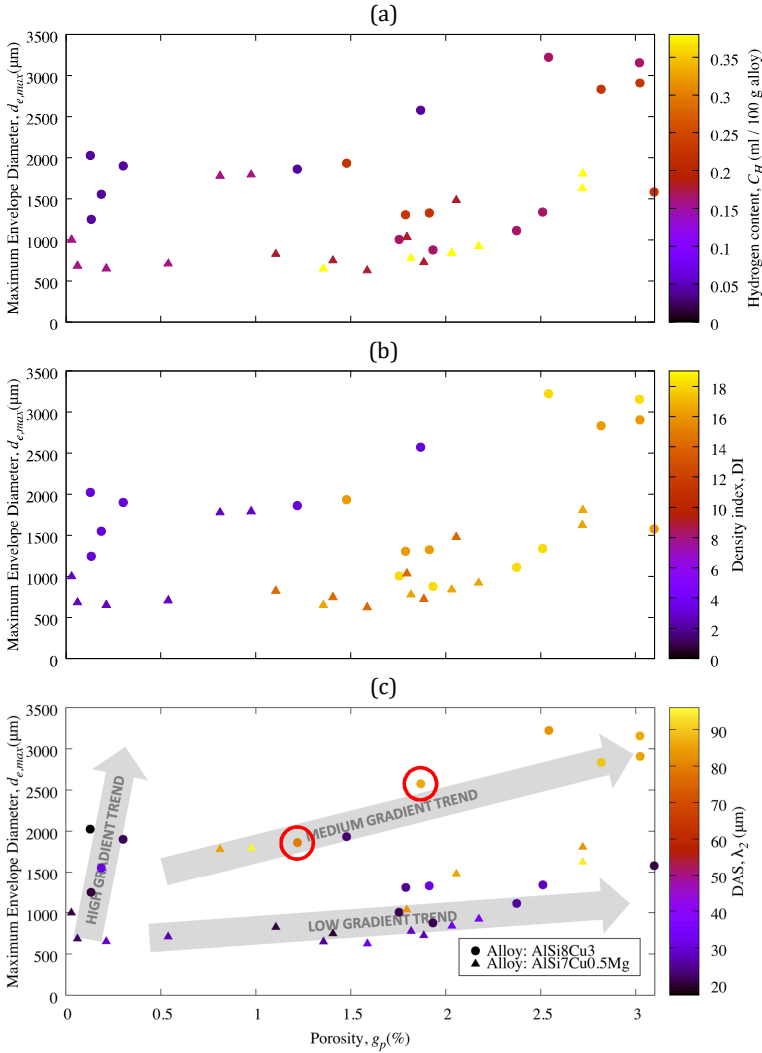


Figure 4-32: Plot of the maximum envelope diameter $d_{e,max}$ versus the average porosity g_p . The hydrogen content (a), density index (b), and DAS (c) are colour-coded. Three presumable trends and two samples (red circles) are indicated in (c).

Finally, in Figure 4-33 the plot of the dendrite arm spacing (DAS) versus the average porosity is shown. The colour indicates the pore number density for each sample. There is no clear correlation between the dendrite arm spacing and the porosity recognisable. Samples with 0.54 % porosity or less are all samples with a low DAS. Above this porosity value, specimen might have a low or high DAS value without any clear trend. If the pore number density is examined more closely (indicated by colour), one can see that it ranges from about 14 mm^{-3} to about 140 mm^{-3} and covers one order of magnitude. There is no apparent correlation between the pore number density and DAS nor the average porosity, which also indicates that there is no systematic change in pore number density with increasing cooling rate (represented by DAS).

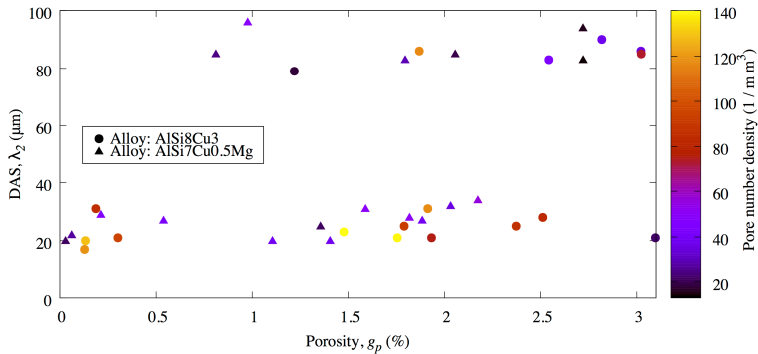


Figure 4-33: Plot of the secondary dendrite arm spacing λ_2 versus the average porosity g_p . The colour indicates the pore number density of each plotted sample.

Interestingly, none of the figures presented in this section show any indication of the influence of the alloy on the data. Two alloys were cast with a significant difference in chemical composition. The alloy AlSi8Cu3 contains approximately 1 wt% more Si, 2.5 wt% more Cu, 0.1 wt% less Mg, and 0.3 wt% (about four times) more Fe than the alloy AlSi7Cu0.5Mg. The higher alloying level of the AlSi8Cu3 alloy is expected to lead to a minor increase in solidification interval (due to the contrary effects of Si and Cu additions on solidification interval), but to a significant extension of the terminal freezing range. Based on a calculation by the software JMatPro®, the terminal freezing range between a solid fraction of 85 % and 95 % (TFR₈₅₋₉₅) increases from approximately 18.5 K to 38 K from AlSi7Cu0.5Mg to AlSi8Cu3. For well-degassed melts, this difference is likely the cause of a significant increase in

average porosity as was observed in the experimental sets AlSi7Cu0.5Mg(Sr) cylinder head in comparison to the AlSi8Cu3(Sr) cylinder head set, as described in Section 3.2 (“Industrial castings”). The extended terminal freezing range is thought to lead to an increase in average porosity by extending the width of the mushy zone and reduce the local feedability in the final stages of solidification. No systematic influence of the chemical composition can be found in the wedge castings. This could be an indication of higher hydrogen levels, compared to the two extensively rotary degassed experimental sets from the industrial castings, and thus a higher share of the local volume deficit is compensated by early nucleation of hydrogen-induced pores, or later nucleated hydrogen inflated shrinkage pores. Interestingly, there was also no significant difference in the porosity level for the two other experimental sets of industrial castings (also AlSi7Cu0.5Mg and AlSi8Cu3), which were also speculated to contain a larger amount of hydrogen. It is possible that a certain amount of hydrogen in the melt could “mask” the porosity difference which is normally expected due to the difference in the solidification characteristics. It cannot be proven by the presented results, but there might be three mechanisms that would explain the suppression of late-stage pores if early-stage porosity forms. First, the total volume deficit, which is created by the solidifying microstructure, is limited. If early pore nucleation compensates a substantial amount of the volume deficit, a sufficient pressure drop in the final solidification stage which leads to “shrinkage” porosity might not occur. Second, the number of potent nuclei in the melt might be limited. If early forming pores, due to hydrogen supersaturation, activate most of the potent nuclei, there might not be sufficient nuclei left for late-stage pores to form. Third, if early-stage pores form, they might interact with the equiaxed dendritic grains by pushing and thus rearrange the solid structure of the solidifying dendritic network, which in turn might lead to a change in the distribution of liquid pockets in the melt. As a result, the isolation or occurrence of these pools at the end of solidification might not take place to the same degree. It is also possible that two or all three mechanisms are working at the same time and in conjunction and effectively inhibit late-stage pore formation.

The correlation between the hydrogen content and the four presented characteristic measures of spherical and envelope diameters to porosity is marginal. The only clear indication is that samples containing below 1 % of porosity also show a relatively low hydrogen level. There are two samples (marked by red circles in Figure 4-32(c)) with a low hydrogen level and 1.22 % and 1.87 % porosity and thus an exception to the general observation. This sample also shows a much larger DAS than the other samples which contain 0.04 ml hydrogen / 100 g. It appears that if a certain amount of hydrogen is not exceeded, the average porosity can be low,

but does not have to be. Long solidification times can lead to high levels of porosity even if the hydrogen content is low. If the hydrogen level becomes higher (in the case of the presented results above 0.179 ml / 100 g), there are no samples which exhibit less than 1 % porosity, which suggests that a low hydrogen level is necessary, but not a sufficient condition to produce low porosity samples. Vice versa, if a specific hydrogen content is exceeded, it seems not to be possible to produce low porosity samples, even under high cooling rates as indicated by Figure 4-29(c) to Figure 4-32(c). This hypothesis is not entirely in agreement with the modelling work by Carlson et al. (33). Carlson et al. predicted, based on a model which incorporates the effect of shrinkage, the induced feeding flow, local pressure variations, and the finite-rate hydrogen diffusion, that a sufficiently high cooling rate suppresses the hydrogen-induced pore formation and reduces the general average porosity level. In the present data, there are multiple samples of high porosity, which show a clear indication of high hydrogen content and at the same time have a very low dendrite arm spacing (correlated to a high local cooling rate). These samples do not show the behaviour proposed by Carlson et al. It is possible that the local cooling rate was not sufficiently high to suppress pore nucleation, but DAS values of almost half the samples below 25 μm indicate the contrary. One other possibility could be that the local volume deficit is at some point not compensated by hydrogen-induced porosity, but by shrinkage-driven porosity. Finally, the stage in which the pores nucleate during solidification might change significantly for different hydrogen levels, and the assumptions of Carlson et al. are based on a pore-dendritic-network interaction which, if the pore formation occurs early, might not influence the final amount of porosity significantly. All these explanations should be indicated by the pore morphology. If pores nucleate early during solidification, high sphericity would be expected. If the pores nucleate later in the solidification sequence, a more tortuous shape is to be expected. This aspect is discussed further in the light of the presented analysis of the mean sphericity (see Section 4.3.5) of each pore, as well as in Section 4.3.4 by individual samples morphology analysis. One of the conclusions from the industrial casting experiments presented in Section 4.2 was that a certain porosity level has to be exceeded (between 0.288 % and 0.583 % average porosity) to be able to observe high sphericity pores in the XCT samples. In the context of the results presented in this section, this observation confirms that there might be a threshold hydrogen level determining if hydrogen-related porosity can form or not. As discussed previously, the modelling work of Fang and Granger (101) also suggest a threshold hydrogen level below which no hydrogen porosity can form. If hydrogen porosity is suppressed by a low hydrogen level or sufficiently high cooling rate, the local volume deficit remaining at the end of solidification has to be compensated by feeding or if this is not possible by “shrinkage porosity” formation.

In the data from the wedge castings, the distinction between a high density index and a low one is more pronounced than between a low and a high hydrogen reading. There is no transition range of intermediate density index values; thus the density index seems to be an easier to interpret indicator if the goal is to produce low porosity material (note, that there are also samples in the data set that exhibit a low density index and 1.87 % average porosity). As discussed in Section 4.3.1 on the hydrogen adjustment and measurement, there is the possibility that in fact only two effective hydrogen levels were achieved (a low one and a high one, as the DI indicates), because Campbell was able to observe a transition from low to higher density index values for increasing hydrogen levels (119). In this case, the density index measurement could represent the actual hydrogen level of the melt quite accurately.

The dendrite arm spacing has the most noticeable effect on the shown characteristic measures. In the two (three) plots of spherical mean diameter and maximum spherical diameter and with reservations the envelope mean diameter versus porosity (see Figure 4-29(c) to Figure 4-31(c)) it is apparent that specimens with a low DAS (below 34 μm) show a smaller increase in each characteristic measure with increasing porosity than samples having a larger dendrite arm spacing (above 83 μm). This means that although the porosity level increases strongly for low DAS samples, the weighted spherical diameter (representing the pore volume) and the weighted envelope diameter (representing the pore dimensions) of each sample only show a minor increase compared to large DAS samples. Note that the volume weighing procedure means that this is true for the largest pores of each sample. Moreover, the same can be concluded for the volume of the largest pore in each sample, represented by the maximum spherical diameter (see Figure 4-30(c)). This effect can be observed independently of the hydrogen content (or the density index), at least in case of the samples with hydrogen levels of 0.157 ml / 100 g or above. As discussed before, it can be assumed that the cooling rate, for melts which contain a sufficient amount of hydrogen, determines and limits the volume of the pores. Hence the cooling rate seems to be an effective process parameter to control average and maximum pore volume as well as average pore dimensions (but not the average porosity in general as discussed before). How the local cooling rate affects the characteristic pore measures in case of low hydrogen levels (0.04 ml / 100 g) cannot be conclusively concluded from the presented data because of the minimal data basis (only two specimens of low cooling rate). Nevertheless, there is the indication of a strong average porosity increase with very low cooling rates at low hydrogen levels. In Section 4.3.4 the previously introduced sample which contains 1.87 % porosity is presented as XCT scan in Figure 4-37(a). It will be discussed in greater detail then, but one can see the mixed porosity type which was observed

before in the industrial BP samples. This indicates that for very low solidification rates, even at low hydrogen level, high sphericity pores start to form. Additionally, late-stage, shrinkage porosity is also present.

The maximum defect size does seem to show a pronounced sensitivity to the hydrogen content since the third (high gradient) population is comprised of the low hydrogen samples. If this low hydrogen level goes along with a high solidification rate (low DAS), the maximum pore size shows a strong dependency on average porosity. Recall that the low DAS, high hydrogen specimens form the population with the lowest sensitivity. Most likely the low hydrogen level did not allow an early pore formation due to hydrogen precipitation, and the dendritic network grew until a high fraction solid was reached. At this point, much of the total volume deficit would be still uncompensated, and because of the highly developed solid network, a significant local pressure drop is likely to occur. At some point, the local feedability dropped to such a degree that the pressure was low enough to nucleate “shrinkage pores”. In this stage, every pore has only very little space (mostly in the interdendritic space which is at this point very tortuous), and so little pore volume leads to the formation of large tortuous pores. A pushing of dendrites by growing pores can be excluded at this stage since the solid network is way past the dendrite coherency point and should have developed a measurable and significant shear strength and deformation resistivity (34–38). Since this interesting third (high gradient) population cannot be found in case of the volume-weighted spherical mean diameter and the maximum spherical diameter, but only for the envelope diameters, it can be concluded that the pore volume is not (strongly) influenced by the hydrogen level of the melt (mind, not the average porosity) but the pore morphology, indicated by pore size, is. This observation should also be confirmed by the mean sphericity, which is discussed further in Sections 4.3.5 and 4.3.6.3.

It seems plausible to assume that a smaller spherical mean diameter and a smaller maximum spherical diameter (smaller largest pores in average and absolute) at a given porosity level go along with a higher pore number density, which would mean more pore nucleation events at higher cooling rates as is predicted by athermal nucleation theory (see Section 2.1.1.1) and as can be deduced from work by Emadi and Gruzleski (133) (calculated from an average pore diameter and the average porosity in unmodified A356 samples). As shown in Figure 4-33, the pore number density (in pores per mm^3) was evaluated for the wedge castings, and there is no indication that the pore number density increases systematically for lower DAS samples. Although the work with the data from the industrial experiments with different XCT scanning resolutions showed a strong influence of the scanning resolution on the pore number density, it should be valid to only relatively compare the pore number density within one experimental set conducted with only one scanning

resolution. As an indicator for the influence of the scanning resolution, the pore number density in the wedge castings with 5 μm resolution was determined to be between $1.4 \times 10^{10} \text{ m}^{-3}$ and $1.4 \times 10^{11} \text{ m}^{-3}$. The respective pore number density for the industrial castings presented in Section 4.2 was between $1.3 \times 10^9 \text{ m}^{-3}$ and $9.3 \times 10^9 \text{ m}^{-3}$ for a resolution of 8 μm and between $6.0 \times 10^{10} \text{ m}^{-3}$ and $6.4 \times 10^{11} \text{ m}^{-3}$ for a resolution of 3 μm . In all analysed XCT scans conducted in this work, the pore number density for 3, 5, and 8 μm scanning resolution shows no explicit correlation to the cooling rate (represented by DAS). Based on experimental work by Fang and Granger (101) no clear increase or decrease of pore number density with increasing cooling rate can be shown (calculated from an average pore diameter and the average porosity in unmodified A356 samples). The fact that the number density did not change systematically with cooling rate could be caused by many small pores which nucleated and grew to a size below the chosen scanning resolution. On the other hand, it seems unlikely that there is a major shift to small pores and there is no systematic effect on pore number density at all. At least in transition cooling rates, there should be an indication of a systematic influence. If this was not the case, and the pore number density at high cooling rates does not increase, but the volume-weighted pore size and the volume-weighted volume are reduced significantly for a given amount of total porosity (as shown in Figure 4-29 to Figure 4-31), it means that the largest pores become smaller, while the number of medium-sized pores increases. More importantly, it would also mean that athermal nucleation in general, meaning the activation and growth of already existing embryos, does not apply to microporosity and thus the bifilm concept presented by Campbell (119) is questionable. A constant number of pores, independent of cooling rate, would more likely be explained by classical heterogeneous nucleation theory (see Section 2.1.1.1), that predicts an almost instantaneous activation of all suitable nuclei (thus also called instantaneous nucleation), independently of cooling rate, once the necessary nucleation conditions (pressure drop or hydrogen supersaturation) are met. Therefore, the total number of suitable nuclei, which might change for different melt conditions, would determine the number density of micropores and not the cooling rate as athermal nucleation theory suggests.

4.3.3. Maximum versus mean diameters

Figure 4-34 shows three times the plot of the maximum spherical diameter versus the spherical mean diameter. The data are fitted by a linear function given by

$$d_{s,max} = 1.07d_{s,mean} + 184 \quad \text{(Equation 139)}$$

In Figure 4-34(a, b, c) the colour indicates the hydrogen content, the density index, and the dendrite arm spacing, respectively. There is a clear linear correlation visible, a continuous linear increase of the maximum spherical diameter (diameter of a volume equivalent sphere for the largest pore by volume) with an increasing spherical mean diameter (the volume-weighted mean spherical diameter). All 36 samples of the wedge casting experiments follow the same correlation. There is no apparent trend regarding the hydrogen content observable (compare Figure 4-34(a)). As already presented in the previous section, there might be a slight indication that the lowest porosity samples also show low hydrogen readings. The same is true for the density index shown in Figure 4-34(b). Again, the distinction between a low and high density index sample and a low and high hydrogen level sample is more pronounced. Low density index samples tend to show, compared to all specimens of this data set, low maximum spherical diameters and low spherical mean diameter values. This is even more true for Figure 4-34(c), which indicates the DAS by colour. Samples which exhibit a small DAS also exhibit a small maximum and mean spherical diameter. The separation from the large DAS samples is quite distinct, although all samples of the dataset follow the same general trend.

Figure 4-35 shows three times the plot of the maximum envelope diameter versus the spherical mean diameter. In Figure 4-35(a, b, c) the colour indicates the hydrogen content, the density index, and the dendrite arm spacing, respectively. The data are fitted by a linear function given by

$$d_{s,max} = 1.37d_{s,mean} + 554 \quad \text{(Equation 140)}$$

As in Figure 4-34, Figure 4-35 shows one distinct linear trend, although the scatter of the maximum to mean envelope diameter relationship seems larger than in the previous plot. Neither the hydrogen level (Figure 4-35(a)) nor the density index (Figure 4-35(b)) or the dendrite arm spacing ((Figure 4-35(c)) alters the general relationship between the maximum envelope diameter and the envelope mean diameter. The density index, as well as the DAS, allow a separation between samples with a low DI and small DAS, which are located in the lower-left corner of the plot indicating smaller maximum envelope diameters, and the samples with higher DI

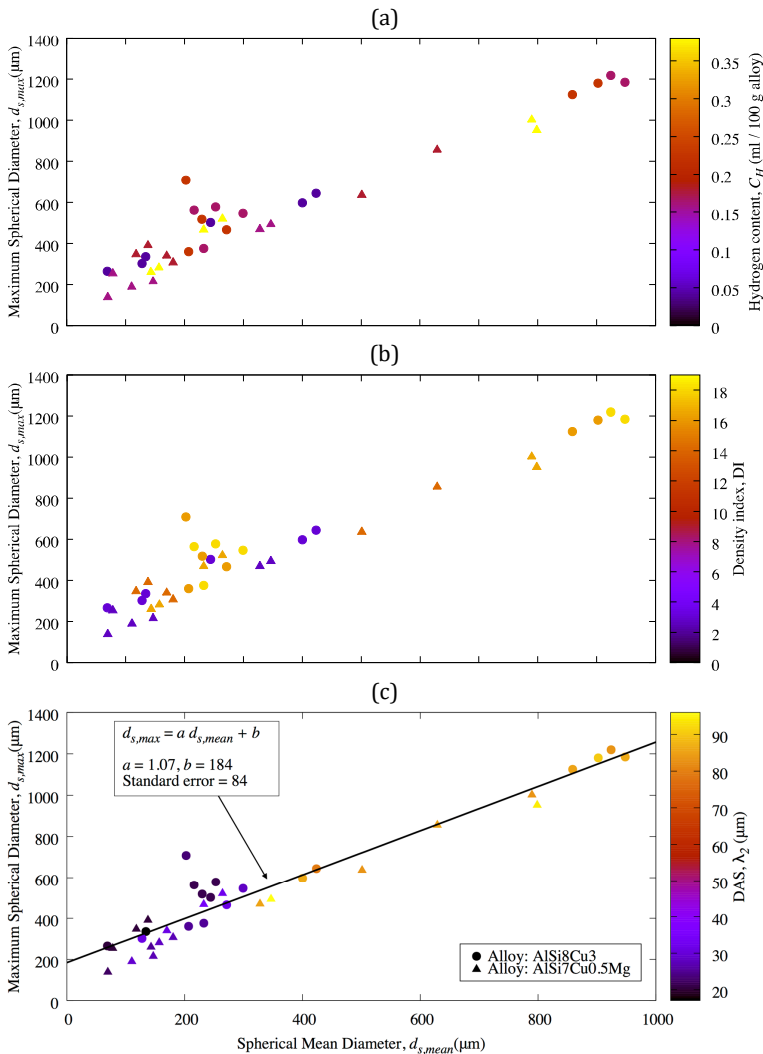


Figure 4-34: Plot of the maximum spherical diameter $d_{s,max}$ versus the spherical mean diameter $d_{s,mean}$. The hydrogen content (a), density index (b), and DAS (c) are colour-coded in the respective plots. The data is linearly fitted and the result marked by the black line.

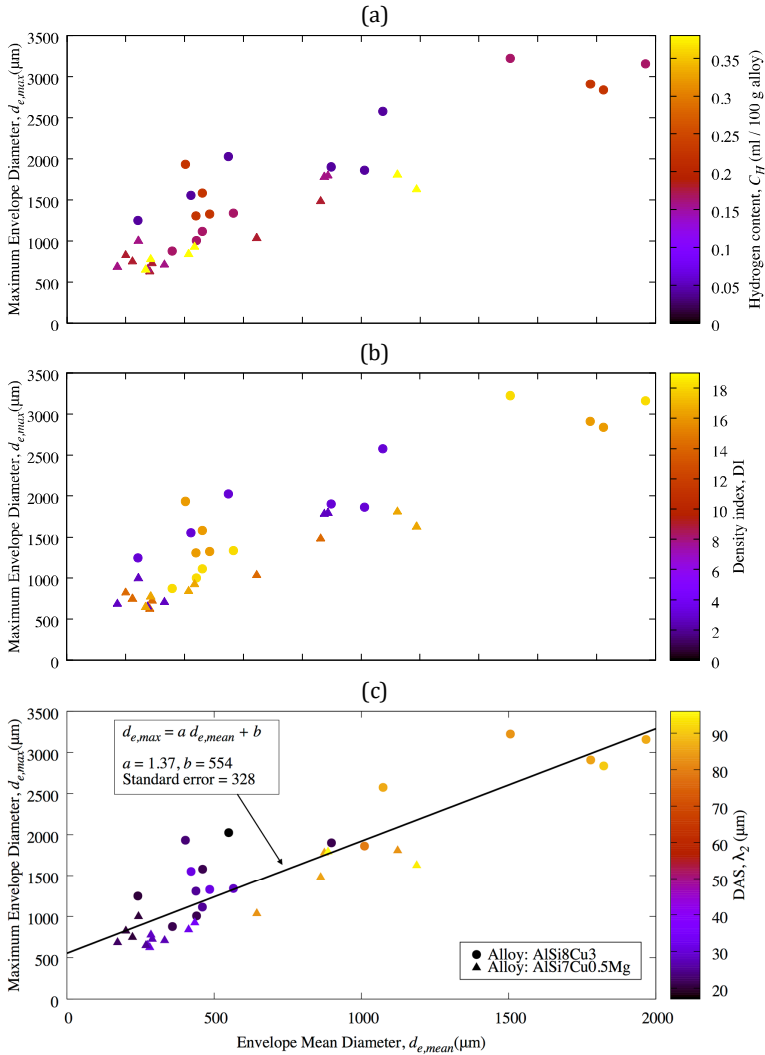


Figure 4-35: Plot of the maximum envelope diameter $d_{e,max}$ versus the envelope mean diameter $d_{e,mean}$. The hydrogen content (a), density index (b), and DAS (c) are colour-coded in the respective plots. The data is linearly fitted and the result marked by the black line.

and higher DAS which are preferentially in the upper right corner of the plot, indicating higher maximum envelope diameters. Both alloys are represented up to about 2000 μm maximum envelope diameter. Above this maximum pore size, the alloy AlSi8Cu3 is exclusively located.

As in the previously studied samples from the industrial castings (compare Section 4.2.3), linear correlations seem to be able to describe the relationship between the maximum spherical diameter (representing the single pore of highest volume) and the mean spherical diameter (representing the volume-weighted mean pore volume). This observation means there is, across the differences in hydrogen level, density index, local cooling rate (represented by DAS) and chemical composition, a simple linear correlation that describes the development of the pore size distribution at different average porosity levels (up to 3.1 % in the wedge casting experiments). These correlations could be of high value for the prediction of the pore size distribution or the maximum defect size. As has been mentioned multiple times before, especially the largest defect is of high interest for the fatigue proof design of cyclically loaded cast components (1–6).

4.3.4. Pore morphology

In the following section, a characteristic selection of seven out of the 36 produced specimens from the wedge castings (compare Table 3-16) are presented. A particular focus is put on the influence of the local solidification rate (evaluated by dendrite arm spacing), the density index and the hydrogen level. The goal is to show characteristic differences in the visual impression of the pore morphologies and to identify representative characteristics in the porosity. For this purpose, individual samples are selected and discussed.

Figure 4-36 shows the first two selected XCT renderings of samples (wedge specimens 4 and 13) extracted from a high cooling rate position of the wedge castings. Both samples are taken from the first experimental set, conducted with the alloy AlSi8Cu3. Figure 4-36(a) shows wedge sample 4 with a hydrogen level, before any addition of tablets to increase the hydrogen level. Figure 4-36(b) shows wedge sample 13 taken from the same specimen location at the end of the first experimental set, thus after the addition of seven HYDRAL 40® tablets. Both samples are of comparable dendrite arm spacing ($\lambda_2 = 21$ and $23 \mu\text{m}$), but show significant differences in porosity level ($g_p = 0.301$ and 1.478%), hydrogen content ($C_H = 0.04$ and $0.224 \text{ ml} / 100 \text{ g}$), and density index ($DI = 2.99$ and 16.10).

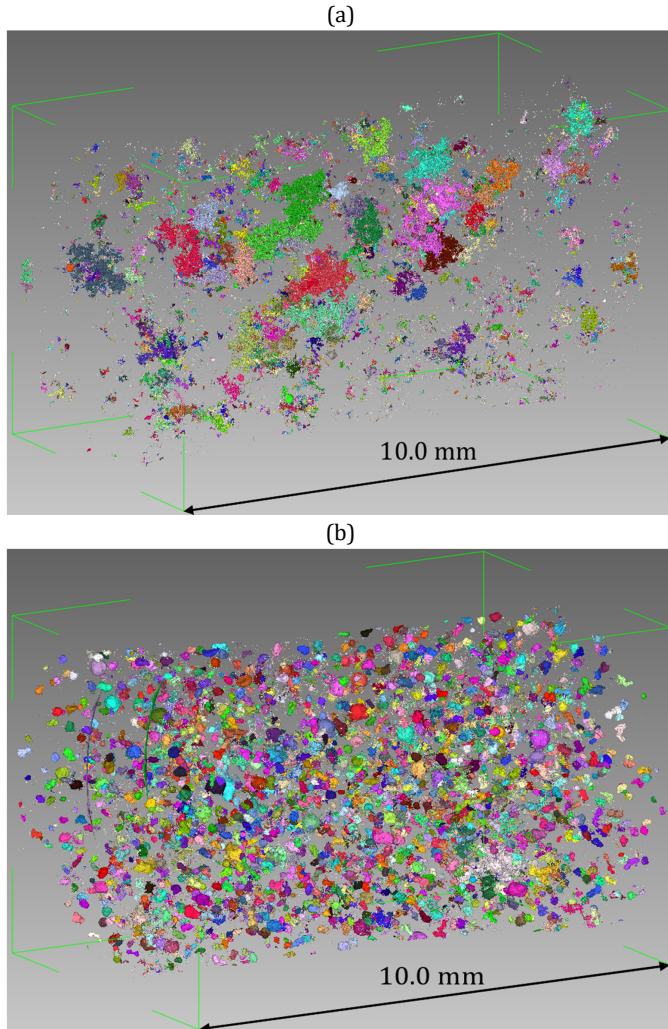


Figure 4-36: Selected XCT-scans performed with $5\ \mu\text{m}$ spatial resolution, AlSi8Cu3(Sr) , wedge castings, high cooling rate: (a) wedge specimen 4, $\lambda_2 = 21\ \mu\text{m}$, $g_p = 0.301\ \%$, $C_H = 0.040\ \text{ml} / 100\ \text{g}$, $\text{DI} = 2.99$; (b) wedge specimen 13, $\lambda_2 = 23\ \mu\text{m}$, $g_p = 1.478\ \%$, $C_H = 0.224\ \text{ml} / 100\ \text{g}$, $\text{DI} = 16.10$ (scan artefacts are excluded from the data evaluation)

The wedge specimen 4 (Figure 4-36(a)) shows primarily late-stage porosity, characterised by large pores which are comparatively low in volume and high in the relative surface area. In between the large pores, a large number of smaller, but also very tortuous pores can be identified. Wedge specimen 13 (Figure 4-36(b)) shows very distinct differences, compared to the wedge sample 4. The pores are much smaller if the pore dimensions are considered. Also, the sphericity of these pores is high, which means the surface area of the pores is close to the surface area of a volume equivalent sphere. Although by the visual impression the smallest pores cannot be evaluated, the porosity in the wedge specimen 13 seems much more homogeneously distributed over many pores of comparable size, than in the specimen 4.

Figure 4-37 shows two XCT renderings of wedge samples 6 and 15 which were extracted from the same two wedges as the specimen shown in Figure 4-36 but extracted from a low cooling rate position. Accordingly, the local dendrite arm spacing is much larger for both samples (wedge samples 6 and 15: $\lambda_2 = 86$ and $90 \mu\text{m}$, respectively). Along with the lower cooling rate, the porosity level of both samples is also much higher compared to the two previously presented high cooling rate samples ($g_p = 1.868$ and 2.818%). A comparison to the two low hydrogen wedge samples 4 and 6 (Figure 4-36(a) and Figure 4-37(a)) shows a significant increase in porosity with decreasing local cooling rate. Although the hydrogen measurement is only $0.04 \text{ ml} / 100 \text{ g}$, the low cooling rate of wedge specimen 6 presented in Figure 4-37(a) leads to the formation of relatively large high sphericity pores, which can be identified additionally to the low sphericity, high relative surface area pores which are exclusively present in the low DAS sample 4 (Figure 4-36(a)). Apart from these high sphericity pores and the, in general, higher porosity level, the porosity characteristic of sample 6 is similar to the low DAS sample 4, including a high number of tortuous smaller pores in-between the larger ones.

If sample 15, which is of high hydrogen level and low cooling rate (see Figure 4-37(b)) is compared to the sample 13, which is of high hydrogen level and high cooling rate (see Figure 4-36(b)), one notices much larger, highly spherical pores in the first one, but concurrently a much smaller number of these high sphericity pores. Some of the large high sphericity pores in specimen 15 (Figure 4-37(b)) seem to show tortuous appendices that seem to have grown into the solid dendritic network and which had to adopt a tortuous shape to fit into the interdendritic spaces. Note that some pores were cut open as they extend over the sample surface and thus the XCT scan shows a flat unnatural looking (corrugated by the mechanical specimen preparation) pore surface. Between the large pores of the high hydrogen, low cooling rate sample 15 (Figure 4-37(b)) there is still a significant number of smaller pores with high tortuosity visible.

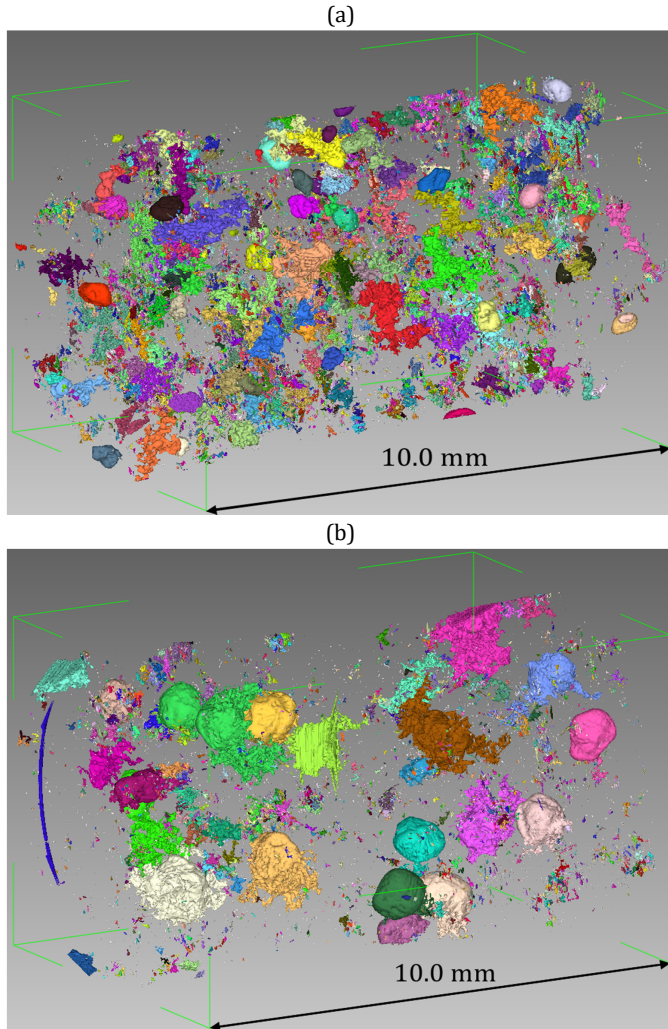


Figure 4-37: Selected XCT-scans performed with $5\ \mu\text{m}$ spatial resolution, AlSi8Cu3(Sr) , wedge castings, low cooling rate: (a) wedge specimen 6, $\lambda_2 = 86\ \mu\text{m}$, $g_p = 1.868\ \%$, $C_H = 0.040\ \text{ml} / 100\ \text{g}$, $\text{DI} = 2.99$; (b) wedge specimen 15, $\lambda_2 = 90\ \mu\text{m}$, $g_p = 2.818\ \%$, $C_H = 0.224\ \text{ml} / 100\ \text{g}$, $\text{DI} = 16.1$ (scan artefacts are excluded from the data evaluation)

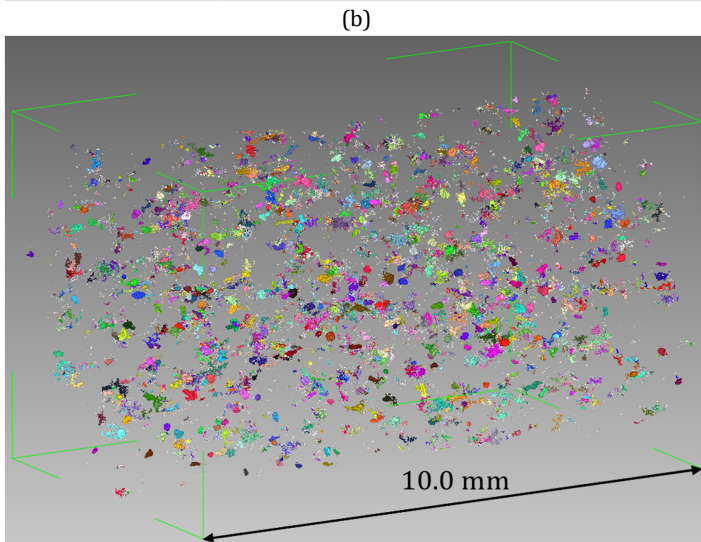
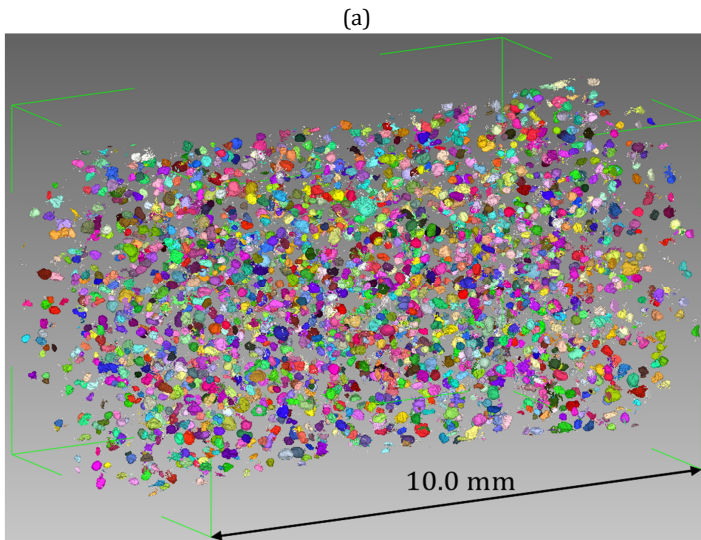
Figure 4-38(a, b, c) shows wedge specimens 20, 26, and 35, which were extracted from the second experimental wedge casting experiments, conducted with the alloy AlSi7Cu0.5Mg(Sr). All samples were taken from the same medium cooling rate wedge position and, as a result, show a similar dendrite arm spacing of λ_2 between 29 and 32 μm . Sample 20 shown in Figure 4-38(a) was cast during the first of the three wedge casting sets of the second experimental set, after the addition of only half a HYDRAL 40[®] tablet. The specimen shows a high number of high sphericity pores throughout the sample. All larger pores are very similar in size. The measured hydrogen content and density index for this sample is $C_H = 0.179 \text{ ml} / 100 \text{ g}$ and $DI = 14.12$, respectively. Figure 4-38(b) shows a sample 26 taken from a wedge after the addition of 12 NITRAL 10[®] tablets (which release nitrogen in a chemical reaction to remove hydrogen and inclusions from the melt). Although the (by HYCAL system) measured hydrogen content only dropped from 0.179 to 0.157 ml / 100 g, the density index dropped significantly from $DI = 14.12$ to 2.62. The apparent effect is much less high sphericity pores, although a small number seems still to be present. Although the number density of pores is difficult to determine absolutely, between both specimens which were scanned both with 5 μm a relative comparison seems to be useful. Before and after the NITRAL 10[®] treatment the pore number density is $4.97 \times 10^{10} \text{ m}^{-3}$ and $4.53 \times 10^{10} \text{ m}^{-3}$, respectively. This observation means that the pore number density effectively did not change by the melt treatment by NITRAL 10[®] tablets. In any case, sample 26 shown in Figure 4-38(b) shows many tortuous pores which are just limited in size because of their relatively low volume. In Figure 4-38(c) sample 35 after the addition of seven HYDRAL 40[®] tablets from the third and last wedge sample pair is shown. Both, the hydrogen level ($C_H = 0.38 \text{ ml}$) as well as the density index ($DI = 16.48$), once more increased strongly compared to the previously introduced sample 26 (Figure 4-38(b)) and even in comparison to the first presented sample 20 of this experimental set (Figure 4-38(a)). The pore number density decreased slightly to $3.49 \times 10^{10} \text{ m}^{-3}$. Specimen 35 can be characterised by high sphericity pores which seem to be of higher volume than the high sphericity pores of the first sample (wedge specimen 20) of this set. Although the pore shapes and visual impression of samples 20 and 35 presented in Figure 4-38(a) and Figure 4-38(c) are very comparable, the about 0.45 % higher average porosity of sample 35 compared to sample 20 yielded noticeably larger pores (concerning pore volume).

The pore morphology of the low hydrogen, high cooling rate sample 4 presented in Figure 4-36(a) is very comparable to the earlier discussed industrial casting samples presented in Section 4.2.4 (compare the two samples presented in Figure 4-16). These industrial samples were characterised as “shrinkage porosity” dominated.

The pore morphology is consistent with the expectation of a low hydrogen level sample which solidified relatively fast. In this case, the hydrogen level is not high enough to precipitate in the form of high sphericity pores in an early solidification stage; thus the solidification progresses and finally pores (probably in this stage strongly driven by the shrinkage-induced pressure drop) form. These pores have to adapt to the shape of the dendritic network and become very complex and tortuous.

Interestingly, the relatively low hydrogen level of 0.04 ml / 100 g seems still to be high enough to lead to early-stage pore nucleation and high sphericity pores if the solidification times are long enough. This can be easily seen in the case of sample 6 presented in Figure 4-37(a). Sample 6 is an especially compelling case (one of the two samples already discussed in Section 4.3.2 and marked by a red circle in Figure 4-32(c)) that is discussed further in Sections 4.3.6.1 and 4.3.6.3 (marked in Figure 4-43 and Figure 4-46). One can see that, given enough time, quite low hydrogen levels are sufficient to nucleate pores at an early (low fraction solid) stage. In contrast to the modelling work of Fang and Granger (101), who predict a threshold value of hydrogen below which no hydrogen-induced porosity should be able to form, the presented sample 6 (Figure 4-37(a)) indicates the opposite. If the solidification time is sufficiently long, in case of a dendrite arm spacing of $\lambda_2 = 86 \mu\text{m}$ a liquidus to eutectic time of approximately 90 s can be estimated, hydrogen seems to be able to nucleate pores or inflate existing pore embryos even at a low total hydrogen content of the melt.

The large pores in sample 15 presented in Figure 4-37(b) show a phenomenon not discussed so far. Some of the largest, highly spherical pores seem to have developed tortuous appendixes in the form of "shrinkage" or late-stage pores. An explanation for this is probably the remaining solidification shrinkage, even after the early-stage pore formation associated with hydrogen precipitation. The highly spherical pores seemed to be unable to compensate the majority of the solidification shrinkage and thus in the final solidification stage shrinkage porosity formed, but not in insulated, liquid pockets, but in the proximity of the already existing "gas" pores. Consequently, these pores were "extended" by the growth of late-stage shrinkage porosity. So far, this phenomenon was only observed in weaker form as small protrusions of pores, for example, in case of the Na modified cylinder head castings from the industrial casting experiments (see Figure 1-2).



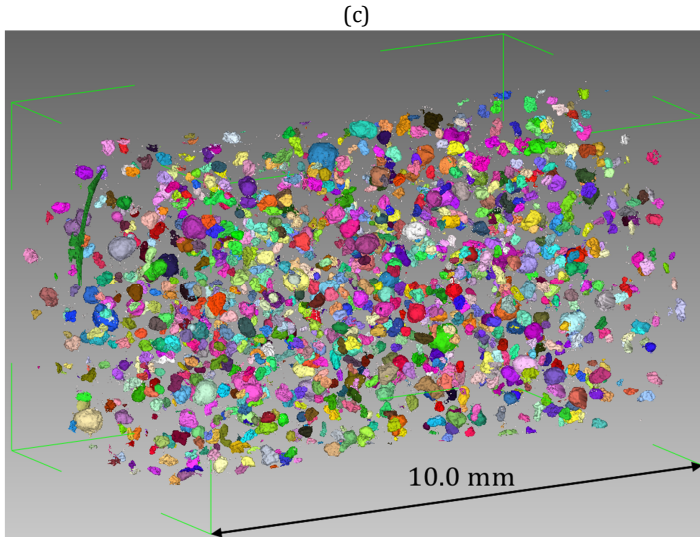


Figure 4-38: Selected XCT-scans performed with $5\ \mu\text{m}$ spatial resolution, AlSi7Cu0.5Mg(Sr) , wedge castings, medium cooling rate: (a) wedge specimen 20, $\lambda_2 = 31\ \mu\text{m}$, $g_p = 1.587\ \%$, $C_H = 0.179\ \text{ml} / 100\ \text{g}$, $\text{DI} = 14.12$; (b) wedge specimen 26, $\lambda_2 = 29\ \mu\text{m}$, $g_p = 0.213\ \%$, $C_H = 0.157\ \text{ml} / 100\ \text{g}$, $\text{DI} = 2.62$; (c) wedge specimen 35, $\lambda_2 = 32\ \mu\text{m}$, $g_p = 2.032\ \%$, $C_H = 0.38\ \text{ml} / 100\ \text{g}$, $\text{DI} = 16.48$ (scan artefacts are excluded from the data evaluation)

If and to what extent these pore protrusions occur is likely determined by the local permeability in the last solidification stages and by the local microstructure (by the number density and size of liquid pockets in the solid network). Yet, it seems important to understand when already formed spherical pores are extended or when new and isolated shrinkage pores are formed, since in case of sample 15 (Figure 4-37(b)), which shows a maximum envelope diameter of about $2500\ \mu\text{m}$, this “extension” of already existing high sphericity pores seemed to have increased the maximum defect size quite significantly. Possibly, the coarse microstructure delayed or even prevented effective isolation of liquid pockets. If there is a definite threshold value regarding the local solidification rate, it cannot be determined due to a quite significant solidification rate gap of the extracted specimens. The local thermal gradient, which was not independently evaluated in this work, might also play an essential role in the isolation of liquid pools.

A final aspect that should be discussed in this section are the changes in porosity and pore morphology due to the melt treatment as illustrated in Figure 4-38. The first two wedge castings showed a hydrogen reading of $C_H = 0.179$ ml / 100 g and a density index of $DI = 14.12$. The observable porosity of specimen 20 (see Figure 4-38(a)) agrees with the expectations of a sufficient hydrogen content to induce early-stage pores and the relatively high cooling rate. These two aspects led to the formation of many highly spherical pores of relatively small size. The melt treatment by 12 NITRAL 10® tablets before pouring the next two wedges reduced the density index significantly (from $DI = 14.12$ to 0.38 after six tablets and back to 2.62 after another six tablets), but altered the hydrogen level only slightly. The result is a significantly reduced average porosity of sample 26 presented in Figure 4-38(b). Also, the pores became much smaller and on average much more tortuous (but still smaller spherical pores can be observed). This development could be caused by a significant drop in hydrogen, which would mean the hydrogen measurement was incorrect or distorted (possibly by the tablet treatment itself, as discussed in Section 4.3.1). A second plausible explanation could be that the hydrogen measurement was, in fact, correct and the hydrogen removal efficiency of the tablets was very low (see Section 4.3.1 for a more detailed discussion). Despite the uncertainty in the hydrogen content, the DI dropped sharply after the tablet treatment. Therefore the melt condition and ability to form pores seemed to have changed markedly. An explanation in the latter case could be that potential embryos or nuclei for pore formation and growth (in the form of oxides, impurities, inclusions or other potential nucleation sites) were effectively removed from or deactivated in the melt (in contrast to the hydrogen). The effect could be that early pore nucleation, without a significant contribution due to a pressure drop, became impossible and only later during solidification pores were able to form. The few small but spherical pores, which can be found in the sample 26 after tablet treatment (Figure 4-38(b)), could be an indication for a higher hydrogen level than the density index indicates or some remaining potential nuclei, even after the tablet treatment. A hydrogen-induced or assisted pore growth in the final stages of solidification should still lead to highly tortuous pores. Besides, the hydrogen diffusion to the pores should be significantly reduced by the solid network as was shown by Carlson et al. (33). Carlson et al. also conclude that the increased capillary pressure inside of the pores, induced by strong impingement with the dendritic network and the associated increasing pore surface curvature, would effectively counteract the diffusion-limited pore growth. This could explain the significant drop in average porosity after the NITRAL 10® tablet treatment, although the hydrogen level presumably was only reduced slightly which would be in agreement with the argumentation and modelling work by Carlson et

al. To investigate the potential for early pore nucleation in the second experimental set after the NITRAL 10[®] treatment, a sample which solidified in the thick wedge section was evaluated by the author (not shown in this work), and it showed a significant similarity to the sample 15 presented in Figure 4-37(b), meaning large spherical pores, only without the previously described pore protrusions. Hence, the second given explanation for the observed development in the pore characteristic could be valid. The unchanged pore number density before and after the NITRAL 10[®] treatment gives no conclusive evidence for one of the presented explanations or the other. In the final solidification stage, the combined effects of hydrogen supersaturation and pressure drop could activate nuclei which are quite unfavourable and stagnant in the earlier stages of solidification. Despite the presumably significant differences in pore development history, the final pore number density could, but not necessarily has to change. Still, it is interesting that intensive melt treatment did not alter the pore number density.

Finally, after the addition of seven HYDRAL 40[®] tablets, the hydrogen content (by HYCAL measurement) and density index increased considerably ($C_H = 0.38$ ml / 100 g, $DI = 16.48$) and the pore number density dropped slightly (from $4.53 \times 10^{10} \text{ m}^{-3}$ to $3.49 \times 10^{10} \text{ m}^{-3}$). This level of hydrogen supersaturation might be sufficient to nucleate pores even at less favourable nucleation sites at an early stage. Either way, the HYDRAL 40[®] tablet treatment did not seem to have introduced more pore nuclei into the melt, at least this cannot be concluded based on the slight drop in pore number density. Additionally, if most of the volume deficit is already compensated before the final solidification stage, a smaller driving force for further pore nucleation and growth seems reasonable and thus a lower pore number density possible.

4.3.5. Sphericity

Figure 4-39 shows the plot of mean sphericity versus average porosity. In Figure 4-39(a, b, c) the colour indicates the hydrogen content, the density index, and the dendrite arm spacing, respectively. All 36 samples from the wedge casting experiments exhibit a mean sphericity between about 0.25 and 0.83. A separation of the samples in different specimen populations is not as easily possible as in some of the previously presented figures of the characteristic measures versus porosity, but the samples with a hydrogen level of 0.04 ml / 100 g seem somewhat separated from the other samples of higher hydrogen content (see the population marked with "DROP IN SPHERICITY" in Figure 4-39(c)). Note that again the two samples (marked by red circles in Figure 4-39(c)) of this separated group show high porosity values, one of them up to 1.87 %, but lie at the boundary of the supposed second specimen population. These samples show, as mentioned before, much larger DAS than the

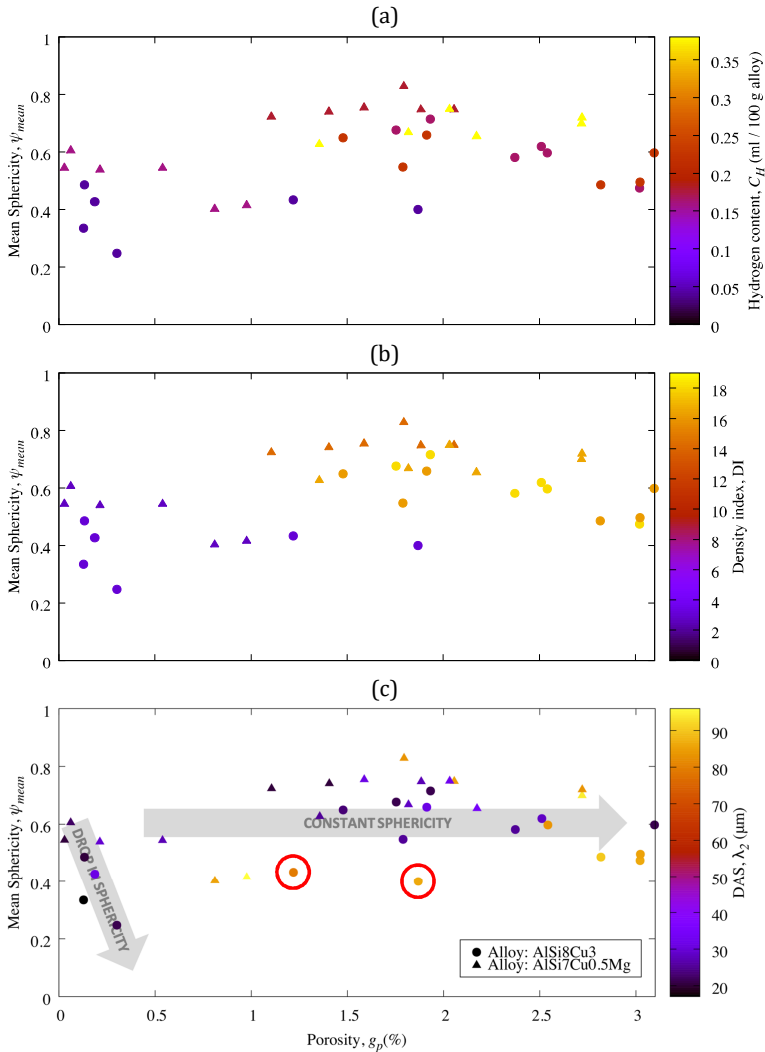


Figure 4-39: Plot of the mean sphericity ψ_{mean} versus the average porosity g_p . The hydrogen content (a), density index (b), and DAS (c) are colour-coded. Two presumable trends and two samples (red circles) are indicated in (c).

other samples with low hydrogen content. The higher hydrogen samples show a high mean sphericity value that does not seem to decrease even at average porosity levels of 3.1 %. A similar presumable separation of specimens can be made based on the density index presented in Figure 4-39(b). Here a separation between lower and higher mean sphericity samples can be drawn up to a density index of 2.99. In Figure 4-39(c) the plot of the mean sphericity versus porosity does not indicate any connection between sphericity and the dendrite arm spacing. There are samples with low and high DAS values of higher and lower mean sphericity, relative to the range of observed mean sphericities in the presented data set. As was already discussed, samples of lower average porosity also are low in DAS, but low DAS samples can be found up to the highest porosity level of approximately 3.1 %, and they do not differentiate in regard of their mean sphericity value as shown in Figure 4-39(c).

The samples which show a drop in mean sphericity with increasing average porosity can be directly linked to the identified high gradient population in the plots of the envelope mean diameter and maximum envelope diameter versus porosity (Figure 4-31 and Figure 4-32). Just as the characteristic mean values of the porosity distributions ($d_{s,mean}$, $d_{e,mean}$, $d_{s,max}$, and $d_{e,max}$) seem directly linked to the average porosity and may follow two or three distinct trends, the mean sphericity of the samples of the wedge castings seems to show two independent trends. This means mean sphericity wise that the pore population of low hydrogen and low DAS (see Sections 4.3.2 for more details) can be distinguished by mean sphericity from the other samples, but the other two pore populations which were identified (the low and high DAS samples with higher hydrogen content) are indistinguishable in the presented mean sphericity versus porosity plot. Again, the presented results suggest that there is a fundamental change in porosity mechanism between the low (0.04 ml / 100 g) and high (above 0.157 ml / 100 g) hydrogen level samples with a relatively sharp turnover point.

If the mean sphericity (which is as all evaluated mean values in this section volume-weighted) is high, it means that the largest pores in those samples are also of high sphericity on average. The question arises how the largest pores up to high average porosity levels and at a significant volume (see Figure 4-30) and size (see Figure 4-32) can retain a highly spherical shape. In general, there seem to be two explanations for high mean pore sphericity in a specimen. The first explanation for a high mean sphericity value is that small pores are formed. These small pores fit into the interdendritic spaces and are primarily in contact with the eutectic and of high sphericity to satisfy the Laplace-Young equation (as Felberbaum et al. (28) showed), which might have been the case for some of the identified medium to high hydrogen level (above 0.157 ml / 100 g), low DAS (up to 34 μm) population in Figure

4-31. The high cooling rates of these low DAS samples are thought to limit the hydrogen redistribution by diffusion in the melt and produce many highly spherical, relatively small pores (for example displayed in Figure 4-38(a)). The second possible explanation for high mean sphericity, even at low cooling rates and higher porosity levels, is an early pore formation of high sphericity pores. This formation is probably driven by hydrogen supersaturation and extensive redistribution, facilitated by a higher hydrogen content and lower cooling rates of the melt. These pores have to nucleate before the dendrite coherency point to be able to push dendrites away to increase their room for further growth while retaining their highly spherical shape. Murphy et al. showed (29) in experiments with an AlCu20 alloy that early nucleating pores, at a solid fraction of only 0.13, can push equiaxed dendritic crystals away. This way a significant amount of the total volume deficit due to solidification can be compensated in an early stage and only a few (or none at all) large pores can form in the final stage of solidification (which would also not be represented by the mean sphericity value if the pore volume is small). This way a significant amount of porosity (up to 3.1 % in the presented data) seems to be able to form, without much impingement of the largest pores. This is a likely explanation for the nucleation and growth history of the specimens of higher hydrogen level (above 0.157 ml / 100 g) and higher DAS (above 83 μm).

Based on the argument presented in the above paragraph, it seems understandable that the cooling rate, represented by the dendrite arm spacing, does not seem to influence the pore shape (represented by mean sphericity) if the hydrogen content is sufficiently high. As Figure 4-39 indicates, the DAS is not linked to the mean sphericity for hydrogen-containing specimens, for example, the specimen which contains most porosity (about 3.1 %) and which shows a mean sphericity of about 0.6 and only 21 μm in DAS. The explanation for this would be early nucleation of relatively small, high sphericity pores. Also, the pores would have to grow rapidly, or a large number of pores would have to grow simultaneously to be able to compensate most of the solidification shrinkage before a high solid fraction is reached so none or little late-stage porosity forms. Even quite small pores which form in a late-stage during solidification have to develop a large surface area because they are strongly confined by the dendritic network and would necessarily reduce the mean sphericity significantly.

For the previously mentioned sample with a DAS of 21 μm of the alloy AlSi8Cu3, this means (based on a simulation of the casting and solidification process with MAGMASOFT®) an approximate liquidus to eutectic time of about 10 s or an average cooling rate between $T_{\text{liq}} = 596 \text{ }^\circ\text{C}$ and $T_{\text{eut}} = 567 \text{ }^\circ\text{C}$ of about 3 K/s. Carlson et al. (33) predict, based on a finite-rate hydrogen diffusion-controlled porosity model that

also takes the effect of feeding flow and melt pressure into account, for a pore number density of 10^{11} m^{-3} and an A356 alloy containing 0.13 ml / 100 g hydrogen that a cooling rate of 3 K/s should already lead to a significant suppression of porosity by impingement with the dendritic structure and a significant increase of the capillary pressure inside of the pore. Their predictions show reasonably good agreement with selected experimental results which indicates that finite-rate hydrogen diffusion might control pore growth. In the results of this section, there is little indication of significant impingement between the pores and the dendritic structure as indicated by the mean sphericity results. Carlson et al. also show by model predictions that a pore number density of 10^{12} m^{-3} would lead to a cooling rate-independent porosity because the pores become so small that no interaction by impingement with the solid phase is likely to occur. As presented in Section 4.3.2, in the data set of the wedge castings, the pore number density lies in the range between $1.4 \times 10^{10} \text{ m}^{-3}$ and $1.4 \times 10^{11} \text{ m}^{-3}$. Possibly the actual pore number density is higher than the XCT results of the wedge XCT analysis shows. The XCT scans of the industrial castings were partly done with $3 \mu\text{m}$ resolution and showed pore densities in the range of 10^{12} m^{-3} . With a pore number density this high, suppression of a significant pore-dendritic-network interaction seems reasonable, and it would explain the observations for the high cooling rate, high hydrogen samples. Nevertheless, their argument would only cover the high sphericity, high cooling rate samples. It fails to capture why samples with an envelope mean diameter (see Figure 4-31) up to about $1400 \mu\text{m}$ (at 2.82 % porosity) do not impinge significantly. As mentioned before, pushing of equiaxed dendrites by pore growth at a low solid fraction seems the only plausible explanation in this case. This indicates that Carlson et al.'s approach is not valid across the presented experimental range of this section and in many cases an increase in capillary pressure is unlikely to reduce the porosity with increasing cooling rate, but the pushing of the equiaxed dendrite is more likely to occur. The two decisive factors might be: how much hydrogen is present in the melt and when do the pores form during solidification.

In case of the high cooling rate samples which also contain medium to high hydrogen levels Carlson et al.'s argument of little pore-dendrite interaction might be valid. The second situation described by Carlson et al. of pore impingement with a solid dendritic network might not arise at all because this necessitates a rigid solid network to increase the capillary pressure in the pore. Possibly in the presented data, some samples were so hydrogen-rich that pore nucleation always occurred before dendrite coherency and thus the pores were able to retain high sphericity.

The low hydrogen and high cooling rate samples are most likely explained by a different mechanism which is not (strongly) influenced by hydrogen precipitation but by solidification shrinkage and significant pore-dendritic-network interaction.

4.3.6. Synopsis of wedge castings and industrial castings

In the following section, the XCT results of the wedge casting experiments are compared to the XCT results generated from the industrial castings. To generate a similar microstructure in the wedge casting as in the industrial casting experiments, the same two alloys (as close to the chemical analysis as available, see Chapter 3), AlSi8Cu3(Sr) and AlSi7Cu0.5Mg(Sr), were poured in a wedge mould. The mould was designed to reproduce the solidification conditions of the CPS process. The purpose of the comparison of both experiments is to investigate how the hydrogen content, the density index, and the cooling rate influence the average porosity as well as the pore distribution characteristics. Additionally, the results of the industrial casting experiments should be assessed in the context of the additional available information (gas level and density index).

4.3.6.1. Spherical and envelope diameter versus average porosity

Figure 4-40 shows two plots of spherical mean diameter versus average porosity. Figure 4-40(a) shows the samples of the industrial castings with the indication of dendrite arm spacing as a colour range. It can be seen that although most samples with a low DAS exhibit low porosity and low spherical mean diameter values, there are samples that do not follow this observation and there are also samples with high DAS that exhibit low porosity and spherical mean diameter. Figure 4-40(b) shows the results of the wedge castings (colour indicates DAS) together with the results of the industrial castings. The industrial castings are shown as the two identified specimen populations: grey population (GP) and black population (BP), which were introduced in Section 4.3.2. The maximum of the spherical mean diameter of the industrial casting experiments is significantly lower than the maximum spherical mean diameter of the wedge casting experiments (about 500 μm compared to almost 1000 μm) but since the specimens with the largest spherical mean diameter values also exhibit about double the amount of porosity compared to the high porosity samples of the industrial casting trials, the general trend of the BP is basically continued. The specimens of the wedge castings which exhibit a low DAS form a third presumable trend with the shallowest gradient compared to the GP and BP (compare Figure 4-40(b)). Some specimens of the wedge castings with porosity below 0.5 % and low DAS may also follow the GP trend showing the highest gradient.

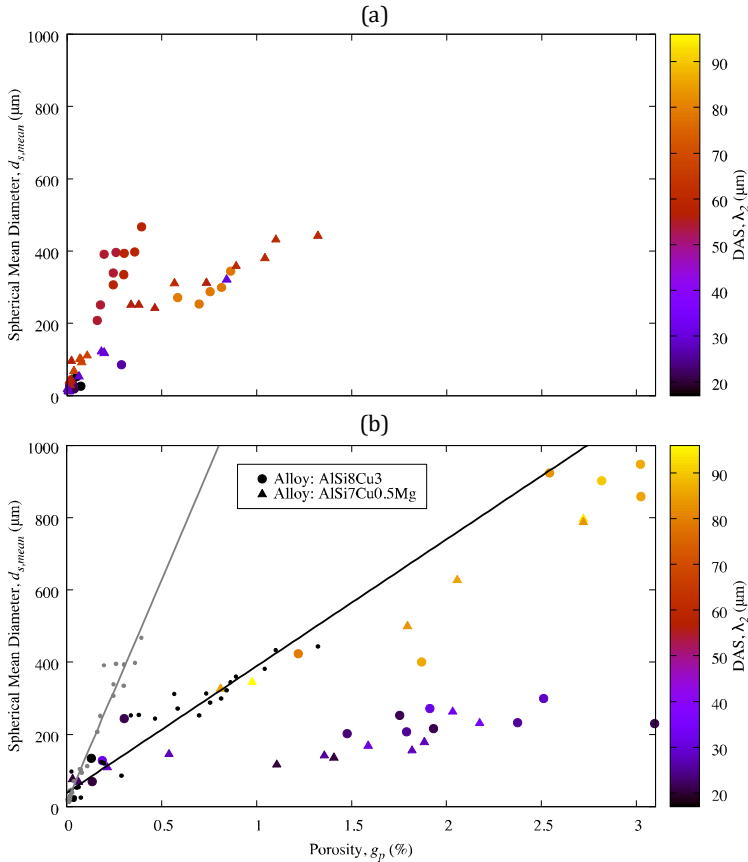


Figure 4-40: Two plots of the spherical mean diameter $d_{s,mean}$ versus the average porosity g_p . In plot (a), the industrial castings are shown with DAS indicated by colour. In plot (b), the industrial castings are shown as the grey and black population, as introduced in Section 4.2, marked by grey and black points and fitted by the grey and black linear functions. Additionally, the specimens of the wedge castings are shown with the DAS indicated by colour.

Figure 4-41 shows two plots of the maximum spherical diameter versus average porosity. The plot in the top (a) shows the samples of the industrial castings with the DAS indicated by colour. The plot in the bottom (b) also shows these samples indicated by grey (GP) and black (BP) points and additionally the samples of the wedge casting experiments. It can be seen that the samples with low porosity and low DAS of the wedge castings might follow the steep GP trend line, whereas most other samples of the wedge castings are slightly below the BP trend line (high DAS samples) or follow a significantly lower gradient relationship (especially the samples of low DAS).

Figure 4-42 shows two plots of the envelope mean diameter versus porosity. As in the two previous figures (Figure 4-40 and Figure 4-41), plot (a) shows the specimens of the industrial castings. The colour indicates the specimens' DAS. Although most low DAS samples are also low in porosity, there are exceptions. There are also samples of high DAS in both visible trend lines of very low porosity, and there is no systematic parameter which determines if a sample follows one trend or the other. Figure 4-42(b) shows the wedge casting samples (DAS indicated by colour) together with the industrial casting samples (identified by black points in case of the black population and by grey points in case of grey population samples). The same principle observations can be drawn as in the two previous bottom figures (Figure 4-40(b) and Figure 4-41(b)). The large DAS samples of the wedge castings are positioned slightly below the BP trend line; the low DAS samples follow a shallower gradient correlation of envelope mean diameter versus porosity. The low DAS, low porosity samples might be correlated to the GP trend. Interestingly, in contrast to the two previously presented figures, which were showing characteristic measures based on the pore volume (spherical mean diameter and maximum spherical diameter), the comparison of the envelope mean diameter (based on pore dimension) of the industrial castings and the wedge castings shows comparable maximum values in both data sets. Here specimen of the GP containing about 0.4 % porosity show approximately the same characteristic pore dimensions as pores in samples showing more than 3 % porosity. Note that the pore shapes are dramatically different, the GP samples containing highly tortuous pores, whereas the respective wedge samples showing highly spherical, high volume pores.

Figure 4-43 shows the two plots of the industrial castings (a) and additionally the wedge castings (b) for the maximum envelope diameter versus porosity. Colour indicates the DAS of the samples. What was only indicated weakly by the three previous plots, is now more pronounced. The low DAS, low porosity and low hydrogen samples (compare Figure 4-32) follow the GP linear trend. As in the three previous plots, the wedge castings of high DAS seem to be positioned slightly below the BP

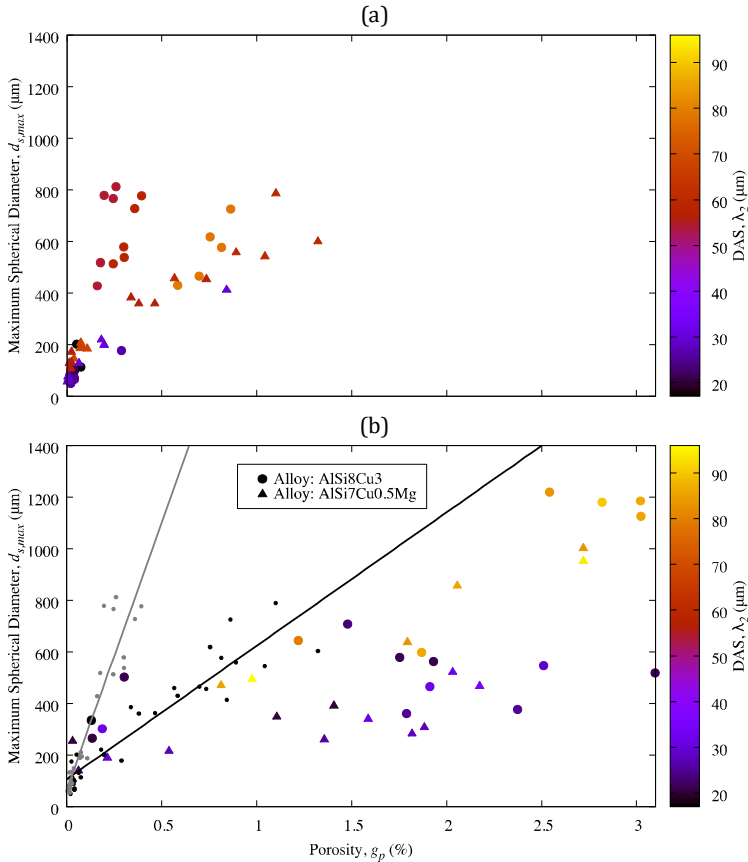


Figure 4-41: Two plots of the maximum spherical diameter $d_{s,max}$ versus the average porosity g_p . In plot (a), the industrial castings are shown with DAS indicated by colour. In plot (b), the industrial castings are shown as the grey and black population, as introduced in Section 4.2, marked by grey and black points and fitted by the grey and black linear functions. Additionally, the specimens of the wedge castings are shown with the DAS indicated by colour.

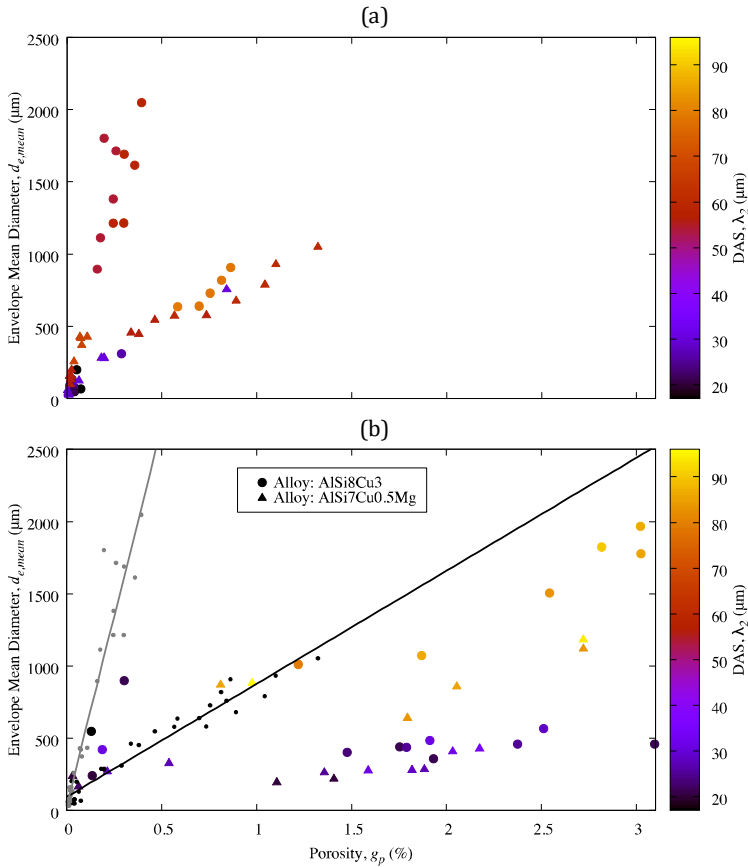


Figure 4-42: Two plots of the envelope mean diameter $d_{e,mean}$ versus the average porosity g_p . In plot (a), the industrial castings are shown with DAS indicated by colour. In plot (b), the industrial castings are shown as the grey and black population, as introduced in Section 4.2, marked by grey and black points and fitted by the grey and black linear functions. Additionally, the specimens of the wedge castings are shown with the DAS indicated by colour.

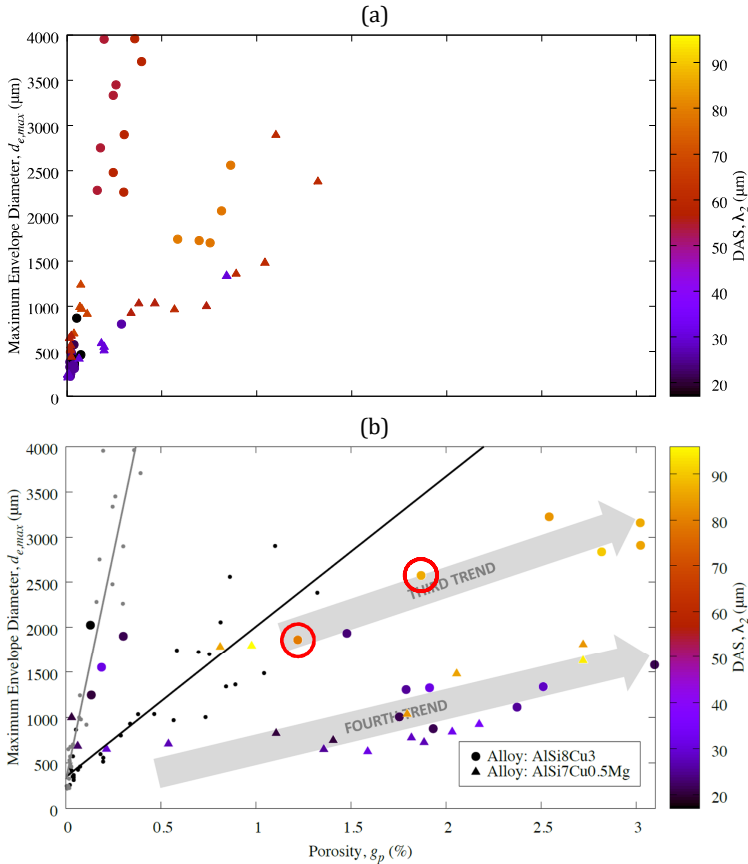


Figure 4-43: Two plots of the maximum envelope diameter $d_{e,max}$ versus the average porosity g_p . In plot (a), the industrial castings are shown with DAS indicated by colour. In plot (b), the industrial castings are shown as the grey and black population, as introduced in Section 4.2, marked by grey and black points and fitted by the grey and black linear functions. Additionally, the specimens of the wedge castings are shown with the DAS indicated by colour. Two red circles mark specimens that are of particular interest.

trend line, whereas the high DAS wedge samples form a new third correction with the smallest gradient. As discussed in Section 4.3.2, these last two specimen populations can probably be linked to a higher (or very high, especially in case of the lowest gradient population) hydrogen level.

There is an interesting difference between the industrial casting experiments and the wedge casting experiments. In the case of the industrial castings, the distinction of the presumably shrinkage-related GP and the presumably gas-related BP can be drawn without consideration of the dendrite arm spacing of the samples. Both characteristic trend populations contain high and low DAS. This is not the case for the wedge casting experiments. Only if the DAS is low (up to $\lambda_2 = 31 \mu\text{m}$), the low hydrogen samples of the wedge experiments follow the GP (see Figure 4-43(b)). The two specimens indicated by red circles in Figure 4-43(b) (also marked before in previous plots) are also low in hydrogen ($C_H = 0.04 \text{ ml} / 100 \text{ g}$) but large in DAS ($\lambda_2 = 79$ and $86 \mu\text{m}$) and are much better described by the BP trend line. For the other wedge samples, the effect is even more pronounced. The DAS becomes the determining factor if a specimen is described by the BP trend (high DAS samples) or if it is better described by a new, small-gradient correlation (low DAS). The explanation could be, that the GP samples, both the industrial castings and wedge samples, only show this high gradient and strong sensitivity to increasing porosity up to a certain critical DAS value. This threshold could be between the largest DAS values of the industrial casting samples in this trend, $\lambda_2 = 67 \mu\text{m}$, and the before mentioned DAS of $\lambda_2 = 79 \mu\text{m}$. It would make sense that if the dendritic structure becomes coarser, the available space for pore growth in the last stages of solidification also become larger and thus a growing pore does not have to spread as strongly between the existing dendrites as for smaller DAS.

Since the total volume deficit should change less than the available space between the dendrites (note that the high gradient, low DAS, low hydrogen population is hardly distinguishable in the plot of spherical mean diameter versus porosity), primarily the degree of pore-dendrite interaction would change. Without impingement, the dendrite interaction could cease quite abruptly. Thus, the driving force for the strong increase in maximum envelope diameter is lost. Besides, there might be a hydrogen level influence. Sufficiently low cooling rates might lead to hydrogen precipitation, even at very low hydrogen levels. The sharp drop in solubility during solidification and the very long solidification times are expected to cause nucleation events. The observed threshold behaviour can better be explained by nucleation than an inflation mechanism. Inflation occurs even below critical hydrogen levels and occurs continuously. A steady change of the porosity type with increasing hy-

drogen level or solidification time would be the result. Instead, an abrupt morphology change is observed between the DAS values of 67 μm and 79 μm and, consequently, a nucleation mechanism seems more reasonable to operate. A second characteristic threshold might explain the degree of pore-dendritic-network interaction in case of the BP industrial samples and the higher hydrogen wedge samples. At medium hydrogen levels (probably the case for the BP samples) the sensitivity for the coarseness of the microstructure might be lost because now, for the first time, hydrogen-driven pores nucleate much earlier and even at low cooling rates at a density that is still sufficient to avoid pores becoming large enough for significant dendrite interaction during growth (retain a high sphericity and show now cooling rate sensitivity), which would explain the BP specimen characteristics. In transition cases, both types of porosity, gas-driven and shrinkage-driven pores might be present. The wedge samples probably contained even more hydrogen, as was indicated by the high density index and HICAL hydrogen measurement, increasing the pore size even further and thus the pore-dendrite interaction once more became controlling for the pore size. Low cooling rates (large DAS) values led to the formation of fewer hydrogen pores (lower pore number density), and by significant inflation, very large pores can form. If on the other hand at high hydrogen levels the cooling rate is high (small DAS) the number density of hydrogen-induced pores increases and each pore becomes smaller. Furthermore, the pore-solid interaction becomes irrelevant for the final characteristic pore size. These explanations are not necessarily in conflict with the previous observations of a cooling rate-independent pore number density (see Section 4.3.2). It could likely be the case that independently of the previous pore nucleation and growth history, in the very last stages of solidification all potent pore nucleation sites are activated. These pores would in case of shrinkage porosity grow to large tortuous micropores (and lead to the observed results), or in case of earlier gas induced porosity, to very tiny pores at or close to the XCT resolution limit. In this case, these pores would not influence the characteristic measures evaluated in this work due to the volume-weighted approach which was taken. The pore number density could also rather be influenced by the number and size of the liquid pools at the end of solidification. These, in turn, might be considerably influenced by the local thermal gradient as a factor which potentially determines the stage of liquid pocket isolation in the mushy zone.

4.3.6.2. Maximum versus mean diameters

Figure 4-44 shows the two plots of the maximum spherical diameter versus the spherical mean diameter. In plot (a), only the industrial casting samples are shown. Colour indicates the DAS. In Figure 4-44(b) the data from industrial casting experiments are shown as black points together with the samples of the wedge casting experiments with DAS indicated by colour. Additionally, in Figure 4-44(b) two linear fit functions are indicated. The solid black correlation is only based on the data from the industrial casting experiments and discussed in detail in Section 4.2.3. The dashed correlation is based on all available data from the industrial casting experiments as well as the wedge casting experiments (96 in total) and given by

$$d_{s,max} = 1.26d_{s,mean} + 107 \quad \text{(Equation 141)}$$

For the samples with a large DAS, which are all located at large spherical mean diameters above approximately 300 μm , a slight deviation from the BP fit function can be observed. Since Figure 4-44(a) already indicates an increase in the scatter of the sample data around the black fit function with an increasing spherical mean diameter, these samples might also be positioned at the outer scatter area of the black trend line and still follow the same correlation.

Figure 4-45 shows two plots of the maximum envelope diameter versus the envelope mean diameter. In plot (a), the samples from the industrial casting experiments are presented, and DAS is indicated by colour. In Figure 4-45(b) the samples from Figure 4-45(a) are displayed as black points. The solid black line indicates the linear fit function. This fit is discussed in detail in Section 4.2.3. Additionally, in Figure 4-45(b) the samples of the wedge castings are displayed; DAS is indicated by colour. Based on all data from the industrial and the wedge casting experiments, a second linear correlation is fitted and indicated by the dashed trend line. The correlation is given by

$$d_{s,max} = 1.76d_{s,mean} + 314 \quad \text{(Equation 142)}$$

The samples showing a small DAS are located in the lower-left (small envelope mean diameters) corner of the plot, the specimen showing a large DAS are located in the upper right corner (larger envelope mean diameters). The same general but less distinct trend can be observed for the industrial castings. Small DAS samples are more likely to be found in the area of small envelope mean diameters and vice versa.

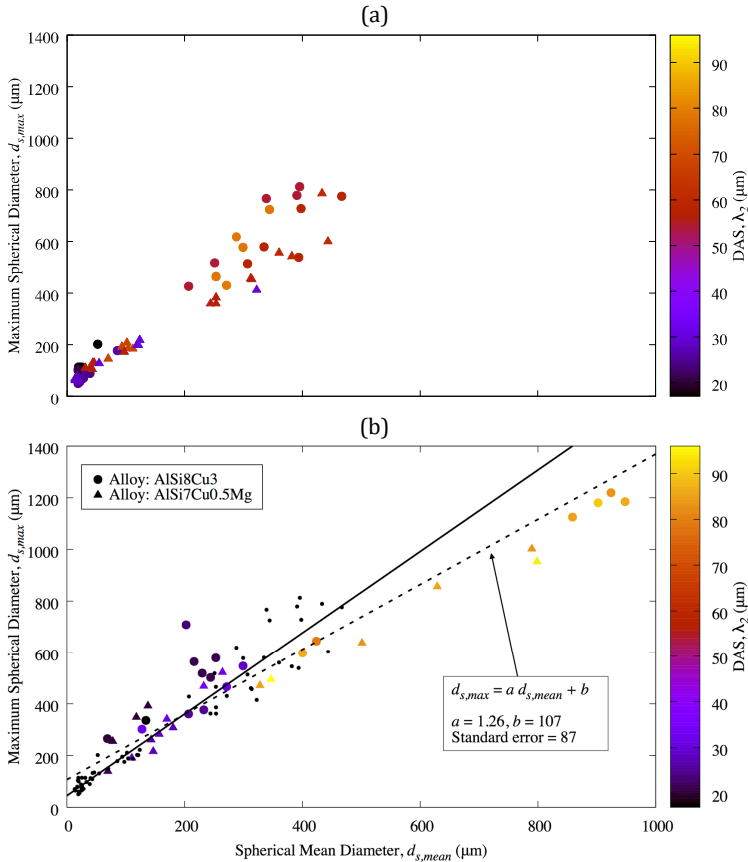


Figure 4-44: Two plots of the maximum spherical diameter $d_{s,max}$ versus the spherical mean diameter $d_{s,mean}$. In plot (a), the industrial castings are shown with DAS indicated by colour. The plot (b) shows the industrial castings marked as black points and fitted by the black linear function (as introduced in Section 4.2.3). Additionally, the specimens of the wedge castings are shown with the DAS indicated by colour and all data points are linearly fitted by the dashed correlation.

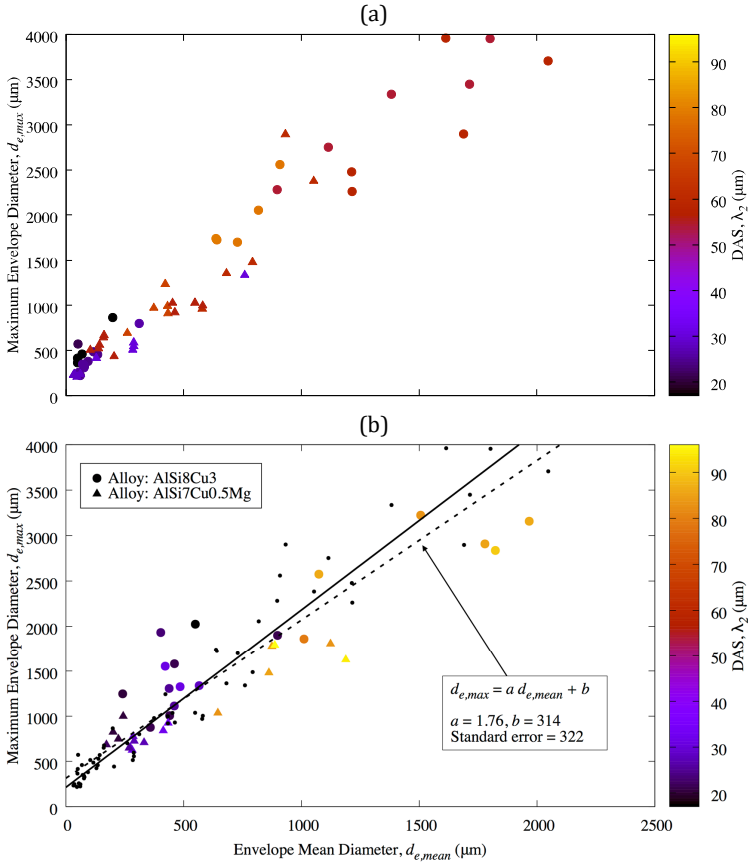


Figure 4-45: Two plots of the maximum envelope diameter $d_{e,max}$ versus the envelope mean diameter $d_{e,mean}$. In plot (a), the industrial castings are shown with DAS indicated by colour. The plot (b) shows the industrial castings marked as black points and fitted by the black linear function (as introduced in Section 4.2). Additionally, the specimens of the wedge castings are shown with the DAS indicated by colour and all data points are fitted by the dashed linear function.

After introducing the plots of the industrial casting data of the maximum versus mean diameters with the developed linear correlations (presented in Section 4.2.3), the observations are once more confirmed by the additional information from the wedge castings, which means that there seems to be a very robust correlation of the mean spherical diameter and maximum spherical diameter (describing the weighted mean and maximum pore volume) as well the mean envelope diameter and maximum envelope diameter (describing the weighted mean and maximum pore dimensions). To summarise once more the many differences between the conducted experiments: two alloys (AlSi8Cu3 and AlSi7Cu0.5Mg) with significant differences in alloy composition were cast. Two different eutectic modifiers (Na, Sr) were used in case of the industrial castings. Three different castings were produced: two industrial castings covering the typical solidification conditions of a permanent mould and a sand mould process, as well as a wedge casting. The extracted specimens cover a wide range of local solidification conditions (DAS ranging from 17 μm to 96 μm) and finally, by melt treatment, a range of 0.04 to 0.38 ml hydrogen / 100 g alloy (by HYCAL measurement) and a wide range of density indexes were investigated. All 96 experimental XCT results show the same fundamental correlation between the mean and the maximum pore distribution characteristics, which suggests that a fundamental and quite universal pore distribution characteristic has been uncovered.

4.3.6.3. Sphericity

Figure 4-46 shows two plots of the mean sphericity versus average porosity. In Figure 4-46(a) the samples from the industrial casting experiments are displayed (colour indicates DAS) and in Figure 4-46(b) both the industrial samples (here indicated as black points) and the wedge samples are shown. One can see that the samples from the wedge castings which exhibit low DAS and low porosity seem to follow the GP trend line which shows a sharp initial decrease of mean sphericity with increasing porosity. The majority of the wedge castings exhibit high mean sphericity at the same level as the industrial castings samples which follow the BP trend line. The black trend line seems fit to describe the specimen behaviour for these samples up to about 3.1 % porosity. As indicated in Figure 4-46(a) for the industrial casting samples, the DAS does not seem to systematically influence the mean sphericity in the DAS range of the industrial castings up to 78 μm . Wedge specimens of large and small DAS are well described by the BP trend line throughout the whole porosity range (Figure 4-46(b)). As before, two cases of particular interest are the samples marked by red circles in Figure 4-46(b).

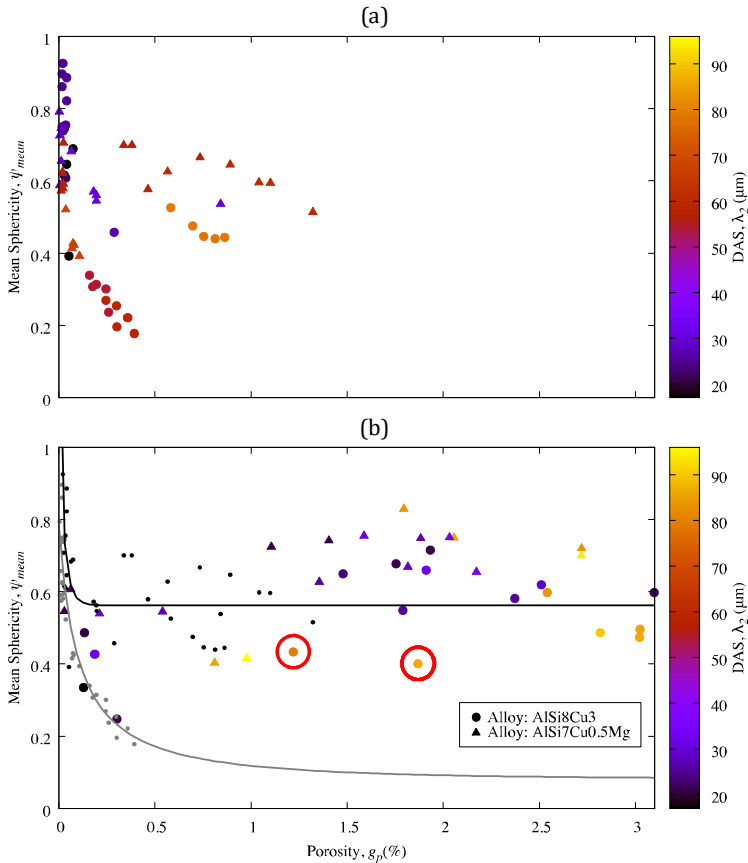


Figure 4-46: Two plots of the mean sphericity ψ_{mean} versus the average porosity g_p . In plot (a), the industrial castings are shown with DAS indicated by colour. In plot (b), the industrial castings are shown as the grey and black population, as introduced in Section 4.2, marked by grey and black points and fitted by the grey and black functions. Additionally, the specimens of the wedge castings are shown with the DAS indicated by colour. Two red circles mark specimens that are of particular interest.

These specimens show large DAS values of 79 and 86 μm , but belong to the low hydrogen level samples (0.04 ml / 100 g) of the wedge experiments which seem to follow the GP trend line. These samples are discussed further in the next paragraph.

It is quite remarkable that the high porosity samples (close to the black fit function) do not seem to decrease in mean sphericity, which means that the largest pores are highly spherical up to porosity values of about 3.1 %. An obvious explanation for this behaviour could be the aforementioned mechanism of early pore nucleation and the pushing of equiaxed dendrites (as observed by Murphy et al. (29)). This way the pores are, even at very high levels of microporosity, not hindered in their growth by the dendritic network and can retain a spherical-like shape. This is even true for low DAS samples, which solidified relatively fast. As an example, the wedge sample with the highest observed porosity level of 3.1 % should be mentioned. This sample exhibits a mean sphericity of 0.6 which is very close to the limiting value of the BP trend line of 0.56 and at the same time a DAS of only 21 μm . Two explanations would explain this behaviour. The first is that the pores in samples of high porosity, low DAS and high mean sphericity form and grow rapidly before the dendritic network reaches dendrite coherency and equiaxed dendrite pushing seems unrealistic.

A second explanation is that a high number density of hydrogen-induced pores, most of them small enough to avoid pore-dendrite impingement. In the case of the previously mentioned specimen showing 3.1 % porosity, the mean envelope diameter is almost 500 μm . In aluminium foundry practice for grain refined Al-Si alloys (e.g. AlSi8), grain sizes between 500 to 1000 μm are typically observed, which means that a potential octahedra gap of 566 μm ($0.7 \times 800 \mu\text{m}$) should be available as a potential space for pore growth without significant impingement and that larger pores are likely to start to impinge with the solid network quite significantly. In this case, a drop in mean sphericity should be a consequence. For the previously mentioned sample with an envelope mean diameter of about 500 μm this explanation seems only just plausible. In case of larger envelope mean diameters of up to almost 2000 μm the theory of dendrite pushing seems more likely. Possibly both mechanisms do occur and a transition from first to the second occurs, dependent on cooling rate. It might also be the case that in samples of high hydrogen level, pores always nucleate very fast and lead to a rearrangement of the crystalline solidifying structure. This rearrangement could decouple the pore shape from the total pore volume as well as the cooling rate.

The crankcase castings produced in the industrial casting experiments, as well as the Na modified AlSi7Cu0.5Mg cylinder head castings, form the experimental database for the black fit function. The hydrogen level of the high sphericity wedge experiment samples which can also be described by the black fit function gave readings from 0.157 to 0.380 ml / 100 g. Except for the industrial cylinder heads cast

from AlSi8Cu3(Sr) and AlSi7Cu0.5Mg(Sr), which were thoroughly rotor degassed before pouring, and the wedge casting samples showing a hydrogen level of 0.04 ml / 100 g, all samples show a high and constant mean sphericity over porosity behaviour. This suggests a sharp turnover point for the hydrogen level that determines the characteristic sphericity behaviour a sample. Simultaneously, a low cooling rate seems also to be able to pull a sample with low hydrogen content (0.04 ml / 100 g) into the characteristic specimen regime described by high constant mean sphericity. In contrast to the other low hydrogen samples (0.04 ml / 100 g) which all follow the GP trend line and show a DAS between 17 and 31 μm (compare Figure 4-39), the samples which are marked by red circles in Figure 4-46(b) show a much larger DAS of 79 and 86 μm and do not follow the GP trend, but the BP trend (or lie slightly below the BP trend). The slow cooling rate which is associated with a DAS this large, leads to the formation of high-sphericity pores, even at very low hydrogen levels. As the morphology analysis (see Section 4.3.4) showed, these samples show a mixed type of porosity, consisting of high sphericity pores and (eventually inflated) shrinkage porosity. As suggested by Carlson et al. (33), who presented a finite-rate hydrogen diffusion dependent porosity model, in this case, the solidification might have been slow enough to enable an extended diffusion of hydrogen to small existing pore nuclei and facilitated extensive growth before dendrite impingement occurred. Concurrently, the very large DAS values should be accompanied by large interdendritic spaces which should also reduce the degree of impingement between pores and dendritic network and increase the mean sphericity. Since the change in behaviour occurs between the specimen with a largest DAS of the GP ($\lambda_2 = 67 \mu\text{m}$), and the previously mentioned marked (red circle) sample with the lower DAS of the two ($\lambda_2 = 79 \mu\text{m}$), there could be another turnover point which determines the pore morphology characteristic for low hydrogen samples between these respective DAS values.

4.3.7. Summary

A total of 36 XCT specimens from 12 laboratory wedge castings were analysed. Two alloys, AlSi8Cu3(Sr) and AlSi7Cu0.5Mg(Sr) were cast and are very close to the alloys which were used for the industrial castings. By melt treatment, different hydrogen levels were adjusted, and quantitative hydrogen measurements were done by the state-of-the-art measurement system "HYCAL". Additionally, the density index (DI) was determined by the reduced pressure test. The goal of the wedge casting experiments was to investigate the (quantitative) effect of hydrogen and cooling rate in commonly used aluminium cast alloys on the amount, distribution, and characteristics of microporosity, which was achieved by producing a wedge casting that was

designed to reproduce the solidification characteristics of the industrial CPS process.

The HYPAL measurement was not as reproducible as expected based on preceding discussions with the supplier company. The low measurement reproducibility can be attributed to the melt treatment by tablet additions, which might interfere with the measurement. The degassing capabilities of the HYDRAL 40® tablets seem to be limited, possibly by the low surface area of the released hydrogen-containing bubbles during submersion. Nevertheless, for applications in typical foundry practice, the achievable hydrogen levels seem to be sufficient.

After the melt treatment with multiple tablets, a significant burn off of Mg and Sr can be determined. The density index determination by the reduced pressure test seems to reach its limit to resolve changes in the hydrogen level of the aluminium melt around 16 to 18. Moreover, the DI seems to be much more sensitive to melt treatment than the hydrogen measurement and was either low or high in the conducted experiments.

The degassing capabilities of the NITRAL 10® tablets are questionable. If the changes in porosity and DI can be attributed to the removal of hydrogen or stem from a cleaning effect or the deactivation of potential nuclei remains unclear. There are points for both theories, and also a combination of both is possible.

By application of the same XCT-data evaluation methods as for the industrial castings, the XCT-samples taken from the wedge casting experiments were analysed. None of the plots in this section shows any influence of the two alloys on the analysed characteristic porosity measures, although the differences in chemical composition between the alloys are significant.

The results indicate that a certain amount of hydrogen, between 0.04 and 0.157 ml / 100 g, can effectively annihilate the porosity difference of the two alloys, which would be expected due to the microstructural differences of the solidifying microstructure.

Hydrogen levels of 0.157 ml / 100 g or more, have only a weak influence on the pore distribution characteristics. The only clear result is that samples with 1 % of average porosity or less also stem from castings which are low in hydrogen. A low hydrogen level seems to be a necessary, but not sufficient, condition to produce low porosity castings. On the other hand, an elevated hydrogen level prevents the formation of low porosity material, based on the evaluated experimental data.

In the wedge castings, the DAS has the most distinct effect on the characteristic porosity distribution measures ($d_{s,mean}$, $d_{s,max}$, $d_{e,mean}$, and $d_{e,max}$) except on the mean sphericity. Specimens which contain at least 0.157 ml / 100 g hydrogen show a high sensitivity to DAS. If these samples solidified rapidly (small DAS) the increase in pore size and volume with average porosity is very low. If these samples solidified

slowly (large DAS), they show a strong sensitivity to average porosity. Samples with a low hydrogen content (in the present data 0.04 ml / 100 g) are not captured by this observation and show, if the DAS is not extremely large, a very strong average porosity dependency (the sharpest increase of pore volume and size of all three identified trends in the wedge castings).

In contrast to the expectations based on the literature review, for samples which contain a least 0.157 ml / 100 g hydrogen, a suppression of porosity formation by cooling rate cannot be confirmed. The reason might be, that sufficiently high hydrogen levels lead to an early pore formation and can form most of the porosity before a pore-dendritic-network interaction (and the associated increase in capillary pressure) can occur. A general conclusion of the evaluation of the characteristic porosity measures is that the hydrogen level does not influence the pore volume (in the form of the mean and maximum values) much, but the pore dimensions under certain conditions (very low hydrogen levels versus higher hydrogen level). Note, that this does not mean that the average porosity is influenced in the same way.

Although the XCT scanning resolution has a strong influence on the pore number density, within one resolution setting no systematic influence of the local cooling rate on the pore number density can be established. Besides the explanation that the scanning resolution was insufficient to resolve a newly formed high number of very small pores (up to a scanning resolution of 3 μm used in the industrial castings), an alternative explanation would be that athermal nucleation theory is not applicable to micropores but rather classical heterogeneous nucleation with the consequence of a cooling rate independent almost instantaneous activation of all suitable nucleation sites.

As presented and discussed previously for the industrial castings, one linear function seems able to describe the correlation between the spherical mean diameter and maximum spherical diameter as well as between the envelope mean diameter and the maximum envelope diameter. This observation is independent of the cooling rate (represented by DAS), chemical composition, and hydrogen content (captured by a quantitative hydrogen measurement as well as in the form of the density index). This aspect is essential for the prediction of the critical defect size for the fatigue proof design of cast components in general.

The pore morphology of the low hydrogen samples is comparable to the previously described pore morphology of the “shrinkage” or late-stage porosity samples from the industrial casting experiments (see Figure 4-16) unless the solidification rate is very low. In this case, even at very low hydrogen levels (0.04 ml / 100 g), hydrogen precipitation seems to occur which also shows in higher mean sphericity of the samples. The result is a mixed type of porosity, consisting of low and high

sphericity pores. This type was observed before in medium solidification rate samples of the BP industrial casting samples.

An intensive melt treatment with NITRAL 10® tablets did decrease the density index significantly, but the hydrogen level (by HYCAL measurement) only decreases slightly. The pore number density was not affected by the NITRAL 10® treatment.

Apart from the low DAS samples of 0.04 ml / 100 g hydrogen content, all samples show a constant (with some scatter) mean sphericity up to about 3.1 % average pore volume. The low hydrogen samples seem to show fundamentally different behaviour concerning the pore nucleation stage (late-stage nucleation and growth) compared to all other samples (early-stage nucleation and growth). The pores formed in these samples are probably driven by the solidification shrinkage and a significant pore-dendritic-network impingement. The hydrogen dependent turnover point can be placed between 0.04 and 0.157 ml / 100 g. The specimens which contain a higher level of hydrogen (above 0.157 ml / 100 g) all show the same high mean sphericity values, but two different mechanisms could lead to this result. At high cooling rates, a higher number of spherical pores nucleate because hydrogen diffusion and redistribution is effectively suppressed. The pore number density is high enough to avoid pore-dendritic-network interaction, and thus the cooling rate (and consequently the fineness of the dendritic network) does not influence the pore morphology or total amount of porosity. At low cooling rates an early formation (with low initial pore number density) of pores which grow to significant size and during their growth push equiaxed dendrites away, seems more likely. In this case, significant pore-dendritic-network interaction can also be avoided. An intermediate hydrogen level in which the solid network could significantly influence the pore shape and amount of porosity by impingement and increase of capillary pressure is probably not covered in the conducted experiments. Though, the BP defined specimen population of the industrial castings might indicate the behaviour which can be expected of an intermediate hydrogen level.

In contrast to the industrial castings, which do not show any consistent influence of the cooling rate (by DAS) on the pore morphology (described by mean sphericity), the wedge castings, except for the low hydrogen samples, show a strong dependency. Where the low hydrogen samples only compensate for volumetric shrinkage by late-stage pore formation, higher hydrogen levels facilitate the formation of early-stage (high sphericity) pores. There seems to be a transition stage in which "shrinkage porosity" and "hydrogen porosity" can coexist in one specimen (low to medium hydrogen levels as well as solidification rates). Very low cooling rates seem to be able to initiate early-stage porosity, even at very low hydrogen levels. It was also observed that these low solidification rates (in this case 79 μm and above) lead, even at a low hydrogen level, to the formation of some high sphericity

porosity. The result is a mixed porosity type (as in some transition samples of the BP). If the hydrogen content then increases further, the pores become larger if sufficient time is available for hydrogen diffusion. Because the pores form very early at low solid fractions, they can push equiaxed dendrites away to increase their space for further growth and to avoid a significant increase in capillary pressure. If finally, at high hydrogen levels the cooling rate is increased, early pore formation leads to a higher density of high sphericity pores. The hydrogen diffusion is effectively suppressed. The pore size is reduced significantly. Because the increase in cooling rate does not lead to a suppression of porosity formation on average, it can be concluded that little pore-dendritic network interaction occurs. Two mechanisms could explain this observation. First, because the smaller spherical pores still nucleate early and because they fit into the interdendritic spaces, effective suppression of porosity is avoided. Second, although the pore number density is higher and the pores are smaller in size, there is dendrite pushing and a rearrangement of the solidifying solid structure around the pores.

Throughout the described development of hydrogen level and solidification rate, the characteristic pore shape (described by mean sphericity) only changes once, between low hydrogen samples and medium to high hydrogen samples.

Despite all these changes in the presumable pore formation mechanism and the differences in chemical composition, cooling rate, eutectic modifier, hydrogen level, or density index leading to significant differences in average porosity, pore volume, pore morphology, and pore size, the correlations of the maximum spherical diameter to mean spherical diameter, as well as the maximum envelope diameter to the envelope mean diameter, stays the same (for all 96 XCT samples). This observation most certainly is a new intrinsic characteristic of microporosity in aluminium cast alloys. Figure 4-47 summarises the developed hypotheses on the development of microporosity based on the evaluation of the industrial casting experiments, together with the wedge casting experiments and all the available information.

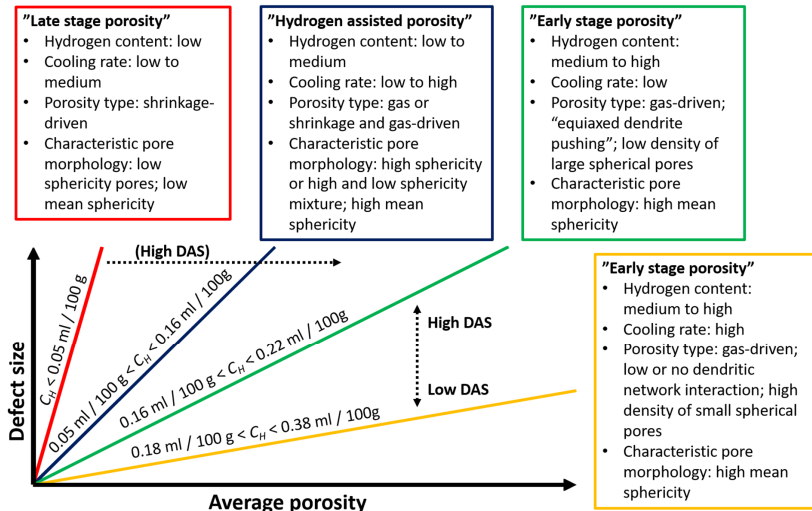


Figure 4-47: Schematic illustration of the results of the conducted experiments regarding the defect size of a micropore versus average porosity. The proposed mechanisms leading to the observed changes are indicated, as is the influence of the hydrogen content as well as the local cooling rate (by DAS).

5. Conclusions

To evaluate the importance of oxides on the porosity development in Al-Si-Cu-Mg cast alloys a first, relatively simple, experiment was conducted. The results showed that for up to 30 min holding time prior to solidification, no qualitative change in porosity could be observed. This is the case for low (approximately 0.07 wt%) and medium (approximately 0.60 wt%) Mg levels. The oxide healing mechanism proposed in the literature due to a spinel formation could not be substantiated. Additions of Mg up to 0.5 wt% to the cast alloy EN AB-46000 lead to a more dispersed, less in the hot spot concentrated, spatial porosity distribution. The effect is attributed to a shift of the formation temperature of the Al_2Cu and a destabilisation of the eutectic mushy zone. Another factor for the increased amount of porosity at higher Mg levels could be a reduced surface tension and thus a promotion in pore nucleation. The introduction of young oxides by melt manipulation before solidification leads to a slight qualitative increase in porosity, but other influential factors like Mg level mask the effect. By conducting a second experimental set where the location of the hot spot was shifted from the top surface to the specimen centre, the previous observations could be confirmed once more. The insights gained allow the conclusion that the influence of oxides (or “bifilms”) on porosity in aluminium casting is not paramount and thus a more detailed investigation of further potential porosity factors is worth pursuing.

In the industrial casting experiments, a wide range of process conditions was varied to investigate the effects on average porosity and pore size distributions in foundry practice. To cover a wide industrial application range, two alloys (AlSi8Cu3 and AlSi7Cu0.5Mg) were cast in two different industrial processes (Rotacast® and CPS).

The analysis of the pore volume distribution with increasing porosity showed a pore volume shift from the smallest pores to the medium-sized pores (AlSi7Cu0.5Mg(Sr) cylinder heads and the AlSi8Cu3(Sr) crankcases) and in one experimental set a transition stage of a bimodal pore volume distribution between samples with a maximum in the smallest and largest pore size bins (AlSi7Cu0.5Mg(Na) cylinder heads). The results suggest that a significant amount of the volume deficit can be compensated by early-stage porosity. In these cases, the driving force for pore growth in the final solidification stages is sharply reduced. The results further suggest destabilisation of the eutectic front at increased Cu levels and concomitantly an increased number of liquid and unfeedable melt pools at the end of solidification.

Since the XCT scanning resolution strongly affects the number density of pores in the evaluated specimens, a volume-weighted approach was chosen to enable comparative evaluations of the porosity characteristics.

In general, the industrial data can be divided into two characteristic specimen populations. The first shows a high sensitivity of the mean and maximum pore volume and size regarding the average porosity level; the second one shows a lower sensitivity. Both correlations are linear correlations and show increasing volume and size with increasing porosity. Additionally, the mean and maximum pore volume, as well as the mean and maximum pore size, are linearly correlated. The described correlations allow the prediction of important pore distribution characteristics if others are known by measurement or prediction. The analysis of the characteristic pore shape and mean sphericity reveals significant differences between both specimen populations. Tortuous, low sphericity pores dominate the high sensitivity population; high sphericity pores dominate the low sensitivity population. The argument is developed, that the pore nucleation stage is decisive for the formed characteristic pore morphology, in other words, early or late pore nucleation and growth relative to the progressing solid fraction. The average porosity and mean sphericity of each sample is used to predict the characteristic mean and maximum pore volume and size.

The two identified specimen populations are independent of the alloy, process, modification or cooling rate, but the hypothesis of a hydrogen dependency is developed, which is then more closely examined in the wedge casting experiments.

In the wedge experiments, a casting was produced which is capable of matching a microstructure gradient that can be found in the CPS process. All experimental conditions were adapted for the best comparison with the industrial castings. Additionally, the hydrogen content was manipulated by tablet treatments and measured by a state-of-the-art hydrogen measurement system (HYCAL). Reduced pressure tests were conducted to evaluate the density index as a commonly used quality control method in foundry practice.

The HYCAL system did not allow hydrogen control as accurately as anticipated. Two reasons for this behaviour were discussed, the tablet treatment itself, which might disturb the measurement system, and the degassing capability of the tablet treatment, which can be questioned based on the observed porosity development. The tablet treatment burns off significant amounts of Mg and Sr.

The density index as a quality indicator seems to lose its capability to resolve changes in gas level between 16 and 18 and generally seems much more sensitive to melt treatment by tablets than the hydrogen measurement.

In separate evaluations of the XCT data from the wedge experiments and joint evaluations together with the data generated in the industrial casting experiments,

the following further conclusion can be drawn. The previously introduced specimen population which shows a high sensitivity regarding the characteristic measures on average porosity is most likely correlated to low hydrogen contents. The second specimen population identified in the industrial casting experiments is probably of low to medium hydrogen content and in some cases shows a mixed shrinkage and gas-driven porosity type. Up to a characteristic dendrite arm spacing of $67\ \mu\text{m}$, no significant influence of cooling rate on both populations can be identified. Between $67\ \mu\text{m}$ and $79\ \mu\text{m}$ DAS a shift from low sphericity, late-stage porosity to a mixed transition form of high and low sphericity porosity, seems to occur. Two additional pore populations could be identified and added to this picture by the wedge casting experiments. The first showing a slightly lower, the second showing a much lower sensitivity of pore volume and size (in average and maximum) to porosity compared to the industrial casting pore populations. These two specimen populations are most likely correlated to high hydrogen levels and show a strong sensitivity to cooling rate. High cooling rates lead to the lowest sensitivity population.

Despite the multitude of variations in the alloy, process, modification, cooling rate and hydrogen level, all analysed samples follow the same correlation between the respective mean and maximum diameters of pore volume and size. This seems to indicate a fundamental and intrinsic characteristic of microporosity in Al-Si-Cu-Mg cast alloys.

The presented results improve the understanding of the correlation between aluminium alloy composition, solidification conditions, gas content, and the resulting average porosity and pore size distribution. The developed correlations will improve the capabilities of the Integrated Computational Materials Engineering (ICME) approach. These correlations are the first steps in a through process modelling framework which begins with the prediction of the microstructural features including the maximum pore size. All subsequent steps (e.g. heat treatment, machining and in-service performance) are based on this prediction, and thus it is of paramount importance for the fatigue proof design of new aluminium cast components.

6. Future work

The conducted experiments led to the answer to many questions on microporosity in aluminium cast alloys, but at the same time, new questions arose which could not be answered within the framework of this thesis.

- The general influence of aluminium oxides on (micro-)porosity could be demonstrated in this work, but the fundamental understanding if and in which way these are involved in pore nucleation and growth remains unclear. The ever-increasing capabilities of synchrotron X-ray analysis, to resolve in-situ processes on smallest spatial ($< 0.1 \mu\text{m}$) and temporal ($< 1 \text{s}$) scales, seem most promising to shine a light on the details of pore nucleation. Moreover, the inconclusive influence of the cooling rate on the pore number density presented in this work might be answered by the aforementioned spatial resolutions provided by a synchrotron X-ray source.
- The quantitative measurement of oxide distributions and sizes in aluminium castings would not only promote the understanding of porosity but would also dramatically enhance the modelling and ultimately the material properties of new aluminium castings by a better flow and transport prediction and control of material quality.
- The presented correlations for the development of the pore size distribution in aluminium castings are most interesting, but the control and measurement of the hydrogen level of an aluminium melt stay very challenging (especially in a foundry environment). Possibly, a better hydrogen control in future experiments can lead to more conclusive results. Moreover, the question arises, if the presented findings can be extrapolated to even more aluminium cast alloys or even to other nonferrous or ferrous cast alloys.
- One of the most pressing issues, the reliable prediction of the total amount of microporosity under varying melt and process conditions, remains unsolved and porosity models to this day fail to cover the whole range of the conditions in foundry practice. Building upon an accurate porosity prediction, the presented results would have even higher applicability, and thus further development in this area seems highly useful.
- The presented results indicate two different mechanisms for pore formation: an early-stage pore formation driven by hydrogen supersaturation and a shrinkage-driven late-stage porosity. In contrast to the first, the second type should be quite sensitive to changes in microstructure development in the last solidification phase. An investigation of the effects of eutectic modification on both porosity formation types might yield very different results.

7. Bibliography

1. WANG, Q.G, APELIAN, D and LADOS, D.A. Fatigue behavior of A356/357 aluminum cast alloys. Part II – Effect of microstructural constituents. *J Light Metals*. 2001. Vol. 1, no. 1, p. 85–97. DOI 10.1016/S1471-5317(00)00009-2.
2. BUFFIÈRE, Jean-Yves, SAVELLI, Stéphane, JOUNEAU, Pierre-Henri, MAIRE, Eric and FOUGERES, Roger. Experimental study of porosity and its relation to fatigue mechanisms of model Al–Si7–Mg0.3 cast Al alloys. *Materials Science and Engineering: A*. 2001. Vol. 316, no. 1, p. 115–126.
3. GAO, Y. X., YI, J. Z., LEE, P. D. and LINDLEY, T. C. The effect of porosity on the fatigue life of cast aluminium-silicon alloys. *Fatigue & Fracture of Engineering Materials & Structures*. 2004. Vol. 27, no. 7, p. 559–570.
4. ZHANG, B., POIRIER, D. R. and CHEN, W. Microstructural effects on high-cycle fatigue-crack initiation in A356.2 casting alloy. *Metallurgical and Materials Transactions A*. 1 October 1999. Vol. 30, no. 10, p. 2659–2666. DOI 10.1007/s11661-999-0306-3.
5. COUPER, M. J., NEESON, A. E. and GRIFFITHS, J. R. Casting defects and the fatigue behaviour of an aluminium casting alloy. *Fatigue & Fracture of Engineering Materials & Structures*. 1990. Vol. 13, no. 3, p. 213–227.
6. GARB, C., LEITNER, M. and GRÜN, F. Fatigue Strength Assessment of AlSi7Cu0.5Mg T6W Castings Supported by Computed Tomography Microporosity Analysis. *Procedia Engineering*. 1 January 2016. Vol. 160, p. 53–60. DOI 10.1016/j.proeng.2016.08.862.
7. AMANATIADIS, Angelos and ANDREADIS, Ioannis. A survey on evaluation methods for image interpolation. *Measurement Science and Technology*. 1 October 2009. Vol. 20, no. 10, p. 104015. DOI 10.1088/0957-0233/20/10/104015.
8. BDG (ed.). *Volumendefizite von Gussstücken aus Aluminium-, Magnesium- und Zinkgusslegierungen [Volume deficits of aluminium, magnesium, and zinc castings]*. BDG, 2010. P, 202.
9. HEIBERG, G., NOGITA, K., RAANES, M., DONS, A. L., DAHLE, A. K. and ARNBERG, L. Effect of magnesium, iron and copper on eutectic solidification of

-
- hypoeutectic aluminum-silicon alloys. *AFS Transactions*. 2002. Vol. 110, p. 347–358.
10. SAMUEL, F. H., SAMUEL, A. M. and DOTY, H. W. Factors controlling the type and morphology of Cu-containing phases in 319 Al alloy. *AFS Transactions*. 1996. Vol. 104, p. 893–901.
 11. SAMUEL, A. M., OUELLET, P., SAMUEL, F. H. and DOTY, H. W. Microstructural interpretation of thermal analysis of commercial 319 Al alloy with Mg and Sr additions. *AFS Transactions*. 1997. Vol. 105, p. 951–962.
 12. MULAZIMOGLU, M. H., TENEKEDJIEV, N., CLOSSET, B. M. and GRUZLESKI, J. E. Studies on the Minor Reactions and Phases in Strontium-treated Aluminium-Silicon Casting Alloys. *Cast Metals*. 1 March 1993. Vol. 6, no. 1, p. 16–28. DOI 10.1080/09534962.1993.11819122.
 13. DJURDJEVIC, M., STOCKWELL, T. and SOKOLOWSKI, J. The effect of strontium on the microstructure of the aluminium-silicon and aluminium-copper eutectics in the 319 aluminium alloy. *International Journal of Cast Metals Research*. 1 September 1999. Vol. 12, no. 2, p. 67–73. DOI 10.1080/13640461.1999.11819344.
 14. LI, Z., SAMUEL, A. M., SAMUEL, F. H., RAVINDRAN, C. and VALTIERRA, S. Effect of alloying elements on the segregation and dissolution of CuAl₂ phase in Al-Si-Cu 319 alloys. *Journal of Materials Science*. 1 March 2003. Vol. 38, no. 6, p. 1203–1218. DOI 10.1023/A:1022857703995.
 15. LI, Z., SAMUEL, A. M. and SAMUEL, F. H. Role of P and Fe on the precipitation of copper intermetallics in 319 alloys. *Journal of Materials Science Letters*. 1 April 2003. Vol. 22, no. 8, p. 585–587. DOI 10.1023/A:1023342227912.
 16. MCDONALD, Stuart D., DAHLE, Arne K., TAYLOR, John A. and STJOHN, David H. Modification-related porosity formation in hypoeutectic aluminum-silicon alloys. *Metallurgical and Materials Transactions B*. 1 December 2004. Vol. 35, no. 6, p. 1097–1106. DOI 10.1007/s11663-004-0065-x.
 17. ROY, N., SAMUEL, A. M. and SAMUEL, F. H. Porosity formation in Al-9 Wt pct Si-3 Wt pct Cu alloy systems: Metallographic observations. *Metallurgical and Materials transactions A*. 1996. Vol. 27, no. 2, p. 415–429.
 18. MONDOLFO, Lucio F. *Manganese in Aluminium Alloys*. Manganese Centre, 1978. ISBN 978-2-901109-01-3. Google-Books-ID: f0N2QgAACAAJ

19. COUTURE, AAFS. Iron in aluminum casting alloys - a literature survey. *International cast metals journal*. 1981. Vol. 6, no. 4, p. 9–17.
20. CREPEAU, P. N. Effect of iron in Al-Si casting alloys: a critical review. *AFS Transactions*. 1995. Vol. 103, p. 361–366.
21. MBUYA, T. O., ODERA, B. O. and NG'ANG'A, S. P. Influence of iron on castability and properties of aluminium silicon alloys: literature review. *International journal of cast metals research*. 2003. Vol. 16, no. 5, p. 451–465.
22. NARAYANAN, L. A. and SAMUEL, F. H. Thermal analysis studies on the effect of cooling rate on the microstructure of 319 aluminum alloy. *AFS Transactions*. 1992. Vol. 100, p. 383–391.
23. IWAHORI, H., TAKAMIYA, H., YONEKURA, K., YAMAMOTO, Y. and NAKAMURA, M. Influence of iron and manganese on feedability of AC2B aluminum alloy. *Casting (Japanese)*. 1988. Vol. 60, no. 9, p. 590–595.
24. SAMUEL, A. M., SAMUEL, F. H., VILLENEUVE, C., DOTY, H. W. and VALTIERRA, S. Effect of trace elements on β -Al₅FeSi characteristics, porosity and tensile properties of Al-Si-Cu (319) cast alloys. *International Journal of Cast Metals Research*. 1 September 2001. Vol. 14, no. 2, p. 97–120. DOI 10.1080/13640461.2001.11819429.
25. VILLENEUVE, C., SAMUEL, A. M., SAMUEL, F. H., DOTY, H. W. and VALTIERRA, S. Role of trace elements in enhancing the performance of 319 aluminum foundry alloys. *AFS Transactions*. 2001. Vol. 109, p. 39–60.
26. DASH, M and MAKHLOUF, M. Effect of key alloying elements on the feeding characteristics of aluminum–silicon casting alloys. *Journal of Light Metals*. 2001.
27. DINNIS, CAMERON. *Porosity formation in unmodified Al-Si-Mg-(Cu) foundry alloys: the role of iron and manganese*. 2004.
28. FELBERBAUM, M. and RAPPAZ, M. Curvature of micropores in Al-Cu alloys: An X-ray tomography study. *Acta Materialia*. October 2011. Vol. 59, no. 18, p. 6849–6860. DOI 10.1016/j.actamat.2011.07.005.
29. MURPHY, A., BROWNE, D., HOULTZ, Y. and MATHIESEN, R. *IOP Conference Series: Materials Science and Engineering*. IOP Publishing, Bristol, 2016.

-
30. PUNCREOBUTR, C., LEE, P. D., HAMILTON, R. W. and PHILLION, A. B. Quantitative 3D Characterization of Solidification Structure and Defect Evolution in Al Alloys. *JOM*. January 2012. Vol. 64, no. 1, p. 89–95. DOI 10.1007/s11837-011-0217-9.
 31. THIELE, Wolfgang. *Die Oxydation von Aluminium- und Aluminiumlegierungs-Schmelzen [The oxidation of aluminium and aluminium alloy melts]*. 1962. Google-Books-ID: ohyNHAAACAAJ
 32. MULAZIMOGLU, H., HANDIAK, N. and GRUZLESKI, J. E. Some observations on the reduced pressure test and the hydrogen concentration of modified A356 alloy. *Transactions of the American Foundrymen's Society*. 1990. P. 225.
 33. CARLSON, Kent D., LIN, Zhiping and BECKERMANN, Christoph. Modeling the Effect of Finite-Rate Hydrogen Diffusion on Porosity Formation in Aluminum Alloys. *Metallurgical and Materials Transactions B*. 18 September 2007. Vol. 38, no. 4, p. 541–555. DOI 10.1007/s11663-006-9013-2.
 34. ARNBERG, L., CHAI, G and BACKERUD, L. Determination of dendritic coherency in solidifying melts by rheological measurements. *Materials Science and Engineering: A*. 20 December 1993. Vol. 173, no. 1, p. 101–103. DOI 10.1016/0921-5093(93)90195-K.
 35. CHAI, Guocai, BÄCKERUD, Lennart, RØLLAND, Tone and ARNBERG, Lars. Dendrite coherency during equiaxed solidification in binary aluminum alloys. *Metallurgical and Materials Transactions A*. 1 April 1995. Vol. 26, no. 4, p. 965–970. DOI 10.1007/BF02649093.
 36. CHAI, Guocai. *Dendrite coherency during equiaxed solidification in aluminium alloys*. Stockholm, Sweden : Stockholm University, 1994.
 37. DAHLE, A. K. and ARNBERG, L. Development of strength in solidifying aluminium alloys. *Acta Materialia*. 1 February 1997. Vol. 45, no. 2, p. 547–559. DOI 10.1016/S1359-6454(96)00203-0.
 38. FLEMINGS, Merton C. Behavior of metal alloys in the semisolid state. *Metallurgical transactions A*. 1991. Vol. 22, no. 5, p. 957–981.
 39. JOHN, A. *The Life of Sir Humphry Davy*. 1831.
 40. ALTENPOHL, D. G. *Aluminum: Technology, Application, and Environment*. . 1999.

41. BECKERMANN, C. Modelling of macrosegregation: applications and future needs. *International Materials Reviews*. October 2002. Vol. 47, no. 5, p. 243–261. DOI 10.1179/095066002225006557.
42. CAMPBELL, John. *Complete Casting Handbook: Metal Casting Processes, Techniques and Design*. Butterworth-Heinemann, 2011. ISBN 978-0-08-096423-2. Google-Books-ID: tMK6lummtq8C
43. DREZET, J.-M. and RAPPAZ, M. Modeling of ingot distortions during direct chill casting of aluminum alloys. *Metallurgical and Materials Transactions A*. 1 October 1996. Vol. 27, no. 10, p. 3214–3225. DOI 10.1007/BF02663872.
44. WRIEDT, H. A. The Al-O (Aluminum-Oxygen) system. *Bulletin of Alloy Phase Diagrams*. 1 December 1985. Vol. 6, no. 6, p. 548–553. DOI 10.1007/BF02887157.
45. WRIEDT, H. A. The Al-N (Aluminum-Nitrogen) system. *Bulletin of Alloy Phase Diagrams*. 1 August 1986. Vol. 7, no. 4, p. 329–333. DOI 10.1007/BF02873001.
46. COUTURIER, Gaël and RAPPAZ, Michel. Modeling of porosity formation in multicomponent alloys in the presence of several dissolved gases and volatile solute elements. . 2006. P. 143–152.
47. DANTZIG, J. A. and RAPPAZ, Michel. *Solidification*. EPFL Press, 2009. ISBN 978-0-8493-8238-3.
48. SIGWORTH, Geoffrey and KUHN, Timothy. Grain Refinement of Aluminum Casting Alloys. *Int J Metalcasting*. 2015. Vol. 1, no. 1, p. 31–40. DOI 10.1007/BF03355416.
49. GREER, A.I., COOPER, P.s., MEREDITH, M.w., SCHNEIDER, W., SCHUMACHER, P., SPITTLE, J.a. and TRONCHE, A. Grain Refinement of Aluminium Alloys by Inoculation. *Advanced Engineering Materials*. 5 February 2003. Vol. 5, no. 1–2, p. 81–91. DOI 10.1002/adem.200390013.
50. QUESTED, T. E. and GREER, A. L. Athermal heterogeneous nucleation of solidification. *Acta Materialia*. May 2005. Vol. 53, no. 9, p. 2683–2692. DOI 10.1016/j.actamat.2005.02.028.

51. LIU, L. X. and KIRKALDY, J. S. Thin film forced velocity cells and cellular dendrites—I. Experiments. *Acta Metallurgica et Materialia*. 1 August 1995. Vol. 43, no. 8, p. 2891–2904. DOI 10.1016/0956-7151(95)00029-U.
52. CHALMERS, B. Principles of Solidification. In : *Applied Solid State Physics* [online]. Springer, Boston, MA, 1970. p. 161–170. [Accessed 4 March 2018]. ISBN 978-1-4684-1856-9. Available from: https://link.springer.com/chapter/10.1007/978-1-4684-1854-5_5
53. TILLER, W. A, JACKSON, K. A, RUTTER, J. W and CHALMERS, B. The redistribution of solute atoms during the solidification of metals. *Acta Metallurgica*. 1 July 1953. Vol. 1, no. 4, p. 428–437. DOI 10.1016/0001-6160(53)90126-6.
54. LIPTON, J., GLICKSMAN, M. E. and KURZ, W. Equiaxed dendrite growth in alloys at small supercooling. *Metallurgical and Materials Transactions A*. 1 February 1987. Vol. 18, no. 2, p. 341–345. DOI 10.1007/BF02825716.
55. LIFSHITZ, I.M. and SLYOZOV, V.V. Kinetics of precipitation from supersaturated solid solutions. *Journal of Physics and Chemistry of Solids*. 1961. Vol. 19, p. 35–50.
56. WAGNER, C. Theorie der Alterung von Niederschlägen durch Umlösen (Ostwald Reifung). *Zeitschrift für Elektrochemie*. 1961. Vol. 65, no. 7–8, p. 581–591.
57. KATTAMIS, TZ and FLEMINGS, MC. Dendrite morphology microsegregation and homogenization of low-alloy steel. *Transactions of the Metallurgical Society of AIME*. 1965. Vol. 233, no. 5, p. 992.
58. AKAMATSU, Silvère, FAIVRE, Gabriel and MOULINET, Sébastien. The formation of lamellar-eutectic grains in thin samples. *Metallurgical and Materials Transactions A*. 1 August 2001. Vol. 32, no. 8, p. 2039–2048. DOI 10.1007/s11661-001-0016-y.
59. JACKSON, K. A. and HUNT, J. D. Lamellar and rod eutectic growth. *AIME Met Soc Trans*. 1966. Vol. 236, p. 1129–1142.
60. TRIVEDI, R., MAGNIN, P. and KURZ, W. Theory of eutectic growth under rapid solidification conditions. *Acta Metallurgica*. 1 April 1987. Vol. 35, no. 4, p. 971–980. DOI 10.1016/0001-6160(87)90176-3.

61. KARMA, Alain and SARKISSIAN, Armand. Morphological instabilities of lamellar eutectics. *Metallurgical and Materials Transactions A*. 1 March 1996. Vol. 27, no. 3, p. 635–656. DOI 10.1007/BF02648952.
62. AKAMATSU, S., PLAPP, M., FAIVRE, G. and KARMA, A. Overstability of lamellar eutectic growth below the minimum-undercooling spacing. *Metallurgical and Materials Transactions*. 2004. Vol. 35, no. 6, p. 1815.
63. WALKER, H., LIU, Shan, LEE, J. H. and TRIVEDI, R. Eutectic Growth in Three Dimensions. *Metallurgical and Materials Transactions A*. 1 July 2007. Vol. 38, no. 7, p. 1417–1425. DOI 10.1007/s11661-007-9163-0.
64. LU, Shu-Zu and HELLAWELL, A. The mechanism of silicon modification in aluminum-silicon alloys: impurity induced twinning. *Metallurgical Transactions A*. 1987. Vol. 18, p. 1721–1733.
65. HELLAWELL, A. The growth and structure of eutectics with silicon and germanium. *Progress in Materials Science*. 1 January 1970. Vol. 15, no. 1, p. 3–78. DOI 10.1016/0079-6425(70)90001-0.
66. GULLIVER, G. H. *Metallic Alloys Griffin*. London, 1922.
67. SCHEIL, Erich. Bemerkungen zur schichtkristallbildung. *Zeitschrift für Metallkunde*. 1942. Vol. 34, no. 3, p. 70–72.
68. BRODY, H. D. and FLEMINGS, M. C. Solute redistribution in dendritic solidification. *Transaction of the Metallurgical Society of AIME*. May 1966. Vol. 236, p. 615–624.
69. CLYNE, T. W. and KURZ, W. Solute redistribution during solidification with rapid solid state diffusion. *Metallurgical Transactions A*. 1 June 1981. Vol. 12, no. 6, p. 965–971. DOI 10.1007/BF02643477.
70. FLEMINGS, MC. Solidification processing. *Metallurgical transactions*. 1974.
71. FELBERBAUM, Milan. *Porosity in Aluminium Alloys: Visualization, Characterization, and Modeling*. ÉCOLE POLYTECHNIQUE FÉDÉRALE DE LAUSANNE, 2011.
72. *ASM Handbook*. ASM International, 1992. Google-Books-ID: _JBUAAAAMAAJ

-
73. DAHLE, Arne K. and ARNBERG, Lars. The rheological properties of solidifying aluminum foundry alloys. *JOM*. 1 March 1996. Vol. 48, no. 3, p. 34–37. DOI 10.1007/BF03222888.
 74. ARNBERG, L., DAHLE, A. K., PARADIES, C. J. and SYVERTSEN, F. Feeding mechanisms in aluminum foundry alloys. *AFS Transactions*. 1995. Vol. 103, p. 753–759.
 75. FLEMINGS, Merton C. *Solidification Processing*. McGraw-Hill, 1974. ISBN 978-0-07-021283-1. Google-Books-ID: Jpg4FBvb8hwC
 76. DAHLE, A. K., ARNBERG, L. and APELIAN, D. Burst feeding and its role in porosity formation during solidification of Al foundry alloys. *AFS Transactions*. 1997. P. 963–970.
 77. LEE, P. D. and HUNT, J. D. Hydrogen porosity in directional solidified aluminum-copper alloys: in situ observation. *Acta Materialia*. 1997. Vol. 45, no. 10, p. 4155–4169.
 78. NI, Jun and BECKERMANN, Christoph. A volume-averaged two-phase model for transport phenomena during solidification. *Metallurgical Transactions B*. 1991. Vol. 22, no. 3, p. 349–361.
 79. HUBBERT, Marion King and OTHERS. Darcy's law and the field equations of the flow of underground fluids. In : [online]. Shell Development Company, Exploration and Production Research Division, 1956. [Accessed 12 November 2016]. Available from: <https://www.onepetro.org/download?id=general%2FSPE-749-G>
 80. NIELSEN, Øyvind, ARNBERG, Sintef L., MO, A. and THEVIK, H. Experimental determination of mushy zone permeability in aluminum-copper alloys with equiaxed microstructures. *Metallurgical and Materials Transactions A*. 1999. Vol. 30, no. 9, p. 2455–2462.
 81. CARMAN, P. C. Fluid flow through granular beds. *Chemical Engineering Research and Design*. 1 December 1997. Vol. 75, p. S32–S48. DOI 10.1016/S0263-8762(97)80003-2.
 82. QIU, Caian, OLSON, Gregory B., OPALKA, Susanne M. and ANTON, Donald L. Thermodynamic evaluation of the Al-H system. *Journal of phase equilibria and diffusion*. 2004. Vol. 25, no. 6, p. 520.

83. PORTER, David A., EASTERLING, Kenneth E. and SHERIF, Mohamed. *Phase Transformations in Metals and Alloys, Third Edition (Revised Reprint)*. CRC Press, 2009. ISBN 978-1-4398-8357-0. Google-Books-ID: axDSBQAAQBAJ
84. ATKINS, Peter W. and PAULA, Julio De. *Physikalische Chemie*. John Wiley & Sons, 2013. ISBN 978-3-527-33247-2. Google-Books-ID: k6AtBAAAQBAJ
85. SIGWORTH, G. K. and ENGH, T. A. Chemical and kinetic factors related to hydrogen removal from aluminum. *Journal of Electronic Materials*. 1 December 1991. Vol. 20, no. 12, p. 447–460. DOI 10.1007/BF02816017.
86. WAGNER, Carl. *Thermodynamics of alloys*. Cambridge : Addison-Wesley Press, 1952.
87. ANYALEBECHI, P. N. Critical review of reported values of hydrogen diffusion in solid and liquid aluminum and its alloys. In : *LIGHT METALS-WARREN-DALE-PROCEEDINGS*-. TMS, 2003. p. 857–872. ISBN 0147-0809.
88. PEQUET, Ch, RAPPAZ, M. and GREMAUD, M. Modeling of microporosity, macroporosity, and pipe-shrinkage formation during the solidification of alloys using a mushy-zone refinement method: applications to aluminum alloys. *Metallurgical and Materials Transactions A*. 2002. Vol. 33, no. 7, p. 2095–2106.
89. LEE, P. D. and HUNT, J. D. Hydrogen porosity in directional solidified aluminum-copper alloys: in situ observation. *Acta Materialia*. 1 October 1997. Vol. 45, no. 10, p. 4155–4169. DOI 10.1016/S1359-6454(97)00081-5.
90. YAO, Lu, COCKCROFT, Steve, ZHU, Jindong and REILLY, Carl. Modeling of Microporosity Size Distribution in Aluminum Alloy A356. *Metallurgical and Materials Transactions A*. 1 December 2011. Vol. 42, no. 13, p. 4137–4148. DOI 10.1007/s11661-011-0811-z.
91. ARNBERG, Lars and MATHIESEN, Ragnvald H. The real-time, high-resolution x-ray video microscopy of solidification in aluminum alloys. *JOM*. 1 August 2007. Vol. 59, no. 8, p. 20–26. DOI 10.1007/s11837-007-0099-z.
92. COUTURIER, G and RAPPAZ, M. Effect of volatile elements on porosity formation in solidifying alloys. *Modelling and Simulation in Materials Science and Engineering*. 1 March 2006. Vol. 14, no. 2, p. 253–271. DOI 10.1088/0965-0393/14/2/009.

-
93. SABAU, A. and VISWANATHAN, S. Microporosity prediction in aluminum alloy castings. *Metallurgical and Materials Transactions B*. 2002. Vol. 33. DOI 10.1007/s11663-002-0009-2.
 94. FELICELLI, Sergio D., WANG, Liang, PITA, Claudio M. and ESCOBAR DE OBALDIA, Enrique. A Model for Gas Microporosity in Aluminum and Magnesium Alloys. *Metallurgical and Materials Transactions B*. April 2009. Vol. 40, no. 2, p. 169–181. DOI 10.1007/s11663-008-9217-8.
 95. TORQUATO, Salvatore. *Random Heterogeneous Materials: Microstructure and Macroscopic Properties*. Springer Science & Business Media, 2013. ISBN 978-1-4757-6355-3. Google-Books-ID: UTfoBwAAQBAJ
 96. STJOHN, D. H., DAHLE, A. K., EASTON, M. A., HUTT, J. E. C. and VELDMAN, N. L. M. Solidification of hypoeutectic aluminium - silicon alloys. *Materials Forum*. 1999. Vol. 23, p. 137–152.
 97. LEE, Y. C., DAHLE, A. K., STJOHN, D. H. and HUTT, J. E. C. The effect of grain refinement and silicon content on grain formation in hypoeutectic Al–Si alloys. *Materials Science and Engineering: A*. 1999. Vol. 259, no. 1, p. 43–52.
 98. EASTON, M. A and STJOHN, D. H. A model of grain refinement incorporating alloy constitution and potency of heterogeneous nucleant particles. *Acta Materialia*. 13 June 2001. Vol. 49, no. 10, p. 1867–1878. DOI 10.1016/S1359-6454(00)00368-2.
 99. TONDEL, Per Arne. *Grain refinement of hypoeutectic Al-Si foundry alloys*. Norwegian Institute of Technology, University of Trondheim, 1994.
 100. DAHLE, A. K., TØNDEL, P. A., PARADIES, C. J. and ARNBERG, L. Effect of grain refinement on the fluidity of two commercial Al-Si foundry alloys. *Metallurgical and Materials Transactions A*. 1 August 1996. Vol. 27, no. 8, p. 2305–2313. DOI 10.1007/BF02651885.
 101. FANG, Q. T. and GRANGER, D. A. Porosity formation in modified and unmodified A356 alloy castings. *AFS Transactions*. 1989. Vol. 97, p. 989–1000.
 102. DAHLE, A. K. *Mushy Zone Properties and Castability of Aluminium Foundry Alloys*. PhD Thesis. The University of Trondheim, 1996.

103. GHOMASHCHI, Reza. The evolution of AlTiSi intermetallic phases in Ti-added A356 Al-Si alloy. *Journal of Alloys and Compounds*. 5 October 2012. Vol. 537, p. 255–260. DOI 10.1016/j.jallcom.2012.04.087.
104. RANSLEY, C. E. and NEUFELD, H. The solubility of hydrogen in liquid and solid aluminium. *Journal of the Institute of Metals*. 1948. Vol. 74, no. 12, p. 599–620.
105. WHITTENBERGER, E. J. and RHINES, F. N. Origin of porosity in castings of magnesium-aluminum and other alloys. *Journal of metals*. 1952. Vol. 7, p. 409–420.
106. CHEN, X.-G. and ENGLER, S. Wasserstoff und Porosität in Aluminium-Silicium- und Aluminium-Magnesium-Legierungen. I, Aluminium-Silicium-Legierungen. *Metall*. 1991. Vol. 45, no. 10, p. 995–1000.
107. CHEN, X.-G. and ENGLER, S. Wasserstoff und Porosität in Aluminium-Silicium- und Aluminium-Magnesium-Legierungen. II: Aluminium-Magnesium-Legierungen und Diskussion über die Porenbildung. *Metall*. 1991. Vol. 45, no. 12, p. 1225–1231.
108. SIGWORTH, G. K. and CÁCERES, C. H. Porosity formation in aluminium alloy castings under quasi-directional solidification. *International Journal of Cast Metals Research*. 1 March 1997. Vol. 9, no. 6, p. 331–336. DOI 10.1080/13640461.1997.11819674.
109. TIEDJE, Niels Skat, TAYLOR, John A. and EASTON, Mark A. A new multi-zone model for porosity distribution in Al-Si alloy castings. *Acta Materialia*. May 2013. Vol. 61, no. 8, p. 3037–3049. DOI 10.1016/j.actamat.2013.01.064.
110. PELLINI, WS. RELATION OF RISER RANGE AND FEEDER ADEQUACY--PARTS I AND II. *AM FOUNDRYMAN*. 1953. Vol. 24.
111. SIGWORTH, Geoffrey K. and WANG, Chengming. Mechanisms of porosity formation during solidification: a theoretical analysis. *Metallurgical Transactions B*. 1993. Vol. 24, no. 2, p. 349–364.
112. GANDIN, Ch. -A. From constrained to unconstrained growth during directional solidification. *Acta Materialia*. 14 June 2000. Vol. 48, no. 10, p. 2483–2501. DOI 10.1016/S1359-6454(00)00070-7.

-
113. HUNT, J. D. Steady state columnar and equiaxed growth of dendrites and eutectic. *Materials Science and Engineering*. 1 July 1984. Vol. 65, no. 1, p. 75–83. DOI 10.1016/0025-5416(84)90201-5.
 114. HEIBERG, G., NOGITA, K., DAHLE, A. K. and ARNBERG, L. Columnar to equiaxed transition of eutectic in hypoeutectic aluminium–silicon alloys. *Acta Materialia*. 12 June 2002. Vol. 50, no. 10, p. 2537–2546. DOI 10.1016/S1359-6454(02)00081-2.
 115. DISPINAR, D. and CAMPBELL, J. Critical assessment of reduced pressure test. Part 2: Quantification. *International Journal of Cast Metals Research*. 1 October 2004. Vol. 17, no. 5, p. 287–294. DOI 10.1179/136404604225020704.
 116. DISPINAR, D. and CAMPBELL, J. Use of bifilm index as an assessment of liquid metal quality. *International Journal of Cast Metals Research*. 1 January 2006. Vol. 19, no. 1, p. 5–17. DOI 10.1179/136404606225023300.
 117. RAISZADEH, R. and GRIFFITHS, W. D. A method to study the history of a double oxide film defect in liquid aluminum alloys. *Metallurgical and Materials Transactions B*. 2006. Vol. 37, no. 6, p. 865–871.
 118. RAISZADEH, R. and GRIFFITHS, W.D. A Semi-empirical Mathematical Model to Estimate the Duration of the Atmosphere within a Double Oxide Film Defect in Pure Aluminum Alloy. *Metallurgical and Materials Transactions B*. April 2008. Vol. 39, no. 2, p. 298–303. DOI 10.1007/s11663-008-9142-x.
 119. ARYAFAR, Majid, RAISZADEH, Ramin and SHALBAFZADEH, Alireza. Healing of double oxide film defects in A356 aluminium melt. *Journal of Materials Science*. June 2010. Vol. 45, no. 11, p. 3041–3051. DOI 10.1007/s10853-010-4308-8.
 120. NYAHUMWA, C, GREEN, NR and CAMPBELL, J. Effect of Mold-Filling Turbulence on Fatigue Properties of Cast Aluminum Alloys (98-58). *AFS Transactions*. 1998. Vol. 106, p. 215–224.
 121. NYAHUMWA, C., GREEN, N. R. and CAMPBELL, J. The concept of the fatigue potential of cast alloys. *Journal of the Mechanical Behavior of Materials*. 1998. Vol. 9, no. 4, p. 227–236.

122. BAKHTIARANI, Fatemeh Najafzadeh and RAISZADEH, Ramin. The behaviour of double oxide film defects in Al-4.5 wt% Mg melt. *Journal of Materials Science*. 1 March 2011. Vol. 46, no. 5, p. 1305-1315. DOI 10.1007/s10853-010-4916-3.
123. BAKHTIARANI, Fatemeh Najafzadeh and RAISZADEH, Ramin. Healing of Double-Oxide Film Defects in Commercial Purity Aluminum Melt. *Metallurgical and Materials Transactions B*. 1 April 2011. Vol. 42, no. 2, p. 331-340. DOI 10.1007/s11663-011-9480-y.
124. NATEGHIAN, Morteza, RAISZADEH, Ramin and DOOSTMOHAMMADI, Hamid. Behavior of Double-Oxide Film Defects in Al-0.05 wt pct Sr Alloy. *Metallurgical and Materials Transactions B*. December 2012. Vol. 43, no. 6, p. 1540-1549. DOI 10.1007/s11663-012-9708-5.
125. BOOM, R., KAMPERMAN, A. A., DANKERT, O. and VEEN, A. Van. Argon solubility in liquid steel. *Metallurgical and Materials Transactions B*. 1 October 2000. Vol. 31, no. 5, p. 913-919. DOI 10.1007/s11663-000-0067-2.
126. GRUZLESKI, J. E. and CLOSSET, B. M. *The treatment of liquid aluminum-silicon alloys*. Des Plaines, IL: American Foundrymen's Society. Inc, 1990.
127. MONDOLFO, Lucio F. *Aluminum alloys: structure and properties*. Butterworths, 1976. ISBN 978-0-408-70680-3. Google-Books-ID: Uu5UAAAAMAAJ
128. CACERES, C. H., DAVIDSON, C. J., GRIFFITHS, J. R. and WANG, Q. G. Hypoeutectic Al-SiMg foundry alloys. [online]. 1997. [Accessed 6 July 2017]. Available from: <https://publications.csiro.au/rpr/pub?list=BRO&pid=procite:d25428e3-6283-4b55-bed0-d12f8a86ae44>
129. IWAHORI, H., YONEKURA, K., SUGIYAMA, Y., YAMAMOTO, Y. and NAKAMURA, M. Behavior of shrinkage porosity defects and limiting solid fraction of feeding on Al-Si alloys. *AFS Transactions*. 1985. Vol. 93, p. 443-451.
130. EDWARDS, G. A., SIGWORTH, G. K., CACERES, C. H., STJOHN, D. H. and BARRESI, J. Microporosity formation in Al-Si-Cu-Mg casting alloys. *AFS Transactions*. 1997. Vol. 105, p. 809-818.
131. KIM, J. M., KWON, H. W. and LOPER, C. R. L. Feeding behavior of modified and unmodified Al-Si alloys. *AFS Transactions*. 1996. Vol. 104, p. 743-749.

-
132. CHEN, X. G. and ENGLER, S. HYDROGEN AND POROSITY IN ALUMINUM-SILICON AND ALUMINUM-MAGNESIUM ALLOYS. 2. ALUMINUM-MAGNESIUM ALLOYS AND DISCUSSION ON PORE FORMATION. *Metall.* 1991. Vol. 45, no. 12, p. 1225–1231.
 133. EMADI, D and GRUZLESKI, JE. Effects of Casting and Melt Variables on Porosity in Directionally-Solidified Al-Si Alloys (94-95). . 1994. Vol. 102, p. 307–312.
 134. HOGAN, L. M. and SHAMSUZZOHA, M. Crystallography of the flake-fiber transition in the Al-Si eutectic. In : *materials forum* [online]. 1987. p. 270–277. [Accessed 2 July 2017]. Available from: http://www.academia.edu/download/40124712/M._Hogan_and_M._Shamsuzzoha_Crystallogra20151117-4107-ymlmpy.pdf
 135. GRUZLESKI, J. E. The art and science of modification: 25 years of progress. *AFS Transactions.* 1992. Vol. 100, p. 673–683.
 136. IWAHORI, H., YONEKURA, K., YAMAMOTO, Y. and NAKAMURA, M. Occurring behavior of porosity and feeding abilities of sodium- and strontium-modified Al-Si alloys. *AFS Transactions.* 1990. Vol. 98, p. 167–173.
 137. FUOCO, R., GOLDENSTEIN, H. and GRUZLESKI, J. E. Evaluation of effect of modification-induced eutectic undercooling formation in A356 Al alloy. *AFS Transactions.* 1994. Vol. 102, p. 297–306.
 138. ANSON, J. P., GRUZLESKI, J. E. and STUCKY, M. Effect of strontium concentration on microporosity in A356 aluminum alloy. *AFS Transactions.* 2001. Vol. 109, p. 3–18.
 139. ARGO, D. and GRUZLESKI, J. E. Porosity in modified aluminum alloy castings. *AFS Transactions.* 1988. Vol. 96, p. 65–74.
 140. OTTE, M. O. *Porosity Formation in AlSi9Cu3 Alloy Castings: The Influence of Iron, Strontium, Sodium, Antimony and Bismuth.* PhD. Thesis. University of Queensland, 2000.
 141. SIGWORTH, G. K., WANG, C., HUANG, H. and BERRY, J. T. Porosity formation in modified and unmodified Al-Si alloy castings. *AFS Transactions.* 1994. Vol. 102, p. 245–261.

142. MCDONALD, S, NOGITA, K, DAHLE, AK, TAYLOR, JA and JOHN, St DH. Eutectic solidification and porosity formation in Al-Si alloys: The role of strontium. . 2000. Vol. 108, p. 463–470.
143. DAHLE, AK, TAYLOR, JA and GRAHAM, D. The role of eutectic growth mode in porosity formation in Al-Si alloys. *Aluminum Transactions*. 2000. Vol. 3, no. 1, p. 17–30.
144. DAHLE, A. K., MCDONALD, S. D. and NOGITA, K. Eutectic solidification in hypoeutectic Al-Si alloys and its effect on porosity. *Advances in Aluminum Casting Technology II*. 1 January 2002. P. 1–10.
145. GRUZLESKI, John E. and CLOSSET, Bernard. *Treatment of Liquid Aluminum-Silicon Alloys*. Des Plaines, Illinois : Amer Foundrymens Society, 1990. ISBN 978-0-87433-121-9.
146. DIMAYUGA, F. C., HANDIAK, N. and GRUZLESKI, J. E. The degassing and re-gassing behavior of strontium-modified A356 melts. *AFS Transactions*. 1988. Vol. 96, p. 83–88.
147. EMADI, D., GRUZLESKI, J. E. and TOGURI, J. M. The effect of Na and Sr modification on surface tension and volumetric shrinkage of A356 alloy and their influence on porosity formation. *Metallurgical Transactions B*. 1993. Vol. 24, no. 6, p. 1055–1063.
148. ANSON, J. P., DREW, R. a. L. and GRUZLESKI, J. E. The surface tension of molten aluminum and Al-Si-Mg alloy under vacuum and hydrogen atmospheres. *Metallurgical and Materials Transactions B*. 1 December 1999. Vol. 30, no. 6, p. 1027–1032. DOI 10.1007/s11663-999-0108-4.
149. CAMPBELL, J. The origins of porosity in castings. In : *4th Asian Foundry Congress*. Broadbeach, Queensland, Australia : Australian Foundry Institute, 1996.
150. FOX, S. and CAMPBELL, J. Visualisation of oxide film defects during solidification of aluminium alloys. *Scripta materialia*. 2000. Vol. 43, no. 10, p. 881–886.
151. LIU, L., SAMUEL, A. M., SAMUEL, F. H., DOTY, H. W. and VALTIERRA, S. Influence of oxides on porosity formation in Sr-treated Al-Si casting alloys. *Journal of materials science*. 2003. Vol. 38, no. 6, p. 1255–1267.

-
152. DINNIS, C. M., DAHLE, A. K., TAYLOR, J. A. and OTTE, M. O. The influence of strontium on porosity formation in Al-Si alloys. *Metallurgical and materials transactions A*. 2004. Vol. 35, no. 11, p. 3531–3541.
 153. NOGITA, Kazuhiro, DRENNAN, John and DAHLE, Arne Kristian. Evaluation of Silicon Twinning in Hypo-Eutectic Al-Si Alloys. *MATERIALS TRANSACTIONS*. 2003. Vol. 44, no. 4, p. 625–628. DOI 10.2320/matertrans.44.625.
 154. CROSLLEY, P. B. and MONDOLFO, L. F. The modification of aluminum-silicon alloys. *AFS Transactions*. 1966. Vol. 74, p. 53–64.
 155. FLOOD, S. C. and HUNT, J. D. Modification of Al-Si eutectic alloys with Na. *Metal Science*. 1 July 1981. Vol. 15, no. 7, p. 287–294. DOI 10.1179/030634581790426813.
 156. HO, C. R. and CANTOR, B. Modification of hypoeutectic Al-Si alloys. *Journal of Materials Science*. 1 January 1995. Vol. 30, no. 8, p. 1912–1920. DOI 10.1007/BF00353013.
 157. NOGITA, K., TSUJIMOTO, K., DAHLE, A. K. and DRENNAN, J. Nucleation of eutectic silicon on aluminium phosphide in hypoeutectic Al-Si alloys. In : *18th Australian Conference on Electron Microscopy*. Geelong, Australia, 2004.
 158. MARKOV, Ivan V. *Crystal Growth for Beginners: Fundamentals of Nucleation, Crystal Growth and Epitaxy*. World Scientific, 2016. ISBN 978-981-314-386-9. Google-Books-ID: VhGyDgAAQBAJ
 159. MCDONALD, Stuart D., DAHLE, Arne K., TAYLOR, John A. and STJOHN, David H. Eutectic grains in unmodified and strontium-modified hypoeutectic aluminum-silicon alloys. *Metallurgical and Materials Transactions*. 2004. Vol. 35, no. 6, p. 1829.
 160. NOGITA, K., MCDONALD, S. D., DINNIS, C. M., LU, L. and DAHLE, A. K. Recent progress in understanding eutectic solidification in aluminium-silicon foundry alloys. *Solidification of Aluminum Alloys*. 1 January 2004. Vol. 2004, p. 93–102.
 161. JIE, Wanqi, CHEN, Zhongwei, REIF, W. and MÜLLER, K. Superheat treatment of Al-7Si-0.55Mg melt and its influences on the solidification structures and the mechanical properties. *Metallurgical and Materials Transactions A*. 1 March 2003. Vol. 34, no. 3, p. 799–806. DOI 10.1007/s11661-003-0115-z.

162. DAHLE, A. K., HJELEN, J. and ARNBERG, L. Formation of eutectic in hypoeutectic Al-Si alloys. In : *4th Decennial International Conference on Solidification Processing*. Sheffield, 1997.
163. DAHLE, A. K., NOGITA, K., MCDONALD, S. D., ZINDEL, J. W. and HOGAN, L. M. Eutectic nucleation and growth in hypoeutectic Al-Si alloys at different strontium levels. *Metallurgical and Materials Transactions A*. 2001. Vol. 32, no. 4, p. 949–960.
164. NOGITA, Kazuhiro and DAHLE, Arne Kristian. Determination of Eutectic Solidification Mode in Sr-modified Hypoeutectic Al-Si Alloys by EBSD. *Materials Transactions*. 2001. Vol. 42, no. 2, p. 207–214. DOI 10.2320/matertrans.42.207.
165. NOGITA, Kazuhiro and DAHLE, Arne Kristian. Eutectic Growth Mode in Strontium, Antimony and Phosphorus Modified Hypoeutectic Al-Si Foundry Alloys. *Materials Transactions*. 2001. Vol. 42, no. 3, p. 393–396. DOI 10.2320/matertrans.42.393.
166. NOGITA, K and DAHLE, A. K. Eutectic solidification in hypoeutectic Al-Si alloys: electron backscatter diffraction analysis. *Materials Characterization*. 1 April 2001. Vol. 46, no. 4, p. 305–310. DOI 10.1016/S1044-5803(00)00109-1.
167. NOGITA, Kazuhiro, MCDONALD, Stuart David, ZINDEL, Jacob Wesley and DAHLE, Arne Kristian. Eutectic Solidification Mode in Sodium Modified Al-7 mass%Si-3.5 mass%Cu-0.2 mass%Mg Casting Alloys. *Materials Transactions*. 2001. Vol. 42, no. 9, p. 1981–1986. DOI 10.2320/matertrans.42.1981.
168. NOGITA, K., KNUUTINEN, A., MCDONALD, S. D. and DAHLE, A. K. Mechanisms of eutectic solidification in Al-Si alloys modified with Ba, Ca, Y and Yb. *Journal of Light Metals*. 1 November 2001. Vol. 1, no. 4, p. 219–228. DOI 10.1016/S1471-5317(02)00005-6.
169. HEIBERG, G. and ARNBERG, L. Investigation of the microstructure of the Al-Si eutectic in binary aluminium–7 wt% silicon alloys by electron backscatter diffraction (EBSD). *Journal of Light Metals*. 1 February 2001. Vol. 1, no. 1, p. 43–49. DOI 10.1016/S1471-5317(00)00005-5.

-
170. MCDONALD, S. D. *Eutectic solidification and porosity formation in unmodified and modified hypoeutectic aluminium-silicon alloys*. Ph.D. Thesis. University of Queensland, 2003.
171. KNUUTINEN, A., NOGITA, K., S, McDonald and DAHLE, A. Porosity formation in aluminium alloy A356 modified with Ba, Ca, Y and Yb. *Journal of Light Metals*. 2001. Vol. 1. DOI 10.1016/S1471-5317(02)00006-8.
172. LI, J. H., YANG, Y. G., SÖMMEZ, S., TAYLOR, J. A., OBERDORFER, B., HABE, D., HEUGENHAUSER, S. and SCHUMACHER, P. Simultaneously refining eutectic grain and modifying eutectic Si in Al-10Si-0.3Mg alloys by Sr and CrB₂ additions. *International Journal of Cast Metals Research*. 3 May 2016. Vol. 29, no. 3, p. 158–173. DOI 10.1080/13640461.2015.1121340.
173. DAHLE, A.K., NOGITA, K., MCDONALD, S.D., DINNIS, C. and LU, L. Eutectic modification and microstructure development in Al–Si Alloys. *Materials Science and Engineering: A*. December 2005. Vol. 413–414, p. 243–248. DOI 10.1016/j.msea.2005.09.055.
174. NOGITA, Kazuhiro, MCDONALD, Stuart D., TSUJIMOTO, Katsuhiro, YASUDA, Kazuhiro and DAHLE, Arne K. Aluminium phosphide as a eutectic grain nucleus in hypoeutectic Al-Si alloys. *Journal of Electron Microscopy*. 1 August 2004. Vol. 53, no. 4, p. 361–369. DOI 10.1093/jmicro/dfh048.
175. GOWRI, S. and SAMUEL, F. H. Effect of alloying elements on the solidification characteristics and microstructure of Al- Si- Cu- Mg- Fe 380 alloy. *Metallurgical and Materials Transactions A*. 1 February 1994. Vol. 25, no. 2, p. 437–448. DOI 10.1007/BF02647989.
176. YEUM, K. and POIRIER, D. R. Predicting microporosity in aluminum alloys. *Light Metals*. 1988. Vol. 1988, p. 469–476.
177. CACERES, C. H., DJURDJEVIC, M. B., STOCKWELL, T. J. and SOKOLOWSKI, J. H. The effect of Cu content on the level of microporosity in Al-Si-Cu-Mg casting alloys. *Scripta Materialia*. 1999. Vol. 40, no. 5, p. 631–637.
178. ANYALEBECHI, Prince N. Analysis of the effects of alloying elements on hydrogen solubility in liquid aluminum alloys. *Scripta Metallurgica et Materialia*. 15 October 1995. Vol. 33, no. 8, p. 1209–1216. DOI 10.1016/0956-716X(95)00373-4.

179. BACKERUD, Lennart, CHAI, Guocai and TAMMINEN, Jarmo. Solidification characteristics of aluminum alloys. Vol. 2. Foundry alloys. *American Foundrymen's Society, Inc., 1990*, 1990. P. 266.
180. ROY, N., LOUCHEZ, P. R. and SAMUEL, F. H. Statistical analysis of porosity in Al-9 wt% Si-3 wt% Cu-X alloy systems. *Journal of Materials Science*. 1 January 1996. Vol. 31, no. 18, p. 4725–4740. DOI 10.1007/BF00355855.
181. PHILLIPS, H. W. L. and VARLEY, P. C. The constitution of alloys of aluminium with manganese, silicon and iron. III - the ternary system: aluminium-silicon-iron. IV - the quaternary system: aluminium-manganese-silicon-iron. *The Journal of the Institute of Metals*. 1943. Vol. 69, p. 317–350.
182. PHRAGMÉN, Gösta. On the phases occurring in alloys of aluminium with copper, magnesium, manganese, iron, and silicon. *Journal of the Institute of Metals*. 1950. Vol. 77, no. 6, p. 489–551.
183. MASCRÉ, C. Influence du fer et du manganèse sur les alliages du type de l'A-S13 (Alpax). *Fonderie*. 1955. Vol. 108, p. 4330–4336.
184. STOCKDALE, D. and WILKINSON, I. Properties of the modified aluminum-silicon alloys. *Journal of the Institute of Metals*. 1926. Vol. 36, p. 313–324.
185. TAYLOR, J. A. Metal-related castability effects in aluminium foundry alloys. *Cast Metals*. 1 January 1996. Vol. 8, no. 4, p. 225–252. DOI 10.1080/09534962.1996.11819212.
186. TAYLOR, John A. The role of iron in the formation of porosity in Al-Si-Cu alloy castings. [online]. 1 January 1997. [Accessed 7 July 2017]. Available from: <https://espace.library.uq.edu.au/view/UQ:365822>
187. CAO, X. and CAMPBELL, J. Precipitation of primary intermetallic compounds in liquid Al 11.5Si 0.4Mg alloy. *International Journal of Cast Metals Research*. 1 November 2000. Vol. 13, no. 3, p. 175–184. DOI 10.1080/13640461.2000.11819400.
188. CAO, X. and CAMPBELL, J. The nucleation of Fe-Rich phases on oxide films in Al-11.5Si-0.4Mg cast alloys. *Metallurgical and Materials Transactions A*. 1 July 2003. Vol. 34, no. 7, p. 1409–1420. DOI 10.1007/s11661-003-0253-3.

-
189. FOX, S. and CAMPBELL, J. Liquid metal quality. *International Journal of Cast Metals Research*. 1 May 2002. Vol. 14, no. 6, p. 335–340. DOI 10.1080/13640461.2002.11819451.
190. AWANO, Y. and SHIMIZU, Y. Non-equilibrium crystallization of AlFeSi compound in melt-superheated Al-Si alloy castings. *AFS Transactions*. 1990. Vol. 98, p. 889–895.
191. PENNORS, A., SAMUEL, A. M., SAMUEL, F. H. and DOTY, H. W. Precipitation of α -Al₅FeSi iron intermetallic in Al-6%Si-3.5%Cu (319) type alloys: role of Sr and P. *AFS Transactions*. 1998. Vol. 106, p. 251–264.
192. SAMUEL, A. M., PENNORS, A., VILLENEUVE, C., SAMUEL, F. H., DOTY, H. W. and VALTIERRA, S. Effect of cooling rate and Sr-modification on porosity and Fe-intermetallics formation in Al-6.5% Si-3.5% Cu-Fe alloys. *International Journal of Cast Metals Research*. 1 December 2000. Vol. 13, no. 4, p. 231–253. DOI 10.1080/13640461.2000.11819406.
193. TAYLOR, J. A., SCHAFFER, G. B. and STJOHN, D. H. The role of iron in the formation of porosity in Al-Si-Cu-based casting alloys: Part I. Initial experimental observations. *Metallurgical and Materials Transactions A*. 1 June 1999. Vol. 30, no. 6, p. 1643–1650. DOI 10.1007/s11661-999-0101-1.
194. TAYLOR, J. A., SCHAFFER, G. B. and STJOHN, D. H. The role of iron in the formation of porosity in Al-Si-Cu-based casting alloys: Part II. A phase-diagram approach. *Metallurgical and Materials Transactions A*. 1 June 1999. Vol. 30, no. 6, p. 1651–1655. DOI 10.1007/s11661-999-0102-0.
195. TAYLOR, J. A., SCHAFFER, G. B. and STJOHN, D. H. The role of iron in the formation of porosity in Al-Si-Cu-based casting alloys: Part III. A microstructural model. *Metallurgical and Materials Transactions A*. 1 June 1999. Vol. 30, no. 6, p. 1657–1662. DOI 10.1007/s11661-999-0103-z.
196. TANG, S. K. and SRITHARAN, T. Morphology of β -AlFeSi intermetallic in Al-7Si alloy castings. *Materials Science and Technology*. 1 August 1998. Vol. 14, no. 8, p. 738–742. DOI 10.1179/mst.1998.14.8.738.
197. SHANKAR, Sumanth, RIDDLE, Yancy W and MAKHLOUF, Makhlof M. Nucleation mechanism of the eutectic phases in aluminum–silicon hypoeutectic alloys. *Acta Materialia*. 6 September 2004. Vol. 52, no. 15, p. 4447–4460. DOI 10.1016/j.actamat.2004.05.045.

198. DINNIS, Cameron M., TAYLOR, John A. and DAHLE, Arne K. Iron-related porosity in Al–Si–(Cu) foundry alloys. *Materials Science and Engineering: A*. June 2006. Vol. 425, no. 1–2, p. 286–296. DOI 10.1016/j.msea.2006.03.045.
199. WANG, Junsheng, LEE, Peter D., HAMILTON, Richard W., LI, Mei and ALLISON, John. The kinetics of Fe-rich intermetallic formation in aluminium alloys: In situ observation. *Scripta Materialia*. April 2009. Vol. 60, no. 7, p. 516–519. DOI 10.1016/j.scriptamat.2008.11.048.
200. WANG, Junsheng, LI, Mei, ALLISON, John and LEE, Peter D. Multiscale modeling of the influence of Fe content in a Al–Si–Cu alloy on the size distribution of intermetallic phases and micropores. *Journal of Applied Physics*. 15 March 2010. Vol. 107, no. 6, p. 061804. DOI 10.1063/1.3340520.
201. PUNCREOBUTR, C., LEE, P. D., KAREH, K. M., CONNOLLEY, T., FIFE, J. L. and PHILLION, A. B. Influence of Fe-rich intermetallics on solidification defects in Al–Si–Cu alloys. *Acta Materialia*. 15 April 2014. Vol. 68, p. 42–51. DOI 10.1016/j.actamat.2014.01.007.
202. BONSACK, W. Effects of minor alloying elements on aluminum casting alloys: part II - aluminum-silicon alloys. *ASTM Bulletin*. 1943. Vol. 124, p. 41–51.
203. GOBRECHT, J. B. Schwereseigerungen von Eisen, Mangan und Chrom in Aluminium-Silicium-Gusslegierungen (Teil 1). *Giesserei*. 1975. Vol. 62, p. 263–266.
204. SCHMITZ, J., BRILLO, J., EGRY, I. and SCHMID-FETZER, R. Surface tension of liquid Al–Cu binary alloys. *International Journal of Materials Research*. 1 November 2009. Vol. 100, no. 11, p. 1529–1535. DOI 10.3139/146.110221.
205. KOROL'KOV, Alekseï Mikhaïlovich. *Casting properties of metals and alloys*. Consultants Bureau, 1963.
206. SIGWORTH, Geoffrey K. and WANG, Chengming. Evolution of porosity in long freezing range alloys. *Metallurgical Transactions B*. 1 April 1993. Vol. 24, no. 2, p. 365–377. DOI 10.1007/BF02659139.
207. LIU, C. Y., MURAKAMI, K. and OKAMOTO, T. Effect of capillary pressure on interdendritic liquid flow. *Acta Metallurgica*. 1 January 1986. Vol. 34, no. 1, p. 159–166. DOI 10.1016/0001-6160(86)90243-9.

-
208. CARLSON, Kent D. and BECKERMANN, Christoph. Prediction of Shrinkage Pore Volume Fraction Using a Dimensionless Niyama Criterion. *Metallurgical and Materials Transactions A*. January 2009. Vol. 40, no. 1, p. 163–175. DOI 10.1007/s11661-008-9715-y.
209. KUBO, Kimio and PEHLKE, Robert D. Mathematical modeling of porosity formation in solidification. *Metallurgical Transactions B*. 1985. Vol. 16, no. 2, p. 359–366.
210. LEE, P. D. and HUNT, J. D. Measuring the nucleation of hydrogen porosity during the solidification of aluminium-copper alloys. *Scripta Materialia*. 15 February 1997. Vol. 36, no. 4, p. 399–404. DOI 10.1016/S1359-6462(96)00411-3.
211. GANDIN, Ch. -A. and RAPPAZ, M. A coupled finite element-cellular automaton model for the prediction of dendritic grain structures in solidification processes. *Acta Metallurgica et Materialia*. 1 July 1994. Vol. 42, no. 7, p. 2233–2246. DOI 10.1016/0956-7151(94)90302-6.
212. LEE, P.D, CHIRAZI, A, ATWOOD, R.C and WANG, W. Multiscale modelling of solidification microstructures, including microsegregation and microporosity, in an Al-Si-Cu alloy. *Materials Science and Engineering: A*. January 2004. Vol. 365, no. 1–2, p. 57–65. DOI 10.1016/j.msea.2003.09.007.
213. KURZ, W., GIOVANOLA, B. and TRIVEDI, R. Theory of microstructural development during rapid solidification. *Acta Metallurgica*. 1 May 1986. Vol. 34, no. 5, p. 823–830. DOI 10.1016/0001-6160(86)90056-8.
214. ATWOOD, R. C. and LEE, P. D. Simulation of the three-dimensional morphology of solidification porosity in an aluminium–silicon alloy. *Acta materialia*. 2003. Vol. 51, no. 18, p. 5447–5466.
215. COUTURIER, G., DESBIOLLES, J. L. and RAPPAZ, M. A porosity model for multi-gas systems in multi-component alloys. *Modeling of Casting, Welding and Advanced Solidification Processes* [online]. 2006. Vol. 10. [Accessed 27 June 2017]. Available from: <https://www.esi-group.com/sites/default/files/resource/publication/1607/couturier-mcwasp-2006.pdf>

216. GARB, Christian. *Materialmodellentwicklung für die betriebsfeste Auslegung von Aluminiumgussbauteilen unter Berücksichtigung mikrostruktureller Größen*. Dissertation. Montanuniversität Leoben, 2018.
217. MEISHNER, H. and FEIKUS, F. J. Gießverfahren zur Herstellung von Aluminium-Zylinderköpfen und -Zylinderkurbelgehäusen [Casting processes for aluminium cylinder head and crankcase production]. *Giesserei*. 2015. Vol. 102, p. 34–41.
218. OBERSCHELP, C., KIRCHMEIER, H., HUBER, G., WAGNER, A., HUBER, J. and STIKA, P. Einsatz dynamischer Gießverfahren bei der Herstellung hoch belasteter Zylinderköpfe [Application of dynamic castings processes in highly stressed cylinder heads]. *Giesserei*. 2011. Vol. 98, p. 26–35.
219. DJURDJEVIĆ, M. B., ODANOVIĆ, Zoran and PAVLOVIĆ-KRSTIĆ, Jelena. Melt quality control at aluminum casting plants. *Metallurgija*. 2010. Vol. 16, no. 1, p. 63–76.
220. *HYCAL Analysis & Control*. EMC Hycal Limited.
221. CAMPBELL, John. *Complete Casting Handbook: Metal Casting Processes, Metallurgy, Techniques and Design*. Butterworth-Heinemann, 2015. ISBN 978-0-08-100120-2. Google-Books-ID: FLiZBQAAQBAJ
222. *BDG-Guideline VDG-Data sheet P220*. July 2011. BUNDESVERBAND DER DEUTSCHEN GIESSEREI-INDUSTRIE (BDG).
223. WANG, Q. G., APELIAN, D and LADOS, D. A. Fatigue behavior of A356-T6 aluminum cast alloys. Part I. Effect of casting defects. *Journal of Light Metals*. 1 February 2001. Vol. 1, no. 1, p. 73–84. DOI 10.1016/S1471-5317(00)00008-0.
224. WEIDT, M., HARDIN, R. A., GARB, C., ROSC, J., BRUNNER, R. and BECKERMANN, C. Prediction of porosity characteristics of aluminium castings based on X-ray CT measurements. *International Journal of Cast Metals Research*. 9 May 2018. P. 1–19. DOI 10.1080/13640461.2018.1467105.
225. WANG, Q. G. and JONES, P. E. Prediction of Fatigue Performance in Aluminum Shape Castings Containing Defects. *Metallurgical and Materials Transactions B*. 18 September 2007. Vol. 38, no. 4, p. 615–621. DOI 10.1007/s11663-007-9051-4.

-
226. MURAKAMI, Yukitaka. *Metal Fatigue: Effects of Small Defects and Nonmetallic Inclusions*. Elsevier, 2002. ISBN 978-0-08-049656-6. Google-Books-ID: FJ_DBHkW9K8C
227. DISPINAR, D. and CAMPBELL, J. Critical assessment of reduced pressure test. Part 1: Porosity phenomena. *International Journal of Cast Metals Research*. 1 October 2004. Vol. 17, no. 5, p. 280–286. DOI 10.1179/136404604225020696.
228. HENSON, Mark. *Private communication with Mark Henson, EMC Limited*. 28 May 2018.

8. Curriculum vitae

Personal information:

Name: Moritz Rudolf Martin Weidt
Date of birth: 19.07.1987 in Duisburg, Germany
Nationality: German
Marital status: married

Education:

1997 – 2006 Secondary school, Luisenschule (Gymnasium) in Mülheim an der Ruhr, Germany
2007 – 2010 Studies of materials engineering, RWTH Aachen University, degree: B.Sc.
2010 – 2012 Studies of materials engineering, RWTH Aachen University, degree: M.Sc.

Professional activity:

2007 – 2007 Internship, MAN Turbo AG, Oberhausen, Germany
2010 – 2010 Internship, ThyssenKrupp Steel Europe AG, Essen, Germany
2011 – 2011 Internship, MAGMA Gießereitechnologie GmbH, Aachen, Germany
2012 – 2018 Development Engineer, MAGMA Gießereitechnologie GmbH, Aachen, Germany
2019 – Today Application Engineer, MAGMA Engineering (Suzhou) Co., Ltd, Suzhou, P.R. China

Suzhou, People's Republic of China, 26 August 2019

9. Scientific publications

1. WEIDT, M., HARDIN, R. A., GARB, C., ROSC, J., BRUNNER, R. and BECKERMANN, C. Prediction of porosity characteristics of aluminium castings based on X-ray XCT measurements. *International Journal of Cast Metals Research*. 9 May 2018. P. 1–19. DOI 10.1080/13640461.2018.1467105.
2. GARB, C., LEITNER, M., TAUSCHER, M., WEIDT, M. and BRUNNER, R. Statistical analysis of micropore size distributions in Al–Si castings evaluated by X-ray computed tomography. *International Journal of Materials Research* [online]. 29 August 2018. [Accessed 4 September 2018]. DOI 10.3139/146.111685.
3. WEIDT, M. and BÜHRIG-POLACZEK, A. Integration der Mikroporositätsvorhersage in die schwingfeste und robuste Auslegung von hochbelasteten Aluminiumgussteilen. *Giesserei-Special*. 2019. Vol. 02, p. 60–67.

Obwohl die Bedeutung von Aluminium als Werkstoff für eine Vielzahl von technischen Anwendungen bereits sehr hoch ist, hat der allgemeine Trend zur Gewichtsreduktion im Mobilitätsbereich das Potenzial, den Einsatz von Aluminium in Strukturbauteilen sowie in Gehäusen, Abdeckungen und im Antriebsstrang noch weiter zu verstärken. Das Aluminiumgussverfahren ist und bleibt ein sehr wettbewerbsfähiges Verfahren zur Herstellung hochkomplexer und integrierter, endkonturnaher Bauteile bis hin zur Großserie. Dies ist der Fall, obwohl die Fähigkeit der qualitativen sowie quantitativen Mikroporositätsvorhersage bis heute eingeschränkt und damit eine genaue Kontrolle nicht möglich ist. Um diese Vorhersagegenauigkeit zu erreichen ist ein besseres Verständnis der Ursachen, der Keimbildung, des Wachstums und der endgültigen Eigenschaften der Mikroporosität in Aluminiumgusslegierungen erforderlich. Ziel dieser Arbeit ist es das Verständnis und das Wissen über Mikroporosität, aufbauend auf den Grundlagen der Erstarrung sowie durch die Auswertung von beinahe 100 Mikro-CT-Scans, zu erweitern und zu vertiefen. Um den Vergleich von XCT-Daten, welche bei drei unterschiedlichen Scanauflösungen erzeugt wurden, zu ermöglichen, wurde ein porenvolumengewichteter Ansatz entwickelt und angewendet. In bis zu vier identifizierbaren Porenpopulationen erlaubt die beschriebene Methode die lineare Korrelation zwischen der Porosität und dem maximalen und mittleren Porenvolumen sowie der charakteristischen Porengröße. Die vier verschiedenen Porenpopulationen können sowohl mit dem Wasserstoffgehalt als auch mit der lokale Abkühlrate in Verbindung gebracht werden. Bei niedrigen Wasserstoffgehalten bestimmen die Unterschiede in der Erstarrungsmorphologie aufgrund der chemischen Zusammensetzung die Höhe der Porosität. Die maximale Porengröße nimmt mit der durchschnittlichen Porosität stark zu. Nur sehr geringe lokale Abkühlraten verändern die beobachtete Porenmorphologie von toridiert nach hoch sphärisch. Bei hohen Wasserstoffkonzentrationen ist die Empfindlichkeit des mittleren und maximalen Porenvolumens und der Porengröße in Bezug auf die durchschnittliche Porosität geringer. Die lokale Abkühlrate beeinflusst die Porosität nun stark. In der Übergangszone zwischen einem niedrigen und hohen Wasserstoffgehalt ist eine Mischung aus Poren mit hoher und niedriger Sphärizität zu beobachten. Bei niedrigem Wasserstoffgehalt zeigt die Analyse der Porensphärizität einen konstanten Abfall mit zunehmender Porosität. Bei mittleren bis hohen Wasserstoffgehalten zeigen die Proben eine konstante und hohe Sphärizität. Es kann eine lineare Funktion zwischen dem mittleren und maximalen Porenvolumen beziehungsweise der mittleren und maximalen Porengröße nachgewiesen werden. Diese Korrelationen sind unabhängig von allen untersuchten Versuchsparametern und stellen somit ein neues und grundlegendes Merkmal von Mikroporosität in Aluminiumgusslegierungen dar. Die vorgestellten Ergebnisse verbessern das Verständ-

nis der Eigenschaften von Mikroporosität und ermöglichen die Vorhersage wichtiger Charakteristika der Porenverteilung. Im Rahmen einer geschlossenen Simulationskette, können die entwickelten Korrelationen dazu beitragen hoch und speziell zyklisch beanspruchte Komponenten bereits am Beginn des Designprozesses optimal auszulegen.

Although the importance of aluminium as a material for a broad variety of technical applications is already very high, the general trend of weight reduction in the mobility sector has the potential to boost the application of aluminium in structural components as well as in housings, covers and the powertrain even further. The aluminium cast process is and remains a very competitive process to produce highly complex and integrated, near-net-shape components up to very large production volumes. This is true, although the capability to predict and thus control the amount and size of microporosity is still worthy of improvement. To achieve better control of microporosity, a better understanding of the causes, the nucleation, the growth, and the final characteristics of microporosity in aluminium cast alloys are necessary. This work aims to expand and deepen the understanding and knowledge of microporosity by looking at the fundamental principles of solidification, and the evaluation of almost 100 micro XCT scans taken from industrial castings and laboratory casting experiments. A pore volume-weighted approach is applied to enable the comparison of XCT data generated at three different spatial resolutions. The weighing procedure leads to linear correlations between average porosity and the maximum and mean pore volume and size for up to four characteristic specimen populations. The four different specimen populations can be related to the hydrogen content as well as the local cooling rate. At low hydrogen levels, the differences in solidification morphology due to chemical composition determine the amount of average porosity. The maximum pore size increases strongly with average porosity, and only very low local cooling rates change the observed low sphericity pore morphology. At high hydrogen levels, the sensitivity of the mean and maximum pore volume and size is lower in respect to average porosity, and the local cooling rate strongly affects the observable high sphericity pores. In the transition zone between low and high hydrogen levels, a mixture of high and low sphericity pores can be observed. For low hydrogen levels, the analysis of the mean pore sphericity shows a constant drop with increasing average porosity. At medium to high hydrogen levels samples show a constant and high mean sphericity value. A single linear relation between the mean and maximum pore volume respectively the mean and maximum pore size can be established. These correlations are independent of all varied experimental parameters and therefore constitute a new and fundamental characteristic of microporosity in aluminium cast alloys. The presented findings improve the understanding of the characteristics of microporosity and allow the prediction of important pore distribution measures. The developed correlations will find application in the Integrated Computational Materials Engineering (ICME) approach and are the first step in a through process modelling framework.

